INFORMATION TO USERS

This manuscript has been reproduced from the microfilm master. UMI films the text directly from the original or copy submitted. Thus, some thesis and dissertation copies are in typewriter face, while others may be from any type of computer printer.

The quality of this reproduction is dependent upon the quality of the copy submitted. Broken or indistinct print, colored or poor quality illustrations and photographs, print bleedthrough, substandard margins, and improper alignment can adversely affect reproduction.

In the unlikely event that the author did not send UMI a complete manuscript and there are missing pages, these will be noted. Also, if unauthorized copyright material had to be removed, a note will indicate the deletion.

Oversize materials (e.g., maps, drawings, charts) are reproduced by sectioning the original, beginning at the upper left-hand corner and continuing from left to right in equal sections with small overlaps.

Photographs included in the original manuscript have been reproduced xerographically in this copy. Higher quality 6" x 9" black and white photographic prints are available for any photographs or illustrations appearing in this copy for an additional charge. Contact UMI directly to order.

ProQuest Information and Learning
300 North Zeeb Road, Ann Arbor, MI 48106-1346 USA
800-521-0600

DYNAMIC PULSE BUCKLING OF SLENDER BEAMS WITH GEOMETRIC IMPERFECTIONS SUBJECTED TO AN AXIAL IMPACT

by

SHAWN KENNY

A Thesis Submitted to the
Faculty of Engineering
in Partial Fulfillment of the Requirements
for the Degree of

DOCTOR OF PHILOSOPHY

Major Subject: Department of Civil Engineering

APPROVED:

Dr. Farid Taheri, Supervisor

Dr. Neil Pegg, Co-Supervisor

Dr. M Chernuka

Dr. V.S. Hoa, External Examiner

DALHOUSIE UNIVERSITY – DALTECH

Halifax, Nova Scotia 2001

National Library
of Canada

Acquisitions and
Bibliographic Services

395 Wellington Street
Ottawa ON K1A 0N4
Canada

Bibliothèque nationale
du Canada

Acquisitions et
services bibliographiques

395, rue Wellington
Ottawa ON K1A 0N4
Canada

Your file Votre référence

Our file Notre référence

The author has granted a non-exclusive licence allowing the National Library of Canada to reproduce, loan, distribute or sell copies of this thesis in microform, paper or electronic formats.

The author retains ownership of the copyright in this thesis. Neither the thesis nor substantial extracts from it may be printed or otherwise reproduced without the author's permission.

L'auteur a accordé une licence non exclusive permettant à la Bibliothèque nationale du Canada de reproduire, prêter, distribuer ou vendre des copies de cette thèse sous la forme de microfiche/film, de reproduction sur papier ou sur format électronique.

L'auteur conserve la propriété du droit d'auteur qui protège cette thèse. Ni la thèse ni des extraits substantiels de celle-ci ne doivent être imprimés ou autrement reproduits sans son autorisation.

0-612-63478-7

Canada

DALTECH LIBRARY

"AUTHORITY TO DISTRIBUTE MANUSCRIPT THESIS"

TITLE:

DYNAMIC PULSE BUCKLING OF SLENDER BEAMS WITH GEOMETRIC IMPERFECTIONS SUBJECTED TO AN AXIAL IMPACT

The above library may make available or authorize another library to make available individual photo/microfilm copies of this thesis without restrictions.

Full Name of Author: Shawn Kenny

Signature of Author:

Date: 01/26/2001

To my parents, Ed and Joan, for their sacrifice and love.

A la mia cara amica Paola.

Table of Contents

LIST OF TABLES ix

LIST OF FIGURES xii

NOMENCLATURE xxiii

ACKNOWLEDGEMENTS xxviii

ABSTRACT xxix

1.0 DYNAMIC BUCKLING OF STRUCTURES 1

1.1 Background 1

1.2 Rationale for Research and Design 2

1.2.1 Engineering Problems in Dynamics 2

1.2.2 Dynamic Pulse Buckling Analysis 3

1.3 Motivation for the Research Activities 5

1.3.1 Elastic Pulse Buckling 7

1.4 Overview of Thesis Investigations 9

2.0 DYNAMIC ELASTIC BUCKLING OF SLENDER BEAMS 11

2.1 Dynamic Equation of Motion 11

2.2 Dynamic Elastic Buckling 14

2.2.1 Fundamental Mode Response 14

2.2.2 Higher Order Modal Response Studies 21

2.2.3 Mode Perturbation Methods 26

2.3.4 Elastic Buckling Criterion 33

3.0 FINITE DIFFERENCE ANALYSIS OF ELASTIC PULSE BUCKLING EVENTS .. 40

3.1 Finite Difference Formulation 40

3.2 Stability Analysis 42

3.3 Elastic Pulse Buckling Analysis 45
3.3.1 Beam Model Parameters 46
3.3.2 Fundamental Mode Imperfection 46
3.3.3 Combined Geometric Imperfections 49
3.3.4 Random Geometric Imperfections 52
3.4 Elastic Pulse Buckling Threshold Limits 64
3.5 Assessment of Finite Difference Models 69

4.0 FINITE ELEMENT ANALYSIS OF ELASTIC PULSE BUCKLING EVENTS 71
4.1 Modelling Considerations 71
4.1.1 Solution Strategies in Structural Dynamic Analysis 71
4.1.2 Modelling Procedure for Pulse Buckling Analysis 75
4.2 Preliminary Investigations 77
4.3 Pulse Buckling Analysis – Beam Elements 79
4.3.1 Introduction 79
4.3.2 Buckled Displacement Response 79
4.3.3 Modal Response Analysis 82
4.4 Pulse Buckling Analysis - Plane Strain Elements 84
4.4.1 Introduction 84
4.4.2 Buckled Displacement Response 86
4.4.3 Modal Response Analysis 90
4.5 Elastic Pulse Buckling Criterion 96
4.6 Conclusions of the Finite Element Analysis 98

5.0 DYNAMIC PLASTIC ANALYSIS 100
5.1 Classical Plasticity Theory 100
5.2 Propagation of Elastoplastic Stress Waves 105
5.3 Strain Rate Effects due to Dynamic Loading 106
5.3.1 Introduction 106
5.3.2 Evaluating Dynamic Mechanical Properties 110

5.3.3 Characteristics of Aluminum 6061-T6 and Mild Steel 111
5.4 Dynamic Plastic Buckling 112
5.4.1 Experimental Studies 114
5.4.2 Simplified Analytical Methods 121
5.4.3 Idealized Mechanical Models 123
5.4.4 Modal Perturbation Analysis 130
5.4.5 Numerical Modeling 134

6.0 EXPERIMENTAL PROGRAM 137
6.1 Experimental Investigations 138
6.1.1 Experimental Apparatus and Procedure 138
6.1.2 Experimental Study Parameters 142
6.2 Analysis of Experimental Data 144
6.2.1 Importance of the Applied Boundary Condition 144
6.2.2 General Response Characteristics 146
6.2.3 Normalized Response Parameter 148
6.2.4 Peak Buckle Displacement Response Analysis 152
6.2.5 Wavelength Analysis 157

7.0 FINITE ELEMENT ANALYSIS OF PLASTIC PULSE BUCKLING EVENTS 164
7.1 Introduction 164
7.2 Model Parameters and Formulation 165
7.3 Finite Element Model Sensitivity Analyses 167
7.3.1 Influence of Boundary Conditions 170
7.3.2 Influence of Imperfection Models 173
7.3.3 Influence of Element Formulation 174
7.3.4 Influence of Constitutive Relationships 175
7.3.5 Influence of Contact Mechanics 176
7.3.6 Influence of Element Aspect Ratio 183
7.4 Peak Buckle Response Analysis 183

7.5 Assessment of the Pulse Buckling Analysis 188
7.5.1 Direct Integration Procedures 190
7.5.2 Element Formulation 191
7.5.3 Constitutive Relationship 192
7.6 Dynamic Plastic Pulse Buckling Criteria 196

8.0 SUMMARY AND CONCLUSIONS 199
8.1 Scope of Analysis 199
8.2 Elastic Pulse Buckling 200
8.3 Experimental Investigations 202
8.4 Plastic Pulse Buckling 203
8.5 Recommendations for Future Research 204
8.5.1 Dynamic Elastic Pulse Buckling 204
8.5.2 Experimental Investigations 205
8.5.3 Dynamic Plastic Pulse Buckling 205

REFERENCES 207

APPENDIX A PRELIMINARY ELASTIC PULSE BUCKLING ANALYSIS 219
A.1 Introduction 219
A.2 Beam Element Models 219
A.2.1 Fundamental Mode Imperfection 219
A.2.2 Combined Geometric Imperfections 222
A.2.3 Random Geometric Imperfections 224
A.3 Pulse Buckling Analysis - Plane Strain Elements 225
A.3.1 Buckled Displacement Response 225
A.3.2 Requirement for Nonlinear Plastic Analysis 226
A.3.3 Discrete Fourier Transform Analysis 227

APPENDIX B NOTES ON EXPERIMENTAL INVESTIGATIONS 242
B.1 Preliminary Impact Investigations 242
B.2 Experimental Data Measurement 243
B.2.1 Data Acquisition System 243
B.2.2 Impact Velocity 243
B.2.3 Accelerometer and Displacement Transducer Sensors 244
B.2.4 Foil Strain Gauges 244
B.2.5 Applied Boundary Condition 246
B.3 Detailed Experimental Procedure 247

APPENDIX C EXPERIMENTAL DATA 257
C.1 Series AI – 6061-T6 Aluminum Bars 260
C.2 Series AII – 6061-T6 Aluminum Bars 272
C.3 Series SI – Cold Rolled 1018 Steel 283

APPENDIX D SENSITIVITY ANALYSIS OF PLASTIC PULSE BUCKLING 297
D.1 Analysis of Boundary Conditions 297
D.2 Analysis of Imperfection Models 297
D.3 Analysis of Element Formulation 298
D.4 Analysis of Constitutive Relationships 298

List of Tables

Table 2-1. Summary of Research Investigations Focused on the Dynamic Fundamental Mode Elastic Buckling Response. 16

Table 3-1. Critical Time Step (Δt_{cr}) Required for a Stable Finite Difference Solution... 46
Table 3-2. Finite Difference Models with Discrete Fundamental Mode Imperfection. .. 47
Table 3-3. Finite Difference Models with Combined Geometric Imperfections..... 50
Table 3-4. Finite Difference Models with Random Geometric Imperfections..... 53
Table 3-5. Summary of Peak Buckle Amplitude (w_{max}), Weighted Mean Buckle Amplitude (w_{wm}) and Wavelength Response (lwm) for Model FD10..... 64

Table 4-1. Summary of Parameters for Preliminary Finite Element Investigations..... 77
Table 4-2. Beam Element Models for Pulse Buckling Analysis. 79
Table 4-3. Plane Strain Element Models with Random Geometric Imperfections..... 86
Table 4-4. Modal Response Characteristics for Model AP8. 96

Table 6-1. Test Parameters for Series AI - 6061-T6 Aluminum ($d = 3.175mm$). 143
Table 6-2. Test Parameters for Series AII - 6061-T6 Aluminum ($d = 4.7625mm$)..... 143
Table 6-3. Test Parameters for Series SI - Cold Rolled 1018 Steel ($d = 3.175mm$)..... 143
Table 6-4. Summary of Mean Characteristics for Analyzed Experimental Impact Events..... 149
Table 6-5. Comparative Assessment of Relative Inertia, Modal and Rigidity Parameters for the Test Series *AI*, *AII* and *SI*. 151
Table 6-6. Experimentally Measured Peak Buckle Half-Wavelength and Predicted Half-Wavelength Response Assuming Elastic and Elastic, Perfectly Plastic Material Behaviour..... 160

Table 7-1. Parameters for Finite Element Analysis of Dynamic Plastic Pulse Buckling. 166
Table 7-2. Parameter Matrix for Finite Element Models with Bilinear Elastoplastic, Linear Strain Hardening Material Behaviour. 169
Table 7-3. Parameter Matrix for Finite Element Models with Elastic, Perfectly Plastic Material Behaviour. 169
Table 7-4. Analytical, Experimental and Finite Element Investigations on the Peak Buckle Half-Wavelength (L_{PK}) Response. 188
Table 7-5. Computed and Theoretical Critical Buckling Times. 198

Table A-1. Critical Integration Time Step as a Function of Aspect Ratio for Beam Elements. 229
Table A-2. Parameters for Beam Element Models with Discrete Fundamental Mode Imperfection. 229
Table A-3. Parameters for Beam Element Models with Combined Geometric Imperfections. 230
Table A-4. Parameters for Beam Element Models with Random Geometric Imperfections. 230
Table A-5. Critical Integration Time Step as a Function of Aspect Ratio for Plane Strain Element Models. 231
Table A-6. Parameters for Plane Strain Element Models with Random Geometric Imperfections. 231

Table B-1. Notes for the Impact Tests Instrumented with Foil Strain Gauges. 249
Table B-2. Notes for Individual Impact Tests of the Experimental Investigations with Questionable Buckling Response. 249

Table C-1. Total Number of Impact Tests for the Experimental Investigations. 258

Table C-2. Notes for Individual Impact Tests of the Experimental Investigations with Questionable Buckling Response. 259
Table C-3. Notes for the Impact Tests Instrumented with Strain Gauges. 259

List of Figures

Figure 1-1. Automotive Industry Crashworthiness Study (a) Action Photo during Impact, (b) Post-Test Damage. (IIHS, 1998). 4
Figure 1-2. Numerical Simulation of Passenger Train Car Impacting a 50 ton Mass (a) Crushing Behavior of Car, (b) Detail of Center Sill Collapse. (SRI, 1998). 5

Figure 2-1. (a) Simply Supported Bar Subject to an Impulsive Axial Load and (b) Free Body Diagram of a Bar Element (Lindberg and Florence, 1987)..... 12
Figure 2-2. Schematic Illustration of Dynamic Buckling Experiments Conducted by Gerard and Becker (1952) and Lindberg (1965)..... 24
Figure 2-3. Amplification Function Gn(h,t) as a Function of the Wavenumber (h)..... 30
Figure 2-4. Growth Rate of the Peak Magnitude for the Amplification Function $G_n(\eta, \tau)$. 30
Figure 2-5. Mean Wavelength (λ_m) and Most Amplified Wavelength (λ_a) Response as a Function of Nondimensional Time (τ)..... 34
Figure 2-6. Schematic Illustration of the Dynamic Buckling Criterion..... 35
Figure 2-7. Relationship Between the Dynamic Load Factor (DLF) and Effective Slenderness Ratio (L_e/r) for Aluminum and Steel Columns (Ari-Gur et al., 1982). .. 36
Figure 2-8. Analytical Curves Defining the Critical Impulse Intensity to Yield for the Peak Buckle Crest Based on the "Preferred" Mode Analysis. Data Points are from Experimental Studies presented by Lindberg and Florence (1987)..... 38

Figure 3-1. Nondimensional Peak Buckle Amplitude (w_{max}) as a Function of Time (τ) for Finite Difference Models with Discrete Fundamental Mode Imperfection..... 49
Figure 3-2. Nondimensional Peak Buckle Amplitude (wmax) as a Function of Time (τ) for Finite Difference Models with Discrete and Combined Geometric Imperfections. 52

Figure 3-3. Nondimensional Buckle Profile (w) as a Function of Nondimensional Axial Coordinate (ξ) and Time (τ) for (a) Finite Difference Model FD10, (b) Digitised Buckle Profile Computed by Lindberg and Florence (1987)..... 54

Figure 3-4. Nondimensional Peak Buckle Amplitude (w_{max}) as a Function of Time (τ) for Finite Difference Models with Random Geometric Imperfections. 55

Figure 3-5. Nondimensional Buckled Wavelength (λ) as a Function of Time (τ) for Finite Difference Models with Random Geometric Imperfections. 57

Figure 3-6. Nondimensional Deformed Geometry Profiles for Model FD6 and Model FD10 at $\tau = 10.6$ ($t = 48$ms)..... 58

Figure 3-7. (a) Theoretical and (b) Experimental Nondimensional Buckle Wavelength (l) Response (Lindberg and Florence, 1987). 59

Figure 3-8. Relative Frequency Distribution of Nondimensional Buckle Wavelengths (l) for Model FD10 at Solution Times (a) $\tau = 1.1, 3.2$ and (b) $\tau = 6.4, 11$..... 61

Figure 3-9. Observed Buckled Profiles from Experimental Investigations. (Lindberg and Florence, 1987). 62

Figure 3-10. Nondimensional Buckle Amplitude (w) as a Function of Nondimensional Buckle Wavelength (λ) for Model FD10 at (a) $\tau = 1.1, 3.2$ and (b) $\tau = 6.4, 11$..... 63

Figure 3-11. Influence of Aspect Ratio on the Computed Normalized Stress Ratio for Finite Difference Models. 67

Figure 3-12. Analytical and Numerical Analysis for Critical Impulse Intensity to Yield for the Peak Buckle Crest Based on the "Preferred" Mode Analysis. 68

Figure 4-1. Nondimensional Peak Buckle Amplitude (wmax) as a Function of Time (t) for Finite Difference and Finite Element Models with Discrete, Combined and Random Geometric Imperfections. 80

Figure 4-2. Nondimensional Buckled Wavelength (λ) as a Function of Time (τ) for Finite Difference and Beam Element Models with Combined and Random Geometric Imperfections (■ λ_{avg} , □ λ_{wm})..... 83

Figure 4-3. Normalized Longitudinal Distribution $(\bar{X})$ of the Normalized Stress for Beam Element Model ANB12 with Random Imperfections. 85
Figure 4-4. Normalized Longitudinal Distribution $(\bar{X})$ of the Displaced Buckled Profile for Beam Element Model (*ANB14*) and Plane Strain Element Model (*AP8*) with Random Geometric Imperfections at Solution Time ($\tau = 22$). 87
Figure 4-5. Nondimensional Peak Buckle Amplitude (w_{max}) as a Function of Time (τ) for Finite Difference and Finite Element Models (Beam, Plane Strain) with Combined and Random Geometric Imperfections. 89
Figure 4-6. Nondimensional Buckled Wavelength (λ) as a Function of Time (τ) for Finite Difference and Finite Element Models (Beam, Plane Strain) with Random Geometric Imperfections (■ λ_{avg} , □ λ_{wm}). 91
Figure 4-7. Relative Frequency Distributions of Nondimensional Buckle Wavelengths (λ) for Plane Strain Element Model AP8 at (a) Solution Times $\tau = 5.5$ and 11 and (b) Solution Times $\tau = 22$ and 33. 93
Figure 4-8. Nondimensional Buckle Amplitude (w) as a Function of Nondimensional Buckle Wavelengths (λ) for Plane Strain Element Model AP8 at (a) Solution Times $\tau = 5.5$ and 11 and (b) Solution Times $\tau = 22$ and 33. 95
Figure 4-9. Critical Threshold Pulse Duration (tcr) for Section Yield Response as a Function of Normalized Compressive Stress Impulse Ratio 97

Figure 5-1. Two-Dimensional Representation of the von Mises Yield Surface. 101
Figure 5-2. Graphical Representation of Strain Hardening Rules (a) Perfectly Plastic, (b) Isotropic Hardening and (c) Kinematic Hardening. 104
Figure 5-3. Wave Front Dispersion as a Function of Time and Stress Level. 107
Figure 5-4. Idealizated Stress-Strain Response for a Ductile Material (a) Elastic-Perfectly Plastic, (b) Bilinear Elastoplastic, (c) Rate-Dependent Elastoplastic, and (d) Rate Dependent, Path-Dependent Elastoplastic. 109

Figure 5-5. Post-Test Buckled Mode Shapes for 12.3mm Diameter Aluminum Rods (a) Projectile, (b) Impacted Bar (Bell, 1988)..... 115
Figure 5-6. Digitised Profiles of Experimental Buckled Mode Shapes of Aluminum Bars Subject to Axial Impact by a Free Fall Hammer (Ari-Gur et al., 1982)..... 117
Figure 5-7. Dynamic Plastic Buckling of a Rod by Longitudinal Impact (Lindberg and Florence, 1987)..... 117
Figure 5-8. Axial Strain as a Function of Distance from the Impacted End (Abrahamson and Goodier, 1966)..... 118
Figure 5-9. Ratio of Kinetic Energy (V_{KE}) to Elastic Strain Energy (V_E) as a Function of Axial Displacement (Abrahamson and Goodier, 1966)..... 120
Figure 5-10. Measured Half-wavelength Response as a Function of Axial Strain (Abrahamson and Goodier, 1966)..... 120
Figure 5-11. Investigations of Calladine and English (1984), (a) Schematic illustration of Type II Structure Loading Event and (b) Load-Deformation Response..... 125
Figure 5-12. Idealised Mechanical Model (Karagiozova and Jones, 1995)..... 127
Figure 5-13. (a) Critical Impact Velocity (V_o) as a Function of the Mass Ratio (M/m_1) and Strain Hardening Parameter (λ), (b) Critical Impact Velocity as a Function of Geometric Imperfection $\left(\overline{\xi}\right)$ and Mass Ratio (Karagiozova and Jones, 1995b)..... 129
Figure 5-14. Amplification Function for (a) Initial Velocity Perturbations, and (b) Initial Geometric Imperfections. (Abrahamson and Goodier, 1966)..... 133

Figure 6-1. Test Frame for Dynamic Impact Experiments..... 139
Figure 6-2. Upper Slide-Bearing Restraint and Impact Mass Assembly..... 140
Figure 6-3. (a) Initial and (b) Deformed Buckled Geometry Profiles for Impact Tests *AId1* and *AId4*..... 145
Figure 6-4. Deformed Buckled Profiles for Tests *AId4* through *AId5*..... 146
Figure 6-5. Representative Buckled Profiles for Series *AI* – 6061-T6 Aluminum..... 147
Figure 6-6. Representative Buckled Profiles for Series *AII* – 6061-T6 Aluminum..... 147
Figure 6-7. Representative Buckled Profiles for Series *SI* - CR 1018 Steel..... 148

Figure 6-8. Conceptual basis for analysis of the experimental data. 150
Figure 6-9. Axial Coordinate $(\bar{x})$ of the Peak Buckle Crest as a Function of the Effective Slenderness Ratio (L_e/r). 153
Figure 6-10. Transverse Deflection $(\bar{x})$ of the Peak Buckle Crest as a Function of the Effective Slenderness Ratio (L_e/r). 153
Figure 6-11. Normalized Mean Axial Response $(\overline{N}\,\bar{x})$ of the Peak Buckle Crest as a Function of the Effective Slenderness Ratio (L_e/r). 155
Figure 6-12. Normalized Mean Transverse Response $(\overline{N}\,\bar{y})$ of the Peak Buckle Crest as a Function of the Effective Slenderness Ratio (L_e/r). 155
Figure 6-13. Representative Examples of Half-Wavelength Response Analysis. 158
Figure 6-14. Mean Half-Wavelength Response for Series *AI*. 162
Figure 6-15. Mean Half-Wavelength Response for Series *AII*. 162
Figure 6-16. Mean Half-Wavelength Response for Series *SI*. 163

Figure 7-1. Schematic Illustration of the Modelled Boundary Conditions. 167
Figure 7-2. Comparison of the Computed Finite Element Response for the Actual and Idealized Boundary Conditions with Respect to the Characteristic (Test *AIc7*) and Spurious (Test *AIc2*) Experimental Buckling Events. 172
Figure 7-3. Impulse Load-Time History for Beam and Plane Strain Element Models with Random Geometric Imperfections for Test Series *AIa* and *AIc*. 178
Figure 7-4. Impact Velocity of the Free Fall Hammer for Beam and Plane Strain Element Models with Random Geometric Imperfections for Test Series *AIa* and *AIc*. 178
Figure 7-5. Computed Buckled Profile Displacement-Time History of Series *AIc* for Plane Strain Element Models with (a) Discrete and (b) Random Geometric Imperfections. 179
Figure 7-6. Buckled Profile Displacement-Time History of Series *AIe* for (a) Beam and (b) Plane Strain Element Models with Discrete Geometric Imperfection. 180

Figure 7-7. Normalized Axial Modal Response $(\overline{N}\,\overline{x})$ of the Peak Buckle Crest as a Function of the Effective Slenderness Ratio (L_e/r) for Finite Element Models with (a) Beam Elements, (b) Plane Strain Elements. 184

Figure 7-8. Normalized Mean Transverse Modal Response $(\overline{N}\,\overline{y})$ of the Peak Buckle Crest as a Function of the Effective Slenderness Ratio (L_e/r) for Finite Element Models with (a) Beam Elements, (b) Plane Strain Elements. 185

Figure 7-9. Mean Half-Wavelength Response of the Peak Buckle Crest for the Finite Element Models (a) Series *AI*, and (b) Series *AII*. 189

Figure A-1. Deformed Buckled Profiles for Beam Element Model *ANB1* as a Function of Normalized Axial Coordinate $(\overline{X})$ for Solution Times (τ). 232

Figure A-2. Normalized Axial Stress Distribution for Beam Element Model ANB1 as a Function of Normalized Axial Coordinate $(\overline{X})$ and Time (τ). 232

Figure A-3. Nondimensional Axial Displacement for Beam Element Model *ANB6*. ... 233

Figure A-4. Nondimensional Transverse Displacement for Beam Element Model *ANB6*. 233

Figure A-5. Adjusted Time Scale Plot of Nondimensional Transverse Displacement for Beam Element Model ANB6 Illustrated in Figure A-4. 234

Figure A-6. Nondimensional Peak Buckle Amplitude (w_{max}) as a Function of Time (τ) for Beam Element Models with Discrete Fundamental Mode Imperfection. 234

Figure A-7. Nondimensional Buckled Profiles as a Function of Normalized Axial Coordinate $(\overline{X})$ for Beam Element Model *ANB9*. 235

Figure A-8. Nondimensional Peak Buckle (w_{max}) and Midspan Amplitude as a Function of Time (τ) for Beam Element Models with Combined Geometric Imperfections. . 235

Figure A-9. Nondimensional Peak Buckle Amplitude (w_{max}) as a Function of Time (τ) for Beam Element Models with Combined Geometric Imperfections. 236

Figure A-10. Nondimensional Buckled Wavelength (λ) as a Function of Time (τ) for Beam Element Models with Combined Geometric Imperfections (■ λ_{avg} , □ λ_{wm})..... 237
Figure A-11. Nondimensional Buckled Profiles as a Function of Normalized Axial Coordinate $(\overline{X})$ for Plane Strain Element Model *AP2*. 238
Figure A-12. Nondimensional Buckled Profiles as a Function of Normalized Axial Coordinate $(\overline{X})$ for Plane Strain Element Model AP8. 238
Figure A-13. Axial Displacement Time History for Nodal Points Near the Fixed Support for Plane Strain Element Model *AP8*..... 239
Figure A-14. Normalized Axial Stress State as a Function of Time (τ) for Plane Strain Element Model *AP7*..... 239
Figure A-15. Normalized Axial Stress State as a Function of Time (τ) for Plane Strain Element Model *AP8*..... 240
Figure A-16. Discrete Fourier Transform Analysis for Plane Strain Element Model *AP8* as a Function of (a) Wave Number, (b) Nondimensional Wavelength..... 241

Figure B-1. Typical Deformed Buckled Profile During Preliminary Investigations..... 250
Figure B-2. Data Acquisition System. 250
Figure B-3. Typical Record for the Proximity Switches from Test *SIc4*..... 251
Figure B-4. Instrumented Strain Gauge Locations for Series AI (Tests *AIc*, *AId*, *AIe*, *AIf*). 251
Figure B-5. Instrumented Strain Gauge Locations for Series *AII* (Tests *AIIb*, *AIc*, *AIId*, *AIIe*). 252
Figure B-6. Instrumented Strain Gauge Locations for Series *SI* (Tests *SIc*, *SId*, *SIf*). .. 252
Figure B-7. Initial Configuration for Test *AIId9*, (d = 4.7625mm) with Slenderness Ratio (L_e/r = *200*), Instrumented with Strain Gauges. 253
Figure B-8. Deformed Buckled Profile for Test *AIId9* Instrumented with Strain Gauges..... 254

Figure B-9. Strain Record for Test *AIf4*, (a) Gauges #1 and #2 (Peak), (b) Gauges #3 and #4 (Off-Peak), and (c) Gauges #5 and #6 (Midspan)..... 255
Figure B-10. Buckled Profiles for Tests Series *AIc1* to *AIc5*. 256
Figure B-11. Datum Level for Measurement of Initial Geometric Imperfections and Final Buckled Profile. 256

Figure C-1. Datum Level for Measurement of Initial Geometric Imperfections and Final Buckled Profile. 258
Figure C-2. General Deformed Buckled Profiles for Series *AI* (Tests *AIa* to *AIf*) Impacted by a 10kg Free Fall Impact Hammer at a Nominal Velocity of 6m/s. 260
Figure C-3. Series *AIa*, Tests: 1 to 6, (a) Initial Global Imperfections and (b) Deformed Buckled Profiles. 261
Figure C-4. Series *AIb*, Tests: 1 to 5, (a) Initial Global Imperfections and (b) Deformed Buckled Profiles. 262
Figure C-5. Series *AIc*, Tests: 1 to 5, (a) Initial Global Imperfections and (b) Deformed Buckled Profiles. 263
Figure C-6. Series *AIc*, Tests: 6 to 10, (a) Initial Global Imperfection and (b) Deformed Buckled Profiles. 264
Figure C-7. Strain Record for Test *AIc10*. (a) Strain Gauges #1 and #2, (b) Strain Gauges #3 and #4, and (c) Strain Gauges #5. 265
Figure C-8. Series *AId*, Tests: 1 to 5, (a) Initial Global Imperfection and (b) Deformed Buckled Profiles. 266
Figure C-9. Series *AIe*, Tests: 1 to 5, (a) Initial Global Imperfection and (b) Deformed Buckled Profiles. 267
Figure C-10. Series *AIf*, Tests: 1 to 5, (a) Initial Global Imperfection and (b) Deformed Buckled Profiles. 268
Figure C-11. Series *AIf*, Tests: 6 to 10, (a) Initial Global Imperfection and (b) Deformed Buckled Profiles. 269

Figure C-12. Strain Record for Test *AIf4*, (a) Strain Gauges #1 and #2, (b) Strain Gauges #3 and #4, and (c) Strain Gauges #5 and #6. 270
Figure C-13. Strain Record for Test *AIf10*, (a) Strain Gauges #1 and #2, (b) Strain Gauges #3 and #4, and (c) Strain Gauges #5 and #6. 271
Figure C-14. General Deformed Buckled Profiles for Series *AII* (Tests *AIIa* to *AIId*) Impacted by a 10kg Free Fall Impact Hammer at a Nominal Velocity of 6m/s. 272
Figure C-15. Series *AIIa*, Tests: 1 to 3, (a) Initial Global Imperfections and (b) Deformed Buckled Profiles. 273
Figure C-16. Strain Record for Test *AIIa3*, Strain Gauges #1 and #2. 274
Figure C-17. Series *AIIb*, Tests: 1 to 5, (a) Initial Global Imperfections and (b) Deformed Buckled Profiles. 275
Figure C-18. Series *AIIb*, Tests: 6 to 10, (a) Initial Global Imperfections and (b) Deformed Buckled Profiles. 276
Figure C-19. Series *AIIc*, Tests: 1 to 5, (a) Initial Global Imperfections and (b) Deformed Buckled Profiles. 277
Figure C-20. Series *AIId*, Tests: 6 to 9, (a) Initial Global Imperfections and (b) Deformed Buckled Profiles. 279
Figure C-21. Strain Record for Test *AIId3*, (a) Gauges #1 and #2, (b) Gauges #3 and #4 and (c) Gauges #5 and #6. 280
Figure C-22. Strain Record for Test *AIId9*, (a) Gauges #1 and #2, (b) Gauges #3 and #4 and (c) Gauges #5, #6 and #7. 281
Figure C-23. Series AIIe, Tests: 1 to 4, (a) Initial Global Imperfections and (b) Deformed Buckled Profiles. 282
Figure C-24. General Deformed Buckled Profiles for Series *AII* (Tests *SIa* to *SIf*) Impacted by a 10kg Free Fall Impact Hammer at a Nominal Velocity of 6m/s. 283
Figure C-25. Series *SIa*, Tests: 1 to 5, (a) Initial Global Imperfections and (b) Deformed Buckled Profiles. 284
Figure C-26. Strain Record for Test *SIa5*, Strain Strain Gauges #1 and #2. 285

Figure C-27. Series *SIb*, Tests: 1 to 6, (a) Initial Global Imperfections and (b) Deformed Buckled Profiles. 286
Figure C-28. Series *SIc*, Tests: 1 to 5, (a) Initial Global Imperfections and (b) Deformed Buckled Profiles. 287
Figure C-29. Series *SIc*, Tests: 6 to 9, (a) Initial Global Imperfections and (b) Deformed Buckled Profiles. 288
Figure C-30. Strain Record for Test *SIc4*, (a) Strain Gauges #1 and #2 and (b) Strain Gauges #3 and #4. 289
Figure C-31. Series *SId*, Tests: 1 to 6, (a) Initial Global Imperfections and (b) Deformed Buckled Profiles. 291
Figure C-32. Series *SIe*, Tests: 1 to 5, (a) Initial Global Imperfections and (b) Deformed Buckled Profiles. 292
Figure C-33. Series *SIf*, Tests: 1 to 6, (a) Initial Global Imperfections and (b) Deformed Buckled Profiles. 293
Figure 34. Series *SIf*, Tests: 7 to 12, (a) Initial Global Imperfections and (b) Deformed Buckled Profiles. 294
Figure C-35. Strain Record for Test *SIf5*, (a) Strain Gauges #1 and #2, (b) Strain Gauges #3 and #4 and (c) Strain Gauges #5 and #6. 295
Figure C-36. Strain Record for Test *SIf6*, (a) Strain Gauges #1 and #2, (b) Strain Gauges #3 and #4 and (c) Strain Gauges #5 and #6. 296

Figure D-1. Buckled Response for Beam and Plane Strain Element Models with Discrete Imperfections (a) Experimental and (b) Idealized Boundary Conditions. 290
Figure D-2. Buckled Response for Beam and Plane Strain Element Models with Random Imperfections (a) Experimental and (b) Idealized Boundary Conditions. 291
Figure D-3. Influence of Geometric Imperfection Formulation on the Computed Buckled Response for Series *AIa* (a) Discrete (b) Random. 292
Figure D-4. Influence of Geometric Imperfection Formulation on the Computed Buckled Response for Series *AIIc* (a) Discrete (b) Random. 293

Figure D-5. Influence of Material Behaviour on the Computed Buckled Response for Series *AIIc* (a) Bilinear Elastoplastic (b) Elastic, Perfectly Plastic Material Response with Aspect Ratio (*AR = 4:1*). 294
Figure D-6. Influence of Bilinear Elastoplastic Material Behaviour on the Computed Buckled Response for (a) Series *AIc* (b) Series *AIIc* with Aspect Ratio (*AR = 1:1*). 295

Nomenclature

Latin Alphabet

A	cross-sectional area
A_n	Fourier coefficient for mode n
A_o	Fourier coefficient of constant amplitude for discrete imperfection
A_p	Fourier coefficient of "preferred" mode for random imperfections
a_n	Fourier coefficient of initial displacement
a_p	nondimensional "preferred" mode random imperfection coefficient
B_n	Fourier coefficient
b	beam width
C_n	Courant number
c	elastic stress wave velocity
[C]	global element damping matrix
DLF	dynamic load factor
D	empirical material constant
d	beam depth
E	elastic modulus
E_n	error term in finite difference stability analysis
E_T	plastic or tangent strain hardening modulus
FD	finite difference
FEM	finite element method
G	shear modulus
G_n	amplification function normalized with respect to the Fourier coefficients (a_n) of the initial displacements
g_n	amplification function
h	distance from the neutral axis to extreme fiber
I	principal moment of inertia or second moment of area

k	characteristic buckling length
$[K]$	global element stiffness matrix
$[\hat{K}]$	global effective stiffness matrix
$[k_\ell]$	local element stiffness matrix
L	beam length
L_{cr}	critical static Euler beam length
L_e	effective beam length
L_{el}	local element length
L_e/r	effective slenderness ratio
L_p	"preferred" wavelength
L_w	buckle wavelength
L_u	unsupported beam length
l	axial deformation for wave equation
ℓ	nondimensional characteristic length
ℓ_{cr}	normalized critical length
M	impact mass
M_{zz}	applied bending moment about the z-axis
$[M]$	global mass matrix
m	power law constant coefficient
$\overline{m}$	mass per unit length
$[m_\ell]$	local mass matrix
N	number of terms in summation series (#), nondimensional normal force
$\overline{N}$	normalized modal response parameter
n	mode number
P	axial compressive force
$(P_{cr})_D$	critical dynamic load
P_{cr}	critical static Euler load
p_n	dynamic stability parameter, $p_n = \eta\sqrt{1-\eta^2}$

q	empirical material constant
r	radius of gyration
s	characteristic parameter between the axial and lateral deformation for an elastic response
s_T	characteristic parameter between the axial and lateral deformation for a plastic response
t	time
u	nondimensional axial displacement
$\{\ddot{u}\}$	acceleration vector
$\{\dot{u}\}$	velocity vector
$\{u\}$	displacement vector
V_E	velocity associated with elastic strain energy
V_I	impact velocity
V_{KE}	velocity associated with kinetic energy
V_p	plastic wave velocity
v_o	initial velocity
w	nondimensional transverse displacement
w_{max}	maximum nondimensional transverse displacement
w_o	nondimensional initial geometric imperfection
$\bar{X}$	normalized axial coordinate
x	axial coordinate
x_c	longitudinal position of experimental buckle crest
x_p	"preferred" wavelength
y	transverse deflection of the beam
$\bar{y}$	ideal beam ordinate
y_c	transverse deflection of experimental peak buckle crest
y_o	initial geometric imperfection

Greek Symbols

Δt	integration time step
Δt_{cr}	critical time step
Δx	grid or nodal point spacing
α	empirical coefficient, generalized coordinate
β	imperfection parameter ($0.0001 \leq \beta \leq 0.001$), Newmark time integration stability parameter
β_n	Fourier term for finite difference stability analysis
δ	axial deformation
ε	strain
ε_b	measured flexural strain
ε_c	measured compressive strain
ε_{cr}	critical strain for "dynamic" Southwell plot
$(\varepsilon_{cr})_D$	critical dynamic strain for DLF
$(\varepsilon_{cr})_E$	critical Euler strain for DLF
$\dot{\bar{\varepsilon}}^p$	uniaxial equivalent plastic strain rate
γ	Newmark time integration stability parameter, wavenumber
η	nondimensional wave number
η_a	nondimensional most amplified wave number
η_{cr}	nondimensional critical wave number
η_p	nondimensional "preferred" wave number
κ	radius of curvature
λ	nondimensional wavelength
λ_{avg}	nondimensional average or mean wavelength
λ_E	nondimensional static Euler wavelength
λ_m	nondimensional theoretical mean "preferred" wavelength
λ_p	nondimensional "preferred" wavelength

λ_{wm}	nondimensional weighted mean wavelength
ν	Poisson's ratio
π	trigonometric constant
θ_n	phase angle ($0 \leq \theta_n \leq 2\pi$)
ρ	mass density
$\bar{\sigma}$	normalized stress parameter that relates the axial stress magnitude to the yield stress (σ_y), dynamic flow stress for nonzero plastic strain rate
σ_o	initial elastic stress
σ_f	failure stress
σ_{th}	theoretical normal or axial stress due to bending
σ_y	yield stress
σ_λ	standard deviation of nondimensional wavelength (λ)
τ	nondimensional time parameter for an elastic response
τ_{cr}	nondimensional critical impulse duration
τ_{mn}	Cauchy stress tensor
τ_T	nondimensional time parameter for a plastic response
ω	excitation or forcing function frequency (radians cycle^{-1})
ξ_s	stability modulus

Subscript or Superscript

i	finite difference axial grid point, axial coordinate
j	axial coordinate
k	finite difference time step increment, axial coordinate
n	number of terms in the series, mode number or power law exponent
m	power law exponent for strain rate effects
o	initial configuration

Acknowledgments

I would like to express my appreciation for Dr. Neil Pegg, of the Defence Research Establishment Atlantic (DREA), whose knowledge and experience has been instrumental throughout the course of these investigations. The early work conducted by Dr. Pegg on dynamic pulse buckling of cylindrical shells was the motivation for the current research. I would like to extend my sincere gratitude for the friendship of Dr. Farid Taheri, Associate Professor DalTech, developed during my studies, in addition to the academic guidance, support as well as the thoughtful input and suggestions.

Direct financial assistance and inkind support for this research project by Defence Research Establishment Atlantic (DREA) is gratefuly acknowledged. In addition, scholarship funding from the Atlantic Accord Career Development Award, sponsored by the Government of Newfoundland and Labrador, and DalTech is recognized.

Abstract

Investigations on the elastic and plastic dynamic pulse buckling response of a slender beam, with geometric imperfections, subject to an axial impulse is presented. The current study is concerned with high order events that can be defined as an intense transient loading condition (i.e. large amplitude, short time period), where considerations of the stress wave front propagation are important. The dynamic buckling instability was primarily viewed as a modal perturbation due to an unbounded growth of transverse deflections due to exploitation of the geometric imperfections by the applied impulse. Experimental investigations and numerical analyses, employing the finite difference and finite element methods, were conducted.

For a slender beam subject to an axial impulse, the elastic studies substantiated the validity and utility of the "preferred" wavelength theory. The peak buckle amplitude and dominant waveform could be effectively defined in terms of a single "preferred" mode. The most significant conclusion was that to accurately model the pulse buckling event, random geometric imperfections were required to develop the hyperbolic growth of transverse displacements for both the finite difference and finite element models. Other modelling considerations were also required for the development of an accurate pulse buckling numerical model with respect to theory and experimental observations. These factors include adopting a finely discretised mesh with aspect ratios on the order of 1:1 and employing plane strain elements. The superior performance of the quadratic plane strain elements was related to inherent curvature restriction of the beam element formulation. For plane strain element models, however, nonlinear geometric and material analysis was required. A threshold elastic pulse buckling criterion was substantiated by the finite difference study and further supported by finite element analyses. The influence of more complex structures, boundary constraints or loading conditions on the accuracy of numerical models investigating elastic pulse buckling events should be examined.

The experimental investigations and finite element analyses demonstrated that, for the parameters investigated, the dynamic plastic pulse buckling events could also be defined by a characteristic modal response. The peak buckle response was assessed in terms of a normalised modal parameter as a function of the effective slenderness ratio. The modal parameter accounted for the longitudinal position of the peak buckle crest with respect to local stiffness terms and natural frequency characteristics defined with respect to the axial and flexural response. The analyses demonstrated the need for further parametric investigations to examine the influence of element formulation and imperfection type on the pulse buckling response. The importance of slenderness ratio, element aspect ratio and constitutive relationships (e.g. dynamic yield flow, rate-sensitive behaviour, viscoplasticity) should also be considered. Furthermore, based on these recommendations, future work should address the development of dynamic pulse buckling threshold limits.

1.0 Dynamic Buckling of Structures

1.1 Background

Static elastic stability has been thoroughly investigated over the past century and has been of significant interest to both research and design engineers. As early as 1729 van Musschenbroek conducted the first empirical studies and concluded that the static buckling load was inversely proportional to the square of column length. Thirty years later, Leonhard Euler substantiated the analysis through the development of a classical solution for the critical load of a simply supported column. This expression is commonly known as the *Euler column formula*.

Buckling has been traditionally studied, as a mode of failure, for slender or thin-walled structures subject to static loading. Interest was developed from empirical and *in situ* experience, as well as theoretical analysis, which demonstrated that collapse failure might occur prior to the material stress state exceeding a governing yield criterion. This loss of structural integrity can be related to a critical combination of geometry, boundary condition and stress. There is a significant volume of literature on this subject and the work of Timoshenko and Gere (1961) provides an excellent discussion.

Structures can also be subject to transient loads with magnitudes that exceed the static critical Euler buckling load. Dynamic bucking, however, cannot be reduced to the static counterpart where the static elastic stability is defined by a unique critical load for a known mode shape. For dynamic buckling, the response frequencies and critical mode shapes are a function of the load intensity, (i.e. load magnitude and duration), structure geometry and material behavior. Systematic investigations on dynamic behavior of materials and dynamic buckling of structures were initiated in the 1930's.

1.2 Rationale for Research and Design

1.2.1 Engineering Problems in Dynamics

Engineers have been faced with an increasing number of challenges, in both the civilian and military domains that must consider the dynamic response of structures subject to impulsive loading events. The primary issues are related to structural integrity, operational constraints, as well as socioeconomic and environmental risk. In addition, the magnitude of shock levels imposed on personnel or critical components (e.g. computer controls) must be considered.

For static structural analysis the displacement response is of primary importance and is related to mechanical stiffness (i.e. potential energy) and load amplitude. Problems in dynamics, on the other hand, must take into consideration load intensity (i.e. magnitude and duration), inertial characteristics (i.e. resistance to acceleration, kinetic energy) and damping properties (i.e. non-conservative energy term) of the system.

Dynamic analysis can be generally categorized into problems relating to structural dynamics and wave propagation, which are a function of the load intensity.

Structural dynamics is a common engineering discipline that considers relatively lower magnitude loading events, on the order of the Euler critical load, and longer duration with loading periods greater than one-quarter of the natural period of the structure. The analysis is primarily concerned with natural frequencies of vibration (e.g. resonance, parametric or vibration buckling) or time–history response (e.g. transient loads, earthquake motion). The importance in conventional structural analysis and design has lead to extensive investigations in this field; see for example Bolotin (1964), and thus is not considered in the present study. Structural stiffness, inertia and damping are parameters to be considered.

Wave propagation analysis can be further subdivided into high intensity and low intensity events in terms of the loading magnitude and duration.

High intensity wave propagation events are associated with extremely short duration loads on the order of 10^{-6}s to 10^{-8}s. Shock waves with steep pressure gradients can develop under plane strain conditions associated with a concave stress–strain material behavior and loss of transverse shear strength. Some examples include the detonation of military ordnance (e.g. high explosives, kinetic energy rounds) and fuel–air explosions (e.g. Piper Alpha disaster).

For the present thesis investigations, the dynamic buckling events of interest occur on the order of milliseconds (10^{-3}s to 10^{-6}s) and are defined as low intensity wave propagation problems. The structural response can be characterized by the rapid growth of out of plane deformations that may lead to structural collapse, which is generally associated with *pulse buckling*. The material behavior can be wholly elastic or can exhibit a nonlinear plastic or viscoplastic response. In general, the dominant structural response occurs during the first cycle of motion and for intense buckling events the bulk of deformational strain energy would be consumed through plastic flow. Consequently, there is limited opportunity to invoke energy dissipation mechanisms and thus damping is not considered.

1.2.2 Dynamic Pulse Buckling Analysis

Pulse buckling can be defined as the structural response to a transient impulsive forcing function, which is a direct parameter multiplying the displacement field in the dynamic equation of motion (Lindberg and Florence, 1987). The initial geometric imperfections, spatial or temporal variations in the load distribution are "magnified" and exploited by the applied impulse. This results in perturbations in the structural response and rapid growth of transverse displacements. The deformed geometry is typically of a higher

order mode shape than the static Euler counterpart. Based on geometric and mechanical properties of the structure, a "preferred" mode tends to dominate the buckling response through modal competition with increasing time.

Dynamic pulse buckling analysis is critical for thin-walled members (e.g. beams, plates, shells), which are advantageous in the structural design optimization process where space and weight are critical parameters. For example, exploitation of higher order mode shapes (wrinkles) of thin-walled structures as energy absorbing failure mechanism is an integral component of crash-worthiness design investigations. Pressure vessels and nuclear reactors must be assessed with consideration to the effects of blast loading to ensure structural integrity and mitigate environmental impact. Resistance to shock loads from hostile weapons or operational conditions have been at the forefront in the design synthesis of military and aerospace structures.

Figure 1-1 and Figure 1-2 present illustrative examples of dynamic pulse buckling events from experimental crash-worthiness studies and numerical investigations, respectively.

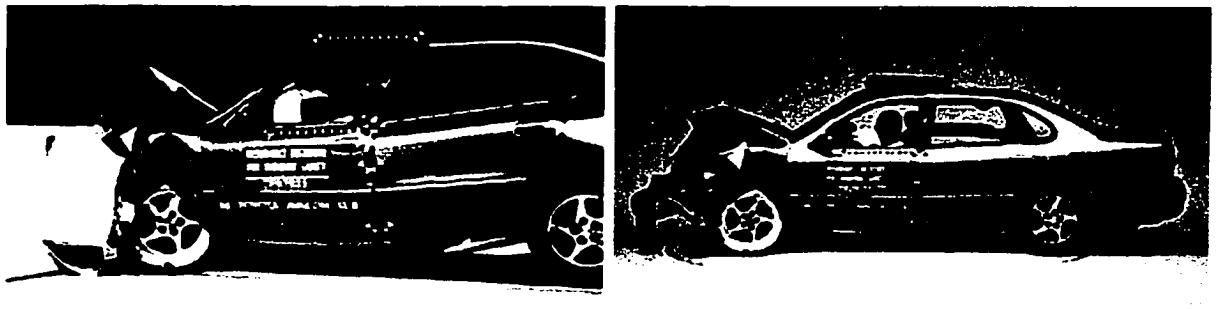

(a) (b)

Figure 1-1. Automotive Industry Crashworthiness Study (a) Action Photo during Impact, (b) Post-Test Damage. (IIHS, 1998).

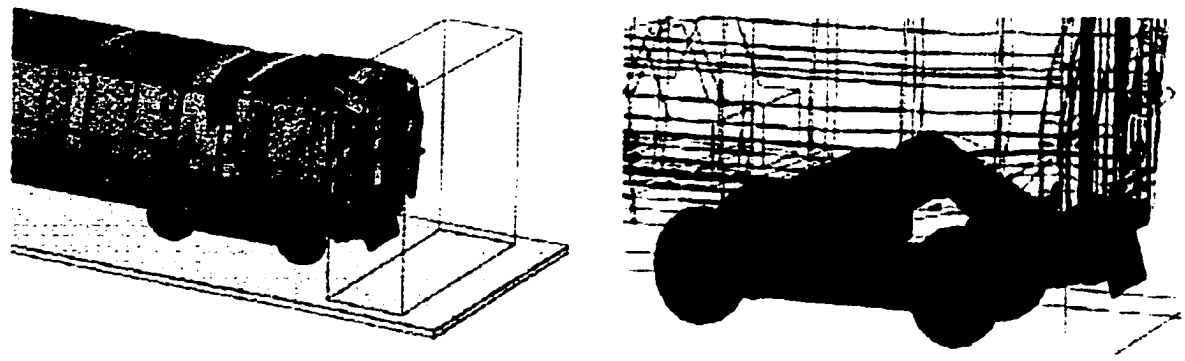

(a) (b)

Figure 1-2. Numerical Simulation of Passenger Train Car Impacting a 50 ton Mass (a) Crushing Behavior of Car, (b) Detail of Center Sill Collapse. (SRI, 1998).

1.3 Motivation for the Research Activities

Although there has been a continued research effort over the past 40 years, the complex nature of the dynamic pulse buckling process has hindered the development of rigorous or tractable, universal solutions. In general, idealizations have been incorporated to facilitate theoretical, experimental and numerical analyses.

A comprehensive understanding of relatively simple events can provide considerable insight to the dynamic pulse buckling process. The acquired knowledge can be applied to complex problems that consider more detailed structural configurations, boundary constraints or loading conditions.

The studies of Lindberg and Florence (1987) and Pegg (1992) provided the motivation for the present research. The thesis investigations are focused on the elastic and plastic dynamic buckling of slender, rectangular beams with geometric imperfections subjected to an intense axial impulse. This provides a basis for conducting an assessment of the

pulse buckling response for a relatively simple geometric form, boundary condition and load character.

Slender beams are integral components of common structural systems such as buildings, body frames for automobiles or train cars, and marine structures. Furthermore, these elements are employed as a secondary stiffening component or bracing system (e.g. cylindrical shells or hollow sections).

The dynamic buckling response of structures can be characterized by buckling deformation (i.e. amplitude and growth rate), modal response (i.e. buckle wavelength) and pulse buckling failure criterion (i.e. critical stress or strain limits). The first two parameters, buckling deformation and modal response, are related to the dominant structural or mechanical behavior to the applied impulsive load. These terms characterize the pulse buckling response and are incorporated in the pulse buckling criterion.

In contrast with the static buckling counterpart, characterization of limit criteria for dynamic instability is relatively arbitrary and open to interpretation. Few studies have developed analytical expressions, empirical formulae or design curves to aid in the determination of dynamic buckling strength and modal response due to impulsive loading.

A dynamic buckling criterion is required to conduct an engineering assessment of structures to impulsive loads. The threshold is typically defined in terms of the load intensity (e.g. axial beam impact, radial shell impulse), functional constraints (e.g. excessive deflection, structural integrity, acceptable damage level) or operational considerations (e.g. dynamic loads imparted to passengers or physical sub-components). Furthermore, a universal dynamic pulse buckling failure criterion does not exist and the definition is partially subjective. For example, space re-entry vehicles (i.e. space shuttle) are for the most part designed for an elastic response. In terms of crashworthiness for

automobiles, the system is designed for zones of localized plastic deformation with low shock load levels imparted to the passengers.

Issues related to buckling displacement, modal response and pulse buckling failure criterion will be addressed in the present study for both elastic and plastic pulse buckling events.

1.3.1 Elastic Pulse Buckling

Historically, elastic pulse buckling studies have been concerned with impulsive loading events that could be characterized as problems in structural dynamics. The theoretical, experimental and numerical analyses have focused on the fundamental mode response of a slender beam subject to an axial impulse.

For intense loading events, with magnitudes significantly exceeding the static Euler load of duration orders less than the fundamental flexural mode, the pulse buckling response exhibits a higher order mode that tends to the development of a "preferred" wavelength. Based on analysis of a differential equation of motion, mode perturbation methods have been employed to characterize the pulse buckling response where inertia forces (e.g. lateral resistance in flexure) play a significant role. The method, however, is limited to simple geometric and boundary configurations, idealized material behavior and boundary conditions, and small departures from the dominant solution.

The primary objective for the present thesis investigations is to advance procedures for the development of numerical models that exhibit a buckling response consistent with the mode perturbation theory. From this perspective, the specific requirements for imperfection formulation, grid or mesh discretization, and general modeling procedures will be addressed. On this basis, the development of more complex numerical models can proceed on a rational basis.

1.3.2 Plastic Impact Buckling

The dynamic plastic response of impulsively loaded beams has been the subject of continued research for over 60 years. Early studies focused on characterizing plastic wave propagation and dynamic material behavior. The majority of experimental investigations on the dynamic buckling response of a slender beam subject to axial impact have focused on lower velocity (e.g. progressive buckling) and higher velocity events (e.g. projectile impact).

For moderate impact velocities, where wave propagation effects are important, experimental and numerical investigations on the dynamic pulse buckling response due to axial impact are limited. In general terms, the studies have considered only a predefined fundamental mode imperfection and pulse buckling response. Although complete understanding of the complex dynamic buckling behavior of structures does not exist, particularly for plastic response mechanisms, significant insight on the dominant factors has been developed. Some of these parameters include impact energy, impact mass/beam mass ratio, geometric imperfection, dynamic material behavior and interaction between the propagating axial stress wave and structural modes.

A more complete understanding of the complex dynamic buckling phenomenon can be achieved through an integrated framework. Experimental investigations provide the essential data required for the development of empirical formulae, and validation of mechanical models and numerical algorithms.

Consequently, the primary objectives of the present thesis investigations are to augment and to extend the current experimental database, to provide an empirical basis to validate numerical models, and to develop relationships that characterize the dynamic pulse buckling response

1.4 Overview of Thesis Investigations

Technological advancements in the computer industry and the development of elegant yet robust computational strategies, such as the finite element method, have provided a rational basis for the analysis of complex nonlinear dynamic problems. A considerable research effort, however, is still required for the comprehensive assessment of the dynamic pulse buckling process.

The present thesis research will consider an integrated framework that incorporates theoretical analysis, experimental investigations and numerical studies, via the finite difference and finite element methods. The work scope presented herein may be summarized as follows:

An overview of dynamic elastic stability will be presented in Chapter 2. A literature review on analytical, experimental and numerical studies investigating the elastic pulse buckling response of beams subject to an axial impact is also discussed.

In Chapter 3, the development of a finite difference model defining the dynamic elastic buckling response of a slender beam, with prescribed initial geometric imperfections, subject to an axial impulsive stress is detailed. The investigations focus on characterizing the parameters required for the development of an accurate numerical procedure that can model intense pulse buckling events associated with higher order mode shapes. Grid discretization level, type of geometric imperfection and applied stress levels are the primary variables. An assessment of the computed displacement, mode and stress state response with respect to theoretical analysis and experimental studies is presented. In addition, a dynamic buckling criterion is addressed.

Continuation of the elastic pulse bucking analysis by the finite element method is detailed in Chapter 4. Several commercial finite element packages (*ANSYS*, *ADINA* and *NISA*)

are employed. The investigations also consider element type and order, kinematic formulation, as well as linear and nonlinear analysis that include the influence of nonlinear geometric and material behavior. Comparison with analytical solutions, experimental data and finite difference computations is presented.

An overview of the concepts of plasticity, plastic stress wave propagation and dynamic plastic behavior is presented in Chapter 5. Details on analytical, numerical and experimental investigations on relevant dynamic plastic pulse buckling events are discussed.

Chapter 6 details an experimental investigation on the dynamic plastic buckling of slender rectangular beams subject to axial impact by a free-fall, dead weight hammer. The laboratory apparatus, experimental procedure and data records are documented. The primary objective was the development of empirical relationships defining the pulse buckling response as a function of slenderness ratio and material properties.

The experimental studies provided a source for validating parallel numerical analyses, based on the finite element method, on the plastic pulse buckling response of slender beams, which are presented in Chapter 7. The parametric investigations will consider mesh topology, element formulation, constitutive relationships, applied boundary conditions and geometric imperfections. The primary objective is the development of an accurate numerical model defining the plastic pulse buckling response.

Finally, a summary of the numerical and experimental investigations conducted as well as a critical assessment of the major findings advanced through the course and development of the thesis is discussed. Recommendations for future research are also proposed.

2.0 Dynamic Elastic Buckling of Slender Beams

Historical research efforts on the elastic pulse buckling response of a slender beam subject to an axial load are presented. The investigations include theoretical, experimental and numerical studies. Pulse buckling threshold limits are also reviewed.

2.1 Dynamic Equation of Motion

To orient the discussion, the governing dynamic equation of motion and general solution will be presented. Consider, the simply supported beam, illustrated in Figure 2-1, subject to a dynamic impulsive axial force (P). The beam geometry and response is defined by the lateral deflection (y) measured from the neutral axis of the initially undeformed bar as a function of the axial coordinate (x). Euler-Bernoulli beam theory within the limits of small displacements and rotations is assumed. The dynamic differential equation of motion can be expressed as,

$$E I \frac{\partial^4 y}{\partial x^4} + P \frac{\partial^2}{\partial x^2}(y + y_o) + \rho A \frac{\partial^2 y}{\partial t^2} = 0 \qquad (2.1)$$

where E is the Young's elastic modulus, I is the moment of inertia, ρ is the material density, A is the cross-sectional area and y_o is the initial geometric perturbation. Introducing the following parameters,

$$k^2 = \frac{P}{EI}, \quad r^2 = \frac{I}{A}, \quad c^2 = \frac{E}{\rho} \qquad (2.2)$$

where c is the speed of the longitudinal stress wave, Equation (2.1) can be rewritten,

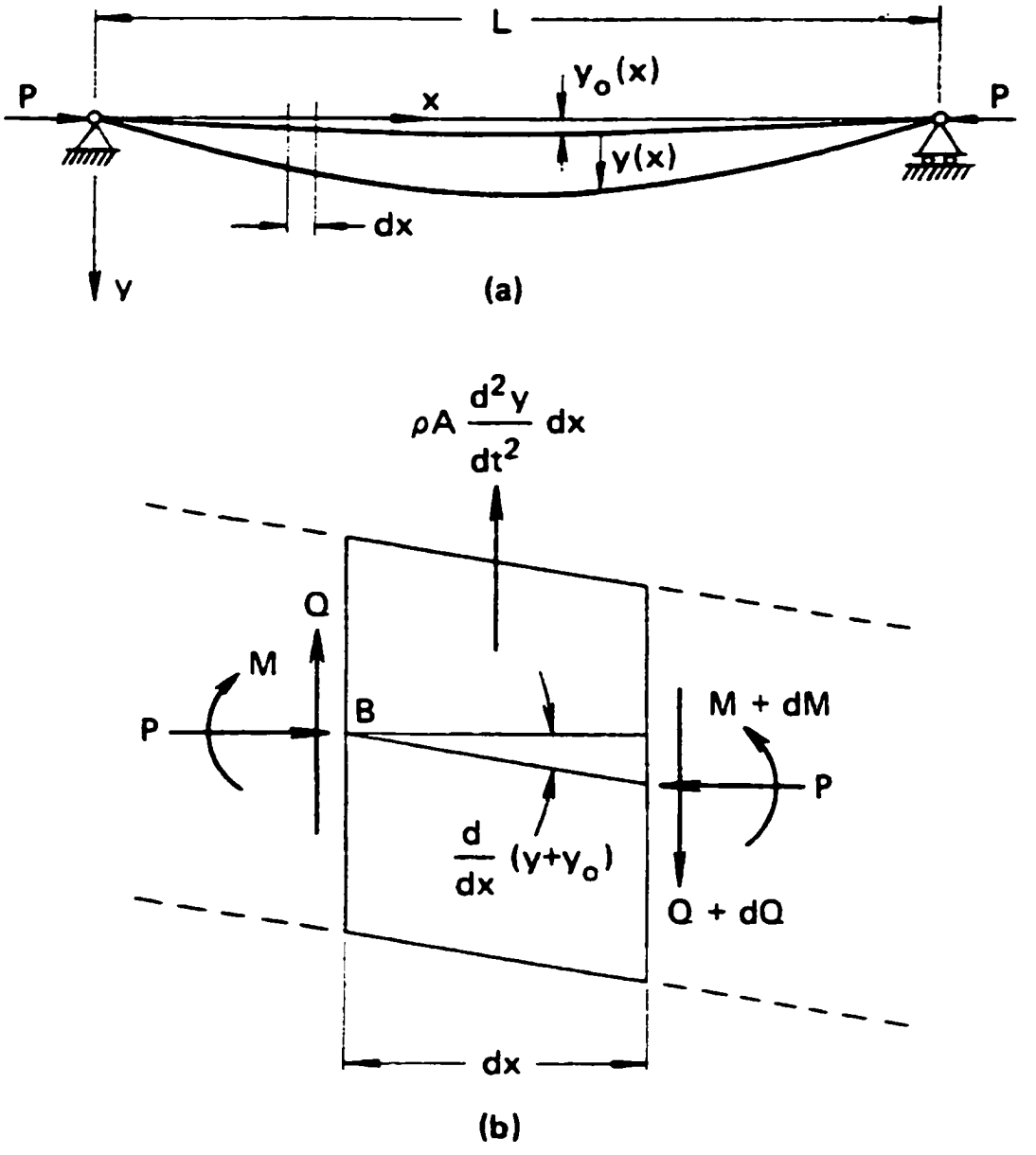

Figure 2-1. (a) Simply Supported Bar Subject to an Impulsive Axial Load and (b) Free Body Diagram of a Bar Element (Lindberg and Florence, 1987).

$$\frac{\partial^4 y}{\partial x^4} + k^2 \frac{\partial^2 y}{\partial x^2} + \frac{1}{r^2 c^2} \frac{\partial^2 y}{\partial t^2} = -k^2 \frac{\partial^2 y_o}{\partial x^2} \tag{2.3}$$

The essential or geometric boundary conditions for a simply supported beam are

$$y\big|_{x=0,L} = 0; \quad \left.\frac{\partial^2 y}{\partial x^2}\right|_{x=0,L} = 0 \tag{2.4}$$

Assuming a product form of the solution for Equation (2.3) in terms of a Fourier series,

$$y(x,t) = \sum_{n=1}^{\infty} B_n(t) \sin\left(\frac{n\pi x}{L}\right) \tag{2.5}$$

and similarly the initial geometric imperfections can be defined by,

$$y_o(x,t) = \sum_{n=1}^{\infty} A_n \sin\left(\frac{n\pi x}{L}\right) \tag{2.6}$$

where the coefficients, A_n, are determined by,

$$A_n = \frac{2}{L} \int_0^L y_o(x) \sin\left(\frac{n\pi x}{L}\right) dx . \tag{2.7}$$

Equations (2.5) and (2.6) can be substituted into (2.3) to give the following equation of motion for the Fourier coefficient (B_n),

$$\frac{\partial^2 B_n}{\partial t^2} + \left(\frac{rcn\pi}{L}\right)^2 \left[\left(\frac{n\pi}{L}\right)^2 - k^2\right] B_n = (krc)^2 \left(\frac{n\pi}{L}\right)^2 A_n \tag{2.8}$$

The characteristic nature of the solution is dependent on the sign of the Fourier coefficient (B_n) and can be classified as bounded or trigonometric $\left(n\pi/L > 1\right)$, static $\left(n\pi/L = 1\right)$ and unbounded or hyperbolic $\left(n\pi/L < 1\right)$. Lindberg and Florence (1987) defined the exponential or hyperbolic solution as the dynamic pulse buckling response.

2.2 Dynamic Elastic Buckling

Early investigations on elastic buckling, from the early 1930's through to the late 1950's, focused on the fundamental mode response of a pin-ended bar subjected to an axial impulse that exceeded the static Euler load. For intense pulse buckling events, however, the importance of considering higher order modal dynamics will be demonstrated. Issues relating to load intensity, form of geometric imperfections, axial inertia and dynamic buckling criteria are also addressed.

2.2.1 Fundamental Mode Response

Historically, the majority of analytical, experimental and numerical investigations have focused on the fundamental mode response for elastic dynamic pulse buckling events. This was due to several factors such as a reduction in analytical complexity, a conventional formulation for the prescribed geometric imperfections and a general trend for assessment of dynamic buckling events that approached a quasi-static response. For these studies, the primary focus was on the critical load magnitude and duration, which could be sustained for the fundamental mode response.

The dynamic buckling of a slender beam subject to an axial impulse has been typically defined by the linear differential dynamic equation of motion (Equation 2.1). Analysis

has also accounted for nonlinear behaviour when the axial strain–displacement relationship considered components due to bending,

$$\frac{P}{AE} = \frac{\partial u}{\partial x} + \frac{1}{2}\left[\left(\frac{\partial y}{\partial x}\right)^2 - \left(\frac{\partial y_o}{\partial x}\right)^2\right]. \tag{2.9}$$

where u is the axial beam displacement for the axial coordinate, x. The longitudinal equilibrium can be defined as,

$$\frac{\partial P}{\partial x} = \rho A \frac{\partial^2 u}{\partial x^2}, \tag{2.10}$$

In lieu of rigorous computational methods, simplifying assumptions were typically considered in order to reduce the analytical complexity. In addition to adopting Euler-Bernoulli beam theory (Equation 2.1), an infinite longitudinal stress wave velocity was assumed. Thus, axial inertia terms (Equation 2.10) were ignored and the applied impulse was instantaneous and constant with all normal modes of vibration excited simultaneously. Furthermore, the effects of transverse shear and damping were generally not considered.

The investigations can be further categorized based on characteristics of the applied axial impulse such as constant velocity or displacement rate (e.g. test frame crosshead), constant mass (e.g. impact hammer), and constant load (e.g. force–time impulse). A review of the major studies conducted, since the 1930's, on the fundamental mode, dynamic pulse buckling response will be presented. The discussion will highlight the essential findings and conclusions of these investigations and a summary is presented in Table 2-1.

Table 2-1. Summary of Research Investigations Focused on the Dynamic Fundamental Mode Elastic Buckling Response.

Reference	Analysis Type	Impulse Load Character	General Comments
Taub (1933)	Linear	Load	▪ Ana lytical solution
Koning and Taub (1935)	Linear	Load	▪ Ana lytical solution
Meir (1945)	Linear	Load	▪ Ana lytical solution ▪ Powe r series
Pian and Siddall (1950)	Linear	Mass	▪ Ex perimental investigations ▪ Ana lytical solution
Hoff (1951)	Nonlinear	Velocity	▪ Ne glected axial inertia ▪ Powe r series
Davidson (1953)	Nonlinear	Mass	▪ Ne glected axial inertia ▪ Rung e-Kutta ▪ Ex perimental investigations
Schmitt (1956)	Nonlinear	Velocity	▪ Ne glected axial inertia ▪ Ste pwise integration ▪ Afte r Hoff (1951)
Erickson et al. (1956)	Experimental	Velocity	▪ Afte r Hoff (1951)
Sevin (1960)	Nonlinear	Velocity	▪ I ncluded axial inertia ▪ F inite difference
Huffington (1963)	Nonlinear	Load	▪ I ncluded axial, transverse shear and rotary inertia terms ▪ F inite difference
Hayashi and Sano (1972a)	Nonlinear	Mass	▪ Suc cessive approximations neglecting axial inertia ▪ F inite difference including axial inertia
Ari-Gur et al. (1982, 1979 and 1978)	Nonlinear	Mass	▪ I ncluded axial and rotary inertia ▪ F inite difference ▪ Pa rallel experimental studies
Ari-Gur and Elishakoff (1993, 1990)	Nonlinear	Load	▪ I ncluded axial, shear and rotary inertia ▪ F inite difference

The detailed and comprehensive pioneering work of Taub (1933) and Koning and Taub (1933) provided the framework for subsequent studies on the fundamental mode response. The investigations examined various support boundary conditions and three impulse load levels, namely, less than, equal to and greater than the critical static Euler load. Stress functions were developed that normalized the impulse magnitude and duration (i.e. impulse intensity) with respect to the static Euler load and fundamental mode of vibration. For magnitudes less than the static Euler load, it was shown that the maximum stress reaches an upper limit regardless of the duration. Conversely, for loads greater than the Euler limit, deflection grew exponentially with shock period and the maximum deflection is sustained during free vibration. For shorter impulse duration, however, it was noted that the limit could be safely exceeded.

In a similar study, Meier (1945) further stated that lateral inertial resistance and increasing beam stiffness at higher modes would cause the deflection to lag behind lower modes. On this basis, it was reasoned how impulsive loads, significantly greater than the critical Euler load, could be imparted without causing elastic instability.

Davidson (1953) extended the work of Koning and Taub (1933) but considered nonlinear axial terms due bending (Equation 2.9). The main conclusion was that, for impulse loads with a period less than the fundamental frequency of beam vibration, the axial stress wave and transverse deflection could be considered uncoupled (i.e. constant axial load). The analysis considered the allowable load ratio (applied dynamic load to static Euler load) as a function of initial curvature and frequency ratio (column natural frequency to applied load frequency).

Pian and Siddall (1950) conducted experiments on eccentric axial impact with load magnitudes between 1.14 and 7.33 times the critical static Euler load (16.1lbs), and impulse durations between 0.017s and 0.092s. A series of gauges were placed at stations

along the length of the bar to measure bending strains. A piecewise analytical solution to the differential equation of motion was developed to calculate the mid-span bending moment–time history. The time dependent impact load was subdivided into a series of impulse events with constant amplitude. The initial conditions for subsequent calculations of each impulse were defined by the previous time step. The analysis compared favorably with the experimental investigations. The main conclusion was that the Euler load could be safely exceeded if the period of loading was small relative to the natural period of flexural vibration. This was consistent with historical observations and substantiated by the work of Davidson (1953).

Hoff (1951) developed an analytical solution based on a power series and defined an average, time dependent constant axial force. The results were presented as a nondimensional buckling parameter, defined as a dynamic similarity number, which was a function of the initial geometric imperfection, slenderness ratio, material wave speed and impact velocity. Erickson et al. (1956) also found a good correlation between the buckling parameter and experimental data.

Application of numerical methods to analyze the dynamic buckling events began to flourish with the evolution of the mainframe computer. Schmitt (1956) developed an approximate solution based on the stepwise integration method, assuming a constant and uniform impulse, consistent with the solution of Hoff (1951). Sevin (1960) conducted a similar study, based on the work of Koning and Taub (1933) and Hoff (1951), which incorporated an explicit finite difference expression for the axial and lateral displacements. The main conclusion was that effects of axial inertia could be neglected with respect to the overall elastic behaviour for slenderness ratios less than 150 and forcing velocities less than 0.01 percent of the elastic wave speed parameter. In addition, Huffington (1963) concluded the effects of transverse shear and rotary inertia was negligible, for the parameters investigated employing finite difference models. These

investigations have considered elastic buckling events, which approach quasi-static conditions with a low order response.

For more intense loads, however, Schmitt (1956) stated that the analysis conducted by Koning and Taub (1933) and Meier (1945) proved inadequate for modelling impact velocities greater than 6m/s. This was based on experimental investigations but unfortunately, details or references concerning the apparatus, procedure or analysis were not documented. Sevin (1960) developed the same conclusions in comparison with the solution of Hoff (1951) for the case of a high loading rate (i.e. impact velocity) on the order of 0.1 percent of the elastic wave parameter.

Hayashi and Sano (1972a) presented two numerical models based on successive approximations and finite difference method. The finite difference model also considered axial inertia as well as the interaction and separation of the mass from the impact face. Comparative experimental studies of a mass pendulum impacting a simply supported, slender beam were also conducted. Beams of constant cross-section ($b = 10mm$, $d = 3mm$) with slenderness ratios ($L_e/r = 99, 148, 197$) and initial half-sine wave imperfection amplitudes ($y_o/L = 0.020, 0.027, 0.041$) were investigated. The analyses considered time histories of the longitudinal distribution of axial displacement and force as well as the midspan lateral deflection. Hayashi and Sano (1972a) concluded that the dynamic buckling response could be adequately characterised by Euler-Bernoulli beam theory. This was consistent with the analysis conducted by Sevin (1960) and Huffington (1963). For the parameters investigated, axial inertia did not significantly influence the dynamic buckling response with only slight effects on the distribution of axial load. Thus, the nonlinear displacement terms (Equation 2.9) were associated with a weak coupling between axial stress wave and lateral response.

Extensive experimental investigations and finite difference analyses on the dynamic impact bucking of bars was presented by Ari-Gur et al. (1982, 1979 and 1978). A series of impact tests were conducted on bars of rectangular cross-section composed of 6061-T4 aluminum, AISI-01 carbon chrome alloy steel and fiberglass-epoxy composite. Columns, with effective slenderness ratios ($71 \leq L_e/r \leq 411$), were subject to free-fall impact by a cylindrical mass ($0.05kg \leq m \leq 0.37kg$) with critical striking velocities ($6m/s \leq V_I \leq 15m/s$). The main objective was the development of a dynamic buckling criterion, which was defined as the transition from a bounded to an unbounded response based on the midspan displacement and strain record. Dynamic elastic stability was concluded to be primarily a function of geometric imperfection amplitude, impulse duration and column slenderness ratio. In addition, it was stated that material and mechanical properties; such as flexural rigidity, axial wave propagation velocity and density, had secondary effects on the dynamic elastic buckling response.

Ari-Gur and Elishakoff (1990) presented results from a finite difference study on the influence of transverse shear and rotary inertia on the dynamic pulse buckling of a beam. Beam length to depth ratios ($L/d = 25, 50$) with initial imperfections ($y_o = 0.01d, 0.375d$) was investigated. The impulse was defined by a half-sine wave, with the period of loading on the order of the fundamental flexural mode of vibration. Simply supported and clamped boundary conditions were considered. The computed response was sensitive to the shear stiffness and pulse duration. Ari-Gur and Elishakoff (1993) also studied the dynamic pulse buckling of a transversely isotropic column and found that effects of transverse shear rigidity were important for a relatively soft modulus ($G \leq 3E/8$).

Historically, dynamic elastic buckling analysis has focused on relatively low intensity impact events that approach quasi-static events and have generally only considered the fundamental mode response. Although a range of boundary conditions (e.g. constant

mass, velocity or load; simply supported or clamped) has been considered based on the discussion presented several generalized statements can be made for relatively low intensity, dynamic buckling events.

- The buckling response could be adequately defined by the dynamic Euler-Bernoulli beam equation
- Dynamic loads greater than the static Euler load could be sustained provided the period of loading was small relative to the natural period of flexural vibration
- Dynamic instability was primarily dependent on the geometric imperfection amplitude, impulse duration and column slenderness ratio
- The axial load can be considered constant. The effects of axial inertia and nonlinear terms of the axial strain–displacement relationship could be neglected. Thus, axial stress wave propagation and lateral mode of deformation is uncoupled

2.2.2 Higher Order Modal Response Studies

Although focusing on the fundamental mode behaviour, the research community had generally acknowledged the influence of a moving stress front on the development of flexural waves and higher order modal response. This analysis is concerned with the evolution of general mode shapes, resulting from the growth of transverse displacements as a function of loading intensity. The main issue to be addressed is the critical buckling length or dominant buckling mode.

Lavrenti'ev and Ishinskii (1949) conducted one of the earlier investigations that considered higher order buckling modes. Initial imperfections were represented as a series of free vibration modes. The study observed that the dynamic buckled response tended toward a dominant mode for impulse loads much greater than the static Euler load.

Lindberg (1965) states, however, that the behaviour may have been more indicative of plastic flow.

Housner and Tso (1962) developed models based on the Euler-Bernoulli, Rayleigh and Timoshenko beam theory. The objective was to determine the dominant modal response for a simply supported strut, with an initial half-sine wave geometric imperfection, subject to a decreasing triangular ramp, axial impulsive load. Propagation of the axial stress wave front was not considered in the analysis but the nonlinear axial strain terms were retained. The results were presented in terms of shock spectra for the fundamental mode characterized by dynamic to static response ratios. The dynamic displacement response, load magnitude and impulse duration were referenced to the initial deflection, critical static Euler load and fundamental mode of flexural vibration, respectively. The Euler-Bernoulli beam formulation proved adequate when compared to experimental results. The analyses demonstrated that for peak applied loads less than half the static Euler load, a bounded elastic vibrational response was exhibited for any impulse duration. Pulse loads significantly greater than the Euler load could be sustained provided the duration was short. Furthermore, the solution was bounded by applied load duration greater than one-quarter the fundamental period of vibration, where the effects of axial stress wave propagation could be assumed negligible.

Hayashi and Sano (1972b) conducted experimental studies and parallel finite difference analyses on the dynamic buckling of a steel beam ($8.7mm \times 0.63m \times 193mm$), with an initial half-sine wave imperfection ($0.76d$). The slender beam was axially impacted by a $0.369kg$ mass with striking velocities of $2.45m/s$, $6.3m/s$ and $10m/s$. The investigations concluded that the effects of rotary inertia, transverse shear and large displacement behaviour on the buckled response were negligible. Thus, for the parameters investigated Euler-Bernoulli beam theory was adequate to define the dynamic pulse buckling response. The axial stress distribution and buckled wavelengths were considered

dependent on the axial inertial term and impact velocity. Although the investigation was primarily concerned with the fundamental mode response, higher order modes were observed with smaller wavelengths associated with increasing impact velocity. The finite difference model was in good agreement with the experimental data and demonstrated the importance for considering grid spacing (aspect ratio of 1.6) on the computed dynamic response.

In similar studies, Ari-Gur et al. (1982, 1979 and 1978) investigated the elastic pulse buckling response by the finite difference method and impact testing. A single column was successively impacted by a free-fall dead weight hammer with increasing drop height until the transition from a bounded to unbounded response, based on a dynamic buckling criterion, was exhibited. Although the initial geometric configuration was defined by a fundamental mode imperfection, the final experimental buckled profiles were characterized by higher order mode response. Unfortunately, the numerical analysis focused on the fundamental mode response and did not consider the evolution of the complete buckled profile. Furthermore, the investigations considered only the elastic response and the final deformed profiles associated with plastic mechanisms were not addressed. More recently, Kadandale and Ari-Gur (1997) have also observed higher order mode response in finite difference investigations on the dynamic pulse buckling response of viscoelastic columns.

Gerard and Becker (1952) conducted innovative experiments to assess dynamic buckling events with respect to propagation of an axial stress wave. The authors considered dynamic buckling as the propagation of an elastic discontinuity as a function of time. The hypothesis was that a column of any length "...under certain conditions of impact loading could momentarily support a compressive stress of any magnitude in excess of the static Euler load..." (Gerard and Becker, 1952). Based on the described experimental procedure, the dynamic buckling test is illustrated in Figure 2-2.

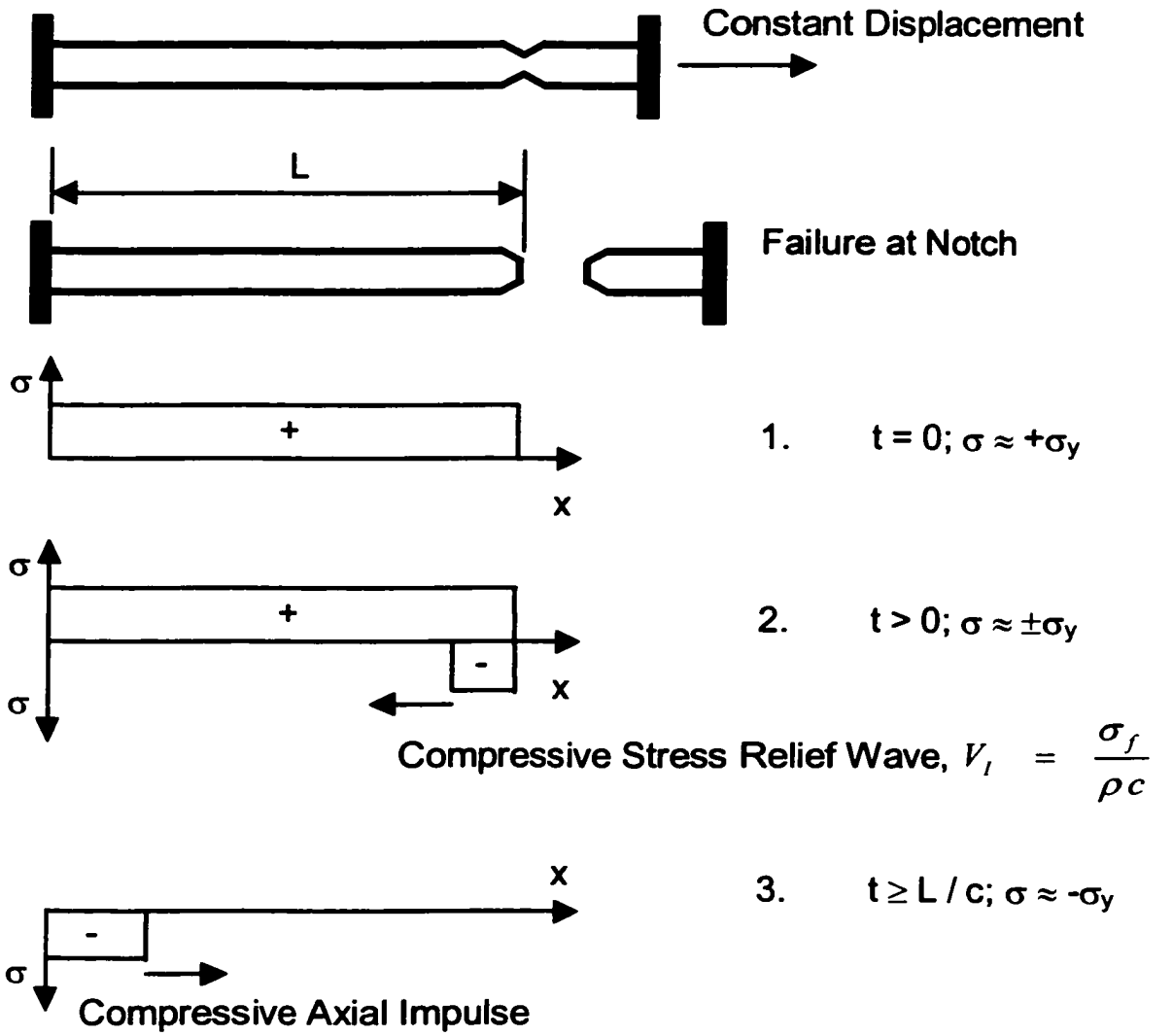

Figure 2-2. Schematic Illustration of Dynamic Buckling Experiments Conducted by Gerard and Becker (1952) and Lindberg (1965).

A rectangular slender beam (0.01"×0.5"×10"), with a precut notch at one end of the sample, was placed in a rigid, test frame. The beam was loaded in uniaxial tension at a constant displacement rate until failure. At time ($t = 0$), the magnitude of the tensile

stress $(+\sigma_y)$ was dictated by the notch size and beam material properties. An equivalent impact velocity could be estimated based on the expression,

$$V_I = \frac{\sigma_f}{\rho c} \tag{2.11}$$

where σ_f is the failure stress, ρ is the material density and c is the elastic stress wave velocity in the material. For threshold pulse buckling, the tensile stress would be on the order of the yield stress (σ_y). An equal and opposite compressive wave $(-\sigma)$ would propagate the beam length (L), for times ($0 \leq t \leq L/c$), toward the fixed support acting in stress relief. Residual stress perturbations would exist predominantly due to local geometric imperfections and load eccentricity. On reaching the lower fixed support, at time ($t = L/c$), the stress wave would reflect from the boundary and impart a compressive impulse to the beam. The load duration is a function of the beam length (L), where the free end condition would impose a tensile stress wave. Meyers (1994) presents further discussion on stress wave propagation in solids.

Gerard and Becker (1952), stated that the growth of buckled lateral displacements occurs after the wave front has propagated a critical beam length (L_{cr}) defined as,

$$L_{cr} = \frac{2\pi r}{\sqrt{\varepsilon}} = 2\pi r\sqrt{\frac{c}{V}} \tag{2.12}$$

where r is the radius of gyration ($r^2 = I/A$), ε is the axial strain, c is the elastic material wave speed constant and V is the impact velocity. Localised effects of notch plasticity and stress concentrations were considered far field and thus neglected. Equation (2.12) was based on simplified analysis that did not consider lateral inertia. The limited

experimental data presented, on buckled wavelengths, was consistent with the analytical expression.

2.2.3 Mode Perturbation Methods

Perturbation methods have also been employed to characterize the dynamic pulse buckling response of beams, plates and shells for intense loading conditions where inertia forces play a significant role. The influence of lateral inertia tends to produce a higher order modal response; that is smaller wavelengths with a wrinkled displaced profile. Perturbation methods consider the governing dynamic equation of motion and assume an initial imperfection, which can be related to geometry, load eccentricity, and spatial distribution of the applied impulse. The analysis would establish a "preferred" modal response (i.e. perturbation to motion). The method is limited, however, to simple geometric and load configurations, ideal boundary conditions and small departures from the dominant solution.

Lindberg (1965) conducted an experimental study, similar to Gerard and Becker (1951), and developed an analytical solution based on the perturbation method for the dynamic buckling response of an Euler-Bernoulli beam. Experimental and analytical investigations concluded that the buckled response was dependent on the impulse intensity and the effects of axial stress wave propagation could be ignored (i.e. uniform, constant axial impulse). In addition, with respect to the modal response, the analysis demonstrated that the exact nature of initial geometric imperfections was not required and could be adequately defined as stationary white noise. The natural local geometric imperfections were considered as a random variable. For a more detailed discussion on the theory of random processes, refer to Wirsching et al. (1995) and Newland (1993). The pulse buckling response exhibited an exponential or hyperbolic growth rate of transverse deflections, which could be characterised by a "most amplified" or "preferred"

mode. The theoretical analysis was consistent with experimental observations. Lindberg and Florence (1987) have also presented a comprehensive discussion on the elastic and plastic pulse buckling of bars, plates and shells. For the present investigations, elastic and plastic pulse buckling analysis will incorporate the "preferred" wavelength theory and thus, a detailed discussion is presented.

For intense pulse buckling events, the theoretical analysis continues from Equation (2.8) for the unbounded or hyperbolic response where the impulse is defined by $P >> (P_{cr})_E$. The beam length (L) does not have any direct significance due to the higher order modal response. Thus, a characteristic length can be defined by the static Euler wavelength parameter, $k^2 = P/EI$. Similarly, transverse deflections can be normalised with respect to the radius of gyration (r). Defining the nondimensional variables,

$$\xi = k\,x = \frac{s}{r}x, \quad w = \frac{y}{r}, \quad \tau = \frac{s^2 c\,t}{r} \tag{2.13}$$

where the parameter s relates the characteristic length to the lateral deflections,

$$s^2 = r^2 k^2 = \frac{r^2 P}{EI} = \frac{P}{EA} = \varepsilon \tag{2.14}$$

Substitution of the expressions (2.13) into Equation (2.1), assuming a general solution of the form, $y = A\sin(k\,x) + B\cos(k\,x) + C\,x + D$, and multiplying through by r^3/s^4 yields,

$$\frac{\partial^2 w}{\partial \tau^2} + \frac{\partial^4 w}{\partial \xi^4} + \frac{\partial^2 w}{\partial \xi^2} = -\frac{\partial^2 w_o}{\partial \xi^2} \tag{2.15}$$

where ξ is the nondimensional axial coordinate, w is the nondimensional lateral deflection of the bar, w_o is the initial geometric imperfection and τ is the nondimensional time parameter. The essential or geometric boundary condition for a simply supported bar is,

$$w\big|_{\xi=0,\ell} = 0; \quad \left.\frac{\partial^2 w}{\partial \xi^2}\right|_{\xi=0,\ell} = 0 \tag{2.16}$$

where $\ell = {}^{sL}\!/_{r}$. The solution for Equation (2.15) can be expressed by a Fourier series,

$$w(\xi,\tau) = \sum_{n=1}^{\infty} g_n(\tau)\sin\left(\frac{n\pi\xi}{\ell}\right) \tag{2.17}$$

and similarly the initial geometric imperfections can be defined by,

$$w_o(\xi) = \sum_{n=1}^{\infty} a_n \sin\left(\frac{n\pi\xi}{\ell}\right) \tag{2.18}$$

where the Fourier coefficient,

$$a_n = \frac{2}{\ell}\int_0^{\ell} w_o(\xi)\sin\left(\frac{n\pi\xi}{\ell}\right)d\xi \tag{2.19}$$

Equations (2.17) and (2.18) can be substituted into (2.15) to give the following equation of motion for the Fourier coefficients $g_n(\tau)$,

$$\frac{\partial^2 g_n}{\partial \tau^2} + \eta^2\left(\eta^2 - 1\right)g_n \;=\; \eta^2 a_n \tag{2.20}$$

where the wave number η is defined as $\eta = {}^{n\pi u}/_{\ell}$. Lindberg and Florence (1987) have derived the general solution for the lateral displacement,

$$w(\xi,\tau) \;=\; \sum_{n=1}^{\infty} \frac{a_n}{1-\eta^2}\left[\begin{matrix}\cos\\ \cosh\end{matrix}(p_n\,\tau) - 1\right]\sin\left(\frac{n\pi\xi}{\ell}\right), \tag{2.21}$$

where $p_n = \eta\sqrt{1-\eta^2}$ is a stability parameter. The characteristic nature of the solution is dependent on the sign of the Fourier coefficient (a_n). For $\eta > 1$ then the response is trigonometric and the amplitude is bounded, whereas for $\eta < 1$ then the displacement is hyperbolic. The transition point, $\eta = 1$, represents the familiar static Euler buckling wavelength.

The ratio between the Fourier coefficients, $g_n(\tau)$, for the buckled mode shape and, a_n, for the initial displacement of the unstressed bar defines the amplification function, $G_n(\eta, \tau)$,

$$G_n(\eta,\tau) \;=\; \frac{g_n(\tau)}{a_n} \;=\; \frac{1}{1-\eta^2}\left[\begin{matrix}\cos\\ \cosh\end{matrix}(p_n\,\tau) - 1\right]. \tag{2.22}$$

The amplification function is illustrated in Figure 2-3 in terms of the wave number (η) for several nondimensional times (τ). The amplification function is defined by exponential growth through the *cosh* term. For increasing time, the relative influence of the amplification function is insignificant for large wave numbers, $\eta > 1.2$, and the peak amplitude is centered between $0.8 \le \eta \le 1.0$. The hyperbolic growth rate of the maximum amplification magnitude with time is illustrated in Figure 2-4.

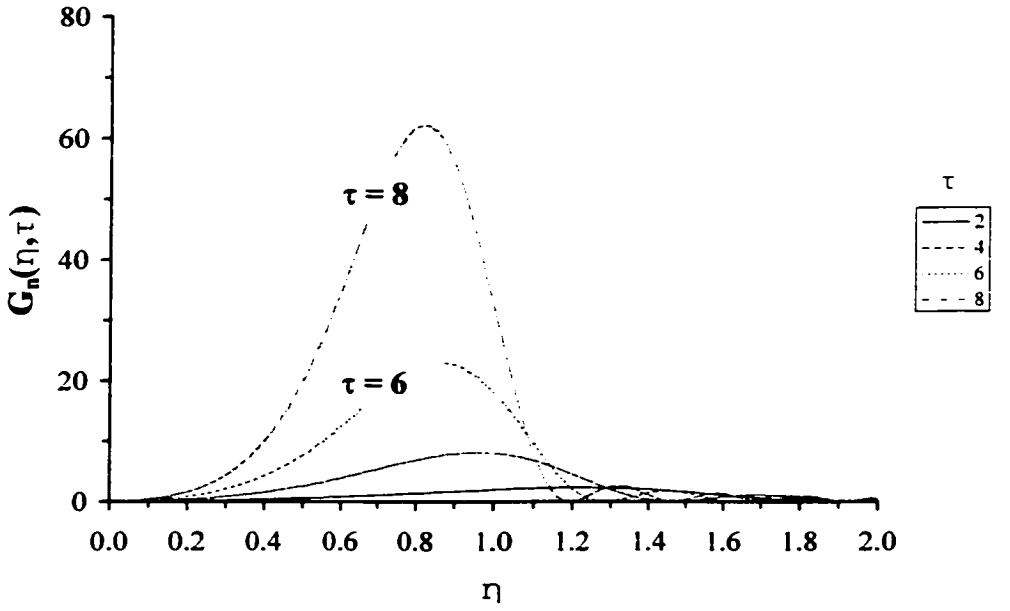

Figure 2-3. Amplification Function $G_n(\eta, \tau)$ as a Function of the Wavenumber (η).

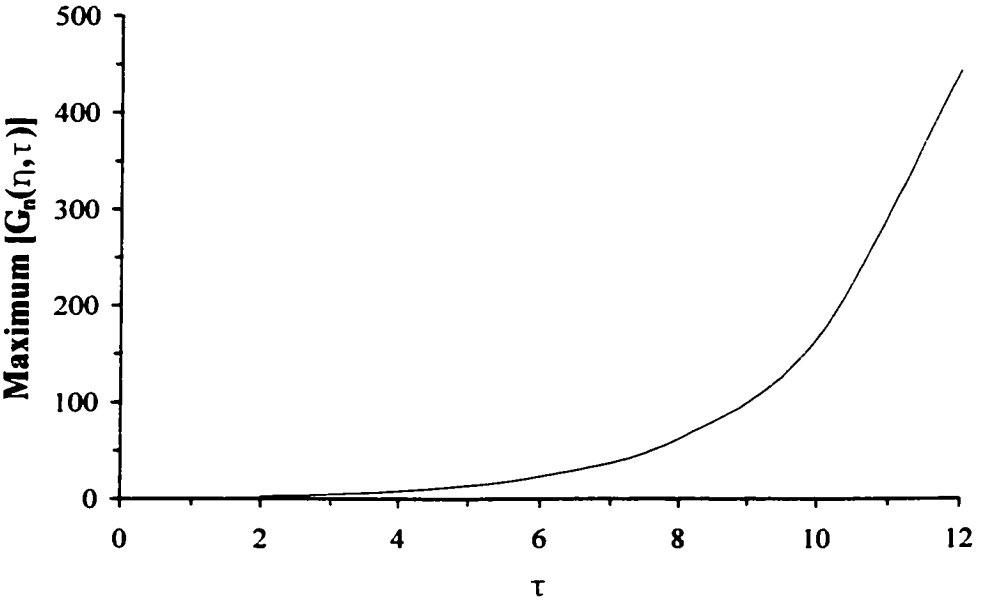

Figure 2-4. Growth Rate of the Peak Magnitude for the Amplification Function $G_n(\eta, \tau)$.

A "preferred" mode within the narrow band of harmonics, illustrated in Figure 2-3, may be determined by differentiating Equation (2.21) with respect to the square of the wave number (η^2),

$$\frac{dG_n}{d\eta^2} = \frac{(1-2\eta^2)}{2\eta^2(1-\eta^2)^2} p_n \tau \sinh(p_n \tau) + \frac{1}{(1-\eta^2)^2} p_n \tau [\cosh(p_n \tau) - 1], \quad (2.23)$$

and setting to zero yields,

$$1 - \frac{1}{2\eta^2} = \frac{1}{p_n \tau}\left[\frac{\cosh(p_n \tau) - 1}{\sinh(p_n \tau)}\right]. \quad (2.24)$$

For large time (τ) where $p_n \tau >> 1$, the wave number of the most amplified mode can be determined through an approximation of Equation (2.24) expressed as,

$$\eta_{cr}^2 = \frac{1}{2}. \quad (2.25)$$

The "preferred" wave number (η_p) and wavelength (λ_p) is,

$$\eta_p = \frac{1}{\sqrt{2}}; \quad \lambda_p = 2\pi\sqrt{2}, \quad (2.26)$$

The dimensional form for the "preferred" wavelength is,

$$x_p = \frac{r}{s}\lambda_p = 2\pi r\sqrt{\frac{2}{\varepsilon}}. \quad (2.27)$$

Note the similarity of Equation (2.27) with Equation (2.12) developed by Gerard and Becker (1951).

To initiate dynamic instability, perturbations to the initial geometric configuration velocity field, applied loads or material properties must be considered. In addition, the formulation must satisfy the geometric boundary conditions. Local geometric imperfections can be incorporated as a random variable,

$$w_o(\xi) = \sum_{n=1}^{N} a_n \sin(\eta \xi + \theta_n), \tag{2.28}$$

where N is an upper limit on the number of terms in the series such that $\eta < 2$ and θ_n is a phase angle uniformly distributed on the interval $0 \leq \theta_n \leq 2\pi$. The Fourier coefficients (a_n) are assumed to be random normal (Gaussian) with a zero mean and unit standard deviation. For practical applications, the imperfections defined by Equation (2.28) must be bounded (N) and, for white noise to be applicable, the bandwidth must extend well beyond the wavelengths of interest. These assumptions are consistent with respect to the weak amplification for modes ($\eta \geq 1.2$) as shown in Figure 2-3, and the most amplified, "preferred" mode as defined by Equation (2.26). Furthermore, with increasing time (τ), the cutoff tends toward ($\eta = 1$), which is illustrated in Figure 2-3 and is expressed in Equation (2.22) by the hyperbolic response ($\eta < 1$).

An analytical expression for the mean wavelength in terms of the amplification function, Equation (2.22), can be derived assuming stationary buckled displacements. This condition is satisfied when the observed wavelengths are small with respect to the total beam length and influence of the boundary conditions can be neglected. Lindberg and Florence (1987) developed an expression defining the mean wavelength response (λ_m) between alternate zero crossings as,

$$\lambda_m(\tau) = 2\pi\left[\frac{\int_0^\infty G^2(\eta,\tau)d\eta}{\int_0^\infty \eta^2 G^2(\eta,\tau)d\eta}\right]^{1/2} \tag{2.29}$$

An approximate expression was also derived for the most amplified mode with respect to the "preferred" response,

$$\eta_a(\tau) = \frac{1}{\sqrt{2}}\sqrt{\frac{\tau}{\tau-2}}. \tag{2.30}$$

Equation (2.29), which was evaluated numerically over the interval ($0 < \eta < 2$), and Equation (2.30) are illustrated in Figure 2-5. For later solution times (τ), the wavelength response (λ) tends toward the "preferred" mode (λ_p). Although Equation (2.29) more accurately represents the statistics of a stationary process, the relative simplicity and utility of the most amplified mode (η_a) through Equation (2.30) was illustrated.

2.3.4 Elastic Buckling Criterion

Specification of pulse buckling threshold limits is required for preliminary and detailed engineering assessment and design of structures subject to dynamic loads. Although somewhat arbitrary, the characterization of limit criteria for elastic pulse buckling instability is typically related to the applied load intensity. The limit is generally bounded by design considerations and functional constraints. For example, an elastic buckling criterion could be defined in terms of the structural behavior (i.e. transition from bounded to unbounded response), critical deflection amplitude, stress or strain magnitude, or elastic shock threshold (i.e. loads imparted to passengers or subcomponents). For the dynamic elastic buckling of beams, subject to an intense axial impulse, there have been few criteria addressed in the public domain.

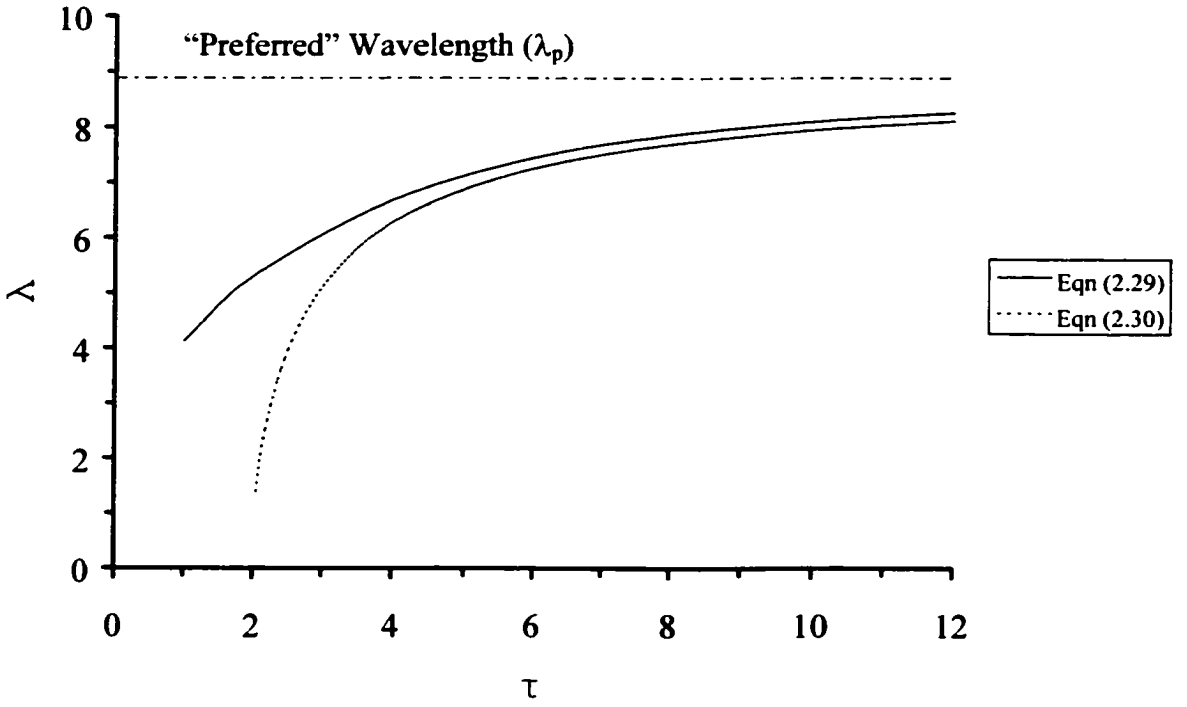

Figure 2-5. Mean Wavelength (λ_m) and Most Amplified Wavelength (λ_a) Response as a Function of Nondimensional Time (τ).

Based on the work of Budiansky and Hutchinson (1966), Ari-Gur et al. (1982) defined a critical state as a large change the in structural response for a small increase in the applied load. This is illustrated in Figure 2-6 where the transverse deflection (w) and slope ($dw/d\varepsilon_c$) are presented as a function of the compressive strain (ε_c). The critical dynamic axial strain ($(\varepsilon_{cr})_D$) is defined by the rapid change in slope ($dw/d\varepsilon_c$). The investigations, conducted by Ari-Gur et al. (1982), considered a column axially loaded by successive free-fall impacts from a dead weight hammer released at increasing drop heights. The procedure was continued until the critical axial strain ($(\varepsilon_{cr})_D$) was established. Two foil gauges, located at, measured the column response midspan, to determine the maximum midspan compressive and bending strains developed for each impact event.

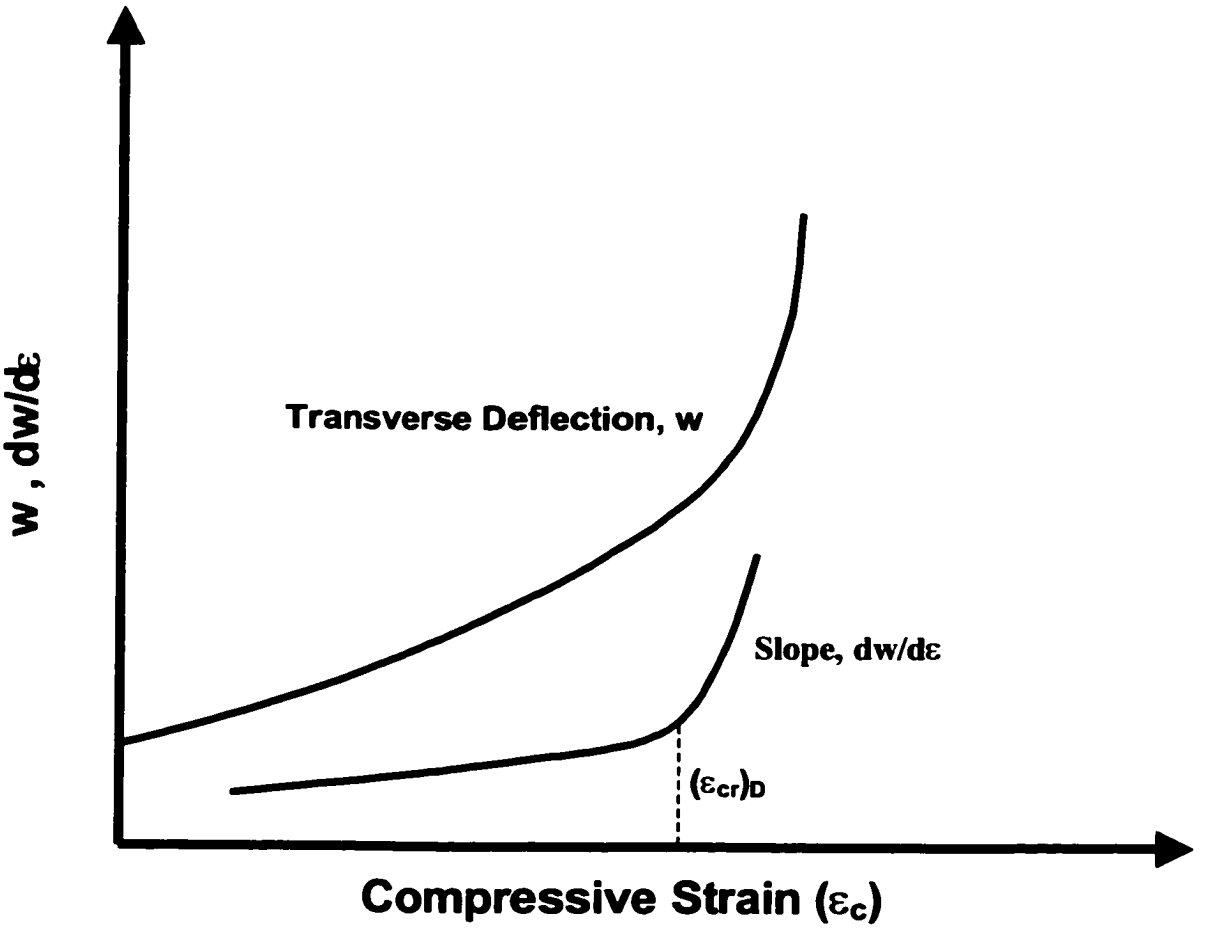

Figure 2-6. Schematic Illustration of the Dynamic Buckling Criterion.

A dynamic buckling criterion, defined as the dynamic load amplification factor (*DLF*), was expressed as,

$$DLF = \frac{(\varepsilon_{cr})_D}{(\varepsilon_{cr})_E}, \tag{2.31}$$

where $(\varepsilon_{cr})_D$ is the measured critical dynamic buckling strain and $(\varepsilon_{cr})_E$ is the theoretical classical static Euler buckling strain. Ari-Gur et al. (1982) showed that the *DLF* could be

represented as a function of the effective slenderness ratio through a power law relationship (Figure 2-7). The study concluded that material and mechanical properties (e.g. flexural rigidity, stress wave velocity and density) had only secondary effects on the dynamic buckling criterion. Later investigations conducted by Ari-Gur and Elishakoff (1993,1990) only considered the axial deformation and lateral displacement or curvature, rather than strain, as a function of load intensity (stress or strain). Although the elastic pulse buckling analysis focused on the fundamental mode response, the experimental investigations illustrated that the transition from elastic to plastic behaviour exhibited higher order modes.

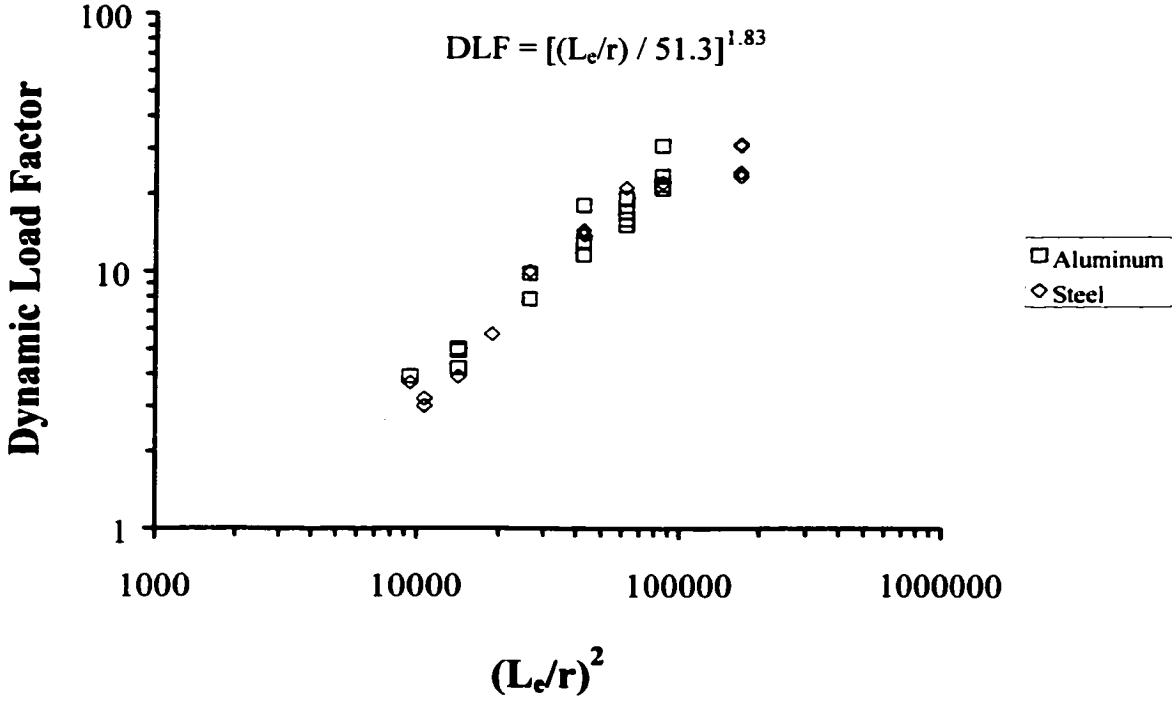

Figure 2-7. Relationship Between the Dynamic Load Factor (*DLF*) and Effective Slenderness Ratio (L_e/r) for Aluminum and Steel Columns (Ari-Gur et al., 1982).

Lindberg and Florence (1987) defined a dynamic buckling criterion in terms of the critical impulse duration to section yield at the peak buckle crest. The analysis assumed a "preferred" mode response with a single equivalent single imperfection related to the dominant wavelength. The geometric imperfections was expressed as,

$$A_p = \beta L_p \tag{2.32}$$

where β is the imperfection coefficient ($0.0001 \leq \beta \leq 0.001$) and L_p is the "preferred" half-wavelength. Lindberg and Florence (1987) and Timoshenko and Gere (1962) present a further discussion on the nondimensional imperfection coefficient (β). Based on Equation (2.27) and $\lambda_p/2 = sL_p/r$, a nondimensional imperfection can be defined,

$$a_p = \frac{\beta \lambda_p}{2s} = \frac{\pi \beta \sqrt{2}}{s} \tag{2.33}$$

Assuming elementary beam theory, the extreme fiber ($\pm h$) theoretical normal stress (σ_{th}) due to bending, for a beam with rectangular cross-section, can be defined as,

$$\sigma_{th} = \frac{Mh}{I} = \frac{Eh}{2}\frac{\partial^2 y}{\partial x^2} = \sqrt{3}Es^2\frac{\partial^2 w}{\partial u^2} \tag{2.34}$$

Substituting Equation (2.14), the appropriate differential expression from (2.21) and the Fourier coefficient from (2.33) into (2.34) yields,

$$\frac{1-\bar{\sigma}}{\sqrt{\bar{\sigma}}} = \pi\beta\sqrt{\frac{6}{\varepsilon_y}}\left[\cosh\left(\frac{\tau_{cr}}{2}\right)-1\right] \tag{2.35}$$

where the normalized stress parameter $(\bar{\sigma})$ relates the applied axial impulse stress magnitude to the yield stress. The expression (2.34) defines the critical impulse duration (τ_{cr}) as a function of the normalized stress parameter to initiate section yield, which assumed $\varepsilon_{y = 0.5\%}$ to be a representative value for engineering metals. The critical impulse intensity to initiate yield response of the peak buckle crest, based on the "preferred mode analysis, is illustrated in Figure 2-8 as a function of the nondimensional imperfection amplitude (β). Lindberg and Florence (1987) also demonstrated that local random geometric imperfections were equivalent to a single imperfection on the order of 1% to 3% of the beam depth of the "preferred" mode.

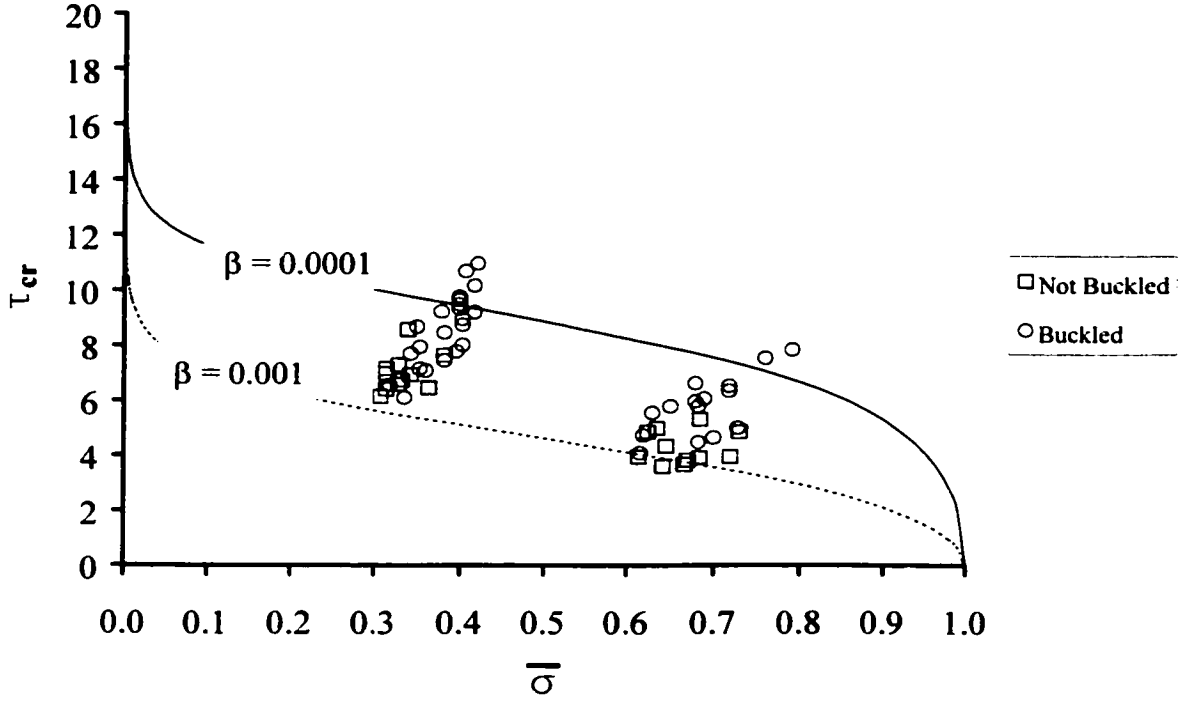

Figure 2-8. Analytical Curves Defining the Critical Impulse Intensity to Yield for the Peak Buckle Crest Based on the "Preferred" Mode Analysis. Data Points are from Experimental Studies presented by Lindberg and Florence (1987).

Since the pioneering work of Taub (1933), a significant number of studies on the dynamic buckling of axially loaded beams have been conducted. The focus, however, has been on relatively low intensity pulse buckling events concentrating on the fundamental mode response. Limited investigations have considered intense elastic pulse buckling problems where higher order modal response has been observed. These events are defined by an impulsive load of large amplitude and short duration relative to the yield stress or static Euler load and fundamental period of vibration, respectively.

The perturbation analysis, conducted by Lindberg and Florence (1987) and Lindberg (1965), has demonstrated the potential for initiating an unbounded exponential growth of transverse displacements due to exploitation of initial local random geometric imperfections. One of the primary objectives for the present thesis is the development of accurate numerical models, by the finite difference and finite element methods, simulating elastic threshold pulse buckling events for axially loaded beams. Establishing the fundamental parameters required for simple models can then be extended to analysis of more complex geometric configurations and boundary conditions.

3.0 Finite Difference Analysis of Elastic Pulse Buckling Events

The development of a finite difference model to predict the elastic pulse buckling response of a slender beam subject to an intense axial impact is presented. The research effort is founded on the the analytical and experimental studies of Gerard and Becker (1952), Lindberg (1965) and Lindberg and Florence (1987). The numerical analysis is focused on modelling the high order mode response associated with intense elastic pulse buckling events. To the author's knowledge, a parametric numerical study on the dynamic pulse buckling response of slender beams with respect to the "preferred" wavelength theory has not yet been conducted. The importance of grid spacing, geometric imperfection formulation and impulse intensity on the computed pulse buckling response is demonstrated.

3.1 Finite Difference Formulation

Consider an isotropic, homogeneous elastic bar subject to a dynamic, axial compressive impulse (Figure 2-1). The nondimensional linear differential equation of motion (Equation 2.15) is restated,

$$\frac{\partial^2 w}{\partial \tau^2} + \frac{\partial^4 w}{\partial \xi^4} + \frac{\partial^2}{\partial \xi^2}(w + w_o) = 0, \tag{3.1}$$

where w is the nondimensional lateral deflection of the bar, w_o is the initial geometric imperfection, ξ is the nondimensional axial coordinate, and τ is the nondimensional time parameter. The equation of motion (3.1) can be approximated by second order, central difference expressions with quadratic convergence,

$$\frac{1}{\Delta\tau^2}\left(w_i^{k-1} - 2w_i^k + w_i^{k+1}\right) +$$
$$\frac{1}{\Delta\xi^4}\left(w_{i-2}^k - 4w_{i-1}^k + 6w_i^k - 4w_{i+1}^k + w_{i+2}^k\right) + \qquad (3.2)$$
$$\frac{1}{\Delta\xi^2}\left(w_{i-1}^k - 2w_i^k + w_{i+1}^k\right) + \frac{1}{\Delta\xi^2}\left(w_{oi-1} - 2w_{oi} + w_{oi+1}\right) = 0$$

where the subscript i refers to the discretized grid point over the spatial domain and k is the time step increment. Rearranging Equation (3.2) in terms of an explicit time integration solution, the nondimensional lateral displacement (w) at time ($k+1$) can be expressed as,

$$w_i^{k+1} = 2w_i^k - w_i^{k-1} - \frac{\Delta\tau^2}{\Delta\xi^4}\left(w_{i-2}^k - 4w_{i-1}^k + 6w_i^k - 4w_{i+1}^k + w_{i+2}^k\right) - \qquad (3.3)$$
$$\frac{\Delta\tau^2}{\Delta\xi^2}\left(w_{i-1}^k - 2w_i^k + w_{i+1}^k\right) - \frac{\Delta\tau^2}{\Delta\xi^2}\left(w_{oi-1} - 2w_{oi} + w_{oi+1}\right)$$

The differential equation of motion is known as an initial value problem and the error term is of order $O(\Delta\xi^2)$. For a simply supported beam at time ($\tau = 0$) the initial conditions are,

$$w(\xi, \tau = 0) = \frac{dw(\xi, \tau = 0)}{d\tau} = \frac{d^2w(\xi, \tau = 0)}{d\tau^2} = 0. \qquad (3.4)$$

The essential (geometry, displacement) boundary conditions and natural (force, moment) boundary conditions are,

$$\xi|_{\xi=L} = 0; \quad w|_{\xi=0,L} = 0; \quad \left.\frac{\partial^2 w}{\partial\xi^2}\right|_{\xi=0,L} = 0 \qquad (3.5)$$

For the grid points adjacent to the boundary nodes (i.e. i = *2,N-2*), a central difference expression for the moment boundary condition is invoked.

$$w_{i-1}^{k} = -w_{i+1}^{k} \tag{3.6}$$

Inherent assumptions associated with elementary bending theory can be stated as small displacements and rotations with the restriction of plane sections to the neutral axis remain plane with deformation and sectional response defined by the moment–curvature relationship. The effects of transverse shear deformation and axial shortening are neglected. For structural dynamic considerations, rotational and axial inertia terms are ignored and lumped mass terms are distributed at discrete grid points to account for flexural inertia.

3.2 Stability Analysis

In order to establish a reliable finite difference model, which is an approximation to the differential quation of motion, a stability analysis must be conducted. The method is valid for the solution of linear differential equations with constant coefficients. The analysis defines conditions for stablilty based on the propagation of a single error term through the solution. For the dynamic pulse buckling, influence of the axial and flexural wave propagation response are important, which are characterized by the spatial domain (Δx) and time increment (Δt) parameters.

Consider the longitudinal wave equation,

$$\frac{\partial^2 u}{\partial t^2} = c\frac{\partial^2 u}{\partial x^2} \tag{3.7}$$

which can be approximated by the finite difference expression,

$$\frac{1}{\Delta t^2}\left(u_i^{k-1} - 2u_i^k + u_i^{k+1}\right) = \frac{c^2}{\Delta x^2}\left(u_{i-1}^k - 2u_i^k + u_{i+1}^k\right) \tag{3.8}$$

The stability of Equation (3.8) can be determined on the basis of an initial line of grid errors in terms of a Fourier series,

$$E_n = \sum_{n=0}^{N} A_n e^{i\beta_n ph}, \quad p=0,1,\ldots N \tag{3.9}$$

where $u = ph$ and $\beta_n = {}^{n\pi}/_{L} = {}^{n\pi}/_{Nh}$. Consider a single term ($e^{-i\beta ph}$) for the initial condition ($\tau = qk = 0$) and assume,

$$E_{pq} = e^{i\beta u} e^{\alpha\tau} = e^{i\beta ph} e^{\alpha qk} = e^{i\beta ph}\xi^q . \tag{3.10}$$

where $\xi = e^{\alpha k}$ and α is a complex constant. A stable solution requires that the modulus, $|\xi_s| \le 1$. Substitution of Equation (3.10) into Equation (3.8) yields,

$$\frac{e^{i\beta ph}}{\Delta t^2}\left(\xi_s^{q-1} - 2\xi_s + \xi_s^{q+1}\right) = \frac{c^2\xi_s^q}{\Delta x^2}\left(e^{i\beta(p-1)h} - 2e^{i\beta ph} + e^{i\beta(p+1)h}\right) \tag{3.11}$$

Dividing Equation (3.11) by Equation (3.10) and using the Euler identities,

$$\xi_s^{-1} - 2 + \xi_s = \frac{c^2\Delta t^2}{\Delta x^2}\left[2\cos(\beta h) - 2\right]. \tag{3.12}$$

Solving for the modulus yields,

$$\frac{c\Delta t}{\Delta x} \geq 1. \tag{3.13}$$

This has also been discussed by Courant et al. (1928) and Bathe (1996). The method can also be applied to the flexural wave equation for the vibrations of a slender beam,

$$\frac{\partial^2 y}{\partial t^2} = -\frac{EI}{\overline{m}}\frac{\partial^4 y}{\partial x^4}. \tag{3.14}$$

where the condition for stability can then be expressed as,

$$\frac{\Delta t}{\Delta x^2} \leq \frac{1}{2rc}. \tag{3.15}$$

Further discussion on the flexural stability parameters is presented in Ames (1977) and Ari-Gur et al. (1979).

In addition to solution stability, the appropriate grid spacing (Δx) and time step increment (Δt) for an accurate and convergent solution must be considered. As a general statement, the accuracy of numerical techniques, such as finite difference or finite element methods, increases as the mesh topology becomes finer and/or the solution time step decreases. In addition to inherent errors; such as truncation and round-off, a balance between the computational effort and solution accuracy must be weighed. Typically the *Courant number* (C_n) is evaluated,

$$C_n = \frac{\Delta t}{\Delta t_{cr}}, \tag{3.16}$$

which expresses the ratio between the solution time step (Δt) and the stability requirement or critical time step (Δt_{cr}). Cook et al. (1989) recommends a maximum Courant number on the order of 0.95–0.98.

For the dynamic response analysis of structural systems with lumped properties, the most accurate solution, when employing explicit time integration procedures, is obtained by integrating with a time step equal to the stability limit. The solution is less accurate when a smaller time step is considered, particularly when a coarse spatial discretization has been defined (Bathe, 1996). This phenomenon is due to spurious oscillations or high frequency noise that the numerical model cannot resolve. Algorithmic or stiffness proportional damping as well as implicit or mixed integration schemes are methods that can be employed to dissipate high frequency numerical noise.

3.3 Elastic Pulse Buckling Analysis

The analysis is concerned with the development of numerical finite difference models investigating the higher order modal response of slender beams subject to an intense axial impact. Although dynamic buckling has received reasonable attention, the historical research effort has generally focused on the fundamental mode response. Based on experimental and analytical investigations of intense pulse loading events, Lindberg and Florence (1987) has demonstrated that the buckling response can be characterized by an unbounded, exponential transverse peak buckle growth and higher order modes associated with a "preferred" wavelength. The main objective for the finite difference analysis is to define the parameters required for accurate numerical modelling with respect to the "preferred" mode response. The influence of grid spacing, geometric imperfection formulation and load intensity will be considered.

3.3.1 Beam Model Parameters

For the finite difference models, the beam geometry was 762mm×12.7mm×0.3175mm, which was adopted from the studies of Lindberg (1965) and Lindberg and Florence (1987). The beam was considered homogeneous and isotropic with an elastic modulus, $E = 69GPa$, and density, $\rho = 2700kg/m^3$. The beam was simply supported and was subjected to a constant axial stress of 276MPa. A constant Courant number of 0.95 was selected based on Cook et al. (1989). Table 3-1 summarizes the parameters required for a stable numerical solution as a function of the discretized aspect ratio. Equation (3.13) and (3.15) define the critical time step (Δt_{cr}) for the axial and flexural stress wave response between successive grid points, respectively.

Table 3-1. Critical Time Step (Δt_{cr}) Required for a Stable Finite Difference Solution.

Number of Grid Points	Aspect Ratio	Axial Mode Equation (3.13) Δt_{cr} (μs)	Flexural Mode Equation (3.15) Δt_{cr} (μs)
100	24:1	1.51	62.66
300	8:1	0.50	6.96
600	4:1	0.25	1.74
1200	2:1	0.13	0.44
2400	1:1	0.06	0.11

3.3.2 Fundamental Mode Imperfection

Numerical methods investigating the dynamic buckling of structures have to account for natural variations in the structural geometry (e.g. surface perturbations), loading conditions

(e.g. eccentric or non-uniform load, velocity profile) or material properties (e.g. elastic modulus) to initiate instability. Historically, investigations have generally only considered the fundamental mode response of a simply supported beam. The imperfections were defined as an initial geometric perturbation in the form of a discrete half-sine wave with the peak amplitude a fraction of the beam depth. For the numerical models developed in this study, the fundamental mode imperfection was superimposed on all grid points of the ideal geometry by the following expression,

$$y_o(x) = \bar{y}(x) + A_o \sin\left(\frac{n\pi x}{L}\right) \tag{3.17}$$

where $y_o(x)$ is the perturbed transverse geometry, x is the axial coordinate, $\bar{y}(x)$ is the ideal transverse geometry $(\bar{y}(x) = 0)$, A_o is the constant amplitude coefficient, n is the mode number ($n = 1$) and L is the beam length.

Table 3-2 summarizes the parameters for the finite difference (*FD*) models that incorporated a discrete, fundamental mode geometric imperfection. A constant Courant number (C_n = *0.95*) was selected to ensure solution accuracy and stability. The selection of a constant stability number would also facilitate comparative analysis on the effects of grid discretisation with respect to the computed modal response.

Table 3-2. Finite Difference Models with Discrete Fundamental Mode Imperfection.

Model	Number of Grid Points	Aspect Ratio	Δt (μs)	$\%d_{max}$
FD1	16	150:1	9.00	25
FD2	2400	1:1	0.06	10
FD3	2400	1:1	0.06	100

Notes: Aspect ratio is the longitudinal grid spacing to beam depth ratio, Δt is the integration time step, $\%d_{max}$ is the maximum imperfection amplitude as a percentage of the beam depth.

Previous investigations have considered coarsely meshed domains. Sevin (1960) and Ari-Gur et al. (1982) considered the beam length to be divided by 16 grid points. For the later study, this corresponded to aspect ratios over the range of 4:1 to 15:1. Hayashi and Sano (1972b) considered a aspect ratios of 2.6:1, 3.8:1 and 7.7:1 and demonstrated the influence of grid spacing on the computed buckled response, in particular with respect to the axial displacement and force. Furthermore, the present study will also demonstrate the requirement for employing aspect ratios on the order of 1:1 for accurate numerical modelling consistent with the "preferred" wavelength theory.

Assuming the dominant wave number or "preferred" mode is, $\eta_p = 1/\sqrt{2}$, Lindberg and Florence (1987) have demonstrated that the transverse peak buckle amplitude can be defined by,

$$w(\tau) = w_o g_p(\tau) = 2 w_o \left[\cosh\left(\frac{\tau}{2}\right) - 1 \right], \tag{3.18}$$

where w_o is the nondimensional equivalent initial imperfection for the Fourier coefficient ($w_o = y_o/r$), and g_p is the amplification function. An alternative relationship was also developed, which considers the initial imperfection (w_o) plus the lateral deflection,

$$w(\tau) = w_o \left[1 + g_p(\tau) \right]. \tag{3.19}$$

These expressions (3.18, 3.19) were validated by experimental observations and measurements on the growth of peak buckle amplitudes.

As shown in Figure 3-1, the computed pulse buckling response for the finite difference model (*FD2* and *FD3*) was not consistent with the perturbation analysis, which exhibits exponential growth. An imperfection coefficient of $w_o = 0.35$ ($y_o = 10\%d = 0.03175mm$)

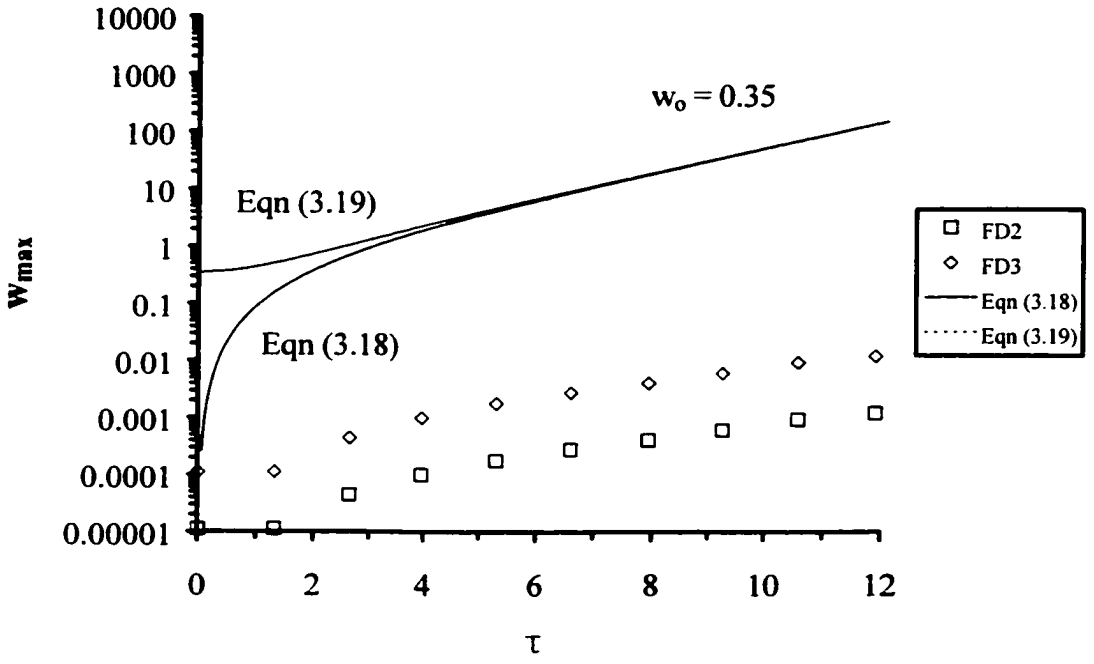

Figure 3-1. Nondimensional Peak Buckle Amplitude (w_{max}) as a Function of Time (τ) for Finite Difference Models with Discrete Fundamental Mode Imperfection.

was used to plot Equations (3.18) and (3.19), which is greater than the equivalent single mode imperfections, on the order of 1% to 3% of the beam depth, as discussed by Lindberg and Florence (1987). The pulse buckling response of the finite difference models was not consistent with the characteristic unbounded growth of transverse deflections. In addition, as will be demonstrated later, the delayed response of the finite difference models for solution times ($\tau \leq 2$) was attributed to the fundamental mode imperfection.

3.3.3 Combined Geometric Imperfections

The finite difference models that incorporated combined (i.e. discrete and random) geometric imperfections are presented in Table 3-3.

Table 3-3. Finite Difference Models with Combined Geometric Imperfections.

Model	Number of Grid Points	Aspect Ratio	Δt (μs)	C_n	$\%d_{max}$
FD4	2400	1:1	0.06	0.95	106
FD5	2400	1:1	0.06	0.95	101

Notes: *A*spect ratio is the longitudinal grid spacing to beam depth ratio, *Δt* is the integration time step, $\%d_{max}$ is the maximum imperfection amplitude as a percentage of the beam depth.

Perturbations to the ideal geometry of the finite difference model were defined by the superposition of a global, discrete half-sine wave (Equation 3.17) with local random imperfections expressed as,

$$y_o(x) = \bar{y}(x) + \sum_{n=1}^{N} a_n \sin\left(\frac{n\pi x}{L} + \theta_n\right), \tag{3.20}$$

where N is the upper limit on the number of terms and θ_n is a phase angle uniformly distributed on the interval ($0 \le \theta_n \le 2\pi$). The maximum number of series terms (N) is related to characteristics of the amplification growth function (Figure 2-3). The nondimensional wave number can be bounded as $\eta = {n\pi}/{\ell} = {n\pi r}/{sL} < 2$ and thus the number of series terms is expressed as $N = {2sL}/{\pi r}$. The Fourier coefficient, a_n, is defined as a stationary normal (Gaussian) random number and expressed as $a_n = \beta L_p$, where β is an imperfection factor and L_p is the "preferred" half-wave length. Lindberg and Florence (1987) define the dominant mode as $\lambda_p = 2\pi\sqrt{2}$ where $L_p = \lambda_p r/2s$. The imperfection parameter (β) is defined within the range ($0.0001 \le \beta \le 0.001$) and was selected as a uniform random number. The parameter (β) was based on investigations by Salmon in 1921 and further discussion on the nondimensional imperfection coefficient (β) is presented by Lindberg and Florence (1987) and Timoshenko and Gere (1962).

For the finite difference models, *FD4* and *FD5*, the discrete fundamental mode imperfection was equal to the beam depth (i.e. *1.0d*) and local random imperfections were superimposed on the fundamental mode geometry perturbation. Mean random imperfection magnitudes were on the order of *0.02d* with a standard deviation of *0.015d*. The random geometric imperfections for Model *FD5* were multiplied by a factor of 0.1 to assess the relative importance of random perturbations on the computed response. Note that at a distance of less than *0.05L* from the support boundary condition, the imperfection amplitudes for the discrete and random imperfections were of the same order.

The significant influence of local random imperfections on the pulse buckling response and growth of transverse deflections is illustrated in Figure 3-2. An imperfection coefficient of $w_o = 0.21$ ($y_o = 6\%d = 0.02mm$), which characterizes Model *FD4*, was used to plot the buckle growth rate Equations (3.18) and (3.19). Although the discrete fundamental mode amplitude was neglected in the imperfection amplitude (w_o) term, the analytical expressions and computed response for Model *FD4* are in good agreement. Data for Model *FD3*, with equal imperfection amplitude but defined only by the fundamental mode, is also shown for comparison. Thus, the importance of local random imperfections on the pulse bucking response of a slender beam subject to an intense axial impact has been demonstrated. In addition, the response of Model *FD5*, with local random imperfection magnitudes one order of lower than Model *FD4*, provides further supporting data.

The exploitation of local random geometric imperfections by the axial impulse was critical for initiating the enhanced growth rate of transverse displacement. The marked improvement in the pulse buckling response was attributed to local load eccentricities arising from random surface perturbations and the coupled influence of relative stiffness and interaction effects between the beam and rigid support boundary condition, which directly impacts modal competition.

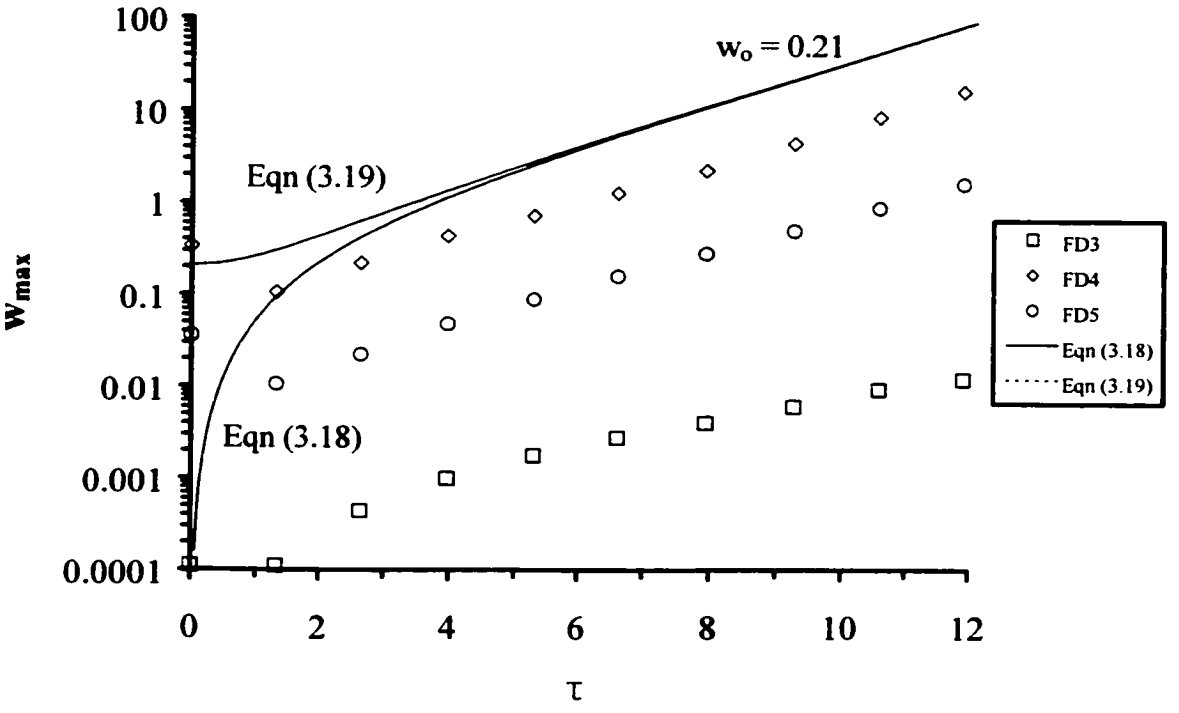

Figure 3-2. Nondimensional Peak Buckle Amplitude (w_{max}) as a Function of Time (τ) for Finite Difference Models with Discrete and Combined Geometric Imperfections.

3.3.4 Random Geometric Imperfections

Based on these investigations, finite difference models that considered only local random imperfections were developed to investigate the pulse buckling response of a slender beam subject to an intense axial impulsive load. Details of the finite difference models are summarised in Table 3-4.

Table 3-4. Finite Difference Models with Random Geometric Imperfections.

Model	Number of Grid Points	Aspect Ratio	Δt (μs)	C_n	$\%d_{avg}$	$\%d_{max}$
FD6	100	24:1	1.40	0.93	2	7
FD7	300	8:1	0.48	0.95	3	9
FD8	600	4:1	0.24	0.95	3	9
FD9	1200	2:1	0.12	0.95	3	9
FD10	2400	1:1	0.06	0.95	3	9

Notes: *A*spect ratio is the longitudinal grid spacing to beam depth ratio, Δt is the integration time step, $\%d_{avg}$ and $\%d_{max}$ is the average and maximum imperfection amplitude as a percentage of the beam depth.

Incorporation of only random imperfections significantly influenced the pulse buckling response as illustrated in Figure 3-3. The buckled profile for Model *FD10* was plotted as a function of the nondimensional axial coordinate (u) for several solution times (τ). The finite difference solution and the representative analytical investigations conducted by Lindberg and Florence (1987), presented in Figure 3-3(b) are in good agreement.

The characteristic exponential growth of transverse displacements, consistent with the perturbation analysis, was exhibited (Figure 3-4). Marked improvement in the computed response for finite difference models with only random imperfections over discrete and combined imperfection models was also illustrated. An average imperfection coefficient of $w_o = 0.087$, equivalent to $y_o = 2.5\%d = 0.008mm$, was selected to plot Equations (3.18) and (3.19). The finely discretised models (*FD9*, *FD10*) best accounted for the unbounded growth of peak buckle displacements throughout the solution.

The significant influence of random geometric imperfections on the buckled response was demonstrated. The effect of discrete imperfections (Model *FD4*) and coarse aspect ratios (Model *FD6*) was to delay the early growth of transverse displacements ($\tau \leq 2$) as illustrated

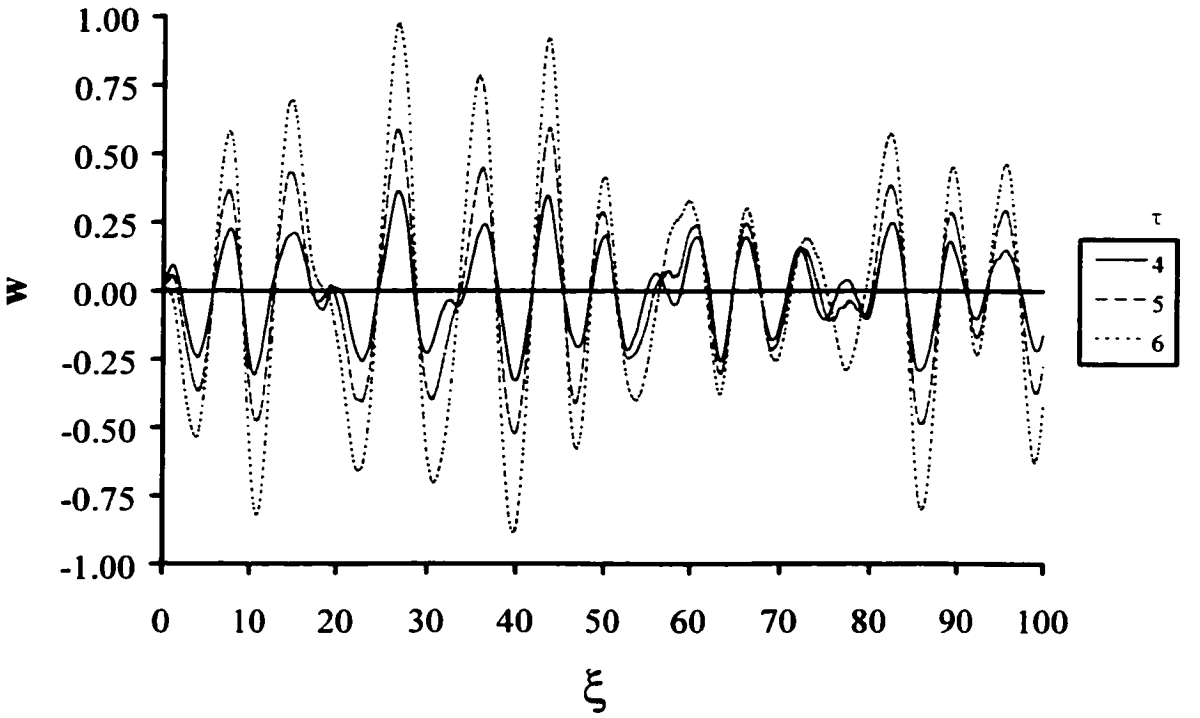

(a)

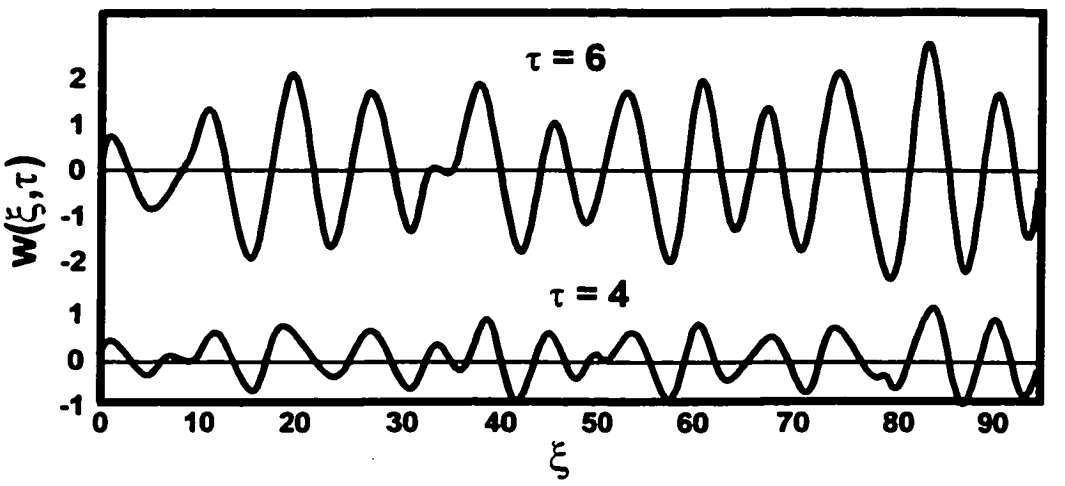

(b)

Figure 3-3. Nondimensional Buckle Profile (w) as a Function of Nondimensional Axial Coordinate (ξ) and Time (τ) for (a) Finite Difference Model *FD10*, (b) Digitised Buckle Profile Computed by Lindberg and Florence (1987).

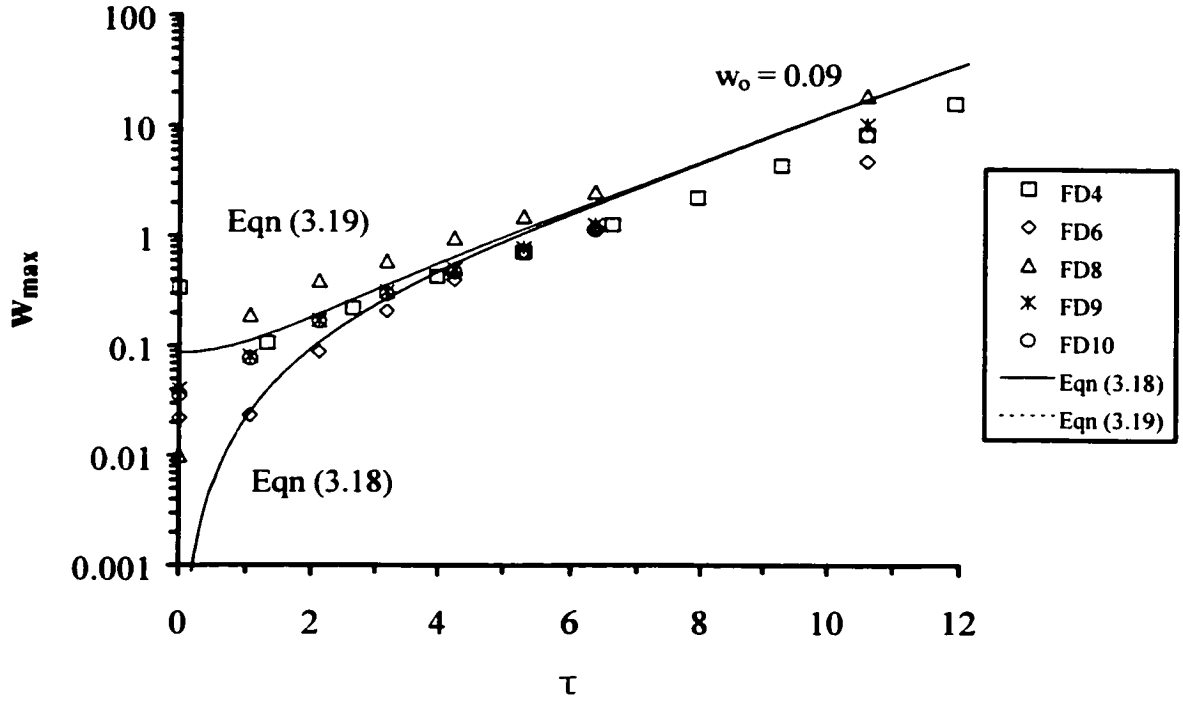

Figure 3-4. Nondimensional Peak Buckle Amplitude (w_{max}) as a Function of Time (τ) for Finite Difference Models with Random Geometric Imperfections.

in Figure 3-4. Relative importance of the aspect ratio, which ranged from 24:1 to 1:1, on the displacement response was secondary. Reasonable agreement was exhibited by Model *FD6*, in particular for early buckling times ($\tau \leq 6$), however, further detailed analysis of the complete modal response will highlight deficencies of coarsely meshed models.

Although the initial geometric perturbations were defined by a set of random harmonics, the buckled profiles (Figure 3-3) exhibited a generally convergent waveform with increasing solution time. Evolution of a dominant wavelength through modal competition is consistent with the diminishing amplification function bandwidth with increasing time (Figure 2-6) and significant unbounded growth rate (Figure 2-7).

The computed displacement-time history response for the finite difference models was analysed to compile statistics on the buckled profile. The number, location or axial coordinate (u) and magnitude of local peak buckle crests (w) as a function of time (τ) were extracted from the data set. Two wavelength parameters were established, namely the average wavelength and weighted mean wavelength.

The average wavelength (λ_{avg}) was defined as the average response for the first three buckle waveforms adjacent to the lower fixed support. This method is inherently biased due to the preferential waveform selection, increased load duration as well as relative stiffness and interaction effects with the support boundary.

The weighted mean buckle wavelength (λ_{wm}) was calculated by a zero crossing technique with a moving window to determine local absolute peaks. The term, weighted mean, was adopted to distinguish the numerical computations from the theoretical mean defined by Equation (2.29). The computations were defined by, $\lambda_{wm} = \sum_i (\lambda_i f_i) \Big/ \sum_i f_i$, where f_i is the frequency of observation for the i^{th} bin. This method accounts for the entire buckled profile subject to the compressive stress front, which is a function of the solution time. In addition, the program calculated statistics of the mode response for nondimensional wavelength bins (λ) at 0.25λ intervals, where the mean, minimum and maximum transverse displacement amplitude for each bin was determined. Statistics of the deformed geometry profile, as a function of time (τ), in terms of buckle amplitude and wavelength distribution were also generated and analyzed.

Theoretical expressions for the mean wavelength, Equation (2.29), most amplified wavelength, Equations (2.30), and the weighted mean wavelength (λ_{wm}), from the finite difference analyses, were plotted as a function of nondimensional time (τ). These parameters are presented in Figure 3-5.

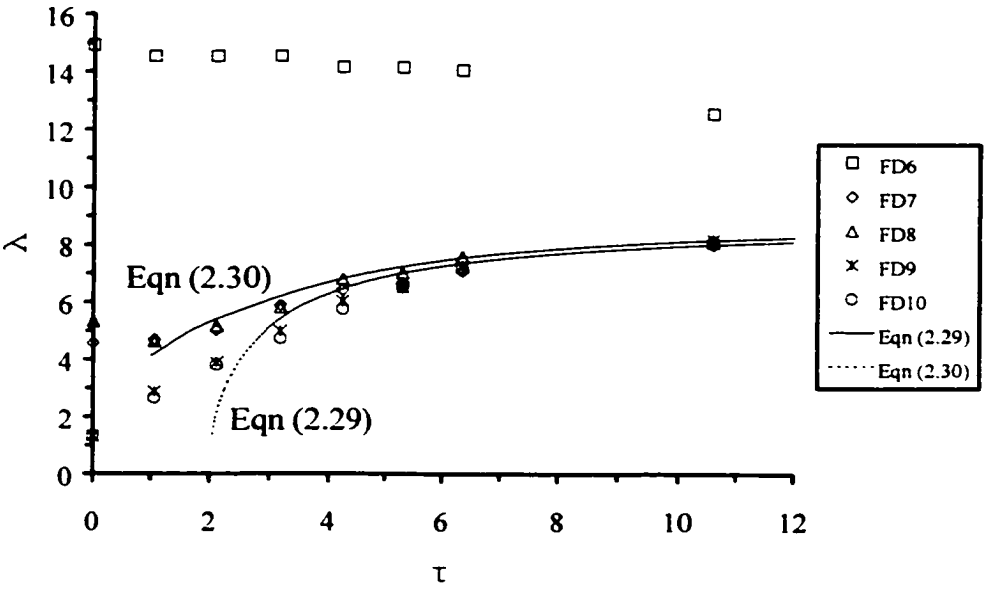

Figure 3-5. Nondimensional Buckled Wavelength (λ) as a Function of Time (τ) for Finite Difference Models with Random Geometric Imperfections.

The relative simplicity and utility of Equation (2.30) based on the most amplified mode is illustrated by the rapid convergence ($\tau \approx 5$) and represents a lower bound to the buckled response. Further, in reference to Figure 3-4, the importance of employing aspect ratios on the order of 2:1 for an accurate solution of the complete modal response, in particular for early solution times ($\tau \leq 2$), was observed. The limitations of finite difference models defined by a coarse grid are further illustrated in Figure 3-6.

The weighted mean wavelength (λ_{wm}) was significantly overestimated, for Model *FD6* in Figure 3-5, due to the finite number of grid points representing the buckled response. For intense pulse buckling events, a finely discretised domain is required to model the high degree of curvature developed during the response. Assuming a dominant waveform of the "preferred" mode ($\lambda_p = 2\pi\sqrt{2} \approx 8.89$, $N_c \approx 0.017$), the number of nodal pointsthat

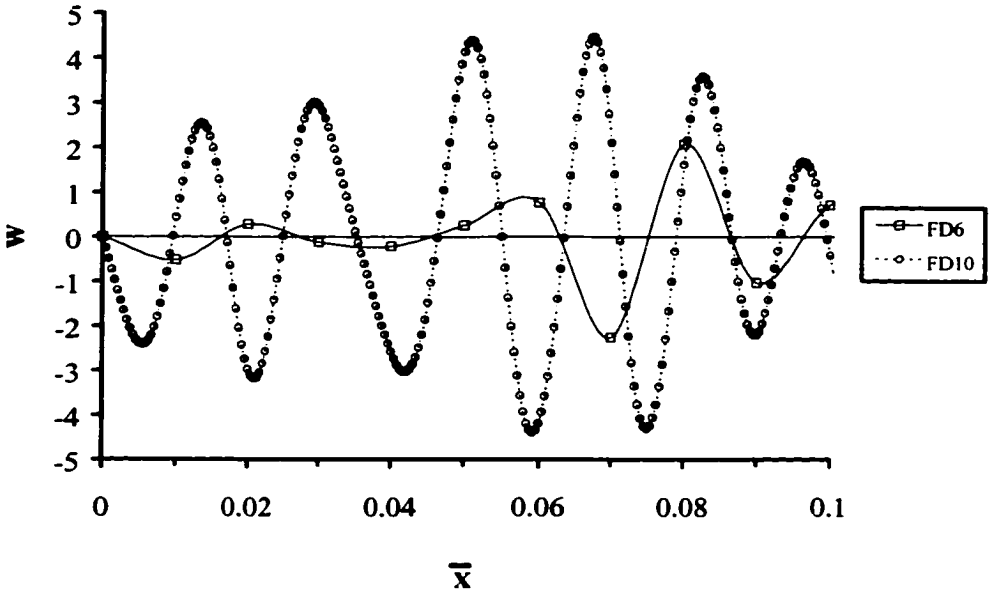

Figure 3-6. Nondimensional Deformed Geometry Profiles for Model *FD6* and Model *FD10* at $\tau = 10.6$ ($t = 48\mu s$).

represents a single buckled wavelength would be 1.7 and 40.6 for the finite difference models *FD6* and *FD10*, respectively. Thus, the coarsely meshed model exhibits a spurious, lower ordered response due to the limited degrees of freedom as shown in Figure 3-6.

The analysis has only considered the buckled response in terms of discrete parameters (i.e. peak amplitude, mean wavelength). Lindberg and Florence (1987) generated theoretical and experimental histograms of the buckled wavelength response for solution time $\tau = 6$. The results are illustrated in Figure 3-7 where the mean theoretical wavelength response was ($\lambda = 7.4$) with a standard deviation of ($\sigma_\lambda = 1.7$).

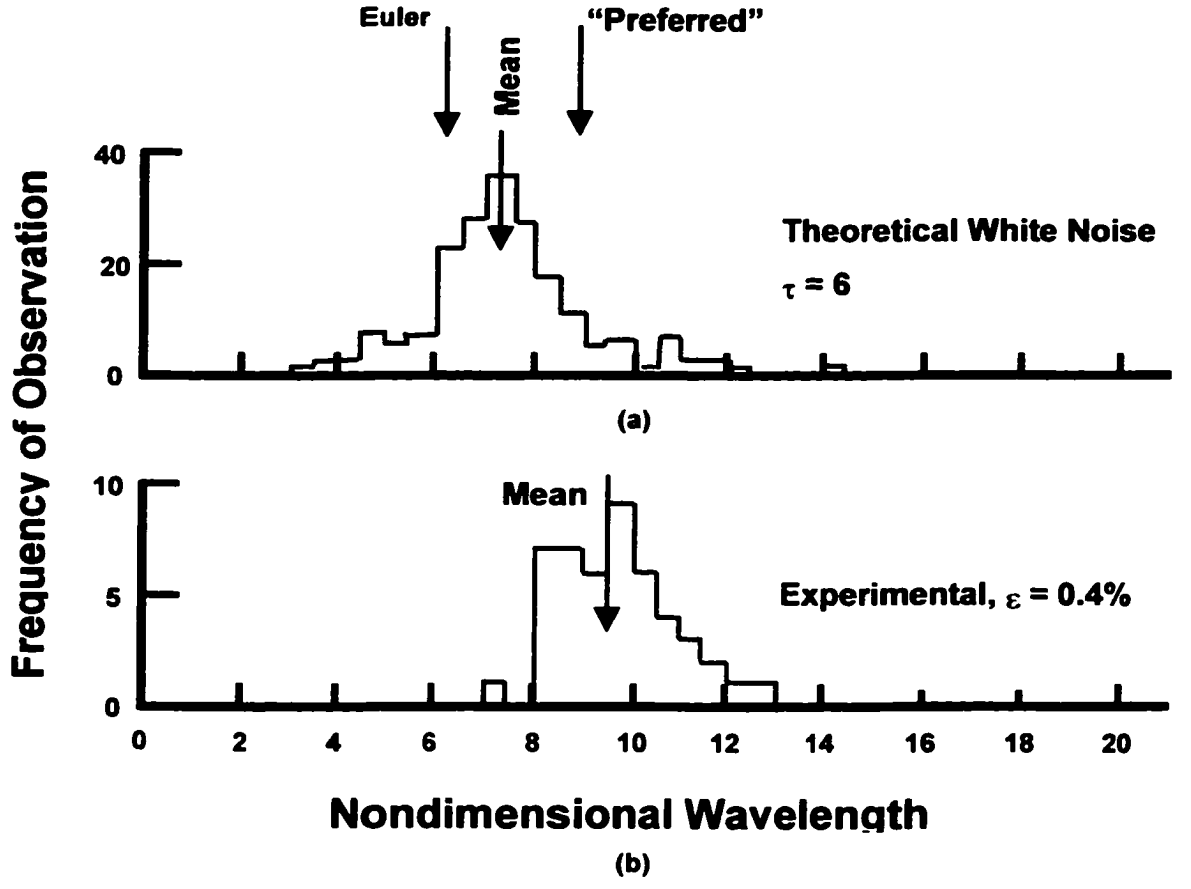

Figure 3-7. (a) Theoretical and (b) Experimental Nondimensional Buckle Wavelength (λ) Response (Lindberg and Florence, 1987).

The theoretical modal response was between the static Euler wavelength ($\lambda_E = 2\pi$) and the "preferred" wavelength ($\lambda_p = 2\pi\sqrt{2}$). The observed experimental mean was higher ($\lambda = 9.5$) with a smaller standard deviation ($\sigma_\lambda = 1.0$). This was attributed to eccentric loading effects inherent with the experimental procedure, which tend to produce a fixed wavelength, developed from the interaction of the applied impulse and transverse deflection with the fixed support (Lindberg and Florence, 1987).

The significant advantage of numerical methods over experimental investigations, with respect to compilation of buckled profile data and statistical analysis, is illustrated in Figure 3-8. Nondimensional wavelength (λ) frequency distributions, for Model *FD10*, as for several solution times (τ = *1.1*, *3.2*, *6.4* and *10.6*) are shown. The weighted mean wavelengths (λ_{wm}) of the finite difference are consistent with the experimental data presented in Figure 3-7.

The early response (Figure 3-8a) can be characterised by high order flexural oscillations, less than the Euler wavelength (λ_E), with approximately equal distribution over the range $1 < \lambda < 4$. Although the bandwidth increases with solution time, the peak relative frequency distributions became more focused. The weighted mean wavelength response for Model *FD10* was $\lambda_{wm} = 7.18$, at $\tau = 6.4$, and the results presented by Lindberg and Florence (1987), $\lambda = 7.4$ at $\tau = 6$, are in good agreement. Progression of the mean response toward the "preferred" mode with increasing solution time was exhibited.

Transition of the computed numerical response towards lower ordered modal response is consistent with the amplification function (Figure 2-6) and observed experimental buckled profiles presented in Figure 3-9. Although, Lindberg and Florence (1987) have also reported that high frequency bending vibrations superimposed on the global motion were observed.

Time history analysis of the nondimensional peak lateral displacement (w_{max}) as a function of the nondimensional buckle wavelengths (λ) was also investigated (Figure 3-10). The response was similar in character to the wavelength histograms presented in Figure 3-8. For early solution times ($\tau < 3.2$) the growth of transverse displacements was exhibited over a broad range of wavelengths and the amplification effects were, in general, evenly distributed.

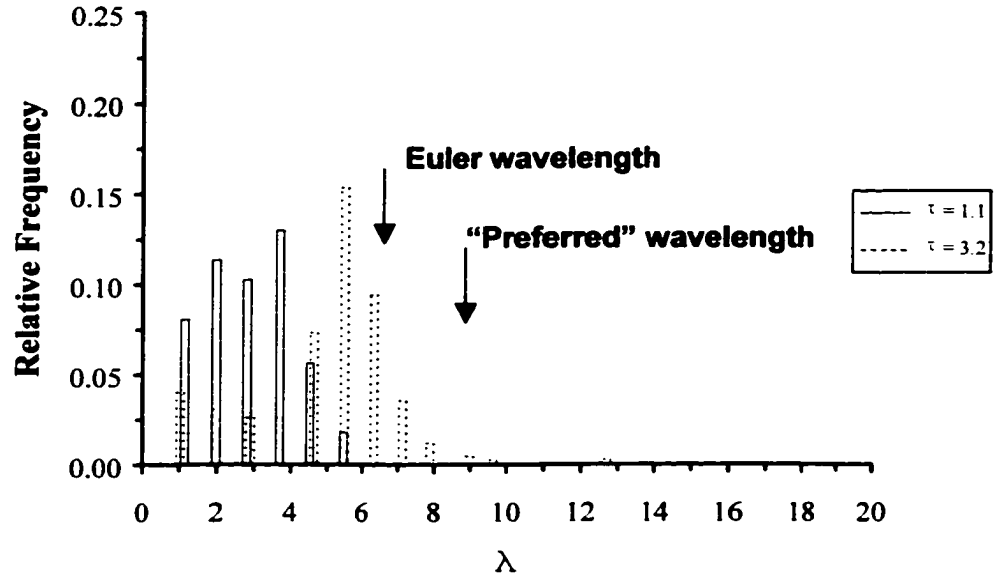

(a)

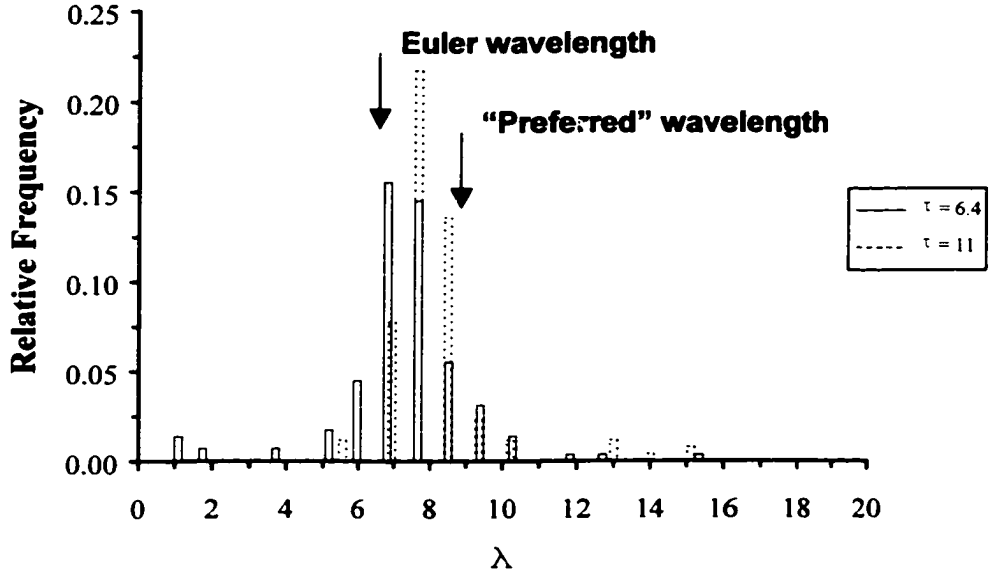

(b)

Figure 3-8. Relative Frequency Distribution of Nondimensional Buckle Wavelengths (λ) for Model *FD10* at Solution Times (a) $\tau = 1.1, 3.2$ and (b) $\tau = 6.4, 11$.

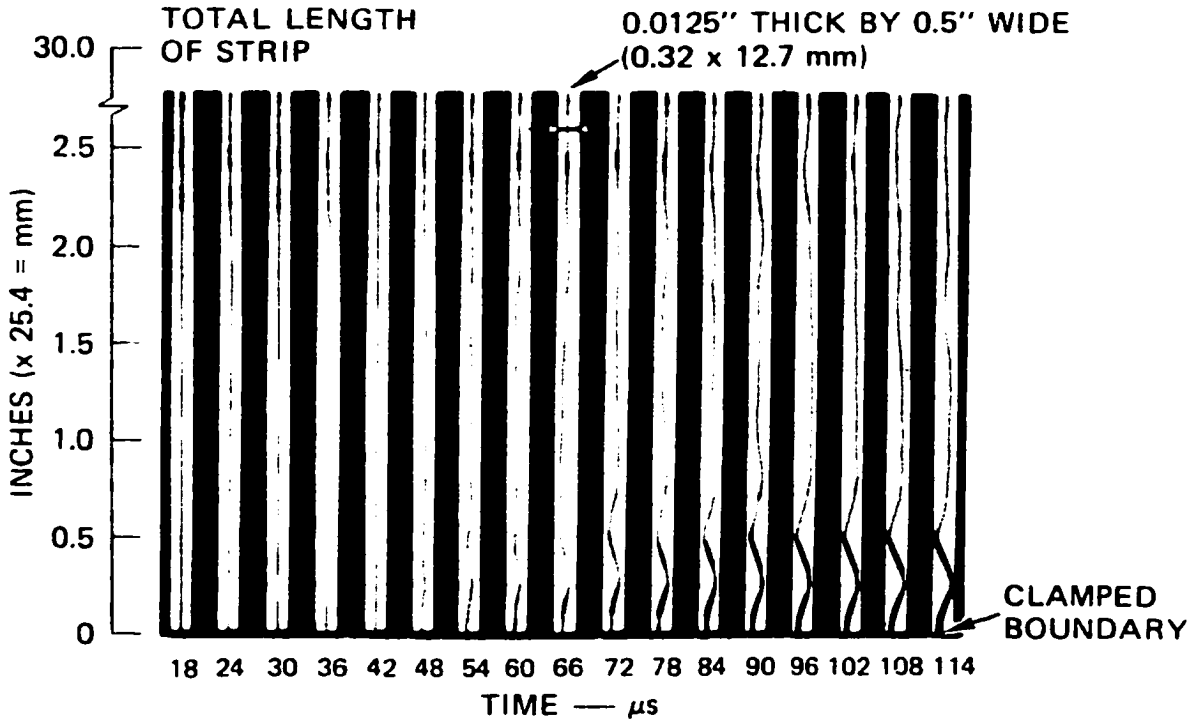

Figure 3-9. Observed Buckled Profiles from Experimental Investigations. (Lindberg and Florence, 1987).

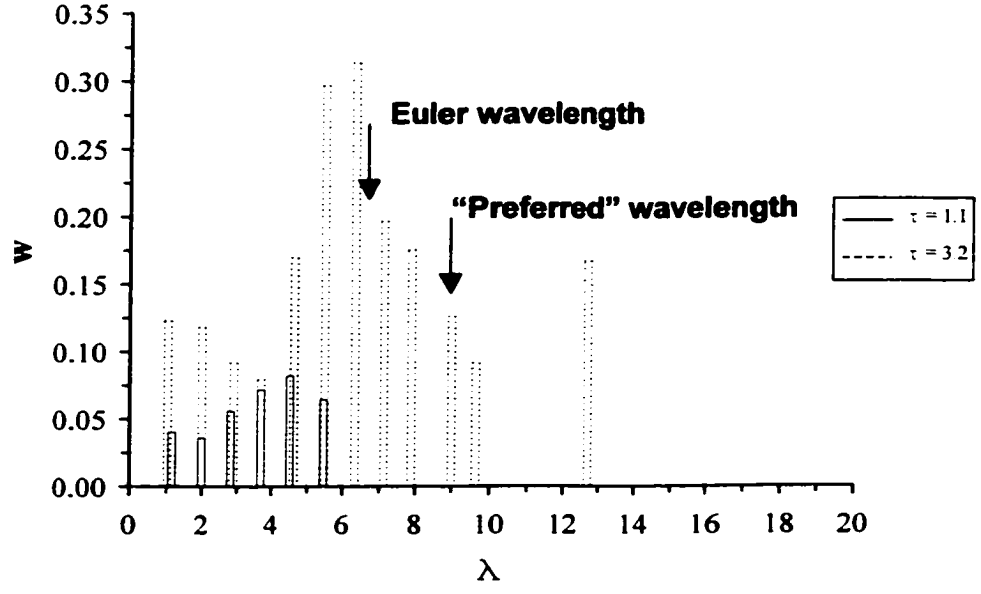

(a)

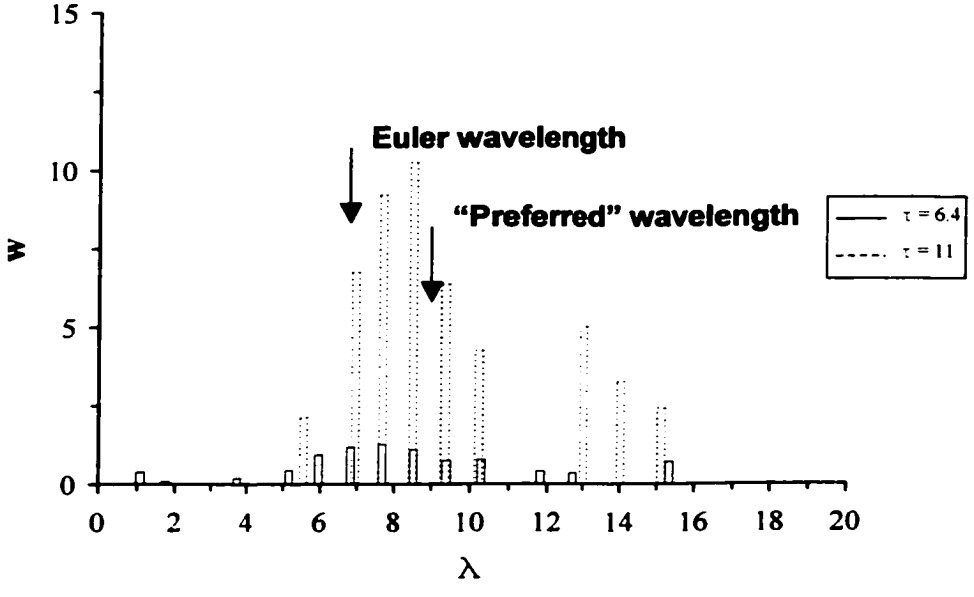

(b)

Figure 3-10. Nondimensional Buckle Amplitude (w) as a Function of Nondimensional Buckle Wavelength (λ) for Model *FD10* at (a) $\tau = 1.1, 3.2$ and (b) $\tau = 6.4, 11$.

The response at later solution times was more prominent for those modes centered about the "preferred" wavelength, which is consistent with the amplification function (Figure 2-3). A summary of the peak buckle amplitude (w_{max}) as well as the weighted mean buckle amplitude (w_{wm}) and wavelength response (λ_{wm}) for the finite difference model *FD10* is summarised in Table 3-5.

Table 3-5. Summary of Peak Buckle Amplitude (w_{max}), Weighted Mean Buckle Amplitude (w_{wm}) and Wavelength Response (λ_{wm}) for Model *FD10*.

τ	w_{max}	w_{wm}	λ_{wm}	Eqn (2.29)
1.1	0.08	0.06	2.7	4.2
3.2	0.30	0.22	4.7	6.2
6.4	1.13	1.04	7.2	7.6
11	8.45	8.28	8.1	8.4

Although the computed modal response could be characterized by a distribution of buckle amplitudes and wavelengths, comparison of the tabulated data (Table 3-5) with the time history response curves (Figure 3-4 and Figure 3-5) and modal response histograms (Figure 3-8, 3-10) illustrates the simplicity and utility for assuming a dominant, "preferred" mode. The peak buckle amplitude is closely associated with the weighted mean wavelength response, which tends to converge towards the "preferred" wavelength and consistent with Equation (2-29), which asymptotically reaches the "preferred" mode at $\tau \approx 30$.

3.4 Elastic Pulse Buckling Threshold Limits

In addition to knowledge of the modal response, defining an elastic buckling threshold limit is an important parameter to consider for preliminary design estimates. In contrast to problems of elastic stability, for example critical loads based on geometry and boundary

conditions, for dynamic pulse buckling an all-encompassing critical state cannot be explicitly defined. As previously discussed this is related to inherent mechanisms of dynamic buckling events and the fact that there are no universal criteria to define pulse buckling threshold limits. The bounds may be defined by critical displacement, load levels imparted to equipment or personnel, or yield response. Lindberg and Florence (1987) have defined the dynamic buckling limit when the combined stress, due to axial compression (σ_c) and flexure (σ_f), exceeds the yield stress (σ_y) of the material.

Following the analysis of Lindberg and Florence (1987), theoretical curves defining the critical thrust duration (τ_{cr}), for the "preferred" mode at two levels of imperfections (β = *0.0001 and* β = *0.001*), were calculated using the expression,

$$\frac{1-\bar{\sigma}}{\sqrt{\bar{\sigma}}} = \pi\beta\sqrt{\frac{6}{\varepsilon_y}}\left[\cosh\left(\frac{\tau_{cr}}{2}\right)-1\right]. \tag{3.21}$$

The expression relates the critical time to first yield (τ_{cr}) to initiate a pulse buckling response as a function of the normalized stress ratio ($\bar{\sigma}$) defined as the applied thrust magnitude (σ_c) with respect to the yield stress (σ_y). The critical load intensity is a function of the imperfection amplitude (β), yield strain (ε_y) and load duration (τ) and was discussed in Section 2.3.4.

A parametric study was conducted by increasing the normalized stress ratio ($\bar{\sigma}$) over the range, $0.05 \le \bar{\sigma} \le 1.0$. The finite difference solution was analysed with respect to the critical buckling time for the stress state within the cross-section (i.e. axial plus flexural) to exceed yield was determined. According to elementary bending theory, the normal stress due to flexure can be calculated by,

$$(\sigma_{xx})_{max} = \frac{E(y)}{R} = Ed\frac{\partial^2 y}{\partial x^2} = \sqrt{3}Es^2\frac{\partial^2 w}{\partial \xi^2}, \quad (3.22)$$

where d is the distance from the neutral axis to the outer fiber and R is the radius of curvature approximation for small deflections. The curvature was calculated using a second order central difference approximation with an error of $O(\Delta x)^2$.

Prior to conducting the parametric analysis, a convergence study was initiated to investigate the effects of grid point spacing on the computed bending stress. The bending stress can be defined as,

$$\sigma_{xx} = \frac{M_{zz}h}{I_{zz}} = \frac{PLh}{2I_{zz}}. \quad (3.23)$$

For a simply supported beam of length (L), subject to a central point load (P) on the elastic curve, lateral deflection (δ_y) can be calculated using the expression,

$$\delta_y = \frac{Px}{48EI_{zz}}\left(3L^2 - 4x^2\right), \quad (3.24)$$

for $0 \leq x \leq L/2$. Thus, for a known normal stress then the corresponding deflected geometry profile can be generated. On this basis, influence of the grid point discretization on the computed normal elastic stress (σ_{xx}) with reference to the theoretical stress (σ_{th}) was conducted. The results are shown in Figure 3-11, which illustrates the relationship between the normalized stress ratio (σ_{xx}/σ_{th}) as a function of the aspect ratio, which is defined as the relationship between the grid point spacing (Δx) and beam depth (d).

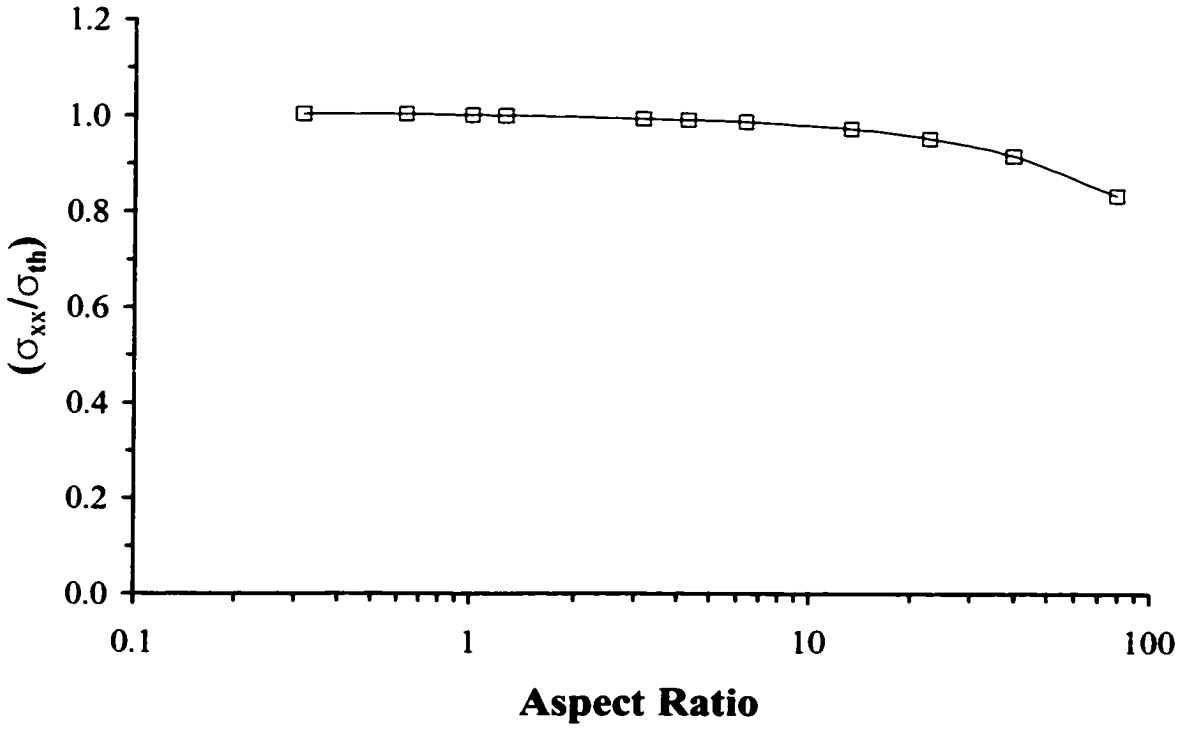

Figure 3-11. Influence of Aspect Ratio on the Computed Normalized Stress Ratio for Finite Difference Models.

For aspect ratios on the order of 10 or less, there was good agreement between the computed finite difference and theoretical normal stress. The discretization error for model *FD6* was approximately 5%. Thus, for the case of simple bending and moderate degree of curvature, finite difference models with aspect ratios ranging from 24:1 to 1:1 should adequately represent the stress state. Assuming a proportional limit at 0.2% axial strain, the theoretical times for yield as a function of the normalized stress level, for buckling in the "preferred" mode, are illustrated in Figure 3-12. The analytical expression (Equation 3.21) was evaluated for the imperfection parameter $\beta = 0.0001$ and $\beta = 0.001$. For the finite difference solutions, the time history displacement data was analysed over a range of

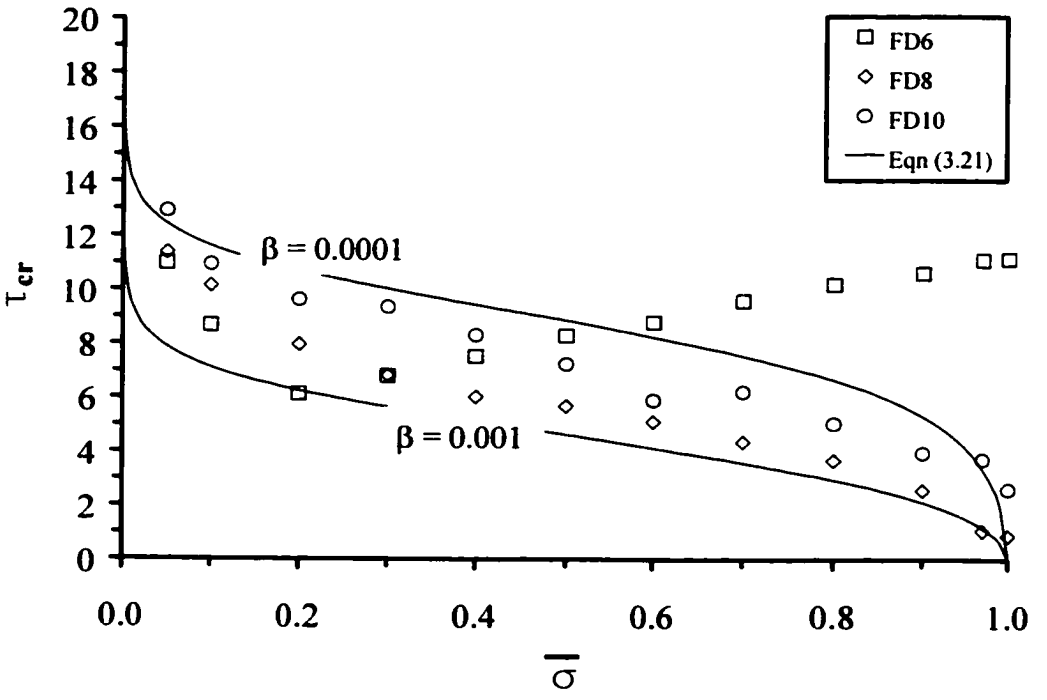

Figure 3-12. Analytical and Numerical Analysis for Critical Impulse Intensity to Yield for the Peak Buckle Crest Based on the "Preferred" Mode Analysis.

compressive stress impulse magnitudes $(\bar{\sigma})$ to determine the critical thrust duration (τ_{cr}) for yielding through the section.

Although the coarsely meshed model, *FD6*, accurately predicted the peak lateral displacement (Figure 3-4), limitations of the coarsely defined domain are illustrated by the weighted mean buckle wavelength (λ_{wm}) response (Figure 3-5) and critical time (τ_{cr}) to first yield (Figure 3-12).

The finite difference models with lower degrees of freedom (i.e. large aspect ratios) cannot account for the required beam curvature to accurately model the pulse buckling response.

For the critical thrust duration calculations this is further influenced by the second derivative ($\partial^2 w / \partial \xi^2$) for the finite difference solution of a differential equation, which is an approximated function. In comparison with Model *FD10*, the more coarsely meshed Model *FD8* appears to exhibit an equivalent increase in the imperfection parameter (β) and reduction in the critical impulse duration (τ_{cr}). Furthermore, aspect ratios on the order of 1:1 (Model *FD10*) were required to characterize the sharp decrease in critical thrust duration as the impulse magnitude approached the yield stress as shown in Figure 3-12.

3.5 Assessment of Finite Difference Models

The pulse buckling response of a slender beam subject to an intense axial impact has been investigated by the finite difference method. Numerical modelling has substantiated the relative simplicity and utility of the "preferred" mode analysis, for preliminary dynamic buckling estimates. The finite difference models were consistent and accurate with respect to the "preferred" wavelength theory, in terms of buckle amplitude growth (Figure 3-4), wavelength response (Figure 3-8, 3-10) and threshold limits (Figure 3-12), provided a fine grid point discretization (aspect ratios on the order of 1:1) was employed. The main disadvantage of perturbation analysis is the restriction to relatively simple structural configurations, boundary conditions and loading events.

In comparison with the experimental observations there are several limitations of the analytical and numerical solutions that need to be addressed. A constant uniform axial thrust, linear elastic mechanical properties and unbounded growth of transverse buckle displacements have been considered. For early solution times these are reasonable and justifiable assumptions but at later buckling times the solutions are not fully consistent with experimental observations. This is demonstrated through a comparison of the peak buckle response (Figure 3-4 and Figure 3-6) with the time frame photographs (Figure 3-9). For the

solution time ($\tau = 22.1$, $t = 100\mu s$) the computed peak buckle amplitude was $w = 1677$ ($y = 154mm$), whereas, the experimental peak amplitudes were on the order of $w = 22$ ($y = 2mm$). Furthermore, the experimental profile was charcatized by a "single" large amplitude, buckle near the support with smaller flexural oscillations prevalent throughout the remaining beam length. Some potential mechanisms contributing to this discrepancy are a variable and propagating axial stress wave, axial inertia or nonlinear terms such as large deformation and local plasticity.

Incorporation of these parameters within a numerical modelling framework requires specialized algorithms and iterative schemes. Consequently, the application of versatile and robust computational procedures such as finite element methods is most promising. Requirements for the development of accurate finite element models defining the elastic pulse buckling response of a slender beam to an intense axial impact will be investigated.

4.0 Finite Element Analysis of Elastic Pulse Buckling Events

The dynamic pulse buckling response of a slender beam subject to an intense elastic axial impulse is investigated by the finite element method. The main objective is to define the characteristics required for the development of accurate finite element models with respect to the "preferred" wavelength theory and experimental observations. The results of a parametric study will be presented, which considered mesh topology, element formulation, applied impulse magnitude and type of imperfection. The analysis will substantiate the basis of the "preferred" wavelength theory and conclusions of the finite difference investigations. Furthermore, the importance of accounting for nonlinear geometric and material behaviour depending on the adopted element formulation will be demonstrated.

4.1 Modelling Considerations

4.1.1 Solution Strategies in Structural Dynamic Analysis

In comparison with the finite difference analysis, the finite element method encompasses significantly distinct characteristics. The finite difference method considers a constant axial stress state, lumped nodal properties, and neglects the effects of axial deformation and axial inertia. Conversely, the finite element analysis considers the spatial and temporal characteristics of the applied impulse and ensuing axial stress wave propagation. This represents a more accurate treatment of the experimental buckling study conducted by Lindberg and Florence (1987). In addition, the stiffness and inertia terms are considered on a consistent basis, and the consideration of axial deformation incorporates the coupled nonlinear term due to bending (Equation 2.9).

In general form, the governing differential equation of motion to be solved by a system of finite elements can be expressed as,

$$[M]\{\ddot{u}\} + [C]\{\dot{u}\} + [K]\{u\} = \{R\}. \tag{4.1}$$

where $[M]$ is the mass matrix, $[C]$ is the damping matrix, $[K]$ is the stiffness matrix, $\{R\}$ is the load vector, and $\{\ddot{u}\}$, $\{\dot{u}\}$ and $\{u\}$ are the acceleration, velocity and displacment vectors, respectively. For the current study, the influence of material or structural damping was not included in the analysis (i.e. $[C]$ was a null matrix).

The solution to Equation (4.1) can be obtained by modal and direct integration methods. Typically, time history dynamic response analysis for multi-degree of freedom systems is computed via modal methods (e.g. mode displacement superposition). The main advantage is that the equation of motion can be transformed through generalised coordinates to a system of uncoupled equilibrium equations. The response can be obtained through superposition of the modal contributions. The major limitation is the assumption of linearity. Although modal methods exist for the solution of nonlinear dynamic problems, in general direct integration methods are preferred. A number of sources provide a complete discussion on the application of the finite element method in structural dynamics, and the discussions presented by Bathe (1996) and Cook et al. (1989) are referenced.

There are two categories for direct integration methods, namely explicit and implicit. The main differences of the integration schemes can be expressed in terms of the finite difference characterisation of displacement, velocity or acceleration vectors, time frame for equilibrium analysis and time step stability criteria. Explicit methods solve for the incremental displacements ($t + \Delta t$) using the equilibrium conditions at time (t), whereas implicit methods use the equilibrium conditions at the time step ($t + \Delta t$).

From the viewpoint of finite element modelling, the dynamic pulse buckling event can be defined as a propagating axial stress wave that induces flexural oscillations through the amplification of initial geometric imperfections. The subsequent growth of transverse deflections and buckled waveforms occurs through modal competition. Wave propagation problems can be characterised by a discontinuity in axial strain.

Typically, explicit integration methods with lumped formulations and low-order elements are employed to analyze the dynamic structural response. The main advantage of an explicit integration scheme lies in the compuational efficiency through vectorization where a lumped mass matrix and velocity independent damping can be employed. Conversely, the major restriction lies in conditional stability imposed by a critical time step, which is dependent on the highest natural frequency of the system. For numerical methods, this can have significant and potentially detrimental effects on both solution stability and accuracy. The consequence could be a prohibitively small time step in order to account for variations in element natural frequencies due to local discontinuities (e.g. high stiffness, low mass). For nonlinear systems, where the modal response can evolve and influence the structural response (e.g. strain-hardening, plastic flow, element distortion), a spurious solution may not be transparent.

Implicit schemes are unconditionally stable and the required time step is based on accuracy considerations. The main drawback emerges through the significant computational effort and solution cost, particularly for nonlinear systems, due to reformulation or factorization of the effective stiffness matrix.

In addition to the available solution methods (implicit or explicit), the selection of an appropriate integration time step magnitude must be considered. The main issue is related to achieving a balance of solution cost (i.e. CPU time) against solution stability and accuracy. The main governing parameters are the time step and degree of mesh

discretization. The selection of an appropriate time step for integration must account for stress wave propagation between adjacent nodal points. For two-dimensional elements, this implies considerations for both the axial and transverse components. A general characteristic of wave propagation problems is the large number of response frequencies excited during the event. This presents difficulties in selecting an appropriate cutoff frequency (i.e. critical time step), particularly for higher-order continuum elements. Consequently, solution strategies developed for explicit finite difference schemes are employed, which provide a rational basis.

For two-dimensional linear plane elements, Bathe (1996) states that the critical time step is governed by,

$$\Delta t_{cr} = \frac{L_{el}}{c}\sqrt{1-\upsilon}\,. \tag{4.2}$$

where ν is the Poisson's ratio. For a two-node beam element,

$$\Delta t_{cr} = \frac{L_{el}^2}{c}\sqrt{\frac{A}{48I}} = \frac{L_{el}^2}{2cd}. \tag{4.3}$$

where the simplification is presented for a rectangular section. Cook et al. (1989) defined a stability equation for plane strain elements as

$$\Delta t = \frac{L_{el}}{\sqrt{3}c} \tag{4.4}$$

For the finite element analysis conducted in the present investigations, a conservative time step was selected based on the minimum of Equations (3.13), (3.15), (4.1), (4.2), (4.3) or (4.4).

4.1.2 Modelling Procedure for Pulse Buckling Analysis

The commercial finite element software packages ADINA (1996) version, ANSYS (1996) version 5.3 and NISA (1997) version 7.0 were employed to investigate the dynamic buckling response of a slender beam subject to an elastic axial impulse. For all models, the beam had the dimensions (762mm×12.7mm×0.3175mm) and was composed of Aluminium 6061-T6 with the mechanical properties ($E = 69MPa$, $\rho = 2700kg/m^3$ *and* $\nu = 0.33$). These parameters were selected for comparison with the experimental studies presented by Linberg (1965) and Lindberg and Florence (1987).

Two-dimensional (ANSYS) and three-dimensional (NISA) beam elements and two-dimensional plane strain elements (ADINA, NISA) were used to discretize the domain. The beam elements were based on Euler-Bernoulli beam theory and included the capability for modelling stress stiffening effects in thin structures. Details regarding element formulation and finite element theory are presented in the respective user manuals. Specific issues regarding the finite element model parameters (e.g. mesh density, element type, beam geometry) are discussed in the next section.

To simulate the pulse buckling analysis and experimental investigations conducted by Lindberg and Florence (1987), the finite element solution considered two separate phases (i) an initial static analysis and (ii) subsequent dynamic response analysis. A schematic illustration of the buckling event was presented in Figure 2-2. The boundary conditions, for the finite element models, were pinned $\left(\overline{X} = 0\right)$ and roller $\left(\overline{X} = 1\right)$ supports, where $\left(\overline{X} = x/L\right)$ is a normalized axial coordinate. The numerical procedures accounted for nonlinear geometry and, as will be demonstrated later, for select cases required the consideration of nonlinear material behaviour.

For the initial static analysis, an axial stress was applied to the beam (Figure 2-2), which represented the static tensile loading phase of the impact buckling experiments discussed by Linberg (1965) and Lindberg and Florence (1987). A series of nonlinear static analyses were conducted to establish the required number of load steps for an accurate solution. The convergence study demonstrated that 50 load steps were adequate. The Newton-Raphson method, with line search during equilibrium iterations, was employed. The complex nature of stress concentrations and notch plasticity effects, required to initiate failure, was ignored since this was considered far field with respect to the pulse buckling response.

The resultant displacement field, from the nonlinear static analysis, was then imposed as the initial condition for dynamic analysis. This step represents the moment at notch failure during the static tensile test, which results in the impositition of a dynamic compressive axial stress wave impulse. Although an explicit time integration scheme was successful, difficulties were encountered with solution convergence, particularly for plane strain element models. Consequently, the implicit Newmark method was selected to directly integrate the dynamic equation of motion. This method was the only available option for analysis with NISA (1997). The selected Newmark values of, $\beta = 0.3025$ and $\gamma = 0.6$, provided an unconditionally stable solution with slight numerical damping. The artificial damping is advantageous in the dissipation of spurious, high frequency modal components introduced by the discrete nature of the finite element method. This aspect is particularly important for higher order elements, which generally exhibit greater numerical "noise" than lower ordered elements. The kinematic formulation was large displacement and small strain. The full-Newton routine, with line search, was used to obtain convergence with default energy and displacement tolerance criteria of 0.001.

4.2 Preliminary Investigations

Based on this procedure, a parametric study was conducted by the finite element method, on the dynamic pulse buckling of slender beams with respect to the "preferred" wavelength theory. The primary objective was to assess the finite element computations, in terms of the peak buckle displacement and modal response with respect to the "preferred" wavelength theory. The parameters considered included imperfection type, mesh aspect ratio and element formulation. Parallel with the finite difference investigations, the initial geometric imperfections were defined as a (i) discrete half-sine wave model, (ii) combined model (discrete plus random) and (iii) random model. The discrete and random imperfections were defined by Equations (3.17) and (3.20). The range of parameters considered for the finite element investigations are summarized in Table 4-1. Specific details of preliminary finite element analyses are presented in Appendix A.

Table 4-1. Summary of Parameters for Preliminary Finite Element Investigations

Element Type	Geometric Imperfection	Number of Finite Element Models	Range	
			Aspect Ratio	$\%d_{max}$
Beam	Discrete	12	150:1, 10:1, 2:1, 1:1	10, 25, 50, 100, 200, 500
	Combined	6	10:1, 2:1, 1:1	15, 100, 200, 500
	Random	5	2:1, 1:1	10
Plane Strain	Random	12	16:1, 8:1, 4:1, 2:1, 1:1	6 – 11

Notes: Aspect ratio defines the ratio of longitudinal to transverse element dimension, $\%d_{max}$ is the peak imperfection amplitude as a percentage of the beam depth.

The finite element investigations, presented in Appendix A, demonstrated that the fundamental mode analyses, discussed in Section 2.2.1, were not valid for the higher order mode response associated with intense pulse buckling events. In addition, the utility of the "preferred" wavelength theory (Lindberg, 1965; Lindberg and Florence, 1987) and validity of the finite difference analyses were substantiated. For a slender beam subject to an elastic axial impulse, the peak buckle amplitude and dominant waveform could be effectively defined in terms of a single "preferred" mode. For early buckling times, the assumption of a constant, uniform axial impulse was confirmed. Thus, the assumption of ignoring the longitudinal position of the stress front, with respect to the evolved buckled response, was also considered a valid assumption. Furthermore, the finite element computations support the finite difference analysis.

A number of important conclusions were derived from the preliminary investigations (Appendix A), for the development of an accurate numerical model consistent with the "preferred" wavelength theory and experimental observations presented by Lindberg and Florence (1987). Similar to the finite difference investigations, the finite element models required a finely discretised domain with an element aspect ratio on the order of 1:1 and the incorporation of local random geometric imperfections. The analysis highlighted the importance of including nonlinear (geometric and material) transient analysis with respect to the element type (i.e. beam, plane strain). In addition, it was established that element formulation also influenced the pulse buckling response characteristics, which was directly related to the axial inertia terms, axial strain–displacement and moment–curvature relationships.

Consequently, a detailed discussion focused on the finite element investigations, for the beam element and plane strain element models, that incorporated random geometric imperfections will be presented.

4.3 Pulse Buckling Analysis – Beam Elements

4.3.1 Introduction

Based on the preliminary analyses presented in Appendix A, the important observations and conclusions developed from these investigations are addressed. The relevant parameters for the beam element models are summarized in Table 4-2.

Table 4-2. Beam Element Models for Pulse Buckling Analysis.

Model	Mesh	AR	Δt (μs)	C_n	$\%d_{max}$	A_{max}/L	Comment
ANB7	1200×1	2:1	0.10	0.80	500	0.002	Discrete
NB6	1200×1	2:1	0.10	0.80	207	0.00086	Combined
ANB12	1200×1	2:1	0.10	0.80	9	0.000037	Random

Notes: *Mesh* is the number of longitudinal × transverse elements, *AR* is the aspect ratio of the longitudinal to transverse element dimension, Δt is the integration time step, C_n is the Courant number, $\%d_{max}$ is the peak imperfection amplitude as a percentage of the beam depth and A_{max}/L is the nondimensional imperfection parameter.

4.3.2 Buckled Displacement Response

Consistent with the finite difference investigations, exploitation of local random geometric imperfections by the applied axial impulse was critical for initiating the characteristic exponential growth of transverse deflections. This was established through analysis of the computed pulse buckling response of finite element models with respect to the "preferred" wavelength theory. Figure 4-1 illustrates the computed peak buckle amplitude–time history for several numerical models and the corresponding analytical expressions that define the response.

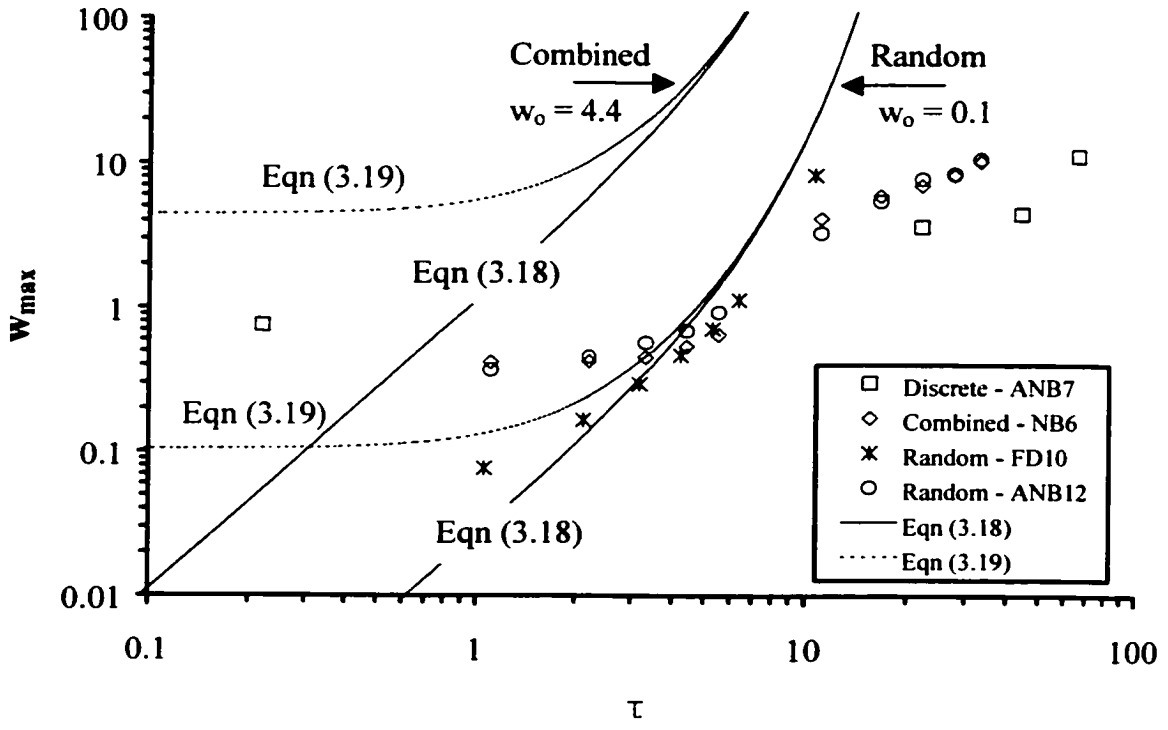

Figure 4-1. Nondimensional Peak Buckle Amplitude (w_{max}) as a Function of Time (τ) for Finite Difference and Finite Element Models with Discrete, Combined and Random Geometric Imperfections.

The finite element models with a fundamental mode imperfection (*ANB7*, Table 4-2, and Table A-1) and the combined imperfection model (*NB6*, Table 4-2, Table A-3) were presented. An average non-dimensional imperfection coefficient of $w_o = 4.4$, equivalent to *1.27d*, was selected to plot the theoretical peak buckle amplitude response, defined by Equation (3.18) and Equation (3.19), for the combined imperfection model. The finite difference model (*FD10*, Table 3-4) and the finite element model (*ANB12*, Table 4-2, Table A-4) incorporated only local random geometric imperfections. An average non-dimensional imperfection coefficient of $w_o = 0.1$, equivalent to *0.03d*, was considered for models with random imperfections. The hyperbolic growth rate of transverse deflection was only developed for numerical models that incorporated local random geometric

imperfections. The finite element model (*ANB12*) was consistent with the analytical expression and finite difference model (*FD10*), which could be characterised by the Fourier coefficient amplitude ($w_o = 0.1$) for local random imperfections.

Although combined imperfection models exhibited an exponential growth rate, the pulse buckling response was due to local random imperfections and not the fundamental mode imperfection. This was established by comparison of the finite element computations with the theoretical growth rates, when the maximum imperfection coefficients (w_o) were considered, as shown in Figure 4-1. In general, the fundamental mode imperfection was one to two orders of magnitude greater than the Fourier coefficient for local random geometric imperfections. For the parameters presented in Figure 4-1, the influence of a fundamental mode imperfection on the pulse buckling response was insignificant for even large amplitudes, $w_o = 17$ equivalent to $5.0d$, as defined by model *ANB7*. These observations are further detailed in Appendix A.

The finite difference model (*FD10*) exhibited an unbounded growth of peak buckle displacements consistent with the "preferred" wavelength theory. In contrast, a limiting plateau response of the transverse deflection was developed by the finite element models for solution times greater than approximately $\tau = 10$. Further analysis (discussed later and also presented in Appendix A) demonstrated that the bounded growth was related to a reduction in the axial impulse and coupled nonlinear terms due to bending defined by the axial strain–displacement relationship. This is illustrated by comparison of the finite difference (*FD10*) and finite element (*ANB12*) solutions with the theoretical "preferred" mode response. For early buckling times ($\tau \leq 5$) the finite element model exhibited a slightly delayed response, related to the beam element formulation, whereas the finite difference models exhibited an unbounded response.

4.3.3 Modal Response Analysis

Historical research efforts have mainly focused on the fundamental mode, where few studies (Sugiura et al., 1985; Hayashi and Sano, 1972a) have considered the higher order modal response. To the author's knowledge, comprehensive numerical investigations, on the dynamic buckling of slender beams subject to an axial impulse, have not yet been conducted with respect to the "preferred" wavelength theory. From this perspective, only the pioneering work of Lindberg (1965) and the monograph of Lindberg and Florence (1987) address this issue. For both of these studies, however, experimental and theoretical statistics of the buckled profile were presented for only one time step ($\tau = 6$).

Modal response analysis of the finite element models was conducted on the basis of an average wavelength (λ_{avg}) and weighted mean wavelength (λ_{wm}), as discussed in Section 3.3.4, is presented in Figure 4-2. The solid symbols represent average wavelengths (λ_{avg}) and the open markers are weighted mean wavelengths (λ_{wm}). Although Equation (2.29) more accurately represents the statistics of a stationary random process, the relative simplicity and utility of Equation (2.30) based on the most amplified mode is illustrated. This is also demonstrated by the rapid convergence of the two theoretical expressions ($\tau \approx 5$).

The influence of imperfection type on the modal response of the finite element models was relatively insignificant. For early solution times ($\tau \leq 5.5$), the average wavelength response (λ_{avg}) was in general agreement with the theoretical and finite difference solutions. For nondimensional times ($\tau > 12$), the average wavelength (λ_{avg}) exceeded the analytical expressions. Analysis presented in Appendix A, showed the deviation was concurrent with a transition from a linear to nonlinear axial displacement response. This was associated with the limiting displacement plateau and departure from the unbounded analytical solution as illustrated in Figure 4-1. For the beam element models, the

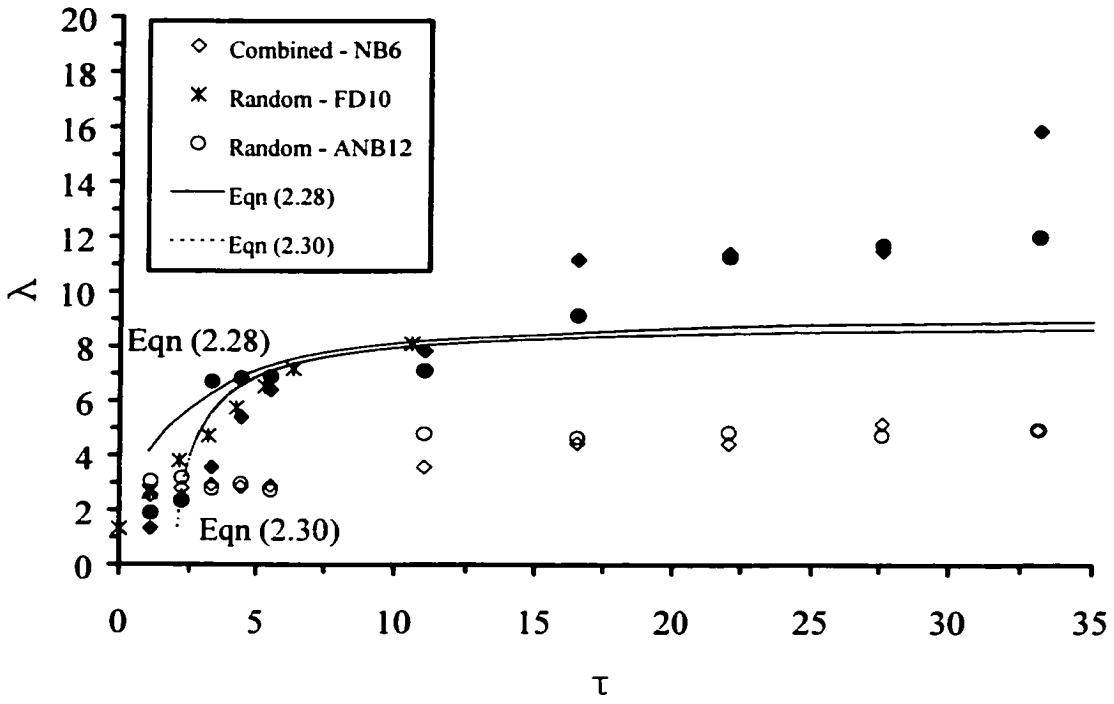

Figure 4-2. Nondimensional Buckled Wavelength (λ) as a Function of Time (τ) for Finite Difference and Beam Element Models with Combined and Random Geometric Imperfections (■ λ_{avg} , □ λ_{wm}).

weighted mean wavelength (λ_{wm}) generally under predicted the "preferred" mode response.

A major assumption of the "preferred" wavelength theory was the propagating axial impulse could be idealized as a constant, uniform thrust. This premise was validated by theoretical arguments presented by Lindberg and Florence (1987). The finite element models further supported this assumption and can be demonstrated through comparison of the axial stress distribution–time history with the computed pulse buckling response (Figure 4-1 and Figure 4-2).

The longitudinal distribution of normalized axial stress ratio $(\bar{\sigma})$, which relates the computed axial stress (σ_{xx}) to yield stress (σ_y), is shown in Figure 4-3. For the nondimensional solution time $\tau = 5.5$ ($t \leq 25\mu s$), variation of the stress wave front magnitude $(\bar{X} \leq 0.10)$ was on the order of 6%. Based on numerical computations and experimental observations, the peak transverse deflection was on the order of 0.05mm, which is within an elastic response, and the stress wave front propagated approximately 10 times the "preferred" buckled wavelength. Consequently, prior to the development of a significant pulse buckling response (i.e. transverse deflection), the axial impulse can be considered uniform and constant. Perturbations to the longitudinal stress state distribution arise, at later solution times, due to the evolution of large buckle amplitudes and curvature response. The stress–time history analysis (Figure 4-3) also demonstrates for later solution times the reduction in the axial impulse with increasing buckle amplitude growth.

4.4 Pulse Buckling Analysis – Plane Strain Elements

4.4.1 Introduction

Finite element analysis employing beam elements has demonstrated that exploitation of local random imperfections, by the axial impulse, was critical in developing the exponential growth of buckled displacements. This was consistent with the experimental observations, theoretical analysis and finite difference modelling previously discussed. In addition to the modelled geometric imperfection type, the present analysis will demonstrate that element formulation also has a significant role on the computed pulse buckling response.

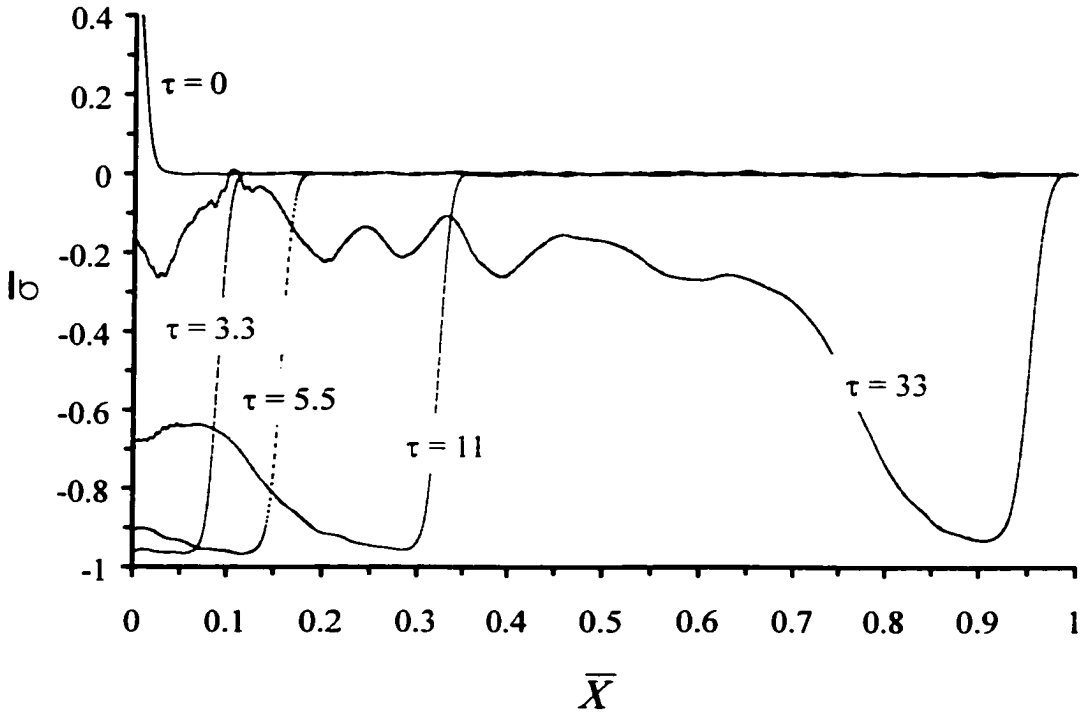

Figure 4-3. Normalized Longitudinal Distribution $(\overline{X})$ of the Normalized Stress $(\overline{\sigma})$ for Beam Element Model *ANB12* with Random Imperfections.

Investigations employing quadratic, plane strain elements, were conducted to comparatively study the influence of the element formulation. Elastoplastic constitutive relationships were utilised and the material properties for 6061-T6 Aluminium were defined as $E = 69GPa$, $\sigma_Y = 285MPa$, $\nu = 0.33$, $\rho = 2700\ kg/m^3$ and $E_T = 900MPa$. A von Mises yield criterion with linear strain hardening was adopted. Although the analysis considered an elastic pulse buckling problem, the requirements for including plasticity are detailed in Appendix A. Table 4-3 summarizes parameters for the plane strain finite element models discussed in this section.

Table 4-3. Plane Strain Element Models with Random Geometric Imperfections.

Model	Mesh	AR	Δt (μs)	C_n	$\%d_{avg}$	$\%d_{max}$	Comments
AP2	300×1	8:1	0.10	0.69	2	8	EP
AP8	2400×1	1:1	0.01	0.55	2	8	EP

Notes: *Mesh* is the number of longitudinal × transverse elements, *AR* is the aspect ratio of the longitudinal to transverse element dimension, Δt is the integration time step, C_n is the Courant number, $\%d_{avg,max}$ is the average and maximum peak imperfection amplitude as a percentage of the beam depth, *EP* indicates elastoplastic constitutive relationship was employed.

Initially, both the finite element software packages *NISA* and *ADINA* were utilized in the study, but due to the significant computational effort required by *NISA*, subsequent investigations were only conducted using *ADINA*. Solution times for a coarsely meshed model, Model *AP4* with an aspect ratio of 4:1 (Table A-6), was 32 hours for *NISA* (installed on a PentiumPro 200MHz PC) and only 6.3 hours for *ADINA* (installed on a VAX DEC Alpha). A more finely discretised model, Model *AP8* with an aspect ratio of 1:1 (Table 4-3, Table A-6) required considerable computational resources with 132 hours of CPU time using *ADINA*.

4.4.2 Buckled Displacement Response

Detailed analysis of the buckled profile and axial stress state, presented in Appendix A, established that finite element models, employing plane strain elements, had to account for both geometric and material nonlinear behaviour. Although, the analysis has considered an elastic pulse buckling event, the requirement for including material plasticity was due to the developed curvature response. This is illustrated in Figure 4-4 where the displaced buckled profile, at solution time $\tau = 22$ ($t = 100\mu s$), for the beam element model (*ANB14*, Table 4-2) and plane strain element model (*AP8*, Table 4-3) are presented.

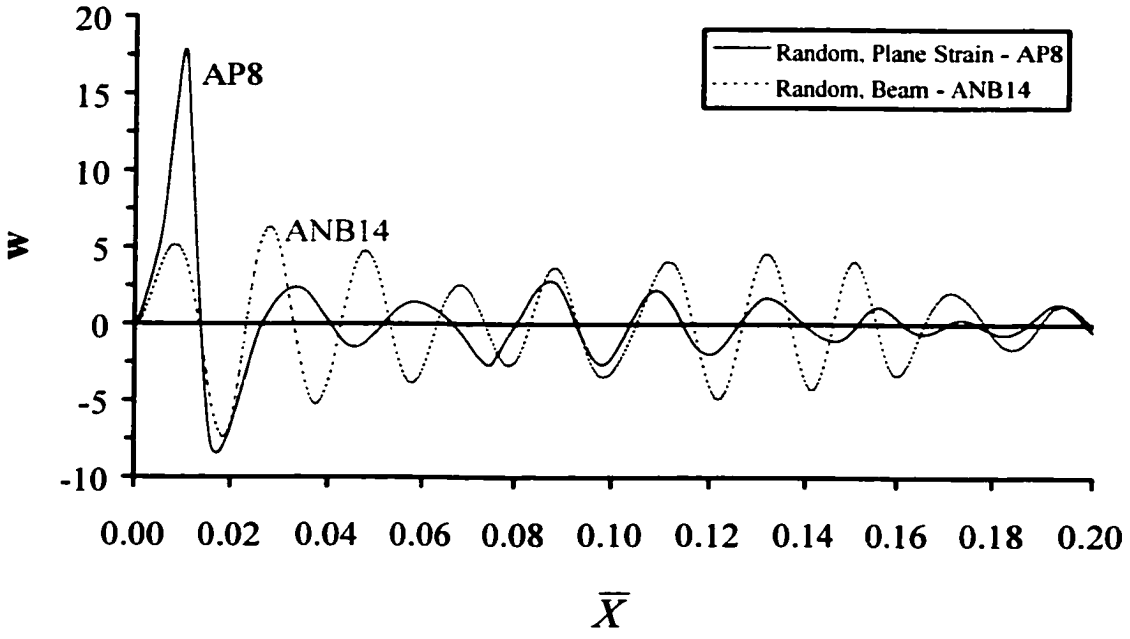

Figure 4-4. Normalized Longitudinal Distribution $(\overline{X})$ of the Displaced Buckled Profile for Beam Element Model (*ANB14*) and Plane Strain Element Model (*AP8*) with Random Geometric Imperfections at Solution Time ($\tau = 22$).

The influence of element formulation on the computed pulse buckling response was one of the more important conclusions developed from the finite element analyses conducted in the present thesis. Models that incorporated plane strain elements were more consistent with experimental observations (Figure 3-11; Lindberg and Florence, 1987), in comparison with the beam element models. Only the pulse buckling response of the plane strain element models exhibited the characteristic peak amplitude, single waveform adjacent to the fixed support.

The relative discrepancy in the computed pulse buckling response can be related to the inherent characteristics that define the element formulation. The behaviour of an Euler-

Bernoulli beam element is expressed through the moment–curvature relationship, which requires plane sections to remain plane and normal to the neutral axis. In addition, for the beam element models, the nonlinear terms of the axial strain–displacement relationship are explicitly defined. Plane strain elements, however, implicitly account for the flexural response through the quadratic displacement field.

The influence of numerical procedure and element formulation on the characteristic exponential growth of transverse peak displacement is illustrated in Figure 4-5. The peak buckle displacement response for the finite difference and finite element models with combined and random geometric imperfections are presented. An average imperfection coefficient of $w_o = 0.06$, equivalent to $0.017d$, was selected to plot Equations (3.18) and (3.19).

Provided random geometric imperfections were incorporated, for relatively early solution times ($\tau \leq 10$) the finite element models exhibited unbounded growth of transverse deflections consistent with theoretical analysis and finite difference solutions. The pulse buckling response, however, deviated from an unbounded growth toward a limiting plateau at later solution times. The behaviour was attributed to the coupled nonlinear terms of the axial–strain displacement response and longitudinal variation in the axial stress state (Figure 4-3). In addition, the 'simplified' theoretical analysis considers only one dominant mode (i.e. the "preferred" wavelength, λ_p) and defines a single equivalent geometric imperfection (w_o), which does not account for the randomly distributed properties of the finite element model. The existence of a limiting plateau was consistent with experimental evidence from time-frame photographs (Figure 3-11) and observations by Lindberg (1965) and Lindberg and Florence (1987). The finite difference solution remains unbounded since the solution assumed a constant and uniform axial impulse with elastic behaviour and neglected the influence of axial inertia and coupled nonlinear terms.

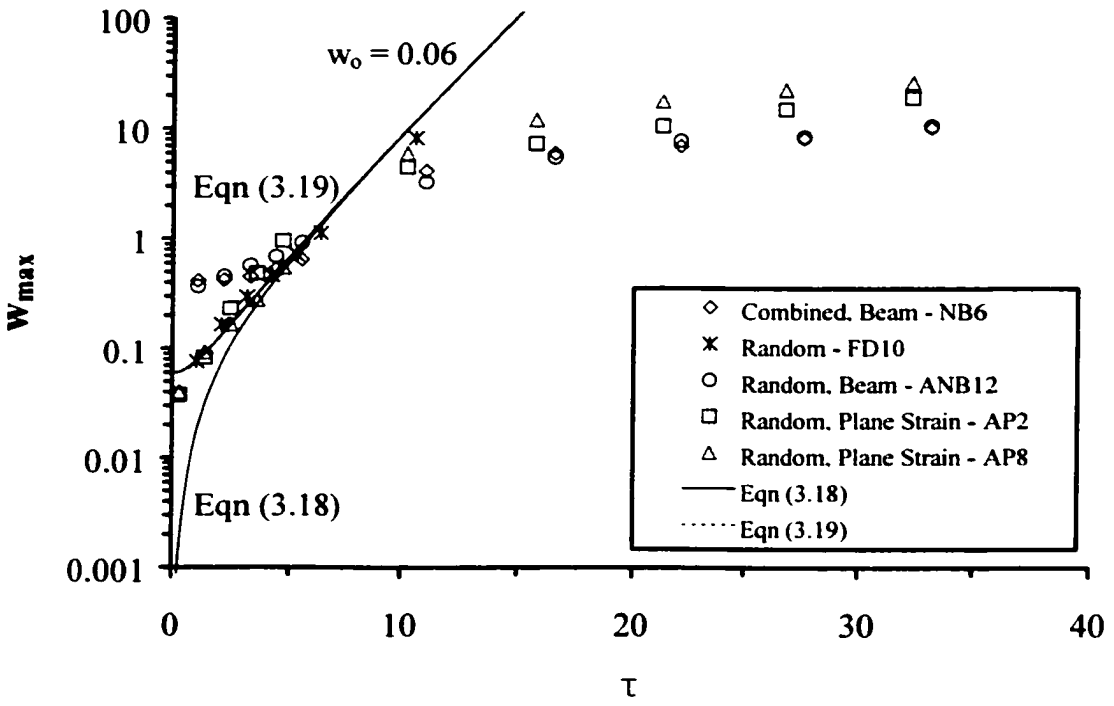

Figure 4-5. Nondimensional Peak Buckle Amplitude (w_{max}) as a Function of Time (τ) for Finite Difference and Finite Element Models (Beam, Plane Strain) with Combined and Random Geometric Imperfections.

The influence of element formulation on the peak buckle displacement response was also observed. In comparison with the beam element models, the finite difference model (*FD10*) and plane strain model (*AP8*) were more accurate with respect to the analytical expressions. The discrepancy was related to inherent characteristics of the beam element formulation, which include the assumption of plane sections remaining normal to the neutral axis with deformation, moment-curvature and nonlinear axial strain–displacement relationships. This was supported by the high degree of curvature developed adjacent to the lower fixed support (Figure 4-4) by the plane strain element models, which was in agreement with experimental observations (Figure 3-11). Due to localized plastic deformation at the peak buckle crest, the plane strain element analysis required a fully

nonlinear (material and geometric) solution. Lindberg and Florence (1987) also reported the development of plastic zones at the peak crest through experimental observation.

4.4.3 Modal Response Analysis

A Discrete Fourier Transform (DFT) analysis of the deformed geometry was initially conducted to characterize the modal response of the plane strain element models. The actual or real magnitude of the Fourier coefficients of the buckled displacements, however, could not be determined accurately. This was attributed to an averaging effect, where the sparse number of large amplitude crests near the support was effectively masked due to the more abundant and smaller amplitudes prevailing throughout the length of the beam. These characteristics are illustrated in Figure 4-4, Figure A-11 and Figure A-12. The analysis presented in Appendix A demonstrated that the Fourier coefficient magnitudes were 10-20 times less than the peak buckle amplitudes. Consequently, modal analysis was conducted using the same algorithms developed for the beam element models (Section 4.3.3).

Figure 4-6 shows the average (λ_{avg}) and weighted mean (λ_{wm}) wavelength response calculations for finite difference and finite element models with local random geometric imperfections. The average wavelength (λ_{avg}) analysis was more consistent with the theoretical expressions (Equation 2.29, Equation 2.30) than the weighted mean (λ_{wm}) response. The average wavelength (λ_{avg}) was inherently 'biased' for buckle waveforms developed near the lower fixed support. Consequently, impulse duration, boundary effects (e.g. relative stiffness and eccentricity) and element response (e.g. curvature) are important factors. Conversely, the weighted mean (λ_{wm}) response consistently underpredicts the "preferred" mode shape. The weighted mean response considers the full beam length subject to the axial compressive impulse, hence, the number of sampling points increases proportionally with mesh refinement and solution time (i.e. $\Delta x = ct$).

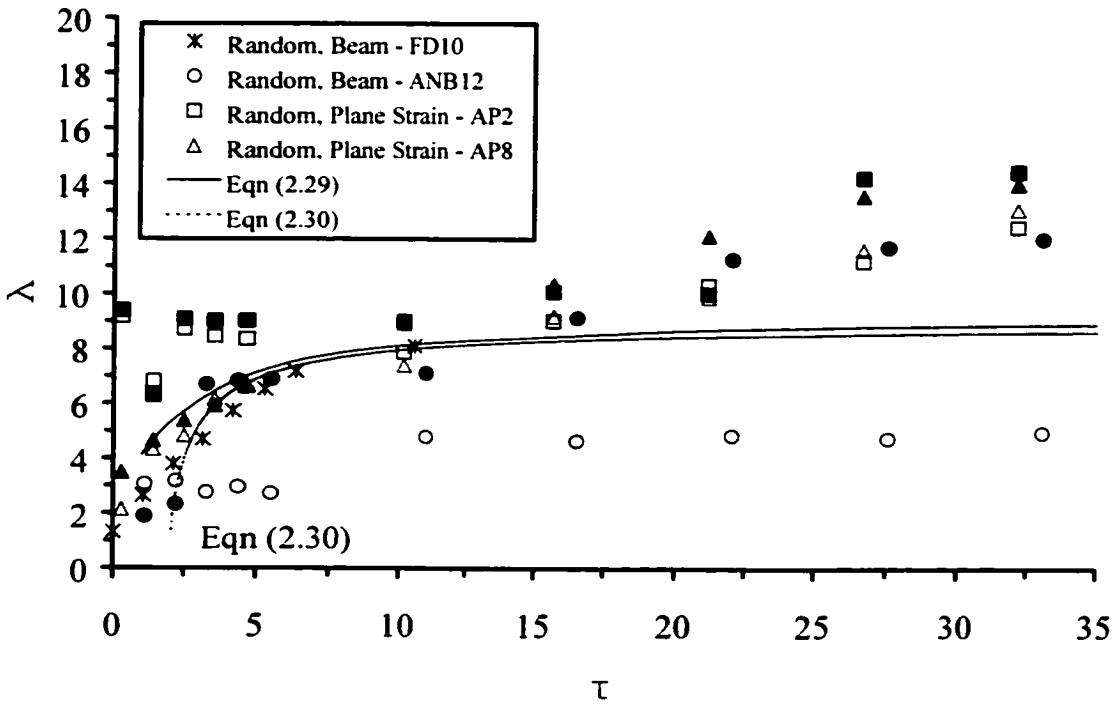

Figure 4-6. Nondimensional Buckled Wavelength (λ) as a Function of Time (τ) for Finite Difference and Finite Element Models (Beam, Plane Strain) with Random Geometric Imperfections (■ λ_{avg} , □ λ_{wm}).

The analysis presented in Figure 4-6 also demonstrated that the computed modal response was influenced by the aspect ratio, particularly for early solution times ($\tau \leq 10$). The plane strain models *AP2* and *AP8* were discretized with element aspect ratios of 8:1 and 1:1, respectively. The coarse mesh (Model *AP2*) over predicted the modal response with respect to the theoretical "preferred" wavelength ($\lambda_p = 2\pi\sqrt{2}$). This was related to the lower number of available energy modes to model the higher frequency response early in the solution due to the limited number of elements and thus degrees of freedom. Consequently, the model cannot account for the higher order flexural vibrations, which was also demonstrated by the relative peak buckle amplitude growth shown in Figure 4-5.

Parallel with the buckle amplitude growth, element formulation also played a role on the modal response. This is illustrated in Figure 4-6, for the beam element models, by the discrepancy between the computed nondimensional buckle wavelengths based on the selected numerical procedure (i.e. λ_{avg} or λ_{wm}). The response is consistent with recent analysis on elastic beam dynamics. Matsunaga (1996) investigated the free-vibration and stability of a simply supported, thin elastic beam, using a power series expansion method, as a function of aspect ratio, in comparison with classical and higher order beam theory. The analysis concluded that for aspect ratios on the order of unity ($AR = 1:1$), the critical buckling load was associated with a higher order modal response. The higher order displacement modes were more influenced by the axial force than the lower order modal response. In addition, the Euler-Bernoulli beam formulation is associated with a slightly overstiff response. These factors may explain the computed higher frequencies of vibration (i.e. lower wavelengths) response.

The plane strain element model *AP8*, with an aspect ratio of 1:1 and random imperfections, exhibited the best performance with respect to the "preferred" wavelength analysis. Modal analysis of the plane strain element computations, using either the average wavelength (λ_{avg}) or weighted mean wavelength (λ_{wm}) algorithm did not exhibit a variation in the modal response characteristics. Thus, the frequency response for the beam length subject to the axial impulse was relatively uniform.

Relative frequency distribution histograms for Model *AP8*, computed by the absolute peak method, are presented in Figure 4-7. Evolution of the pulse buckling response through modal competition are illustrated. For the time frame, $5.5 \leq \tau \leq 11$, transverse perturbations were dominated by wavelengths within the range $5 \leq \lambda \leq 8$. The weighted mean wavelength was $\lambda_{wm} = 6.7$ at a solution time of $\tau = 5.5$. This was in agreement with the theoretical and experimental histograms of the buckled wavelengths for $\tau = 6$, which were presented in Figure 3-7. The mean theoretical wavelength response was $\lambda = 7.4$, with a

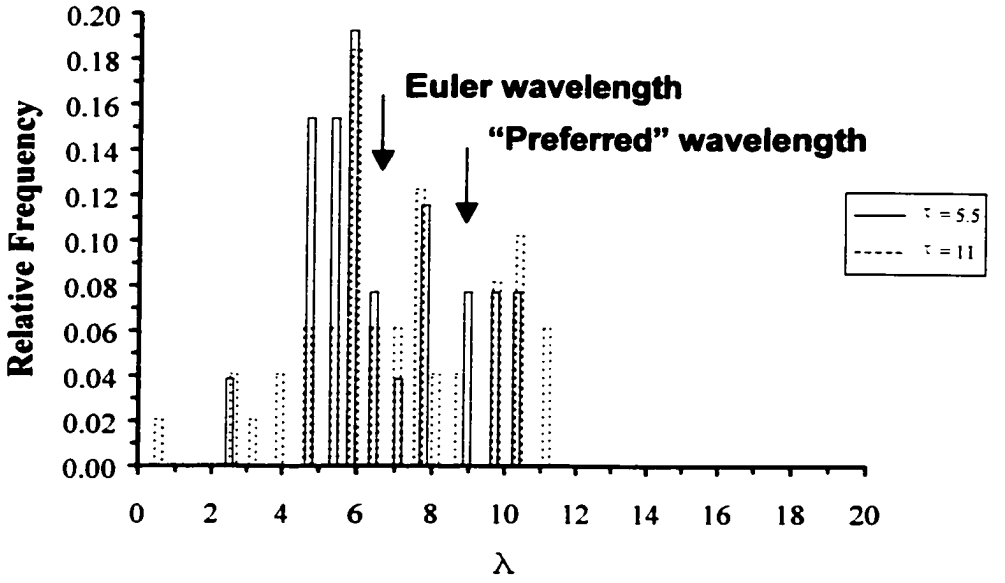

(a)

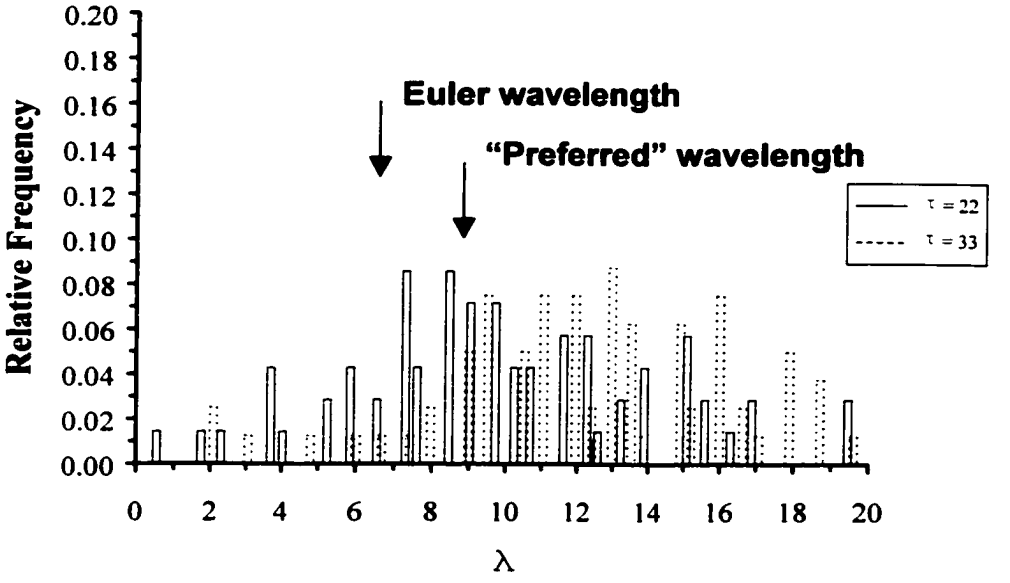

(b)

Figure 4-7. Relative Frequency Distributions of Nondimensional Buckle Wavelengths (λ) for Plane Strain Element Model *AP8* at (a) Solution Times τ= 5.5 and 11 and (b) Solution Times τ= 22 and 33.

standard deviation of $\sigma_\lambda = 1.7$, and experimental mean of $\lambda = 9.5$ with a standard deviation of $\sigma_\lambda = 1.0$. For later solution times, $22 \leq \tau \leq 33$, a broad range of buckle waveforms were excited ($\lambda \leq 20$) with relatively even frequency distribution as shown in Figure 4-7(b). A shift in the dominant mode to longer wavelengths, greater than the "preferred" mode ($\lambda_p = 2\pi\sqrt{2} \approx 8.9$), was also observed where the weighted mean increased from $\lambda_{wm} \approx 9$ to $\lambda_{wm} \approx 13$. The continued growth of lower order mode shapes from an initial high frequency response is consistent with investigations on the pulse buckling of thin cylindrical shells – see for example Lindberg and Florence (1987) and Pegg (1992).

Figure 4-8, illustrates the nondimensional buckle amplitude (w) as a function of wavelength (λ) and time (τ). The transverse deflection magnitudes for ($\tau = 5.5$) has been scaled by a factor of 10. In general, the buckle amplitudes (w) increased with time (τ) and were associated with longer wavelengths (λ). For the solution time, $22 \leq \tau \leq 33$, two dominant wavelengths evolved with the peak buckle amplitude response bounded by the Euler and "preferred" wavelengths. The peak buckle response was characterised by a mode transition from $\lambda = 4.8$ at $\tau = 5.5$ to $\lambda = 9.0$ at $\tau = 33$. The convergence toward the the "preferred" wavelength ($\lambda_p = 2\pi\sqrt{2} \approx 8.9$) was consistent with Equation (2.29), which does not asymptotically reach the "preferred" mode until $\tau \approx 30$.

For all solution times, the wavelength associated with the peak buckle amplitude, adjacent to the lower fixed support, was less than the weighted mean. This is presented in Table 4-4 where the weighted mean wavelength (λ_{wm}), peak buckle amplitude (w_{max}) and wavelength associated with the peak buckle amplitude ($\lambda[w_{max}]$) are summarised. The maximum amplitude (w_{max}) corresponds to the single dominant sine waveform adjacent to the lower fixed support. The evolution of a single dominant peak buckle crest is due to the high degree of curvature developed for the wavelength adjacent to the fixed support (Figure 3-9,

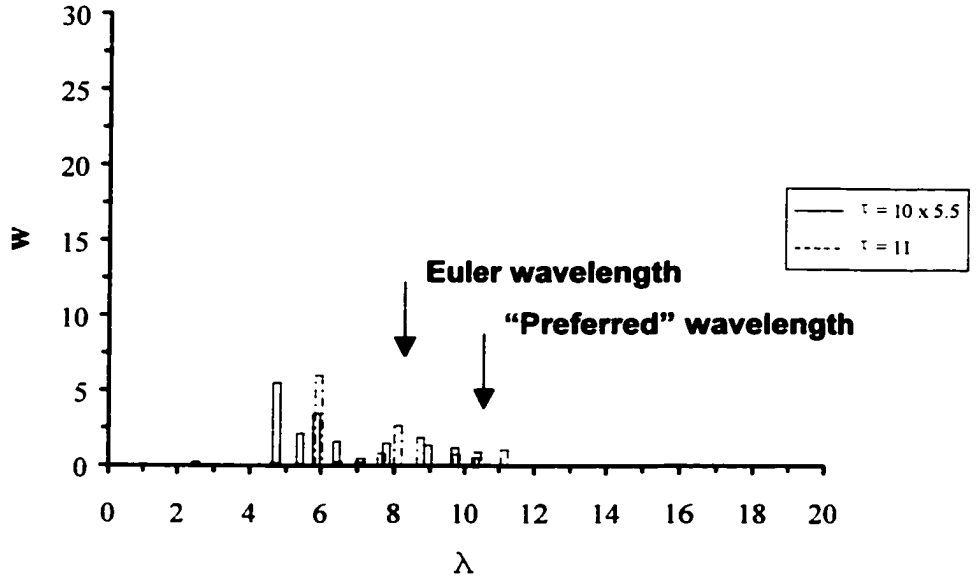

(a)

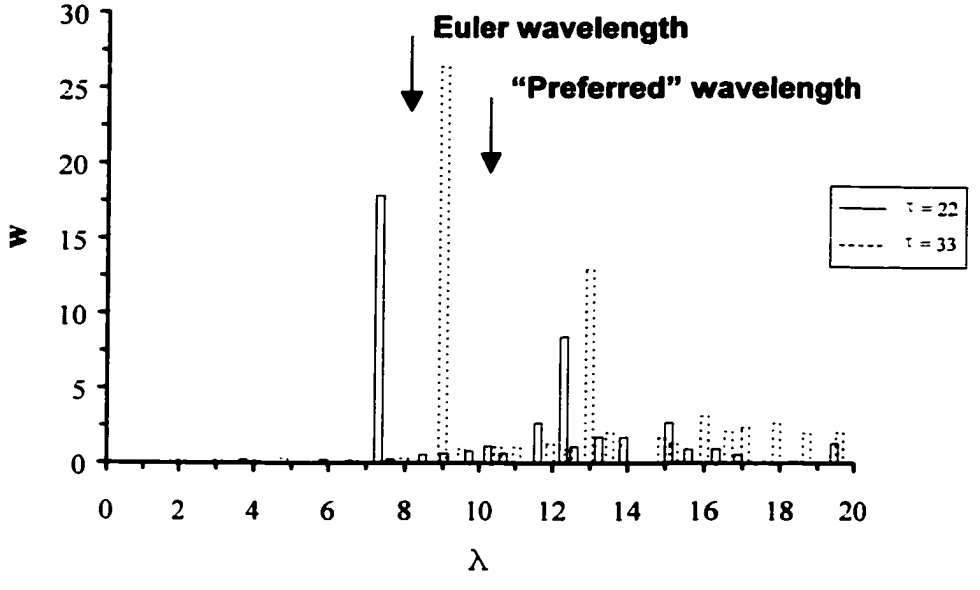

(b)

Figure 4-8. Nondimensional Buckle Amplitude (w) as a Function of Nondimensional Buckle Wavelengths (λ) for Plane Strain Element Model *AP8* at (a) Solution Times $\tau =$ 5.5 and 11 and (b) Solution Times $\tau = 22$ and 33.

Table 4-4. Modal Response Characteristics for Model *AP8*.

Time τ	Weighted Mean Wavelength λ_{wm}	Peak Buckle Wavelength $\lambda[w_{max}]$	Peak Buckle Amplitude w_{max}
5.5	6.9	4.7	5.5
11	7.4	5.8	6.0
22	9.9	7.2	17.8
33	13.1	8.9	26.4

Figure 4-4) and the reduction in axial thrust (Figure 4-3, Figure A-15) throughout the beam length. Although the observed modal response was characterized by a distribution of wavelengths, the utility of the 'simplified' theoretical analysis (Equation 2.30) has been demonstrated. For a slender beam subject to an elastic axial impulse the buckling event, in terms of the peak response, could be effectively defined in terms of a single dominant "preferred" mode.

4.5 Elastic Pulse Buckling Criterion

The pulse buckling threshold limit defined by Equation (3.21) and considered by the finite difference investigations is further addressed for selected finite element models. Assuming a proportional limit at 0.2% axial strain, the theoretical times for yield as a function of the normalized stress level, for buckling in the "preferred" mode, are illustrated in Figure 4-9. The analytical expression (Equation 3.21) was evaluated for the imperfection parameter $\beta = 0.0001$ and $\beta = 0.001$.

The displacement–time history data, of the finite difference solutions, was assessed in terms of the aspect ratio (AR) and normalized compressive stress ratio $(\bar{\sigma})$ to determine

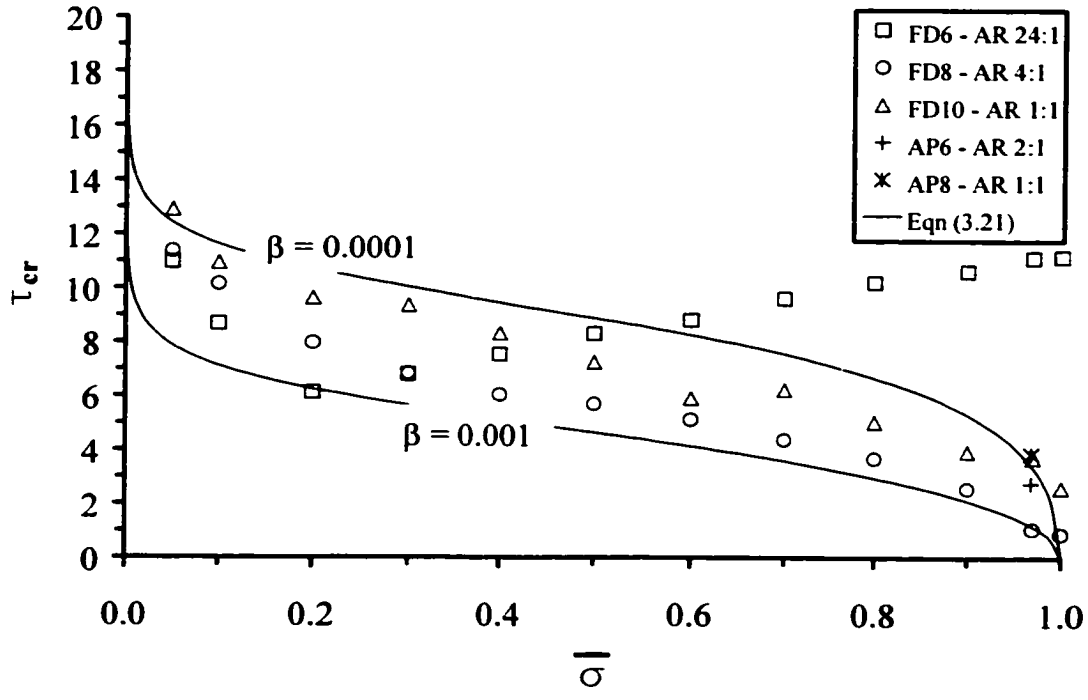

Figure 4-9. Critical Threshold Pulse Duration (τ_{cr}) for Section Yield Response as a Function of Normalized Compressive Stress Impulse Ratio ($\bar{\sigma}$).

the critical duration (τ_{cr}) for section yield. Select results from the finite difference study (Models *FD6*, *FD8* and *FD10*) are also illustrated. As discussed in Section 3.4, the importance of a finely discretized domain to accurately predict the peak buckle amplitude growth, modal response and pulse buckling threshold limit was demonstrated by the parametric finite difference investigations. For the finite element analyses (Models *AP6* and *AP8*) the applied impulse magnitude was held constant, $\bar{\sigma} = 0.97$. The significant computational effort required to conduct a parametric analysis, of the same level as the finite difference investigations, precludes a similar detailed study. The few data points, however, are consistent with the finite difference and theoretical analysis.

4.6 Conclusions of the Finite Element Analysis

The utility and simplicity of the "preferred" wavelength theory to analyze the elastic pulse buckling of a slender beam subject to an intense axial impulse has been illustrated. A series of investigations have defined the basis for the development of finite element models to accurately predict the pulse buckling response consistent with the "preferred" wavelength theory and the experimental observations presented by Lindberg and Florence (1987).

Historically, dynamic buckling analysis has generally considered only a discrete sinusoidal imperfection and fundamental mode response. Consequently, one of the more significant conclusions developed was the requirement of incorporating local random geometric imperfections. The interaction and exploitation of local geometric perturbations by the applied axial impulse was critical for developing the hyperbolic growth of transverse displacements.

For the parameters investigated, there are a number of factors that must be considered in order to accurately model the complete pulse buckling response, of a slender beam subject to an intense axial impulse, by the finite element method. In summary, the investigations should consider a finely discretised domain with aspect ratios on the order of 1:1, local random geometric imperfections and plane strain elements. Beam element models were adequate but the pulse buckling response was limited, due to inherent characteristics of the element formulation, in terms of curvature and modal behaviour. These factors may also be influenced by the boundary conditions considered due to the effects of load duration, relative stiffness and eccentricity.

Although modal perturbation techniques can provide considerable insight on the pulse buckling buckling process, the analysis has inherent limitations. The analysis is constrained

to problems defined by relatively ideal parameters (e.g. axial beam impact, radial impulse loading of shells). For structures with more complex configurations, the modal response has to be addressed on a rational basis through engineering tools such as the finite element method. Some examples include distributed boundary conditions, spatial or temporal variation in the applied load impulse, distributed boundary conditions, or varied mechanical properties. Consideration of relatively simple pulse buckling events is critical for the development and assessment of finite element models that accurately define the complete modal response. The acquired knowledge can be used as the foundation for advancement of more complex numerical models having developed confidence in the adopted numerical procedures.

5.0 Dynamic Plastic Analysis

The fundamental characteristics of classical plasticity theory are reviewed. In reference to dynamic plastic buckling, the issues addressed include elastoplastic wave propagation, dynamic plastic flow, and material strain rate behavior. Details of analytical, numerical and experimental investigations on dynamic plastic pulse buckling are discussed.

5.1 Classical Plasticity Theory

A brief treatment on classical plasticity theory is presented and the works of Hill (1971), Mendelson (1968) and Prager (1959) are referenced for a more detailed discussion. Plasticity can be generally defined as a time independent, path dependent, material response to an applied stress state or strain field exceeding the elastic limit, which exhibits irrecoverable deformation. Three fundamental parameters required for the evolution of a plasticity law are (i) a yield criterion, (ii) a flow rule and (iii) a strain hardening rule. The yield criterion defines the limit of purely elastic behavior for any applied stress state and can be generally expressed as,

$$f(J_1, J_2, J_3) = K(h) \tag{5.1}$$

where J_1, J_2, J_3, are the first, second and third stress invariants respectively, K is an empirical material constant which is a function of the hardening parameter, h. In reference to empirical investigations, the two common yield criteria applied for the behavior of isotropic materials are the Tresca (maximum shear stress) and von Mises (maximum distortional energy). For most metals, the von Mises yield condition best represents material behavior,

$$\sqrt{J_2'} = \frac{1}{2}\sigma_{ij}'\sigma_{ij}' = K(h) \tag{5.2}$$

where J_2' is the second deviatoric stress invariant. The von Mises yield criterion is independent of the hydrostatic stress and states that yielding occurs when the recoverable or elastic distortional energy reaches a critical value. The yield surface is schematically illustrated in Figure 5-1.

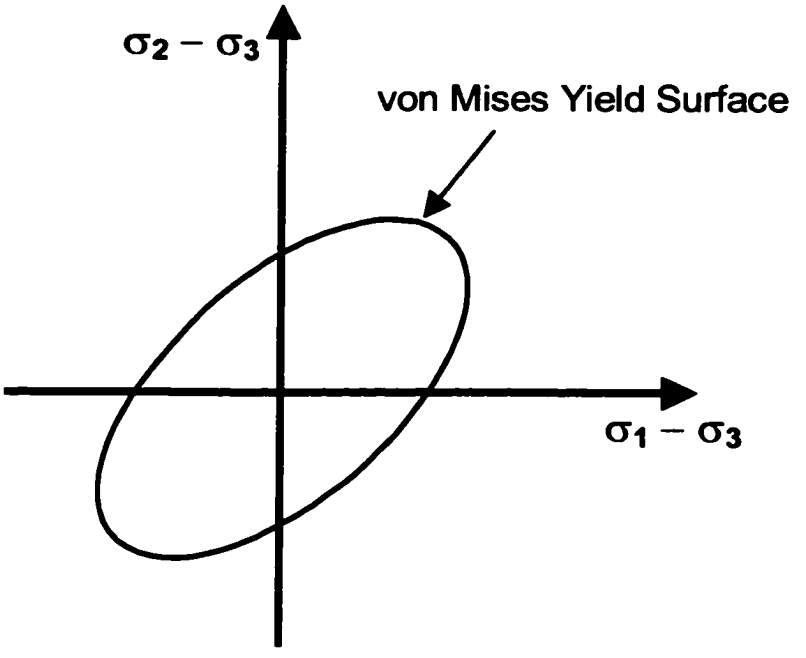

Figure 5-1. Two-Dimensional Representation of the von Mises Yield Surface.

The relatively simple, continuous function is readily adapted and commonly applied in numerical methods (Owen and Hinton, 1980; Hunsaker et al., 1976). This is also evident by the incorporation of the von Mises yield function in most commercially available finite element packages.

Once yielding has been initiated, additive decomposition of the total strain response into elastic and plastic components is required,

$$d\varepsilon_{ij}^{T} = d\varepsilon_{ij}^{e} + d\varepsilon_{ij}^{p} \tag{5.3}$$

where $d\varepsilon_{ij}^{T}$, $d\varepsilon_{ij}^{e}$, $d\varepsilon_{ij}^{p}$ are the total, elastic and plastic incremental strain components respectively. The elastic strain is defined by,

$$d\varepsilon_{ij}^{e} = C_{ijkl}^{-1}\, d\sigma_{kl} \tag{5.4}$$

where C_{ijkl} is the elastic stress-strain constitutive relationship (i.e. stiffness matrix) and $d\sigma_{kl}$ is the stress increment. The plastic strain increment is defined by the flow rule,

$$d\varepsilon_{ij}^{p} = d\lambda \frac{\partial Q}{\partial \sigma_{ij}} \tag{5.5}$$

where $d\lambda$ is a proportionality constant (plasticity multiplier) and Q is the plastic potential.

For the finite element analysis conducted in the present thesis investigations, the theoretical basis for $d\lambda$ is detailed in the NISA User's manual (NISA, 1997). For metals, the flow rule is also known as the normality condition where the plastic strain increment is a vector directed normal to the plastic potential function (Hunsaker et al., 1976; NISA, 1997). The normality condition implies incompressible behavior. For the current study, only associated plasticity is considered such that the plastic potential is defined by the yield function; i.e. $Q \equiv f(J_1, J_2, J_3)$. This model is appropriate for metals where the primary mechanism of plastic flow is through dislocation movement and there are no

abrupt changes in the strain rate at a point. For incremental plasticity theory, the rate form of the flow rule allows history dependent response to be modeled.

Evolution of the yield surface with increasing stress state or imposed strain fields is accounted through the hardening rule, which also defines the material strain-hardening characteristics. There are numerous hardening models available with varying degrees of complexity and range of applications; for example, fatigue (cyclic loading), rate sensitive processes (metal forming, high-temperature creep). There are three fundamental hardening models, (i) perfectly plastic, (ii) isotropic hardening and (iii) kinematic hardening, which are illustrated in Figure 5-2 for a two-dimensional stress state.

Perfectly plastic is the simplest model that does not consider any change in the shape, size, orientation or position of the yield surface for any plastic deformation increment. Numerical procedures must address potential convergence issues sine the plastic strain increment is not uniquely defined by the stress state, since Equation (5.5) is satisfied by any arbitrary constant.

Isotropic hardening assumes only a uniform expansion of the yield surface about the origin in stress space. The yield surface increases in size as a function of the hardening parameter, typically based on plastic work done, with a constant shape. In considering the von Mises yield criterion, the rate of strain hardening can be determined from a simple, uniaxial tensile test. The model is well suited to problems where the stress state significantly exceeds the yield (e.g. monotonic loads, impact) and does not experience rate reversal of plastic strains (e.g. cyclic loads) synonymous with the Bauschinger effect (Rice, 1975). Consequently, the isotropic hardening rule is commonly applied in engineering analysis and numerical modeling procedures.

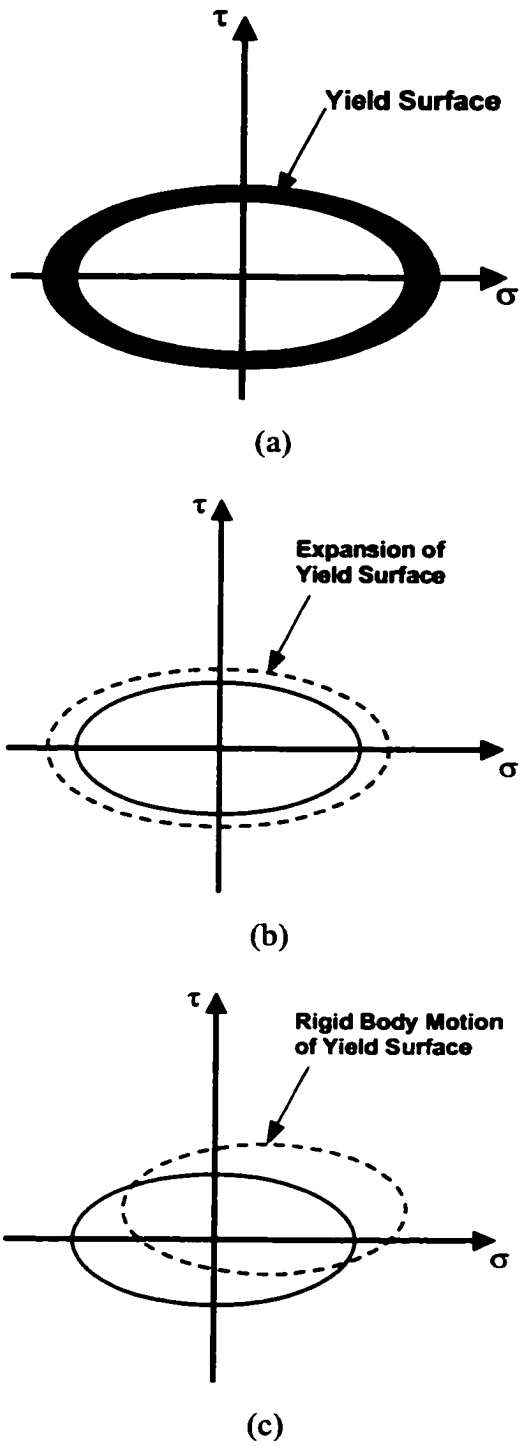

Figure 5-2. Graphical Representation of Strain Hardening Rules (a) Perfectly Plastic, (b) Isotropic Hardening and (c) Kinematic Hardening.

The kinematic hardening model accounts for rigid-body translation of the yield surface in stress space, with constant size, shape and orientation, in a direction vector connecting the yield surface locus with the stress point. The formulation is generally based on the work of generally based on Prager (1959) and Ziegler (1959). The kinematic hardening rule can account for the effects of load reversal and an ideal Bauschinger response.

Further details of the theoretical basis and discussions on plasticity hardening models are presented in NISA (1997), Al-Bermani and Zhu (1995), Jiang (1994) and Thomas et al. (1983). For mathematical simplicity and computational efficiency, typically only the expansion and translation of the yield surface is considered. In consideration of the dynamic plastic pulse buckling events considered in the present investigations, classical metal plasticity models that consider perfectly plastic or isotropic formulations are appropriate. Engineering applications can include crash worthiness studies, metal forming processes and general collapse analysis.

5.2 Propagation of Elastoplastic Stress Waves

The mechanics of plastic stress wave propagation in slender rods due to axial impulsive loads has been the subject of extensive investigations; see for example Meyers (1994), Bell (1988, 1968). The classical theory of uniaxial stress wave propagation has been attributed to von Kármán and Duwez (1950). The axial plastic wave velocity (V_p) can be expressed as,

$$V_p = \sqrt{\frac{\left(\frac{d\sigma}{d\varepsilon}\right)}{\rho}} \tag{5.6}$$

which is similar to the elastic stress wave solution where the elastic modulus (E) is replaced by the tangent modulus $\left(\frac{d\sigma}{d\varepsilon}\right)$. Since the tangent modulus is less than the elastic stiffness, the corresponding axial stress wave must propagate at a lower velocity. The net effect is for the wave front to be dispersed as shown in Figure 5-3, where E_o is the initial elastic modulus and E_{T1} and E_{T2} are the successive tangent moduli.

The elastic wave propagation can be considered constant with a square profile whereas the effects of plasticity and work hardening disperse the wave front with time (i.e. axial distance, x) and stress level (σ). Consequently, the displacement field is also affected by the stress front variation as a function of time, since a finite time is required for the wave front to propagate a unit distance. Increased duration of the load event causes the wave front to become more dispersed due to variation in the wave speeds (i.e. $v_o > v_1 > v_2$) as a function of the stress state. For dynamic pulse buckling events with coupled axial and flexural modal response, the analysis can be compounded by strain rate and path dependent deformation, as well as elastoplastic stress wave boundary reflection and pattern interference.

5.3 Strain Rate Effects due to Dynamic Loading

5.3.1 Introduction

The influence of strain-rate dependent mechanisms, exhibited by most metals and alloys, on the mechanical response has been well established. Stronge and Yu (1993), Jones (1989), Harding (1987), Wilkins (1984), Clifton (1983), Campbell (1970) and Bodner (1968) present detailed discussions and analyses. To enhance general understanding of the issues related to analyzing and modeling dynamic pulse buckling events, the fundamental characteristics are reviewed.

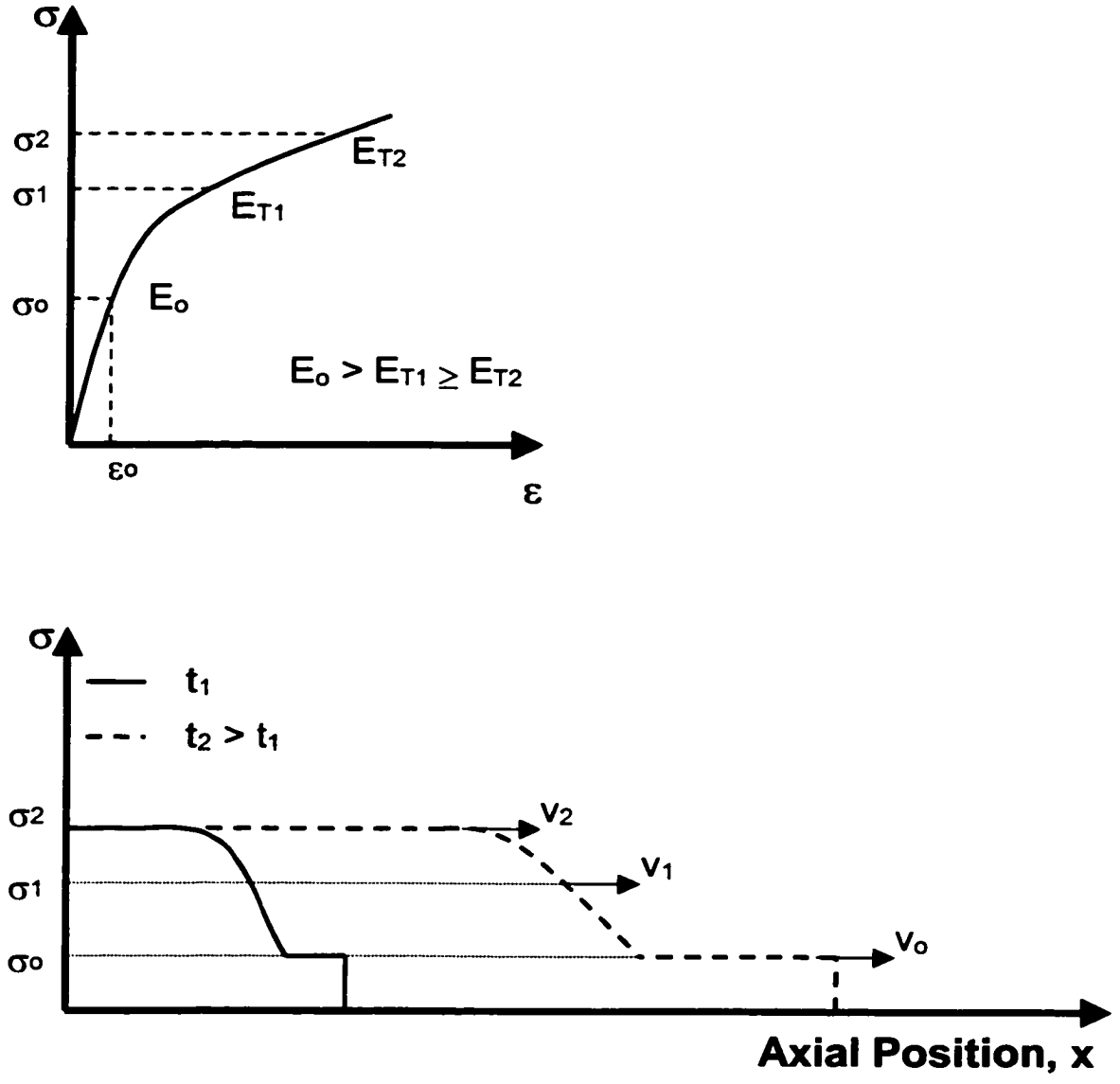

Figure 5-3. Wave Front Dispersion as a Function of Time and Stress Level.

The focus is on impact events where the load intensity, structural geometric imperfections, dynamic material response and wave propagation can be coupled parameters in the transient response. For low velocity impacts, typical of structural crashworthiness studies and general impact loads, the strain rates are on the order of 1 /s –

100 /s. Lower energy events such as quasi-static buckling or higher energy modes such as hypervelocity or shock loading events are not considered. A general discussion of strain rate effects on ductile materials will be presented. The behavior of mild steel and aluminum (6061-T6) will be highlighted in context of the experimental investigations, presented in Chapter 6, and subsequent finite element analyses, discussed in Chapter 7.

To illustrate the effects of strain rate dependent or independent behavior, general examples of idealized stress-strain relationships are illustrated in Figure 5-4. The first case is an elastic, perfectly plastic response at the corresponding yield stress (σ_y). Although the model cannot account for work hardening, Jones (1989) demonstrates that theoretical models with perfectly plastic material response are in agreement with experimental observations, for specific materials and structural configurations.

An elastic, linear strain hardening response is illustrated in Figure 5-4(b), which is a relatively simple but commonly utilized model. Variants also incorporate piecewise linear and nonlinear, power law (e.g. Ramberg-Osgood) formulations. The main limiting factor is an assumption of a constant elastic response and thus does not accurately model the Bauschinger effect.

A number of methods have been proposed to account for the influence of strain rate on the stress–strain response as illustrated in Figure 5-4(c); for example Malvern (1984), Duffy (1982, 1979) and Lindohlm and Besseny (1969). A constitutive relationship that is typically employed is an overstress power law relationship known as the Cowper-Symonds equation (Symonds, 1967),

$$\dot{\bar{\varepsilon}}^p = D\left(\frac{\bar{\sigma}}{\sigma_y} - 1\right)^q, \tag{5.7}$$

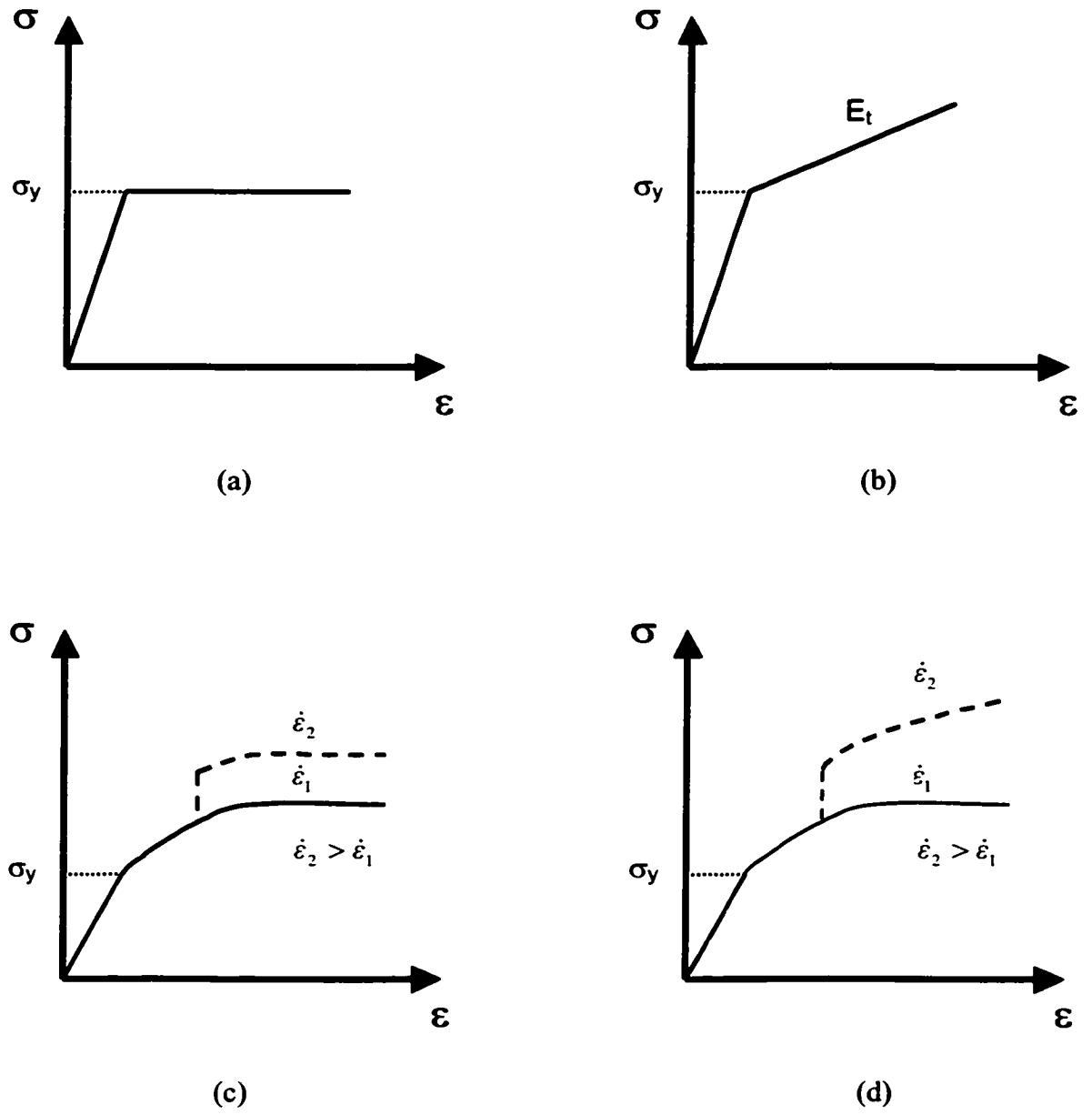

Figure 5-4. Idealizated Stress-Strain Response for a Ductile Material (a) Elastic-Perfectly Plastic, (b) Bilinear Elastoplastic, (c) Rate-Dependent Elastoplastic, and (d) Rate Dependent, Path-Dependent Elastoplastic.

where $\dot{\bar{\varepsilon}}^p$ is the uniaxial equivalent plastic strain rate, $\bar{\sigma}$ is the dynamic flow stress for nonzero plastic strain rate, σ_y is the static yield stress that can be a function of temperature, plastic strain or other field variables, D and q are empirical material constants. Bodner (1968) presents further discussion on the reference static yield stress. In general, it is assumed that the work hardening rate remains constant for different strain rates and flow stress levels. The overstress function is dependent on the instantaneous plastic strain rate and load history independent. Based on plasticity theory, the formulation is readily incorporated in numerical methods and can be adapted to various hardening rules under general stress states.

Some materials exhibit path dependence, where the flow stress could exhibit a different path and strain rate response due to a change in the work-hardening parameter as shown in Figure 5-4(d).

For mathematical simplicity, most commercial finite element packages, such as NISA (1997), only account for work hardening through an idealized elastic, perfectly plastic stress–strain relationship. Robust computational algorithms that consider rate-dependent response (e.g. viscoplasticity, strain-rate sensitive yield flow behavior) are incorporated by advanced finite element packages.

5.3.2 Evaluating Dynamic Mechanical Properties

A significant volume of literature has been dedicated to investigating the mechanical response of slender bars subject to intense axial impulse loads or high strain rates. The emphasis has been on the detailed characterization of stress–strain relationships at high loading/strain rates. The corresponding influence of stress wave interference effects and measurement techniques on the empirical mechanical response was also assessed. Some of the historical investigations include the referenced works of Jones (1989), Malvern

(1984), Nicholas (1982), Duffy (1982, 1979), Lindohlm and Besseny (1969), Symonds (1967), Davies (1948) and Hopkinson (1914). In addition, a number of studies have evaluated the influence of experimental apparatus and procedure on the dynamic mechanical response of materials at high strain rates, such as Albertini et al. (1978), Clifton (1983) and Hauser (1966).

The experimental investigations typically employed a variant of the split-Hopkinson pressure bar. The apparatus was valid for strain rates in the range of 10^{-1} /s to 10^{4} /s, where a small specimen would be placed collinear between two identical long, slender rods. The specimen size was selected to produce a uniform strain distribution over a finite time interval. An elastic axial or torsional impulse would be applied to one of the slender rods, as an input device or transmitter and the other rod would serve as the output or receiver. The rod slenderness ratio was selected to ensure that the pulse wavelength was greater than the diameter so that one-dimensional wave propagation theory could be considered. The apparatus also eliminated inertia effects of a crosshead and load cell associated with a conventional test frame. Strain gauges on the input and output rods measured the axial stress wave propagation and the mechanical response of the specimen was inferred from the data records.

5.3.3 Characteristics of Aluminum 6061-T6 and Mild Steel

Experimental investigations on the strain-rate sensitivity of Aluminum 6061-T6 have exhibited some discrepancy. For strain rates up to 10^{3} /s, Maiden and Green (1966) and Lindholm and Yeakley (1968) did not observe strain rate dependence. Jones (1989), Bodner (1968) and Gerard and Papirno (1957) made similar observations. Ng et al. (1979) and Hoge (1966) concluded that the material response exhibited dependence on strain rates greater than 10/s. For work hardened specimens, Hauser (1966) demonstrated that dependence on strain rate was observed particularly for rates greater than 10^{3} /s. The

influence on aluminum behavior, however, was significantly less pronounced than the response of mild steel. Langseth et al. (1994) conducted axial impact tests on thin-walled aluminum (6061-T4, 6061-T6) extrusions and showed that the peak dynamic loads were 1.2 to 2 times the peak static loads.

In contrast, the literature is quite conclusive on the strain rate sensitivity of mild steel. For strain rates on the order of 10^3 /s, the flow stress exhibits an increase by a factor of approximately three. This issue has been thoroughly reviewed and discussed by Jones (1989), Chang et al. (1989), Bodner (1968), and Marsh and Campbell (1963). Furthermore, Harding (1987) states that an increase in the quasi-static strength raises the threshold strain rate required for rate dependent behavior. For moderate strain rates, associated with impulsive events of interest for the current investigation, the importance of considering rate effects on the stress-strain response of mild steel has been recognized. The importance of rate sensitivity on the plastic pulse buckling response will be further addressed through the experimental investigations (Chapter 6) and the finite element modeling (Chapter 7).

5.4 Dynamic Plastic Buckling

The plastic response of beams to transient loading events has received considerable interest over the past four decades and has encompassed a broad subject area. An extensive number of studies have been conducted on parametric buckling arising from pulsating loads; for example Bažant and Cedolin (1991) and Bolotin (1964). In addition, a significant research effort has investigated the plastic buckling response of beam subject to transverse loads (Jones, 1989) and dynamic progressive buckling of axially loaded thin-walled sections (Belingardi and Vadori, 1993; Abramowicz and Jones, 1984). For the present study, these issues are not considered. The dynamic buckling response of

slender beams, subject to intense axial impulsive loads where inertia effects and plastic flow influence the modal response, is examined.

The elastic pulse buckling analysis addressed in Chapter 2 through Chapter 4, considered an impulsive stress less than the proportional limit. The observed plastic flow response, from experimental (Gerard and Becker, 1952; Lindberg and Florence, 1987) and numerical (Chapter 4) investigations, occurred only after buckling was well developed and was localized to the single peak buckle crest. Plastic pulse buckling, however, can be characterized by large permanent strain where the stress state exceeds the elastic limit prior to significant growth of lateral displacements. The dynamic plastic pulse buckling of structures is a complex subject area of continued research. Past investigations have focused on a variety of interests including (i) empirical studies characterizing the buckled wavelength, (ii) theoretical analysis defining stability based on limit bound plasticity theory, (iii) investigations on fundamental, higher order or "preferred" mode response by theoretical or idealized mechanical models or (iv) numerical investigations on dynamic buckling.

Based on these studies, a preliminary framework has been developed to assess the dynamic plastic buckling response of axially loaded beams. Karaziagova and Jones (1996), Jones (1989) and Ari-Gur et al. (1987) have all stressed the importance for continued research in this field. In order to reduce the analytical complexity, the performance of available engineering tools is constrained by limiting assumptions (e.g. equation of motion, constitutive relationship) and simplifications (e.g. structural geometry, boundary conditions). Although the analysis can provide considerable insight on the buckling process, for complex dynamic buckling events numerical methods are required and provide a rational basis for detailed investigations. A review on dynamic plastic buckling of structures, with particular reference to axially loaded slender beams, will be presented.

5.4.1 Experimental Studies

Since the 1940's, experimental investigations on the behavior of bars subject to intense loads were generally concerned in defining elastoplastic constitutive relationships or characterization of the stress wave front (Meyers, 1994; Abramson et al., 1958). For dynamic pulse buckling, Bell (1988) proposed a semi-empirical expression for the critical buckled wavelength based on the quasi-static buckling response of struts,

$$L_{cr} = \frac{\left(\frac{3}{2}\right)^{3/4} n \pi \alpha r}{\sqrt{8}\,\sigma_{\max}}, \tag{5.8}$$

where α is an experimentally measured material constant (N/m^2) and σ_{max} is the maximum uniaxial stress (N/m^2). Figure 5-5 illustrates typical deformed geometry profiles, for a 12.3mm diameter aluminum bar subject to an impact velocity of 40.6m/s.

Variation in the buckled profile geometry between the projectile and impacted sample was due to inertia of the steel sabot, which fixed the impacted specimen in place. The analysis considered a constant stress state and particle velocity with finite strain field behind the propagating plastic wave front. The effects of axial inertia and strain rate sensitivity are ignored. Analysis conducted by Karagiozova and Jones (1996) demonstrated that for dynamic plastic buckling response, the quasi-static analysis could not predict the final deformed buckled shape unless the impact energies were small. Thus, the analysis of Bell (1988) was limited to lower bound estimates for the initiation of dynamic instability.

Although primarily concerned with an elastic buckling response, the experimental data presented by Ari-Gur et al. (1982, 1979, 1978) was of tangible interest. A series of

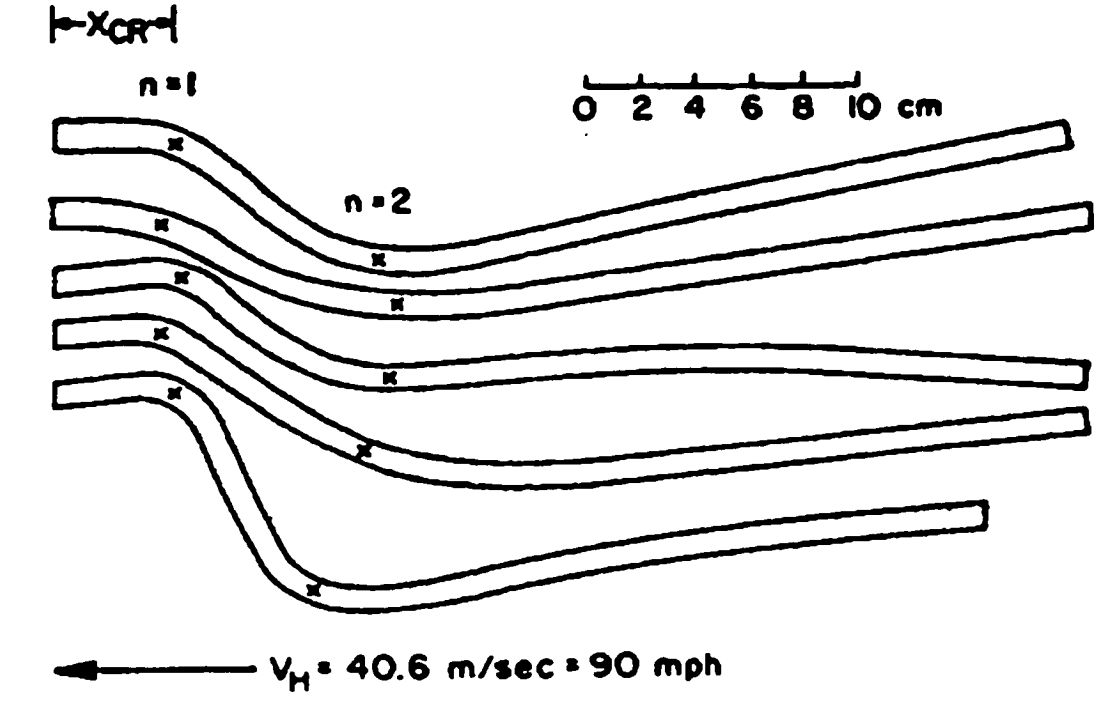

(a)

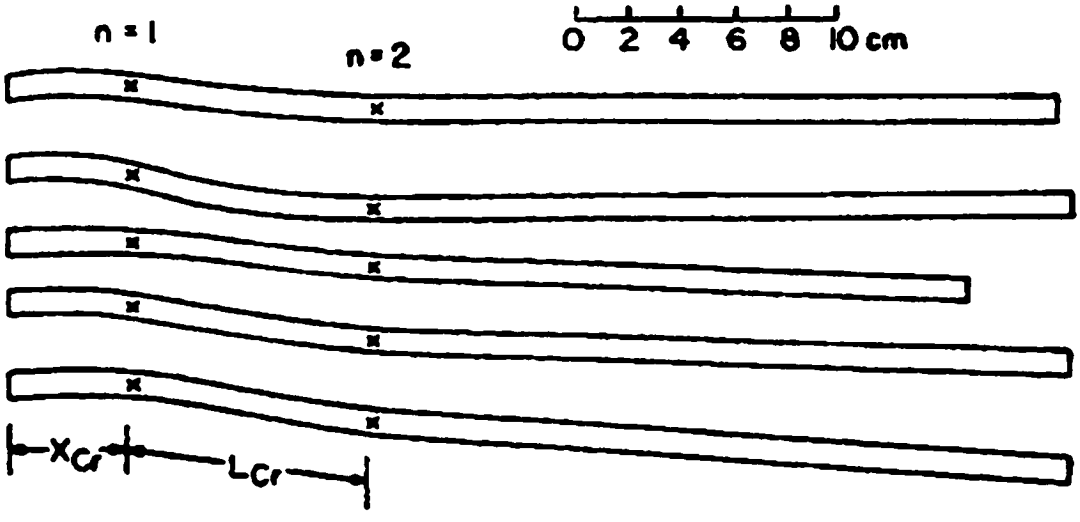

(b)

Figure 5-5. Post-Test Buckled Mode Shapes for 12.3mm Diameter Aluminum Rods (a) Projectile, (b) Impacted Bar (Bell, 1988).

impact tests were conducted on bars of rectangular cross-section composed of 6061-T4 aluminum, AISI-01 carbon chrome alloy steel and fiberglass-epoxy composite. Columns, with effective slenderness ratios ($71 \leq L_e/r \leq 411$), were subjected to free-fall impact by a cylindrical mass, ranging from 0.05kg to 0.37kg, with critical striking velocities between 6m/s and 15m/s. The significance for plastic flow buckling is illustrated in Figure 5-6, where the final deformed profiles exhibited a higher order response than the initial imposed half-sine wave imperfection magnitude, which was on the order of *1.1d*. This observed modal response will be further addressed in Chapter 6 and Chapter 7.

Abrahamson and Goodier (1966) conducted a series of experiments where round aluminum bars were fired as free-flight projectiles against a heavy steel slab with increasing impact velocities. Figure 5-7 illustrates the buckled profiles for 6061-T6 aluminum rods (0.454" diameter and 18" length) impacting a rigid steel target at velocities of up to 650ft/s (~198m/s). The ratio $(V/V_o)^2$ relates the impact kinetic energy to the static elastic strain energy of the rod. The top bar is the reference condition or unstressed state. In addition to the more prevalent axial shortening and transverse deformation, local effects of plasticity through diametral expansion are evident near the impacted end particularly for the higher velocities. Assuming a "preferred" mode ($\lambda_p = 2\pi\sqrt{2}\,;\eta = 1/\sqrt{2}$), for plastic buckling response the dominant half-wavelength can be defined as (Abrahamson and Goodier, 1966),

$$L_p = \frac{\lambda_p r}{2s} = \pi r\sqrt{\frac{2E_T}{\sigma}} \tag{5.9}$$

A typical axial strain response is illustrated in Figure 5-8, where the peak strain was measured at one diameter from the contact interface and considered twice the diametrical strain. For the particular bar geometry, the time (243μs) was on the order of the return period for the propagating elastic unloading wave.

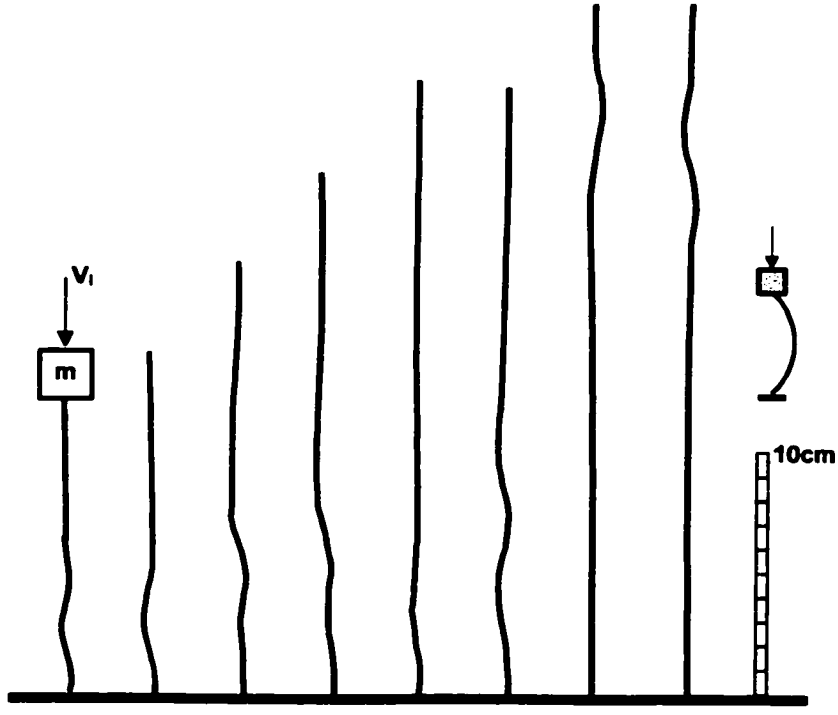

Figure 5-6. Digitised Profiles of Experimental Buckled Mode Shapes of Aluminum Bars Subject to Axial Impact by a Free Fall Hammer (Ari-Gur et al., 1982).

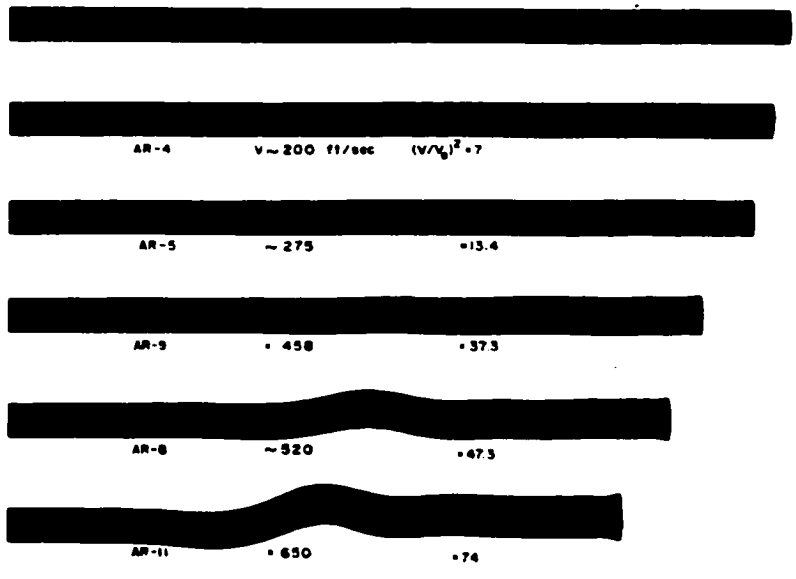

Figure 5-7. Dynamic Plastic Buckling of a Rod by Longitudinal Impact (Lindberg and Florence, 1987).

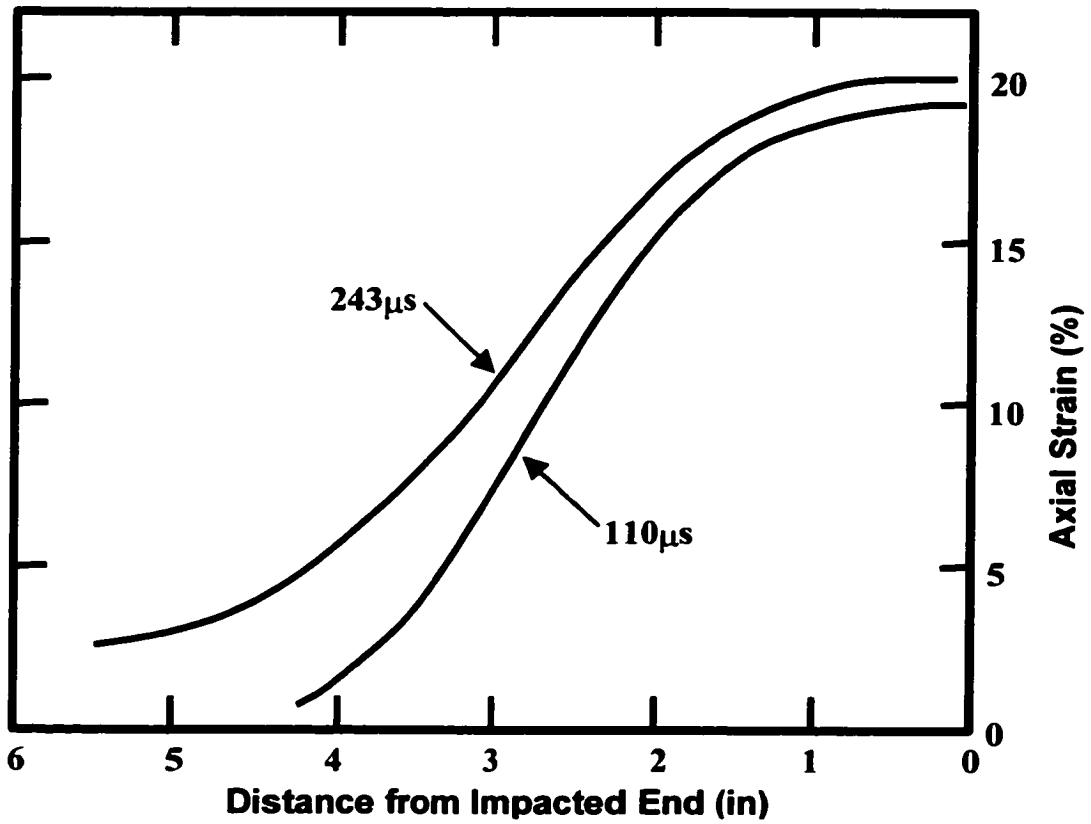

Figure 5-8. Axial Strain as a Function of Distance from the Impacted End (Abrahamson and Goodier, 1966).

An empirical expression was also developed relating the work done in axial shortening to the kinetic energy in excess of the elastic strain energy. For a beam of length (L), elastic modulus (E) and yield stress (σ_y), the axial shortening (δ) is defined by,

$$\delta = \frac{\sigma_y L}{2E}\left(\frac{V_{KE}^2}{V_E^2} - 1\right), \tag{5.10}$$

where V_{KE} is the kinetic energy velocity term in excess of the elastic strain energy velocity, V_E.

The linear relationship, illustrated in Figure 5-9, was consistent with experimental data (Abrahamson and Goodier, 1966). Equation (5.10) was evaluated with a yield stress, (σ_y = 300MPa) and an elastic modulus (E = 69GPa). Although deviation from linearity at higher energy ratios was exhibited, the basic assumption of a uniform axial thrust appears valid. The measured wavelength response data compiled by Abrahamson and Goodier (1966) was assessed as a function of the axial strain, which is illustrated in Figure 5-10. For the 0.454", 0.209" diameter rods and the 0.454" diameter tube, the theoretical dominant half-wavelengths are 1.01", 0.46" and 1.70", respectively. Significant experimental scatter is evident and linear trend lines, fitted by a least squares analysis, are shown for illustrative purposes.

The buckled response for the impacted rods exhibits a general decreasing "preferred" half-wavelength with increasing axial strain (i.e. kinetic energy). The variation is probably related to a number of factors including dynamic yield stress material behavior, as well as axial and flexural mechanical and modal characteristics (e.g. stiffness, natural vibration frequencies). For the impacted tube, data for the increasing wavelength response with axial strain may be related to the shell-like nature of the cross-section. Pegg (1992) demonstrated effects of curvature, strain-rate reversal and elastic unloading influenced the modal response of impulsively loaded cylinders.

The empirical expressions have provided a basis for estimating dominant mode response for specific pulse buckling events. Extrapolation of the modal relationships outside the domain of the investigated parameters; for example variation in material properties or structural configurations, may not be valid. Experimental data, however, is invaluable for the development and validation of analytical or numerical models characterizing the pulse buckling response.

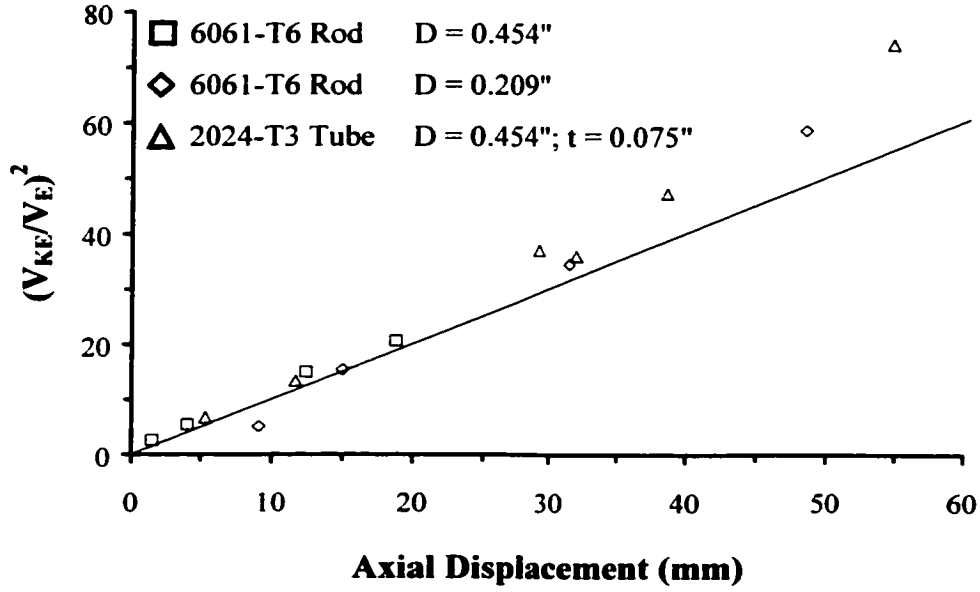

Figure 5-9. Ratio of Kinetic Energy (V_{KE}) to Elastic Strain Energy (V_E) as a Function of Axial Displacement (Abrahamson and Goodier, 1966).

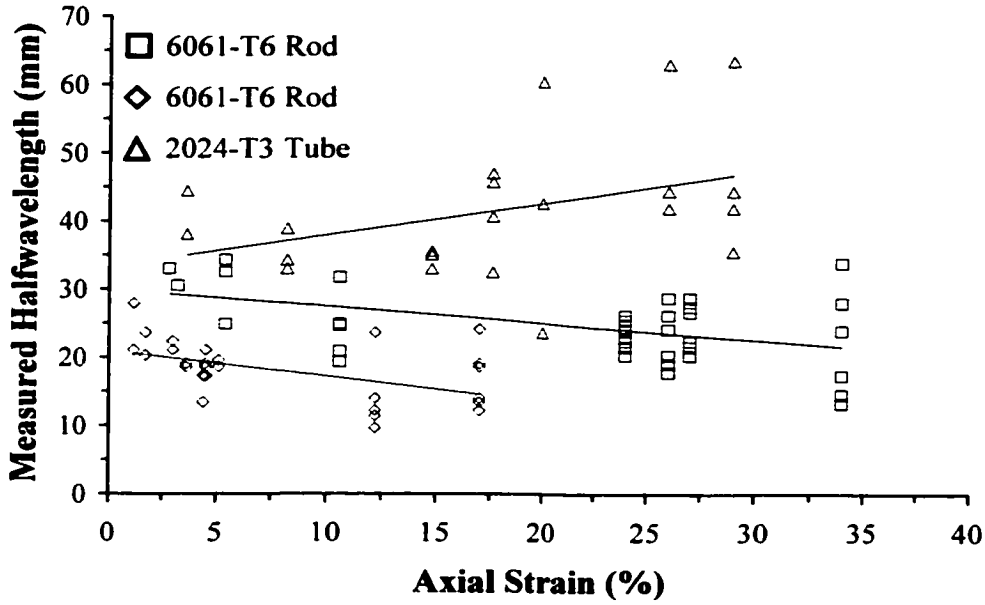

Figure 5-10. Measured Half-wavelength Response as a Function of Axial Strain (Abrahamson and Goodier, 1966).

5.4.2 Simplified Analytical Methods

For the past three decades, a significant volume of literature has been developed on the dynamic plastic buckling of structures. Jones (1989) provides a comprehensive treatment on the dynamic plastic response of beams, plates, shells as well as the challenges of model similitude. In general, the simplified methods of analysis presented are bounded by the defined assumptions, which can include infinitesimal displacements, linear material constitutive relationships (e.g. rigid plastic, linear strain hardening) and structural response (e.g. the Euler-Bernoulli beam theory).

Limit bound rigid plasticity theorems have been applied but the methods are restricted in terms of peak deflection and response time. Although not a viable procedure for the analysis of large deflection dynamic pulse buckling events, which is of current interest, the method could be employed as a preliminary assessment tool. Approximate kinematic methods have been applied to account for finite deformation (Jones, 1971). The literature, however, has concentrated on the transverse loading of beams and plates (Jones, 1989).

For the dynamic response of beams, a number of investigations have considered oblique and transverse pulse loads. Although not directly applicable, there are related issues that may contribute to the understanding and model development of axial pulse buckling events. For example, Yu et al. (1997) and Zhang et al. (1995) have provided insight on plastic hinge response as well as the interaction of elastic and plastic stress waves assuming perfectly plastic material behaviour. Yu and Jones (1997) have demonstrated the importance of stress wave effects, material strain rate sensitivity and inertia terms for low velocity impact on the order of 10m/s.

In terms of axial pulse buckling, Perrone (1965) and more recently Symonds and Frye (1988) investigated the effects of rigid plastic and elastoplastic material behaviour, on the dynamic response of a single degree of freedom model. Rigid plastic analysis was adequate for impact energies on the order of three times the elastic strain energy and pulse duration less than the natural period of vibration. For rate sensitive materials, incorporation of a rigid, perfectly plastic material model that could account for a dynamic yield stress was adequate since the bulk of energy dissipation occurred prior to variation in the strain rate response. The analysis characterized upper displacement bounds and lower pulse duration bounds for a dynamic response that can be defined by a simple, single degree of freedom oscillator.

Lee (1981) applied quasi-bifurcation theory for the dynamic buckling analysis of an axially loaded, simply supported column. The dynamic Euler-Bernoulli equation of motion was considered, which neglected axial inertia and assumed a bilinear elastoplastic stress–strain response. The perturbed flexural motion was determined as the sum of uncoupled eigenmodes, defined by a quadratic functional, for the column motion. Initiation of an eigenmode and the critical time for quasi-bifurcation compared favorably with numerical analysis. For lower impact velocities, the first mode of vibration dominated; however, with increasing velocity higher order modes were evident. The theoretical work could not account for modal response during post-bifurcation. Lee (1981) and Jones (1989) stated that further investigations are required before a suitable design procedure can be developed.

Mode approximation methods have also been developed for the analysis of structures (Symonds et al., 1984; Symonds, 1980). The procedure is based on decomposition of the structural response into distinct phases. The initial and final phase is governed by theory of elastic structural dynamics. Rigid plastic material behaviour and a prescribed modal form define simplifications for the intermediate response. The procedure has been

applied to the transverse loading of clamped beams and portal frames where the mode shape and plastic hinge locations are known *a priori*. Analysis of axial impact buckling events associated with wave propagation was not considered. Mode approximation methods have been applied to both small and large deflection regimes for a specific structural geometry. Jones (1989) states that further studies are required in order to examine the accuracy and efficiency of this method for a broader class of structural configurations.

5.4.3 Idealized Mechanical Models

Simplified mechanical models addressing the dynamic buckling response of axially loaded beams have generally considered lower order degree of freedom systems. The investigations focused on an assessment of the governing parameters.

Hartz and Clough (1957) studied the inelastic behaviour of columns subjected to an arbitrary dynamic load. Modal superposition was employed for the elastic response and a single degree of freedom (SDOF) rigid hinge represented the plastic behaviour. Similar to the studies on elastic buckling, discussed in Chapter 2, only the fundamental mode response was considered. Higher modes could be included, with increased computational effort, provided a single plastic hinge was analyzed.

Calladine and English (1984) conducted a series of investigations on the dynamic behavior of energy absorbing structures through experimental impact studies on aluminum HP-30 and mild steel. The focus was on the dynamic response of cylindrical tubes and slender beams subject to radial and axial impact, respectively. The simple structures were classified on the observed load–deflection behaviour. The beam model was designated Type II response, which exhibited an early peak stress with an ensuing rapid load decrease caused by dynamic instability. This is schematically illustrated in

Figure 5-11. The initial configuration was slightly bowed at the midspan to introduce an initial geometric imperfection and initiate a predefined buckled response.

Zhang and Yu (1989) modeled the buckling event of Calladine and English (1984) as a four-hinge deformation mechanism with a rigid viscoplastic material behavior. The analysis concluded that the dynamic response was dependent on the ratio of impact hammer mass to beam mass and magnitude of the initial geometric imperfection. The velocity sensitivity, observed by Calladine and English (1984) for constant input energy, was accounted through material strain rate effects and dynamic yield response. A later investigation by Tam and Calladine (1991), concluded the dissipation of kinetic energy could be attributed to two mechanisms, an initial compressive response (i.e. axial inertia) followed by flexural motion about the midspan plastic hinge. The analysis considered rigid plastic behaviour and an empirical expression was developed relating the ratio of initial kinetic energy to the compressive strain energy. The importance of impact mass to beam mass ratio on the dynamic response was also reported.

Based on the analysis of Type II structures, Su et al. (1995a, 1995b) developed a simplified mechanical model that accounted for large deformation, axial inertia, elastoplastic behaviour and material strain rate effects. The analysis considered a symmetric deformational response, Figure 5-11(a), with the axial force members interconnected at four elastoplastic hinges. The hinge mechanism accounted for the flexural mode response and lumped mass properties were assigned to these nodes. The investigations were in general agreement with the dual phase response described by Calladine and Tam (1991) but considered inertia effects as significant throughout the solution. Defining an elastic response allowed the determination of peak load estimates (Su et al., 1995a). The significance of viscoplastic material behaviour on the increased proportion of elastic strain energy, due to the dynamic yield stress dependence on rate sensitivity, was demonstrated (Su et al., 1995b).

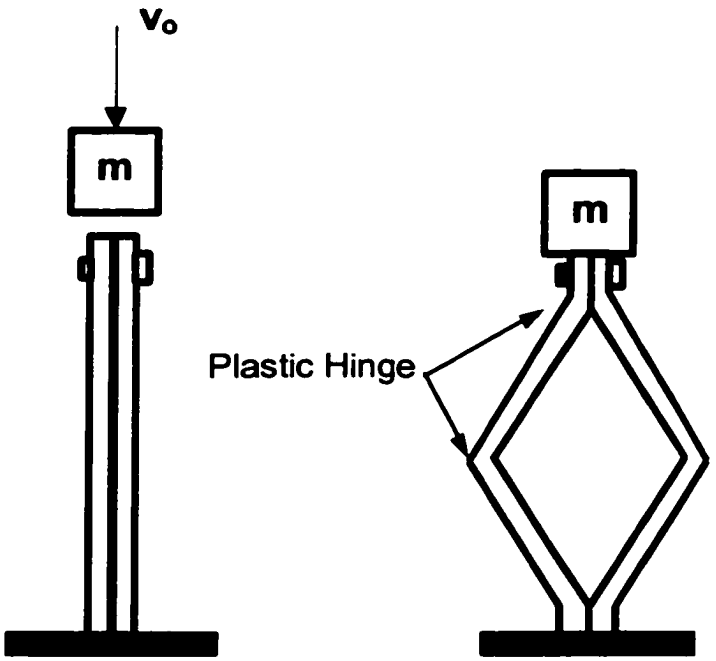

(a)

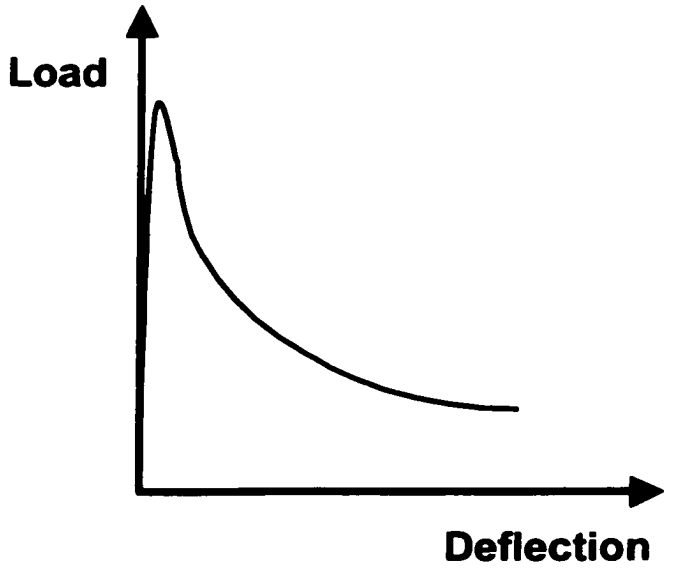

(b)

Figure 5-11. Investigations of Calladine and English (1984), (a) Schematic illustration of Type II Structure Loading Event and (b) Load-Deformation Response.

Karagiozova and Jones (1995a) conducted further parallel investigations with the Tam and Caladine (1991) study, as part of research program aimed at defining the fundamental parameters that govern the dynamic plastic buckling of structures. Similar to the analysis of Su et al. (1995a), a relatively simple mechanical model was developed, which is illustrated in Figure 5-12. A slender beam was characterised by two weightless rigid links of length (L) with an initial geometric imperfection (δ_o) and central lumped mass (m_l). The beam was impacted by a mass (M) with an initial velocity (v_o) and the transfer link was considered rigid with zero mass ($m_l = 0$). The axial (K_a) and flexural (K_f) response was defined by nonlinear, elastoplastic spring elements with strain rate effects defined by the Cowper-Symonds relationship. For a particular beam geometry, the model retains an equivalent static Euler buckling load and first natural frequency of elastic vibration such that the mass $m_l = 4m/\pi^2$, where m is the mass of the actual structure. An important point to consider is that the derived relationships were limited to small deflections where $\delta_o/L = \sin\theta \cong \theta$.

The investigation of Karagiozova and Jones (1995a) was consistent with the analyses of Tam and Calladine (1991) and Su et al. (1995a, 1995b) in terms of energy dissipation mechanisms (i.e. axial inertia, flexural response). The importance of considering elastic, viscoplastic material behaviour on the energy distribution (i.e. proportion of elastic and plastic compression or flexure) for rate dependent material was demonstrated. The numerical models were more accurate with respect to the experimental data for rate independent aluminum. The analysis showed the dynamic yield behaviour was a strong function of the impact velocity and mass ratio. The influence of increased geometric imperfections on decreasing the critical buckling energy was also demonstrated. Finally, the development of larger degree of freedom models required for investigating wave propagation effects and higher order modal response associated with higher impact velocities was recognized.

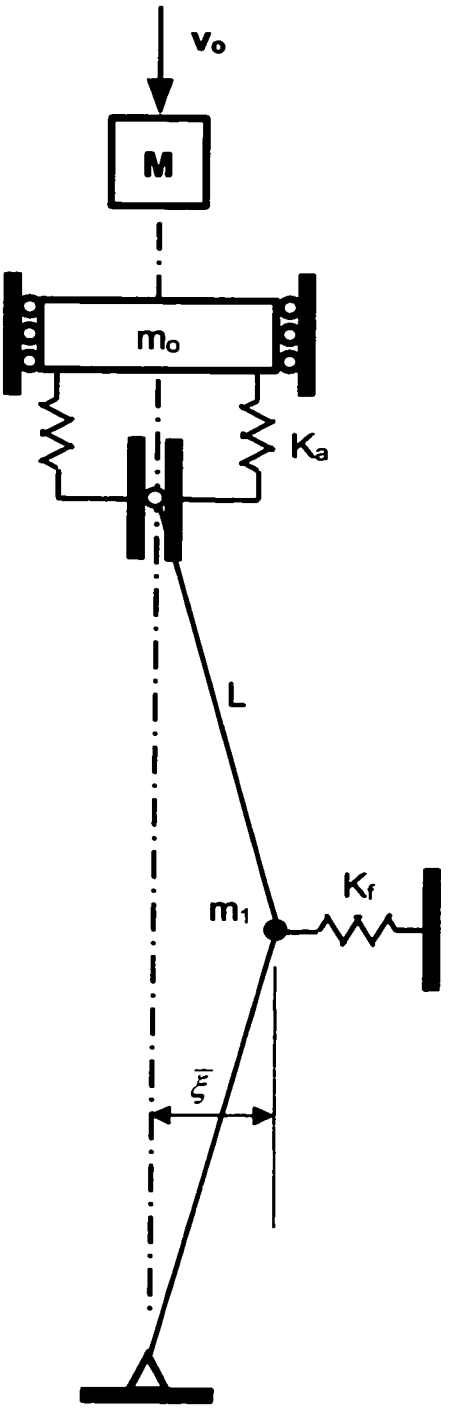

Figure 5-12. Idealised Mechanical Model (Karagiozova and Jones, 1995).

In a similar study, Karagiozova and Jones (1995b) considered a parametric variation of mass ratio, impact velocity, and rate independent, elastoplastic material properties. The effects of a dynamic yield stress were not considered. For mass ratios ($M/m_l < 25$), the analysis illustrated that the critical buckling energy required to initiate dynamic instability was significantly influenced by the strain hardening parameter (λ). The term (λ) was defined as the ratio of the plastic to elastic spring constant stiffness. The structural response was dominated by compression and the critical velocity required was greater than that for an elastic material, as shown in Figure 5-13(a). The discontinuity for the strain hardening parameter ($\lambda = 1.0$), which represents the fully elastic case, is characterised by instability of the nonlinear terms associated with the Mathieu solution. Conversely, for the higher mass ratios ($M/m_l > 50$), the structural response was predominantly flexural and the critical buckling energy for elastoplastic behaviour was lower due to the softening effect of the tangent modulus. The critical impact velocity was significantly influenced by a coupled increased geometric imperfection ($\bar{\xi}$) and decreased mass ratio (M/m_l) as shown in Figure 5-13(b). The term ($\bar{\xi}/h$) represents the geometric imperfection as a fraction of the beam depth (h). Furthermore, the elastoplastic response was more sensitive to initial imperfections ($\bar{\xi}$) than the elastic models.

In view of the quasi-bifurcation studies of Lee (1981), Karagiozova and Jones (1996) developed a multi-degree of freedom mechanical model. A lower bound analysis was conducted that considered the critical buckling energy as a function of impact mass and velocity. The investigations demonstrated that the proportion of compression energy absorbed significantly increased with decreasing magnitude of the geometric imperfection. For low kinetic energy events, quasi-static analysis could predict the onset of buckling but not the final deformed mode shape. The importance of considering higher degree of freedom systems in consideration of wave propagation effects on dynamic pulse buckling and determining the range of validity for quasi-static methods was also recognized.

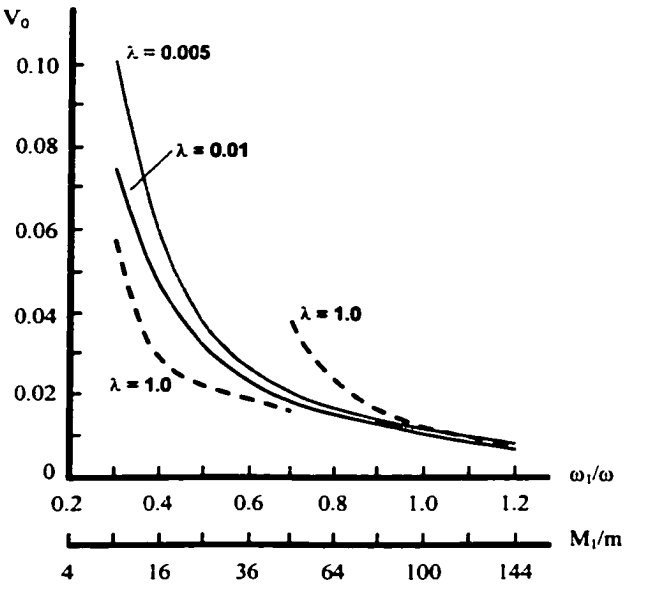

(a)

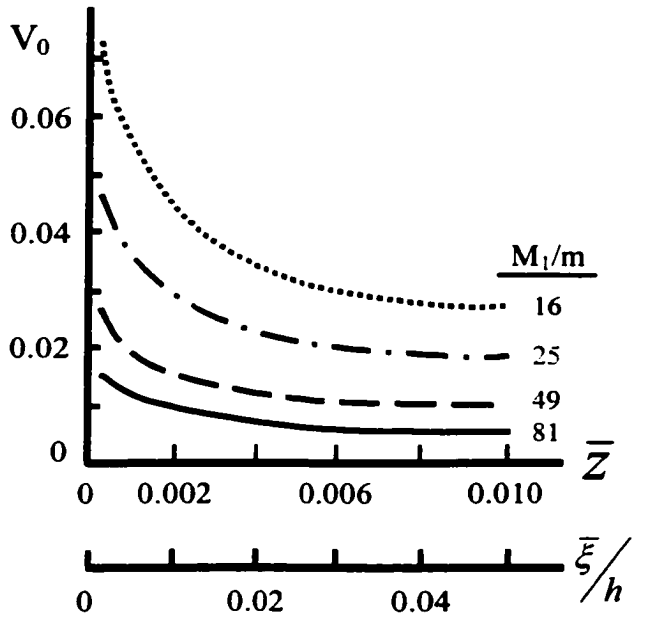

(b)

Figure 5-13. (a) Critical Impact Velocity (V_o) as a Function of the Mass Ratio (M/m_1) and Strain Hardening Parameter (λ), (b) Critical Impact Velocity as a Function of Geometric Imperfection $\left(\bar{\xi}\right)$ and Mass Ratio (Karagiozova and Jones, 1995b).

Karagiozova and Jones (1997) have also investigated the importance of considering dynamic yield surface and strain rate effects on the elastoplastic, buckling of a simple mechanical model (Figure 5-12). The dynamic peak force magnitude was dependent on the impact velocity and sensitive to large mass ratios at lower velocities. The analysis demonstrated that for the parameters investigated, the approximation of Perrone (1965) was adequate to define the dynamic elastic, viscoplastic response. The strain-rate sensitive models predicted higher critical impact velocities, which was primarily related to the dynamic yield surface. The model was best suited to low velocity impact events associated with a lower ordered modal response due to the limited degrees of freedom defined by the relatively simple mechanical model. From this perspective, note that a higher order modal response has been observed during dynamic buckling events with impact velocities on the order of 6m/s, as shown in Figure 5-6. This issue will be further addressed through experimental investigations (Chapter 6) and by finite element analysis (Chapter 7) conducted for the current thesis.

5.4.4 Modal Perturbation Analysis

For dynamic plastic buckling, perturbation analysis is effectively based on the same fundamental assumptions of the elastic "preferred" wavelength solution (Lindberg and Florence, 1987) as discussed in Chapter 2. Modal perturbation techniques are restricted to analysis of ideal structures, characterized by linear material constitutive relationships and relatively simple boundary and loading conditions. Beams subject to axial impact (Lindberg, 1965) or radial impulsive loading of shells (Pegg, 1992) are representative examples.

Consider the beam, illustrated in Figure 2-4, subject to an axial impulse that exceeds the material yield stress. Neglecting transverse shear and rotary inertia terms, the dynamic equation of motion is,

$$E_T I \frac{\partial^4 y}{\partial x^4} + P \frac{\partial^2}{\partial x^2}(y + y_o) + \rho A \frac{\partial^2 y}{\partial t^2} = 0. \qquad (5.11)$$

The expression is of the same form as stated in Equation (2.8) except that the elastic modulus (E) has been replaced by the tangent or strain hardening modulus (E_T). The axial force (P) is assumed uniform throughout the beam length.

The theory is based on defining a linear, constant tangent modulus with minimal effects of strain hardening. The dynamic buckling event is considered a perturbation of motion associated with the propagation of an axial stress wave. The beam is subject to a state of plastic flow with continuously increasing compressive strain. A transverse flexural response develops due to initial imperfections (e.g. geometry, stress pulse variation, velocity distribution).

Strain hardening is fundamental for flexural mode perturbations due to a stress differential across the beam depth. The assumption of a constant tangent modulus is required to define a linear moment-curvature relationship. Thus, for low strain hardening ratios (E_T/E), the axial load (P) can be considered constant across a defined cross-section. The compressive strain rate is assumed to dominate the flexural strain rate until buckling has been well developed and thus the effects of strain-rate reversal are neglected. Sustained axial flow is arrested on the return of the unloading elastic axial stress wave. Similar to elastic buckling analysis, position of the wave front was neglected, as supported by experimental observations of the buckled profile, and a state of uniform axial strain was assumed. Redefining the following nondimensional terms,

$$s_T^2 = \frac{\sigma}{E_T} \quad and \quad \tau_T = \frac{\sigma t}{r(E_T P)^{1/2}} \qquad (5.12)$$

Considering the axial thrust as $P = \sigma A$, then Equation (5.11) can be rewritten,

$$\frac{\partial^2 w}{\partial \tau_T^2} + \frac{\partial^4 w}{\partial \xi^4} + \frac{\partial^2}{\partial \xi^2}(w + w_o) = 0 \tag{5.13}$$

Similar to the elastic analysis (Figure 2-6), hyperbolic magnification functions are illustrated in Figure 5-14 for initial velocity and displacement perturbations. The "preferred" wave number, $\eta_p = 1/\sqrt{2}$, is shown for reference.

As shown by Lindberg and Florence (1987), the amplification function for unbounded growth ($\eta < 1$) of the buckle solution terms for initial velocity perturbations is,

$$G_v(\eta, \tau_T) = \frac{\tau_T}{p_n \tau_T} \sinh(p_n \tau_T), \tag{5.14}$$

and for initial displacement perturbations,

$$G_d(\eta, \tau_T) = \frac{1}{1-\eta^2}[\cosh(p_n \tau_T) - 1]. \tag{5.15}$$

The amplification function represents the ratio of the buckled bar or perturbed motion coefficients (velocity or displacement) to the initial Fourier coefficients. For $\eta > 1$, the solution would be defined by the circular or trigonometric form and $\eta = 1$ represents the critical Euler wave number (i.e. $\lambda_E = 2\pi r$). The solution of interest is the hyperbolic form represented by $\eta < 1$.

Perturbation analysis is a relatively simple method that can provide preliminary estimates on buckling threshold limits for axially loaded beams. As shown in Figure 5-14, the

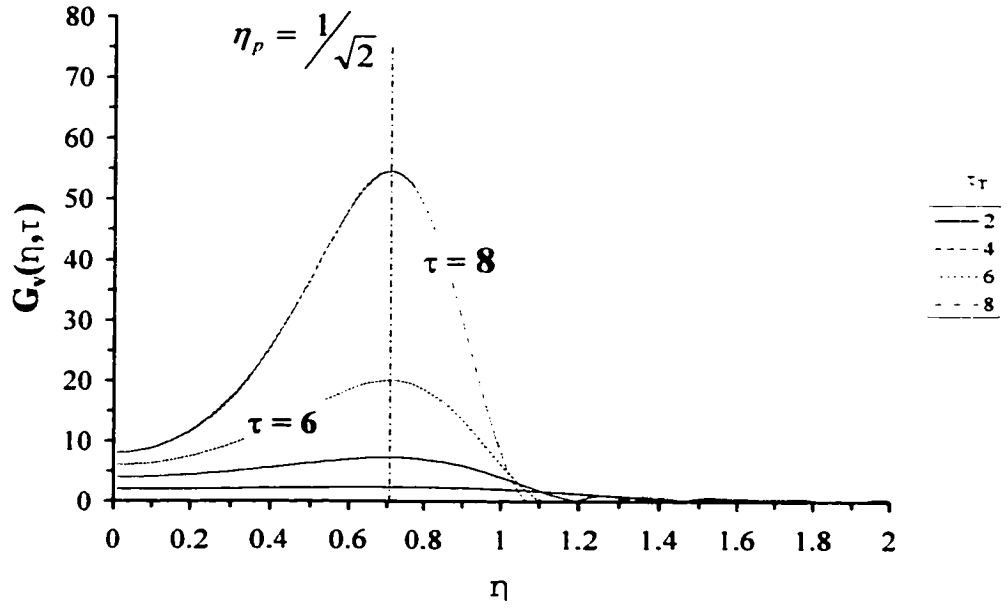

(a)

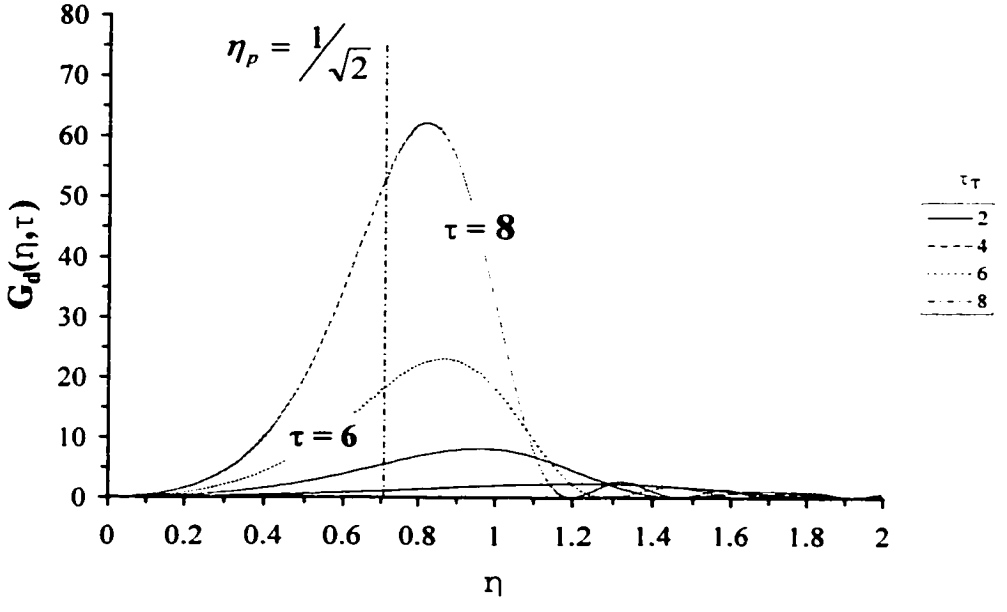

(b)

Figure 5-14. Amplification Function for (a) Initial Velocity Perturbations, and (b) Initial Geometric Imperfections. (Abrahamson and Goodier, 1966).

pulse buckling response is associated with a dominant mode that converges to a "preferred" mode with increasing nondimensional time. Analysis of pulse buckling events that consider complex structural configurations (e.g. geometry, boundary conditions), or impulse events with spatial and/or temporal variations (e.g. applied loads, velocity field) requires numerical solutions.

5.4.5 Numerical Modeling

Over the past three decades, the application of numerical methods to simulate the response of structures to impulsive loading events has flourished and the scope has covered a wide range of interest. A significant volume of literature has matured within the field of high-energy events that considers such factors as shock waves, thermal effects, kinetic energy or penetrating weapons. Analysis of these intense impulsive loads has been conducted on nuclear, aerospace, military and civilian structures. The works of Bulson (1994), Brebbia and Sánchez-Gálvez (1994) and Ammann et al. (1988) are referenced for further information. Numerical investigations have also been conducted for lower intensity events such as progressive buckling (Langseth et al., 1994; Belingardi and Vadori, 1993) and transverse loading (Yu and Jones, 1997; Nurick et al., 1994; Jones, 1989) events.

The present investigations are focused on pulse buckling events where factors such as plasticity, inertia, stress wave propagation, and higher order modal response are important parameters on the pulse buckling response of axially loaded beams. Two numerical procedures often employed for modelling the dynamic response of structures, which exhibit large deformations and strains, are the finite difference and finite element methods. Relatively few studies have considered the characteristic higher order, modal response (e.g. Lindberg and Florence, 1987; Gary, 1983; Karagiozova and Jones, 1996). These investigations, however, encompassed analytical, experimental and 'simplified'

mechanical modelling procedures. A limited number of studies have employed the finite difference method to model the pulse buckling response and the specific details will be discussed.

Discussed in Chapter 2, Ari-Gur et al. (1982, 1979, 1978) investigated the pulse buckling response of axially loaded beams by the finite difference method. The analysis was primarily concerned with the elastic response and defining an envelope for buckling initiation. Details of the stress–strain or modal response–time history (e.g. buckled profile development) were not presented. In addition, the analysis focused on the fundamental mode response despite the observed higher order buckled waveform (Figure 5-6). Hayashi and Sano (1972a, 1972b) also observed a higher order mode, elastic pulse buckling response and demonstrated excellent agreement between the finite difference models and experimental studies.

Sugiura et al. (1985) developed a finite difference model, which accounted for the effects of plasticity, strain-rate and observed higher order buckled profile. The dynamic instability of axially impacted columns, with simply supported boundary conditions, was investigated as a function of slenderness ratio. The Euler-Bernoulli beam theory and consideration of axial inertia effects was employed. The constitutive relationships were defined by linear elastic, perfectly plastic model and a viscoplastic theory presented by Perzyna (1963). The beam geometry was defined by a fundamental mode imperfection where one end was impacted by a mass with an initial velocity. Amplification of the half-sine wave imperfection was a significant feature of the global response, however, the growth of higher modes dominated the buckling response for later times. A dynamic instability criterion was defined, with respect to energy loss of the striker, and was dependent on the normalized striker mass, initial impact velocity and slenderness ratio. The modal response was dependent on the impact velocity and the ratio of the lateral to axial mode of vibration. The dynamic instability analysis, however, was limited to small

transverse deflections defining the axial-displacement and curvature-displacement relationships. For the parameters investigated, the analysis was in good agreement with the analytical and experimental works of Hayashi and Sano (1972a, 1972b).

Dynamic, plastic flow buckling is a complex interaction that presents a considerable challenge in developing comprehensive models. A number of factors must be considered, which can include the structural configuration (e.g. geometry, essential boundary conditions), constitutive relations (e.g. elastoplastic, dynamic yield, strain rate effects), impulse event (e.g. load intensity, spatial and/or temporal variation), and general response characteristics (e.g. modal response, stress wave propagation). The discussion presented in the current section highlights the paucity of numerical models developed to investigate plastic buckling response of beams subject to an axial impulse.

To the author's knowledge, a detailed parametric finite element investigation characterizing the complete modal response of axially loaded beams has not yet been conducted. The finite element method provides a rational basis for the model development and validation of a relatively simple model is critical for future analysis of more complex pulse buckling events. The investigations will consider an integrated approach that considers analytical methods and experimental studies. The elastic pulse buckling analysis presented in Chapter 3 and Chapter 4 has illustrated the importance of a coupled approach. For the dynamic plastic bucking response of a slender beam subject to an axial impulse, the study objectives to be addressed in the following chapters can be summarized as (i) to develop a comprehensive finite element model that accounts for the experimentally observed modal response, (ii) to assess the computed response in terms of analytical solutions (e.g. mode perturbation theory), (iii) to identify the dominant parameters that influences the pulse buckling response and (iv) to develop an appropriate dynamic pulse buckling criterion.

6.0 Experimental Program

The dynamic plastic response of impulsively loaded beams has been the subject of continued research for over 60 years. Early studies focused on characterizing plastic wave propagation and dynamic material behaviour. The majority of experimental investigations on the dynamic buckling response of a slender beam subject to axial impact have focused on lower velocity (e.g. progressive buckling) and higher velocity events (e.g. projectile impact). For moderate impact velocities, where wave propagation effects are important, experimental data on dynamic buckling response due to axial impact is limited.

For axial impact events with moderate velocities on the order of 5m/s to 10m/s, the experimental record is based on the studies conducted by Calladine and English (1984), and Tam and Calladine (1991). These investigations considered the dynamic response of a beam, with a predefined fundamental mode imperfection and buckling response, subject to axial impact. As discussed in Chapter 5, however, several analytical and experimental studies have shown that for intense impulsive loads the dynamic behaviour can be characterised by a higher mode response.

An experimental investigation on the dynamic plastic buckling of slender beams subject to axial impact is presented. Details on the experimental apparatus, procedure, study parameters and experimental data are discussed. The primary focus was the development of empirical relationships characterizing the dynamic plastic buckling response of a slender beam, subject to axial impact, with respect to a variation in the effective slenderness ratio and material properties. The experimental investigations would also provide the basis for validating parallel numerical analyses by the finite element method.

6.1 Experimental Investigations

6.1.1 Experimental Apparatus and Procedure

A summary description of the experimental apparatus and procedure will be presented. A more comprehensive discussion detailing the experimental investigations, including the apparatus, procedure and data, is presented in Appendix B.

The main support frame and test apparatus is illustrated in Figure 6-1 with a schematic illustration shown in Figure 6-2. The axial load was delivered by a 10kg, free-fall impact hammer. An aluminum tube housed the impact hammer and two interior aluminum alignment discs guided the hammer during free-fall (Figure 6-2). The drop tower tube was bolted to the upper crosshead of a static test frame (200 metric tonne capacity) and suspended vertically (Figure 6-1).

The boundary condition for all tests was a fixed restraint ($x = 0$) and slide bearing support ($x = L_u$) at the impact interface. The lower fixed boundary condition ($x = 0$) was developed through a stiffened vice-grip platen connected to a steel base plate, which was bolted into the static test frame. The test beam was in direct contact with the steel base plate and held rigidly in place, by applying a constant torque of 50N-m, through a support depth of 75mm. The upper support was designed as a lightweight, "frictionless" slide bearing and was 25mm in depth, which was fabricated from polyvinyl chloride (PVC). The bearing surface prevented transverse out of plane displacements and rotations but allowed axial translation. Prior to each test, the bearing surface of the PVC discs and the bar length held within the fixed support was sprayed with a commercial *Teflon* lubricant to reduce the axial frictional resistance. Transverse horizontal rods braced the drop tower against the static test frame in order to stabilize the upper support during free-fall and to resist the generation of any lateral forces during impact (Figure 6-1).

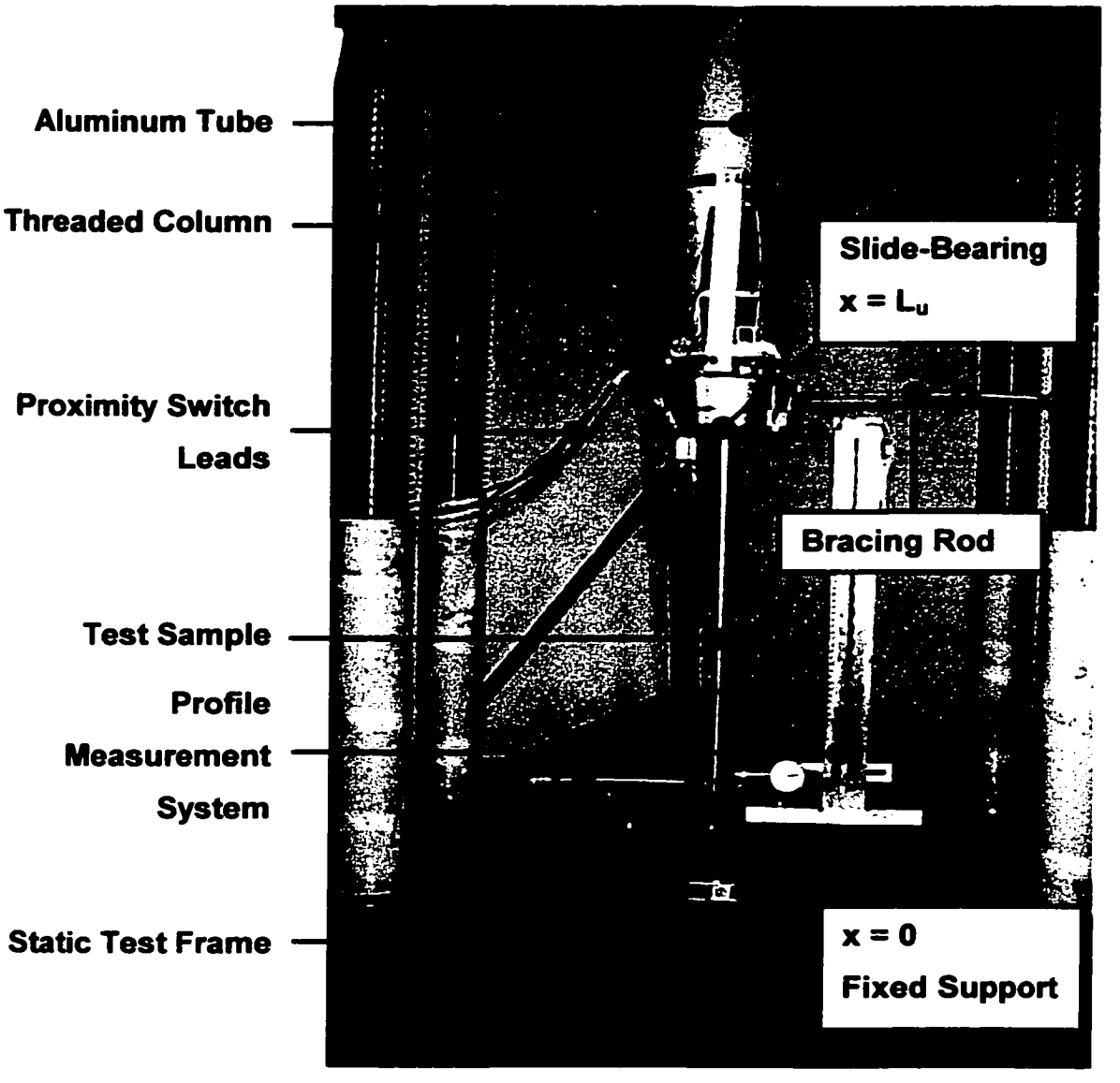

Figure 6-1. Test Frame for Dynamic Impact Experiments.

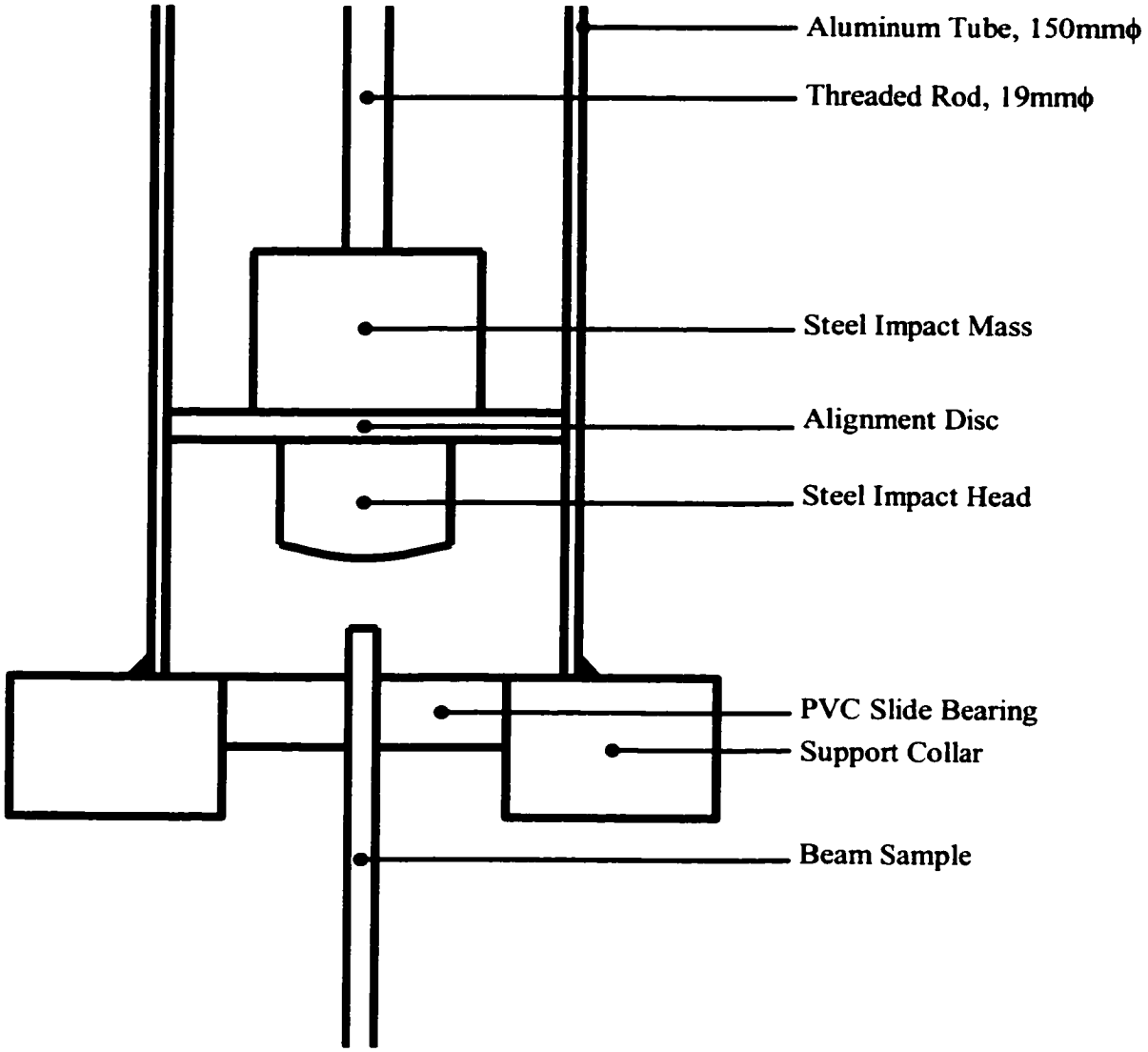

Figure 6-2. Upper Slide-Bearing Restraint and Impact Mass Assembly.

For all tests, the longitudinal axis of the hammer and the test sample was aligned to be collinear. The initial global, geometric imperfection was measured at 25mm stations along the longitudinal axis of the beam by a mechanical, spring-loaded dial gauge as shown in Figure 6-1.

A wire pulley system was used to raise the impact hammer through the drop tower. The nominal impact velocity was 6.2m/s, which was measured by three capacitive proximity switches (Omron Model E2K-F10MC1). As the lower alignment disc passed the lead proximity switch, the output signal served as a trigger pulse for the data acquisition system. The data acquisition board was a BE490™ Series Advanced Transient Recorder Plug-in (ATP) card by Bakker Electronics Dongen bv. The board was installed on a 486-33MHz personal computer and the sampling rate was 100kHz per channel.

After the impact test was completed, the mass was secured in a neutral position. The post-test buckled geometry was also profiled at 25mm stations with the locations of minima or maxima noted. Data records for all impact tests conducted during the experimental program are presented in Appendix C. The samples were tested in "as is" condition with the only constraint that the mill stamp faced the same direction for all impact events.

Epoxy bonded, foil strain gauges were also employed, to measure axial and flexural deformations. The gauges were attached in symmetric pairs, on opposite beam faces, at several stations along the beam length. The objective was to measure the axial and flexural strain response on or near the peak buckle crest to compare with the midspan response. The data would allow one to assess the dynamic buckling criterion proposed by Ari-Gur et al. (1982). Significant difficulties were encountered during the test program, however, to maintain working foil gauges. Due to the intense lateral stress wave and buckling motion, the strain gauges would fail at the solder joint of the coupled positive and neutral leads and/or on the epoxy-bar interface. This issue is further discussed in Appendix B.

For elastic pulse buckling events, Lindberg and Florence (1987) stated the lateral velocity for the peak buckle crest was on the order of 23m/s. Finite element analysis, presented in Chapter 7, computed a peak transverse velocity on the order of 37m/s.

6.1.2 Experimental Study Parameters

The 10kg free fall impact hammer applied an axial impulsive load to aluminum (6061-T6) and cold rolled steel beams (CR1018) with a fixed–slide bearing boundary condition. Two rectangular cross-sections (50.8mm×3.175mm and 50.8mm×4.7625mm) with effective slenderness ratios ranging from 75 to 300 were investigated. The experimental study parameters are summarized in Tables 6-1 through 6-3.

The beam depth (d), impact mass (m), unsupported beam length (L_u), effective slenderness ratio (L_e/r), mean impact velocity (V_I), mean nondimensional imperfection amplitude (β) and number of tests conducted are tabulated. A range of slenderness ratios, $75 \leq L_e/r \leq 300$, were investigated with a total of 115 impact tests were conducted. The average peak initial imperfection for all test series was bounded by the interval $0.0017 \leq \beta \leq 0.0029$. The nondimensional imperfection amplitude ($\beta = A_o/L_u$) is defined by the ratio of the imperfection amplitude (A_o) and unsupported column length (L_u). The initial imperfections were slightly higher than typical engineering magnitudes, $0.0001 \leq \beta \leq 0.001$, (Lindberg and Florence, 1987) but less than those considered by Ari-Gur et al. (1982), $0.005 \leq \beta \leq 0.02$.

Table 6-1. Test Parameters for *Series AI - 6061-T6* Aluminum (*d = 3.175mm*).

Series	L_u (mm)	L_e/r	Mean V_I (m/s)	$\beta = A_o/L_u$	Number of Tests
AIa	137	75	6.20	0.0029	6
AIb	183	100	6.20	0.0023	5
AIc	275	150	6.19	0.0020	10
AId	367	200	6.14	0.0019	5
AIe	458	250	6.18	0.0021	5
AIf	550	300	6.28	0.0024	10

Table 6-2. Test Parameters for *Series AII - 6061-T6* Aluminum (*d = 4.7625mm*).

Series	L_u (mm)	L_e/r	Mean V_I (m/s)	$\beta = A_o/L_u$	Number of Tests
AIIa	206	75	6.28	0.0019	3
AIIb	275	100	6.19	0.0019	10
AIIc	412	150	6.20	0.0019	5
AIId	550	200	6.24	0.0020	9
AIIe	687	250	6.14	0.0020	4

Table 6-3. Test Parameters for *Series SI* - Cold Rolled *1018* Steel (*d = 3.175mm*).

Series	L_u (mm)	L_e/r	Mean V_I (m/s)	$\beta = A_o/L_u$	Number of Tests
SIa	137	75	6.22	0.0027	5
SIb	183	100	6.22	0.0017	6
SIc	275	150	6.20	0.0020	9
SId	367	200	6.14	0.0021	6
SIe	458	250	6.31	0.0023	5
SIf	550	300	6.22	0.0025	12

6.2 Analysis of Experimental Data

6.2.1 Importance of the Applied Boundary Condition

As described in Appendix B, considerable effort was expended during the preliminary stages of the experimental program to achieve consistent and repeatable buckled mode profiles. Although the majority of the impact tests were considered successful (94 out of 115), some results were discarded, which was primarily due to problems encountered with the upper slide-bearing restraint. This issue can be further addressed through direct example from experimental observations.

Figure 6-3 illustrates the measured initial and final geometry profiles for two separate impact tests (*AId1* and *AId4*). For comparison, the buckled profiles for tests *AId1* through *AId5* are also illustrated in Figure 6-4. Although the same test procedure, impact event and global imperfection magnitude ($\beta \approx 0.0002$) was considered, the relative post-test buckled profiles were markedly different. The typical pulse buckling response (represented by test *AId4*) was characterized by the development of a peak transverse buckle near the lower fixed support. The development of a peak buckle at the upper support ($x = L_u$), for test *AId1*, was associated with a loss of integrity in the upper restraint. For impacts events with buckled response similar to test *AId1*, this was attributed to the observed partial ejection of the bearing disc (Figure 6-2) from the support collar. Consequently, the upper support was not representative of the intended boundary condition and thus the data was not analyzed.

In addition, for the higher slenderness ratios, acceptable impact events were difficult to achieve where data for *Series AIIe* and *AIIf* were rejected. A complete data record, of the measured buckled profiles for all impact tests, is presented in Appendix C.

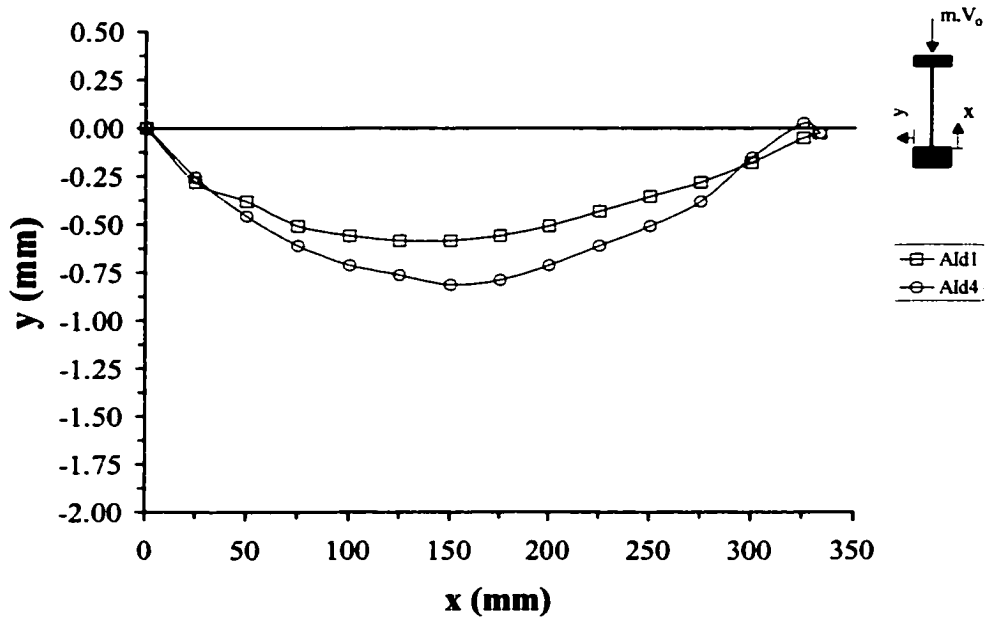

(a)

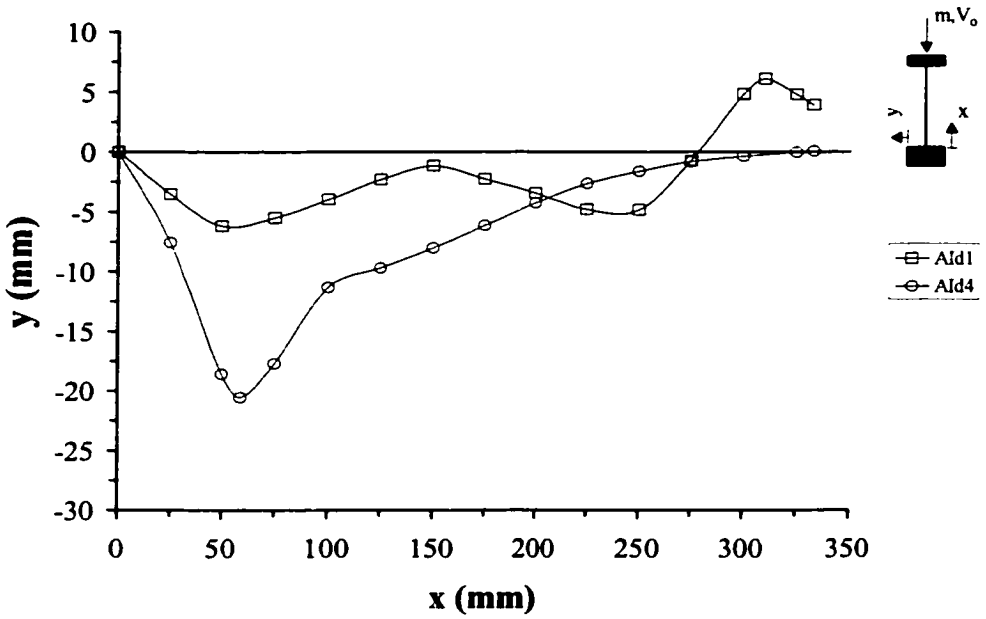

(b)

Figure 6-3. (a) Initial and (b) Deformed Buckled Geometry Profiles for Impact Tests *AId1* and *AId4*.

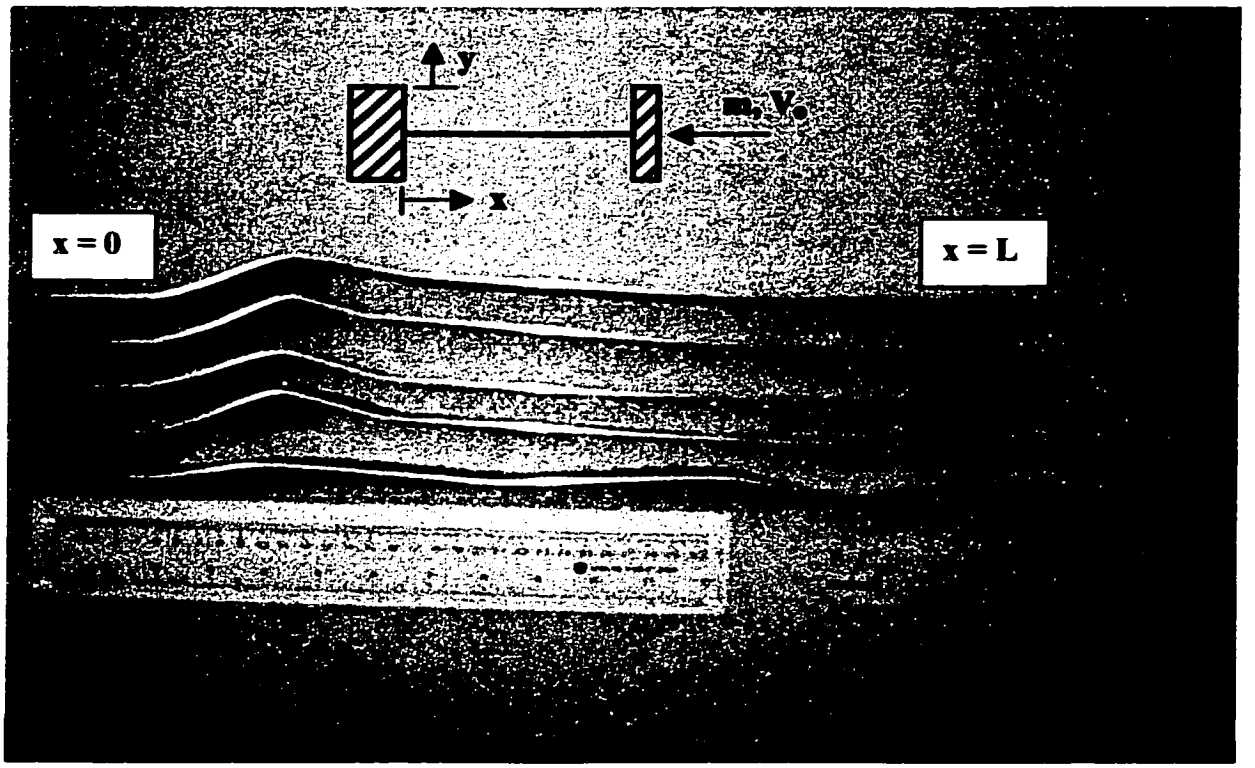

Figure 6-4. Deformed Buckled Profiles for Tests *AId4* through *AId5*.

Ari-Gur et al. (1982,1978) also observed a similar mode transition toward the impact interface but the contributing mechanism was not addressed. Finite element analysis, presented in Chapter 7, further demonstrates the importance of modeling the actual, applied boundary condition (i.e. the full 75mm depth of the fixed lower support at $x = 0$) in order to accurately predict the buckled response.

6.2.2 General Response Characteristics

Representative buckled profiles for the test series *AI*, *AII* and *SI* are illustrated in Figures 6-5 through 6-7, respectively. Rotation of the impacted beams about the *75mm* lower fixed restraint ($x = 0$) is evident. The characteristic response was the development of a

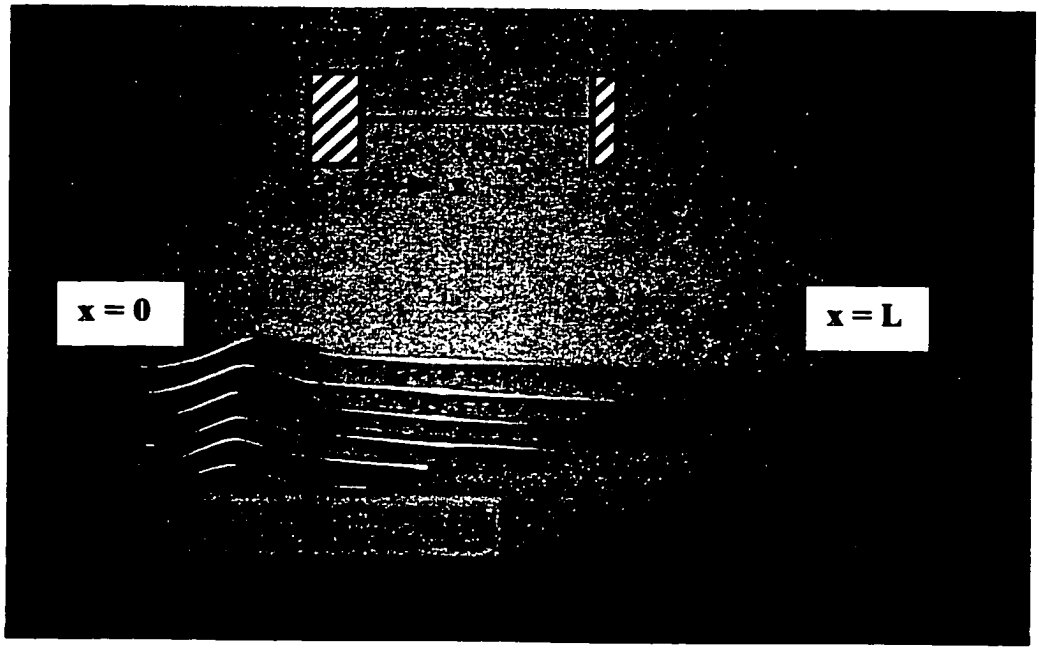

Figure 6-5. Representative Buckled Profiles for Series *AI* – 6061-T6 Aluminum.

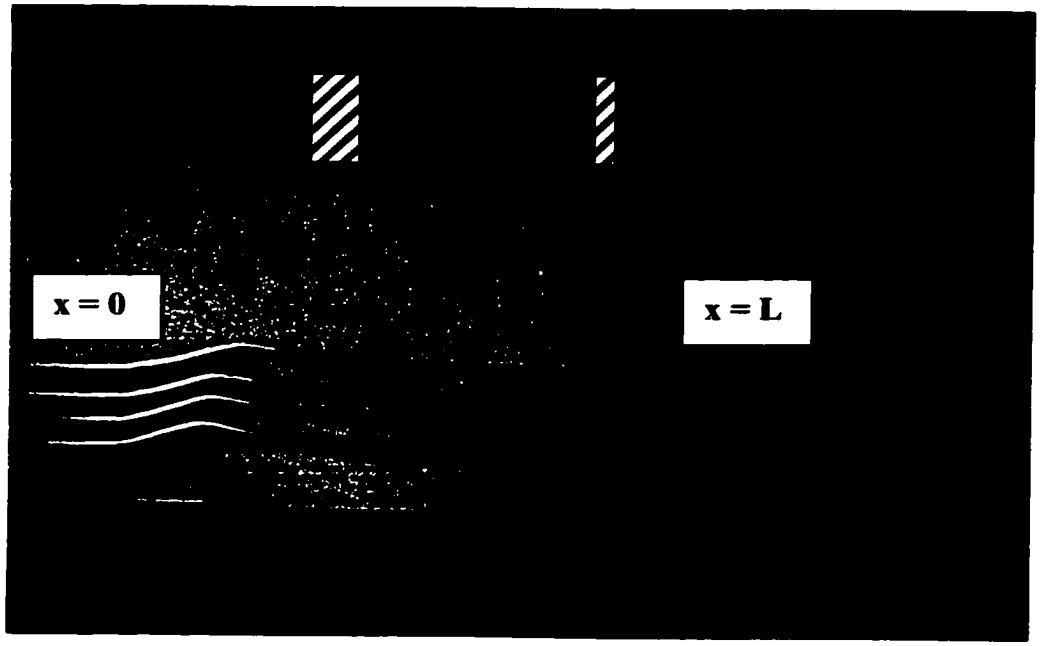

Figure 6-6. Representative Buckled Profiles for Series *AII* – 6061-T6 Aluminum.

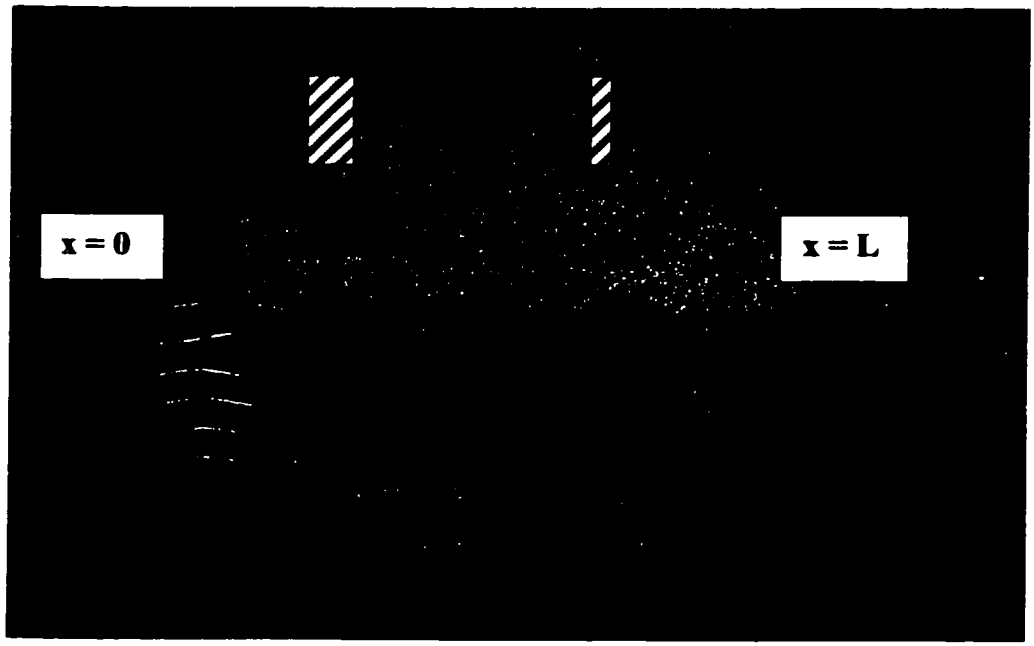

Figure 6-7. Representative Buckled Profiles for Series *SI* - CR 1018 Steel.

peak buckle crest adjacent to the fixed restraint. In general, the peak buckle location tended to shift away from the fixed restraint ($x = 0$) with increasing effective slenderness ratio (L_e/r). A summary of the mean response characteristics for the deformed buckled geometry of the analyzed experimental data record is listed in Table 6-4. Note that the number of tests and mean impact velocity differ from the raw data (Table 6-1, 6-2 and 6-3), since several impact events were rejected due to problems associated with the upper restraint boundary condition.

6.2.3 Normalized Response Parameter

The conceptual basis for analyzing the experimental data is illustrated schematically in Figure 6-8. On impact of the free-fall hammer with the beam, an elastic stress wave propagates from the upper restraint ($x = L_u$) toward the fixed boundary ($x = 0$). For

Table 6-4. Summary of Mean Characteristics for Analyzed Experimental Impact Events.

Test Series	Number of Tests	Mean Impact Velocity (m/s)	Mean Longitudinal Position of Peak Buckle (mm)	Mean Transverse Deflection of Peak Buckle (mm)
AIa	6	6.20	51.3	14.1
AIb	5	6.20	57.8	19.4
AIc	7	6.24	60.0	21.3
AId	4	6.14	59.5	18.3
AIe	4	6.19	68.8	22.0
AIf	7	6.22	71.9	20.8
SIa	5	6.22	54.2	10.8
SIb	6	6.22	52.5	12.7
SIc	7	6.24	63.7	8.0
SId	5	6.14	130.0	7.3
SIe	5	6.31	92.6	5.4
SIf	8	6.18	125.6	5.0
AIIa	3	6.28	75.0	17.6
AIIb	9	6.21	80.4	18.0
AIIc	3	6.21	84.0	17.6
AIId	8	6.23	97.5	17.0
AIIe	2	6.15	102.5	11.6

modeling purposes, the beam is considered to be in a state of uniaxial stress. On successive interaction with the fixed support, the elastic stress wave is reflected and the axial stress state exceeds yield, whereby a plastic axial stress wave is generated that travels from the fixed support toward the upper slide bearing. The elastic and plastic stress waves interact with the fixed boundary and geometric imperfections through the development of perturbations in the transverse motion. The buckling event is "terminated" through dissipation of kinetic energy through plastic work and flexural stiffening due to the elastic unloading stress wave, where the tangent modulus is typically two orders of magnitude less than the elastic modulus.

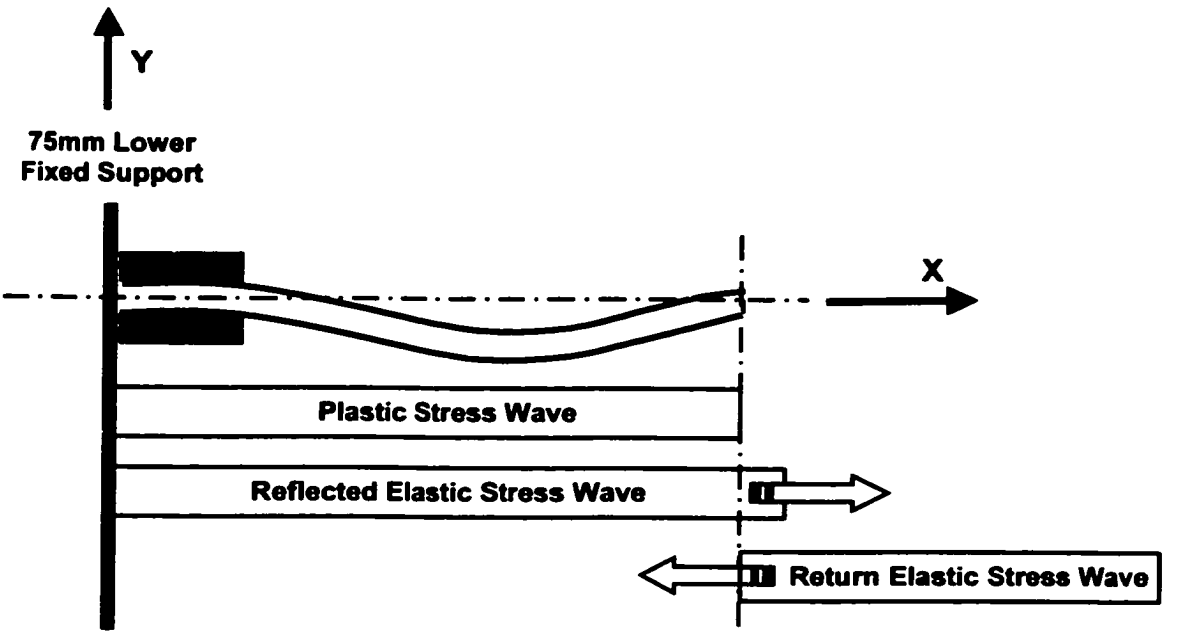

Figure 6-8. Conceptual basis for analysis of the experimental data.

The experimental data was analyzed to develop an empirical relationship that could characterize the main parameters influencing the dynamic buckling response. For the single defined impact event (10kg mass at a nominal contact velocity of 6m/s) these parameters included slenderness ratio (related to impact mass/beam mass ratio), inertia, mechanical rigidity, natural frequency and material behavior.

Sugiura et al. (1985) concluded that the mode of lateral displacement was strongly dependent on the relationship between the natural period of vibration for the lateral and axial modes. A higher order buckled response would develop when the natural period of the first-order lateral mode was longer than the first-order axial mode (i.e. lower natural frequency). On this basis, the present experimental data was assessed. A summary of the inertia, modal and mechanical rigidity properties are presented in Table 6-5.

The flexural mode parameter was three orders of magnitude lower than the axial response mode parameter. As will be shown in the present investigations, the measured buckling response is consistent with the conclusions stated by Sugiura et al. (1985). Normalized magnitudes, relative to test Series AI, are also presented in Table 6-5, where the terms were constant throughout the range of slenderness ratios (L_e/r) investigated.

Table 6-5. Comparative Assessment of Relative Inertia, Modal and Rigidity Parameters for the Test Series *AI*, *AII* and *SI*.

Parameter	Expression	Units	Series			Relative to AI	
			AI	AII	SI	AII	SI
Inertia	ρA	kg/m	0.44	0.65	1.16	1.50	2.67
Axial Mode	$\frac{c_e}{2\pi L_u}$	Hz	1500 – 5900	1200 – 3900	1500 – 6100	0.67	1.04
Flexural Mode	$\frac{r c_p}{2\pi L_u^2}$	Hz	2.44 – 39.3	2.34 – 26.1	2.54 – 41.0	0.67	1.04
Axial Rigidity	EA	MN	11.1	16.7	32.3	1.50	2.90
Flexural Rigidity	EI	Nm^2	9.35	31.6	27.1	3.38	2.90

A normalized response parameter $(\overline{N})$ was defined as,

$$\overline{N} = \frac{k_f \omega_a^2}{k_a \omega_f^2} = \left(\frac{c_e}{c_p}\right)^2 \frac{3L_u^5}{\bar{x}^2 (L_u - \bar{x})^3} \tag{6.1}$$

where

$$\omega_a = \sqrt{\frac{EA}{\bar{m}L_u^2}} = \frac{c_e}{L_u} \qquad \omega_f = \sqrt{\frac{EI}{\bar{m}L_u^4}} = \frac{rc_p}{L_u^2}$$
$$k_a = \frac{E_T A}{\bar{x}} \qquad k_f = \frac{3E_T I L_u^3}{\bar{x}^3 (L_u - \bar{x})^3} \tag{6.2}$$

represents the global axial (ω_a) and flexural (ω_f) frequency response parameters, and the local axial (k_a) and local flexural (k_f) stiffness characteristics, L_u is the unsupported beam length, $\bar{x}$ is the axial coordinate of the peak buckle crest measured from the lower fixed support ($x = 0$), E is the elastic modulus and E_T is the tangent modulus. The flexural stiffness is based on assuming a fixed–fixed beam restraint in consideration of the lower fixed boundary support ($x = 0$) and the relative magnitude of the tangent modulus to the elastic modulus (Figure 6-8).

The primary assumptions for the normalized response parameter (Equation 6.1) are that the propagating elastic axial stress wave dominates the axial frequency response and the effects of plasticity govern the local mechanical response (i.e. peak buckle growth) and flexural mode behaviour.

6.2.4 Peak Buckle Displacement Response Analysis

The peak buckle response was analyzed in terms of the axial coordinate $(\bar{x})$ and transverse deflection $(\bar{y})$. The data is presented as a function of the effective slenderness ratio (L_e/r) in Figures 6-9 and 6-10 for the axial and transverse response, respectively.

A least squares analysis was conducted on the mean response for each slenderness ratio investigated. For the limited data set, quantitative statistics of the least squares analysis is

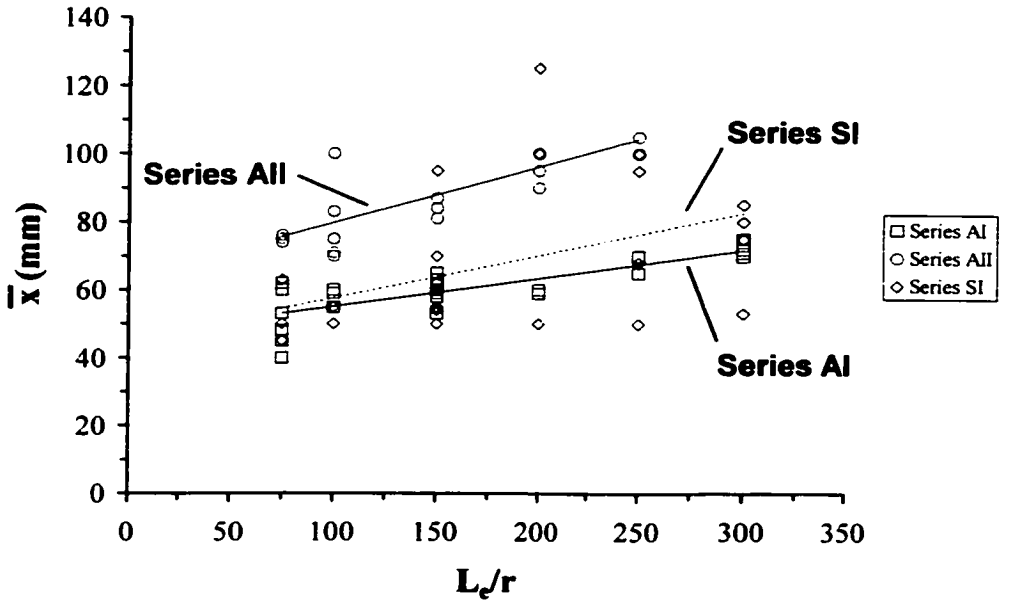

Figure 6-9. Axial Coordinate $(\bar{x})$ of the Peak Buckle Crest as a Function of the Effective Slenderness Ratio (L_e/r).

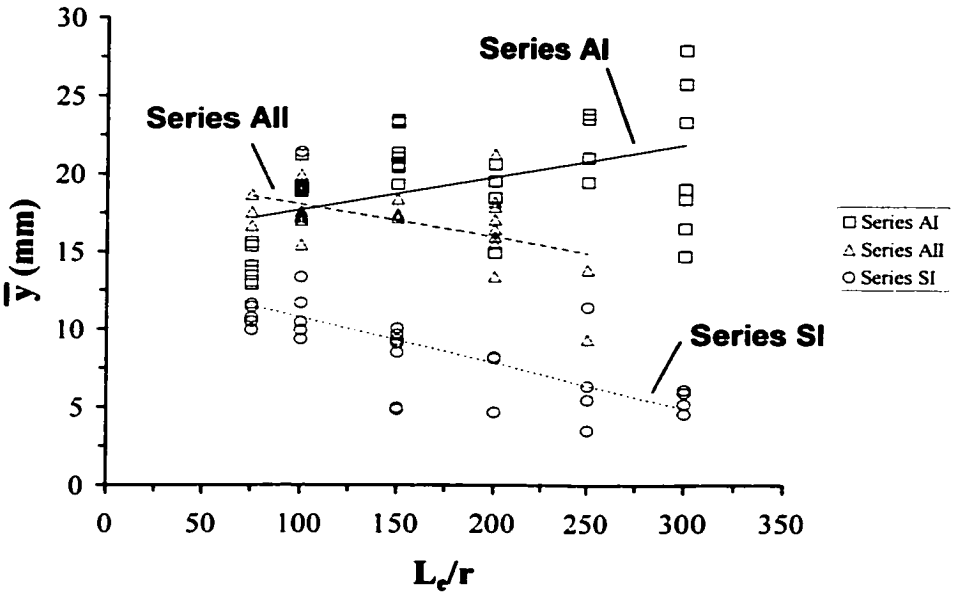

Figure 6-10. Transverse Deflection $(\bar{y})$ of the Peak Buckle Crest as a Function of the Effective Slenderness Ratio (L_e/r).

relatively unimportant, and the curve fit highlights general observed trends. The longitudinal position of the peak buckle tended to shift away from the lower fixed support with increasing slenderness ratio (L_e/r). This would be consistent with the conceptual basis presented in Section 6.2.3. The transverse peak buckle amplitude response was relatively more complex. The post-test midspan deflection was on the same order of magnitude as the initial profile, whereas the peak buckle amplitude was 20-40 times the initial imperfection, depending on the slenderness ratio and test series considered.

For the longitudinal position of the peak buckle crest, the mean normalized axial response $(\overline{N}\,\overline{x})$ is illustrated in Figure 6-11. The axial response exhibited a proportional increase with the effective slenderness ratio and the analysis suggests that in addition to the normalized parameter $(\overline{N})$ inertia effects are important, which is consistent with the conclusions presented by Su et al. (1995a,b) and Karagiozova and Jones (1995a). The functional dependence of the axial response with increasing slenderness ratio was also indirectly supported by the investigations of Ari-Gur et al. (1982), which defined an elastic dynamic buckling criterion on the basis of axial strain.

The mean normalized transverse response of the peak buckle crest $(\overline{N}\,\overline{y})$ is presented in Figure 6-12. The importance of local stiffness characteristics and natural frequency response parameters is exhibited. Convergence of the normalized transverse response at lower slenderness ratios, for all test series, further illustrates this relationship and indicates the relative influence of the imposed boundary conditions. The influence of flexural rigidity and dynamic yield behaviour on the buckling response was also observed, particularly for higher slenderness ratios. Although, the absolute magnitudes are presented, for the normalized response data, shown in Figure 6-11 and Figure 6-12, the relative comparison of the response parameters $(\overline{N}\,\overline{x}, \overline{N}\,\overline{y})$ between the respective datasets (*AI*, *AII* and *SI*), is the significant characteristic to be recognized.

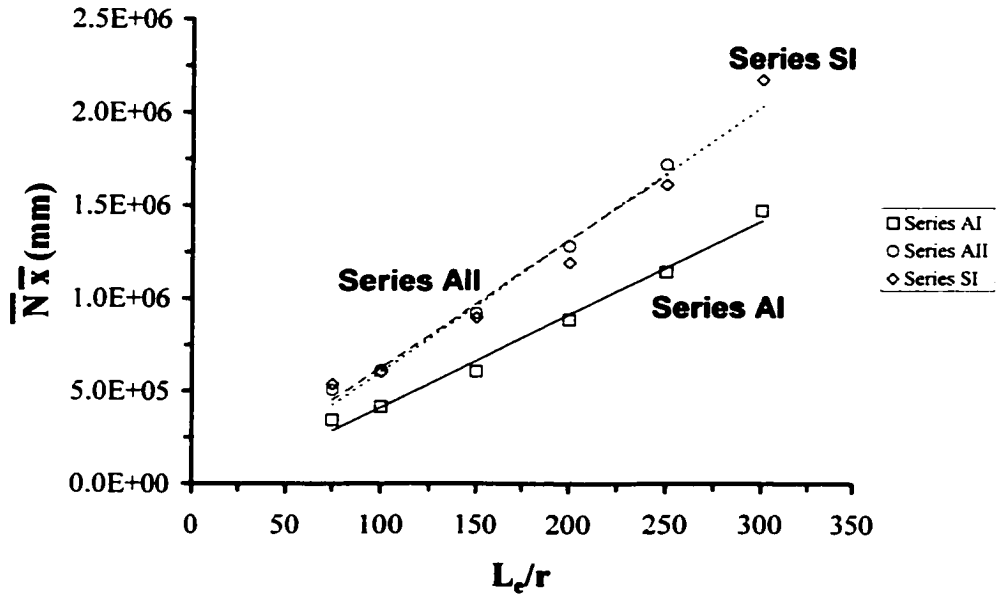

Figure 6-11. Normalized Mean Axial Response ($\overline{N}\,\overline{x}$) of the Peak Buckle Crest as a Function of the Effective Slenderness Ratio (L_e/r).

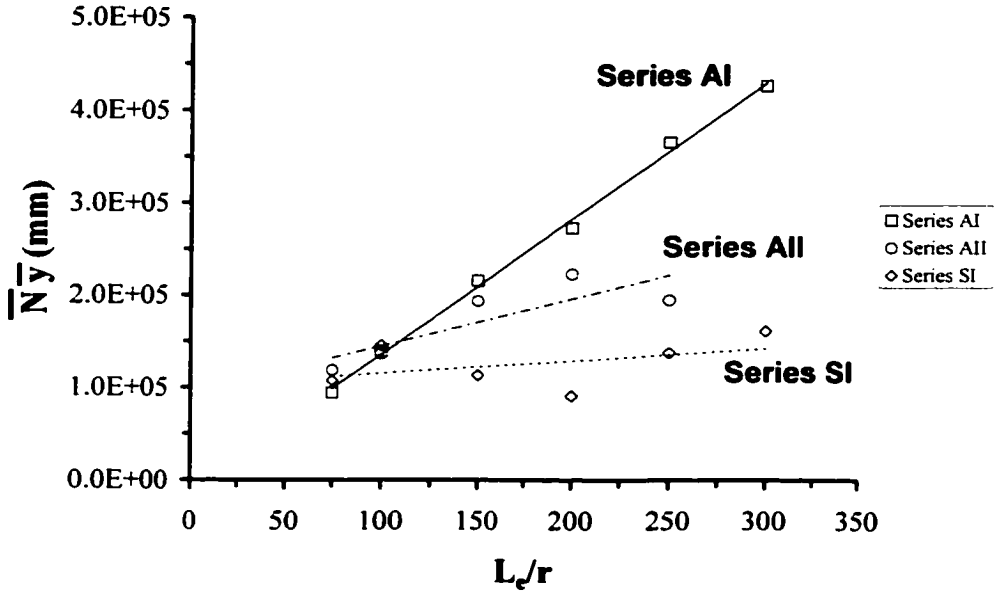

Figure 6-12. Normalized Mean Transverse Response ($\overline{N}\,\overline{y}$) of the Peak Buckle Crest as a Function of the Effective Slenderness Ratio (L_e/r).

As discussed in Chapter 5, for strain rates on the order of 10^3 /s, the flow stress of mild steel exhibits an increase by a factor of approximately three over the static values. Jones (1989) and Chang et al. (1989) have discussed the importance of considering rate effects on the dynamic stress-strain response of mild steel. In contrast, the literature is not as conclusive on the strain rate sensitivity for 6061-T6 aluminum. For example, Maiden and Green (1966), and Lindholm and Yeakley (1968) did not observe strain rate dependence at strain rates up to 10^3 /s. Conversely, Ng et al. (1979) and Hoge (1966) concluded that the material response exhibited dependence on strain rates greater than 10 /s. Hauser (1966) demonstrated that for work hardened specimens, a dependence on strain rate was observed particularly for strain rates greater than 10^3 /s but significantly less than mild steel. For the present investigations, the local strain rates for the peak buckle were on the order of 10^2 /s.

Dynamic mechanical properties can influence the initial buckling response (e.g. flow stress, stress-strain characteristics to yield), the development of the peak buckle crest through plastic deformation (e.g. tangent modulus, strain-rate sensitivity) and the subsequent elastic unloading process. During the impact event, sustained axial compression and transverse buckle growth would continue until unloading by the elastic stress wave has occurred. The elastic unloading corresponds to a change in the "effective stiffness", since for most metals the tangent modulus is approximately two orders of magnitude lower than the elastic modulus. As illustrated in Figure 6-12, this effect was exhibited by the limited transverse response of test series SI (mild steel) in comparison with series AII (6061-T6 aluminum), which had a greater flexural rigidity (Table 6-5) with comparable static yield strength and tangent modulus.

Karagiozova and Jones (1997, 1995b), and Su et al. (1995a,b) demonstrated that rate-sensitive behaviour increases the peak load and stored elastic compression energy, and decreases buckle amplitudes. The peak dynamic impact load for rate sensitive behaviour

was influenced by the impact velocity and large impact mass to beam mass ratios. Although, the compression phase was primarily equated to inertia and the flexural response to rate-sensitive behaviour, Su et al. (1995b) states that inertia was a dominant factor throughout the deformation process. In addition, "... the combined effects of strain-rate and inertia make the peak load much higher and the final displacement much smaller" (Su et al., 1995b). These factors are consistent with the experimental observations on the normalized transverse response, for the cold rolled steel test series SI, as shown in Figure 6-12.

6.2.5 Wavelength Analysis

In addition to characterization of the peak buckle response, wavelength analyses were also conducted. Illustrative examples of the half-wavelength response are presented in Figure 6-13 for impact tests *AIa4*, *AIId1* and *SIe1*. The parameter $\bar{x}$ defines the peak buckle half-wavelength measured from the lower fixed support (x = 0) to the crest, L_1 is the half-wavelength for the trailing edge from the peak buckle crest, L_2 is the half-wavelength for any observed intermediate modes and L_B is the half-wavelength adjacent to the upper slide bearing support ($x = L_u$). For the impact test *AIa4*, the limited beam length precludes measurement of wavelengths L_2 and L_B.

Simplified theoretical expressions were employed to predict the peak buckle wavelength in comparison with the observed buckled response. The approach was based on three strategies that included the quasi-static analysis of Bell (1988), perturbation theory of Abrahamson and Goodier (1966) and bound limit analysis based on stress wave propagation (Figure 6-8).

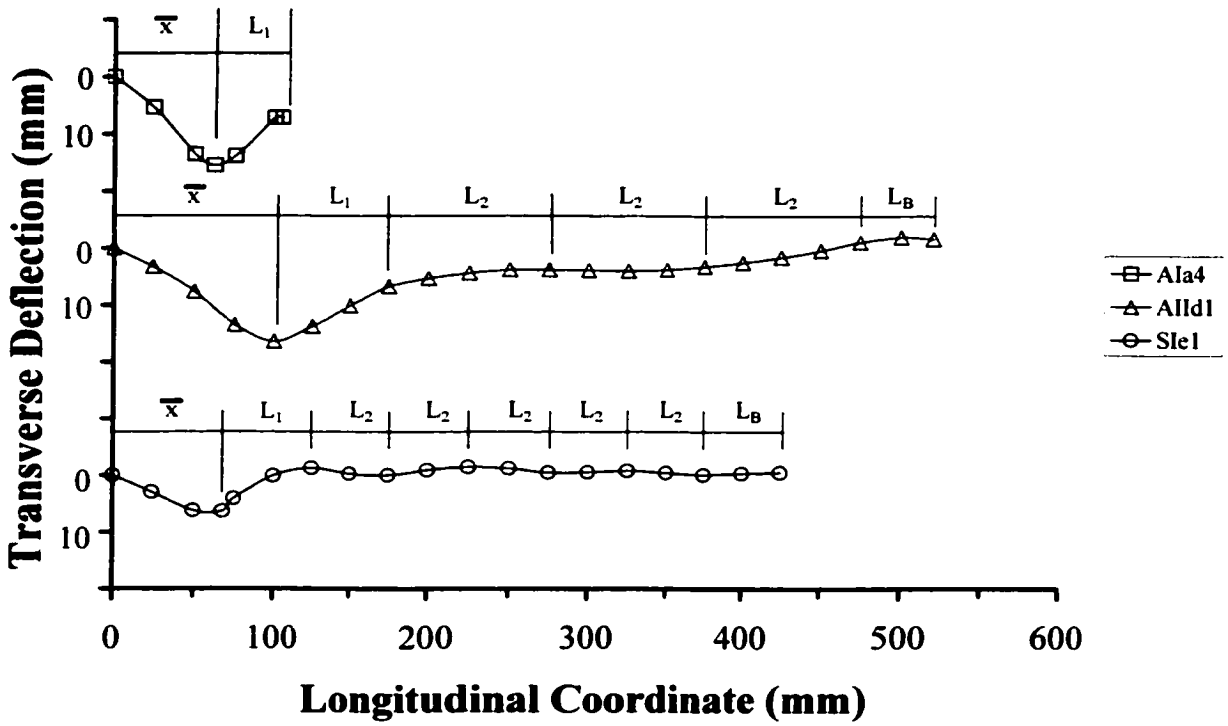

Figure 6-13. Representative Examples of Half-Wavelength Response Analysis.

Bell (1988) derived an expression for the critical buckled wavelength (L_{cr}) based on the Euler-Engesser expression for the quasi-static nonlinear buckling of struts. For a rectangular cross-section the critical buckled wavelength can be defined as,

$$L_{cr} = \frac{n\pi r}{\kappa}\sqrt{\frac{E_T}{\sigma_{max}}} = \frac{n\pi r\, c_p}{\kappa}\sqrt{\frac{\rho}{\sigma_{max}}} \tag{6.3}$$

The analysis assumed a state of constant stress behind the plastic wave front, a buckling response on a quasi-static basis, strain hardening was negligible (i.e. "constant" axial

stress) and the elastic/plastic wave front generates a discontinuity in the material stiffness and effective boundary condition.

Reid et al. (1981) developed a similar upper bound expression, $L_{cr} \cong 0.414L_u$ based on a traveling hinge mechanism. The formula was compared with experimental data on the response of long rods (length to diameter ratio of 24:1) impacting a rigid target at velocities of 70m/s – 350m/s.

Abrahamson and Goodier (1966) defined the half-wavelength (λ) as,

$$\lambda = \pi r \sqrt{\frac{2E_T}{\sigma}} \tag{6.4}$$

for projectile impact of aluminum rods and tubes on a rigid target with initial impact velocity that ranged from 36m/s to 200m/s.

The final approach was formulated on the conceptual basis for the impact event discussed in Section 6.2.3 and illustrated in Figure 6-8. Bound limits on the peak buckle half-wavelength were assessed through consideration of the elastic and plastic stress wave propagation and interaction by the expression,

$$\bar{x} = \frac{2L_T}{n\left(\frac{c_e}{c_p} - 1\right)} \tag{6.5}$$

This method only considers axial stress wave propagation and does not account for flexural properties or influence of boundary conditions on the modal response. Furthermore, Equation (6.5) neglects the dynamic response due to elastic wave

propagation until a plastic wave front has developed. In terms of a bound limit, the data analysis will illustrate that these assumptions are reasonable.

Based on the material properties presented in Table 6-6, the half-wavelengths were assessed using the expressions presented in Equations (6.3, 6.4 and 6.5) assuming elastic and elastic, perfectly plastic material behaviour. A summary of the predicted buckle half-wavelengths is also presented in Table 6-6.

Table 6-6. Experimentally Measured Peak Buckle Half-Wavelength $(\bar{x})$ and Predicted Half-Wavelength Response Assuming Elastic and Elastic, Perfectly Plastic Material Behaviour.

Parameter		AI	AII	SI
Elastic Modulus	E	69GPa	69GPa	200GPa
Tangent Modulus	E_T	900MPa	900MPa	1.75GPa
Yield Stress	σ_y	285MPa	285MPa	300MPa
Density	ρ	2700kg/m3	2700kg/m3	7200kg/m3
Experimental	$\bar{x}$	51mm – 72mm	75mm – 103mm	53mm – 78mm
Equation (6.3) Elastic; n =1	$0.5L_{cr}$	45mm	67mm	74mm
Equation (6.3) Plastic; n = 1	$0.5L_{cr}$	5mm	9mm	7mm
Equation (6.4) – Elastic	λ	63mm	95mm	105mm
Equation (6.4) – Plastic	λ	7mm	13mm	10mm
Equation (6.5) – n = 1	$\bar{x}$	61mm–168mm	79mm–203mm	49mm–134mm
Equation (6.5) – n = 2	$\bar{x}$	31mm–84mm	39mm–101mm	24mm–67mm

Assuming elastic material parameters, equations (6.3) and (6.4) provide a reasonable estimate of the half-wavelength response, for the lower slenderness ratios, in comparison with the experimental data. A number of factors may account for the discrepancy when assuming plastic material behavior, which may include impact mechanics and dynamic material behavior. The investigations of both Bell (1988), and Abrahamson and Goodier (1966) considered "free-flight" projectile events with significantly greater impact velocities ranging from 40m/s to 350m/s. The load intensity for these events would be sufficient to develop an immediate plastic wave front. In addition, Abrahamson and Goodier (1966), reported that the measured wavelengths were 1.2 to 2 times the theoretical wavelengths where this discrepancy was related to the magnitude of axial strain and corresponding variation in the tangent modulus.

The experimentally measured half-wavelength response as a function of effective slenderness ratio is illustrated in Figures 6-14, 6-15 and 6-16, for impact test series *AI*, *AII* and *SI*, respectively. The total beam length (L_T) is the sum of the unsupported beam length (L_u) and the 100mm boundary condition.

Although based on a simplified analysis of elastic–plastic stress wave interaction, Equation (6.5) provides a reasonable estimate of the buckled half-wavelengths over the range of slenderness and material parameters investigated. The empirical expression is consistent with the present experimental observations, which show that for the lower slenderness ratios ($Le/r \leq 125$) the dominant response can be effectively characterized by the fundamental mode. For higher slenderness ratios, more complex mode interaction mechanisms develop and for the cold rolled steel series a rate-dependent material response was inferred. These characteristics are illustrated by the digitized buckled profiles (Figure 6-13) and convergence of Equation (6.5), assuming the "second mode" response ($n = 2$) at higher slenderness ratios (Figure 6-14, 6-15 and 6-16).

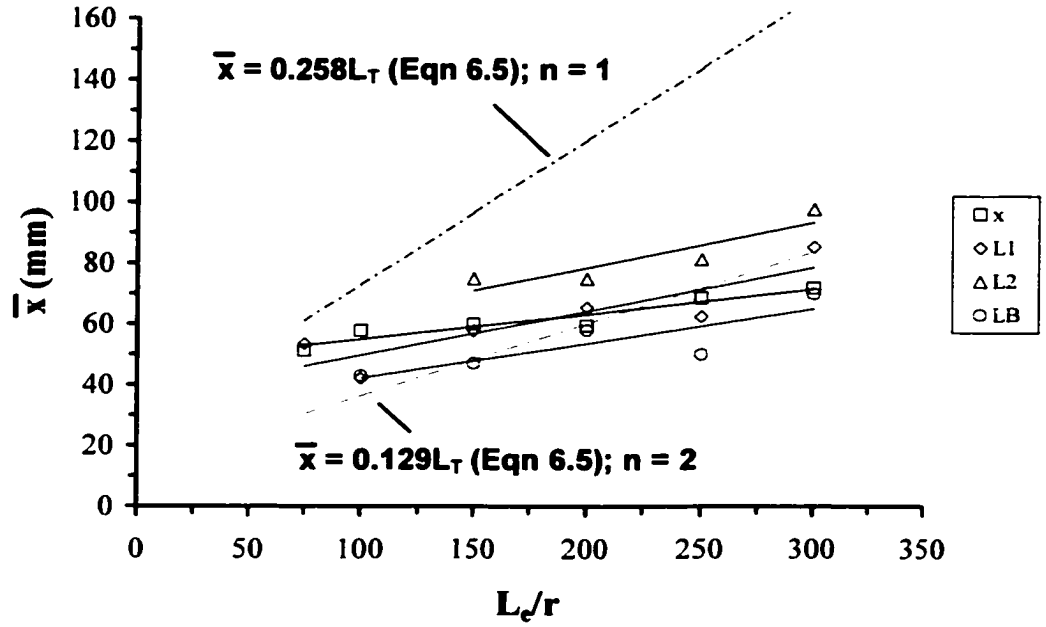

Figure 6-14. Mean Half-Wavelength Response for Series *AI*.

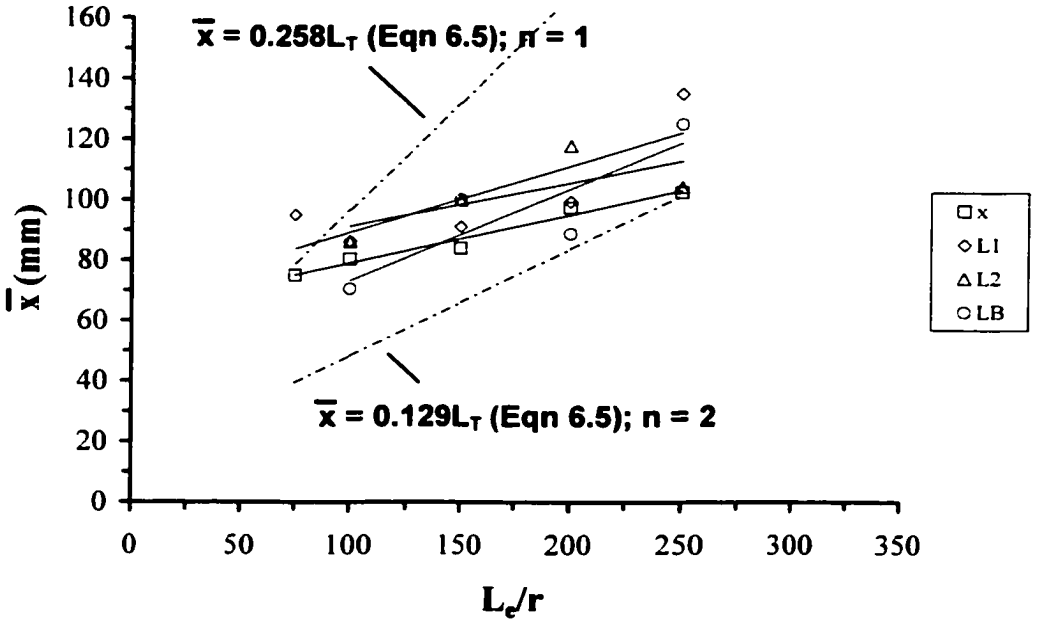

Figure 6-15. Mean Half-Wavelength Response for Series *AII*.

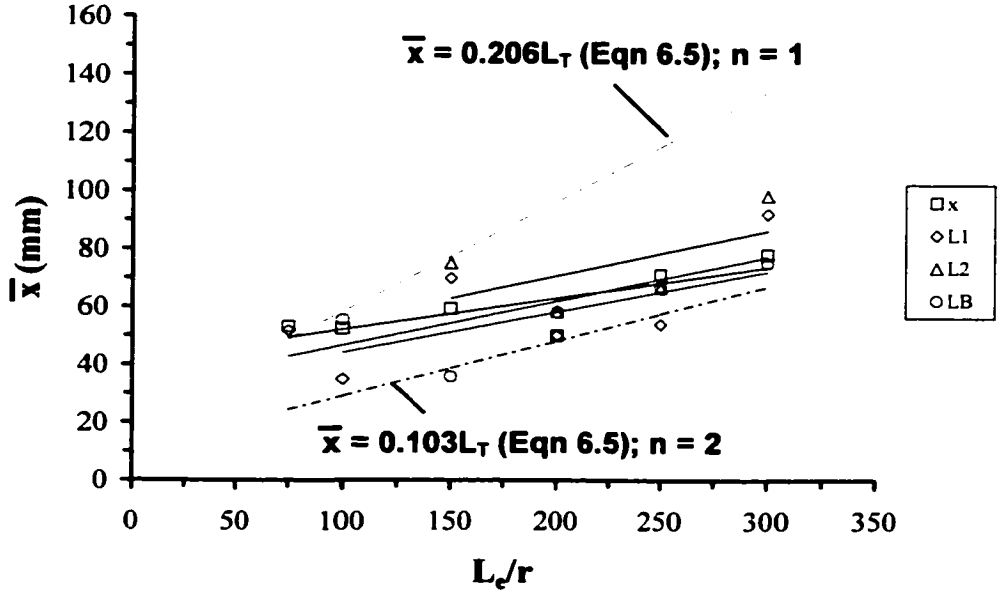

Figure 6-16. Mean Half-Wavelength Response for Series *SI*.

Numerical analysis conducted by Karagiozova and Jones (1996), employing an elastoplastic multi-degree of freedom mechanical model, concluded the quasi-static analysis of Bell (1988) could predict only the final deformed buckled mode provided the impact energy was relatively small.

The pulse buckling response of the peak crest has been characterized by a normalized modal parameter as a function of the effective slenderness ratio. The modal parameter accounted for the local stiffness and natural frequency response. In addition, the influence of dynamic material behavior on the transverse amplitude of the peak buckle response was inferred from experimental observation. Simplified theoretical expressions defining the critical buckle wavelength were in reasonable agreement with the experimental data. The experimental investigations will provide a rational basis for the development and validation of finite element models simulating the impact event.

7.0 Finite Element Analysis of Plastic Pulse Buckling Events

The development of a finite element model examining the experimentally observed plastic pulse buckling response of a slender beam subject to axial impact is presented. A parametric investigation is conducted, which considers factors such as element aspect ratio and formulation, constitutive relationships, boundary conditions and geometric imperfection models. The objective is the development of a finite element model to predict the dynamic plastic pulse buckling response consistent with the observed behaviour during the present experimental studies. The fundamental goal is a reliable modelling procedure that can be applied to more complex structural configurations, material response and/or impulse characteristics.

7.1 Introduction

Historically, the majority of analytical research and numerical modelling efforts on the elastic and plastic pulse buckling response have focused on the fundamental mode. As discussed in Chapters 5 and 6, relatively few experimental studies have addressed the dynamic plastic buckling response of slender beams subject to an intense axial impact. Several analytical and experimental studies, including the present investigations, have shown that for intense impulsive loads the dynamic instability may be characterized by a higher order modal response. Some of these investigations include Bell (1988), Abrahamson and Goodier (1965), Hayashi and Sano (1972a, 1972b), Suguira et al. (1985), Gary (1983) and Kenny et al. (2000). The present study is primarily concerned with the development of a finite element model, to predict the dynamic plastic pulse buckling of a beam subject to axial impact. The experimental investigations conducted during the current thesis research, presented in Chapter 6, provide a basis for validating

the finite element computations. Details of the finite element model and results of the parametric analysis are presented. Characteristic relationships of the peak buckle and mode behaviour of the pulse buckling response are developed and compared with experimental data. Finally, a dynamic pulse buckling criterion is addressed.

7.2 Model Parameters and Formulation

The parameters considered for the finite element investigations are summarized in Table 7-1. Comparison of the computed response with the experimentally observed behaviour was based on modelling only the slenderness ratios of *75, 150* and *250.* A single, axial impact scenario, consistent with that imposed during the experimental studies, was defined as a 10kg mass impacting the beam with a nominal contact velocity of 6.2m/s. The structural configuration considered for the numerical investigations is illustrated in Figure 7-1.

The finite element package *NISA* was employed to model the pulse buckling event. The beam response was modelled by *2D Plane Strain (NKTP=2)* elements with quadractic shape functions or *3D General Beam (NKTP=39)* based on the Kirchoff hypothesis. The physical impact of the free fall hammer with the beam was accounted through added mass element(s), which neglected rotary inertia, with the prescribed initial nominal contact velocity. For models employing plane strain elements, the added mass was distributed on a consistent basis. The constitutve relationships for the 6061-T6 aluminum beams were defined by two material response functions, which employed the von Mises yield criterion. An idealized elastic, perfectly plastic material behaviour and bilinear elastoplastic material behaviour with linear, isotropic strain hardening were considered. The pulse buckling response of the cold rolled 1018 steel beams were only investigated using idealized elastic, perfectly plastic material behaviour.

Table 7-1. Parameters for Finite Element Analysis of Dynamic Plastic Pulse Buckling.

Beam Characteristics			
Beam Lengths	L_u (mm)	137, 275, 458	206, 412, 687
Beam Depths	d (mm)	3.175	4.7625
Slenderness Ratio	L_e/r	75, 150, 250	
Material	6061-T6Aluminum	E = 69GPa; E_T = 900MPa; σ_Y = 285MPa; ν = 0.33; ρ = 2700 kg/m^3	
	1018 Steel	E = 69GPa; σ_Y = 300MPa; ν = 0.33; ρ = 7200kg/m^3	
Impact Characteristics			
Impact Mass	m	10kg	
Impact Velocity	V_I	6.2m/s	
Finite Element Characteristics			
Element Type	2-D Plane Strain	NKTP = 2, quadratic shape function	
	2-D Mass	NKTP = 25 (degrees of freedom: U_x, U_y)	
	3-D Beam	NKTP = 39, Kirchoff hypothesis	
	3-D Mass	NKTP = 26 (degrees of freedom: U_x, U_y, U_z)	
Aspect Ratio	Element length to depth ratio	1:1	

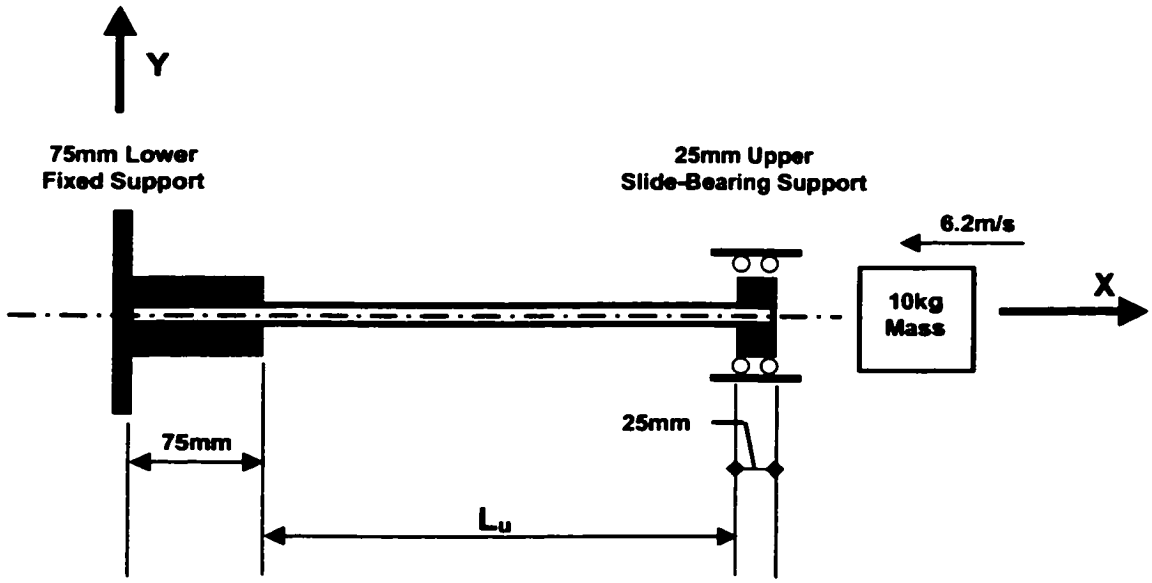

Figure 7-1. Schematic Illustration of the Modelled Boundary Conditions.

The implicit Newmark method was selected to directly integrate the dynamic equation of motion. The selected integration values of, $\beta = 0.3025$ and $\gamma = 0.6$, provided an unconditionally stable solution with artificial numerical damping. The kinematic formulation was large displacement and finite strain. The full-Newton routine, with line search, was used to obtain convergence with default energy and displacement tolerance criteria of 0.001. The stability equations, presented in Chapter 3 and Chapter 4, were employed to determine the required integration time step for the selected element formulation and selected aspect ratio.

7.3 Finite Element Model Sensitivity Analyses

A series of preliminary investigations were conducted to assess the influence of several parameters on the computed dynamic buckling response with respect to the measured

experimental modal response. The sensitivity analysis considered element aspect ratios, element formulations, constitutive relations, boundary conditions and geometric imperfection models and contact mechnics. A matrix of the model parameters is summarized in Table 7-2, for models defined by bilinear elastoplastic material behaviour, and Table 7-3, for models with elastic, perfectly plastic material behaviour. The imperfection models were incorporated through the same procedures adopted for the elastic pulse buckling analysis and was defined by Equation (3.17) and Equation (3.20).

The results from 76 finite element models were examined in the sensitivity analysis. Further details of these investigations are presented in Appendix D, which analyzed the computed buckling response with respect to measured experimental data in terms of the buckled profile. For the defined impact scenario and sensitivity parameters considered, the modeled boundary condition and element formulation had the most significant influence on the computed pulse buckling response. In relative terms, the element aspect ratio, which considered ratios of 4:1, 2:1 and 1:1, imperfection model and contact mechanics was of secondary importance on the computed modal behavior. Based on the experimentally observed and computed buckling response, it was speculated that dynamic material properties should be considered when modeling the pulse buckling behavior of the cold rolled (CR1018) steel beams. On this issue, a definitive conclusion could not be developed due to software limitations, where dynamic, rate dependent material properties could not be modeled.

Although a "simple" axial impact event has been considered, numerical modelling of the dynamic, plastic pulse buckling response is a complex and demanding task. The investigations, presented in Appendix D, determined that spurious mode shapes, in comparison with the observed experimental buckling response, occasionally developed in the numerical solution. The sensitivity analysis suggested that additional parameters, which may be coupled to the complex nonlinear buckling process, should also be

Table 7-2. Parameter Matrix for Finite Element Models with Bilinear Elastoplastic, Linear Strain Hardening Material Behaviour.

Series	Element Type	Aspect Ratio	Imperfection
AIa	Beam, Plane Strain	4:1, 2:1, 1:1	Random
AIc	Beam, Plane Strain	4:1, 2:1, 1:1	Random
AIe	Beam, Plane Strain	4:1, 1:1	Random
AIIa	Beam, Plane Strain	4:1, 2:1, 1:1	Random
AIIc	Beam, Plane Strain	4:1, 2:1, 1:1	Random
AIIe	Beam, Plane Strain	4:1, 1:1	Random

Table 7-3. Parameter Matrix for Finite Element Models with Elastic, Perfectly Plastic Material Behaviour.

Series	Element Type	Aspect Ratio	Imperfection
AIa	Beam, Plane Strain	1:1	Discrete, Random
AIc	Beam, Plane Strain	4:1, 2:1	Random
		1:1	Discrete, Random, Combined
AIe	Beam, Plane Strain	4:1	Random
		1:1	Discrete, Random
AIIa	Beam, Plane Strain	1:1	Random
AIIc	Beam, Plane Strain	4:1	Random
		1:1	Discrete, Random
AIIe	Beam, Plane Strain	4:1	Random
		1:1	Discrete, Random
SIa	Beam, Plane Strain	1:1	Random
SIc	Beam, Plane Strain	1:1	Random

considered. These potentially interdependent factors include the strain field discontinuity, element frequency characteristics, local stiffness effects (e.g. material and structural), as well as stress wave propagation and boundary interaction effects. The importance of any correlation with the modal response, however, was not resolved in the present study and further investigations are warranted.

7.3.1 Influence of Boundary Conditions

During the course of the experimental investigations, considerable effort was expended to develop competent structural boundary conditions that would ensure a consistent pulse buckling response. The numerical sensitivity analysis considered two scenarios to investigate the influence of the modelled boundary condition on the computations. The baseline case, described in Section 7.2 and illustrated in Figure 7-1, was consistent with the applied boundary condition for the current experimental studies. The variant scenario was based on an idealized boundary condition, which did not account for the fixed (75mm) or slide bearing (25mm) support depths.

Numerical pulse buckling analyses has typically only considered the later, idealized boundary conditions, which neglect the support depth to define the imposed structural restraint. The numerical investigations of Ari-Gur and Elishakoff (1993), Ari-Gur and Elishakoff (1990), Ari-Gur et al. (1982) and Sugiura, et al. (1985) are representative examples. Some of these studies have also included parallel empirical investigations but details on the applied experimental boundary conditions were only qualitatively discussed. Although the experimental boundary condition was not realistically modelled in these numerical investigations, statements regarding the corresponding influence on the computed pulse buckling response would be speculative.

For the parameters considered in the present sensitivity analysis, however, the investigations presented in Appendix D has demonstrated that the actual imposed experimental boundary conditions must be modelled for accurate pulse buckling predictions. The influence of the adopted imperfection model and element formulation, if any, was considered secondary.

As previously discussed in Chapter 6, the evolution of a mode shape inconsistent with the predominant observed buckled response was developed for spurious impact events. The buckled response was associated with two mechanisms, a loss of competent structural integrity for the upper slide bearing support and a "dead" impact where little or no recoil of the impact hammer occurred. These events are further discussed in Appendix C.

For the parameters investigated, the finite element computations supported this hypothesis, which was based on experimental observations. A representative example is illustrated in Figure 7-2, for the pulse buckling response of the beam element model *AIc* presented in Table 7-3.

The experimental buckled profiles for an impact event with competent boundary conditions (*AIc7*) and an impact test with a loss of the upper slide bearing support (*AIc2*) are shown for comparison. The computed buckling response for the finite element model (Beam – Actual) employing boundary conditions consistent with the experimental test (*AIc7*) was in good agreement with the measured response. The finite element analysis that considered an idealized boundary condition (Beam – Idealized) exhibited a shift in location of the peak buckle crest toward the impact interface and upper slide bearing support. The computed response was generally consistent with the spurious impact event (*AIc2*) observed during the experimental investigations.

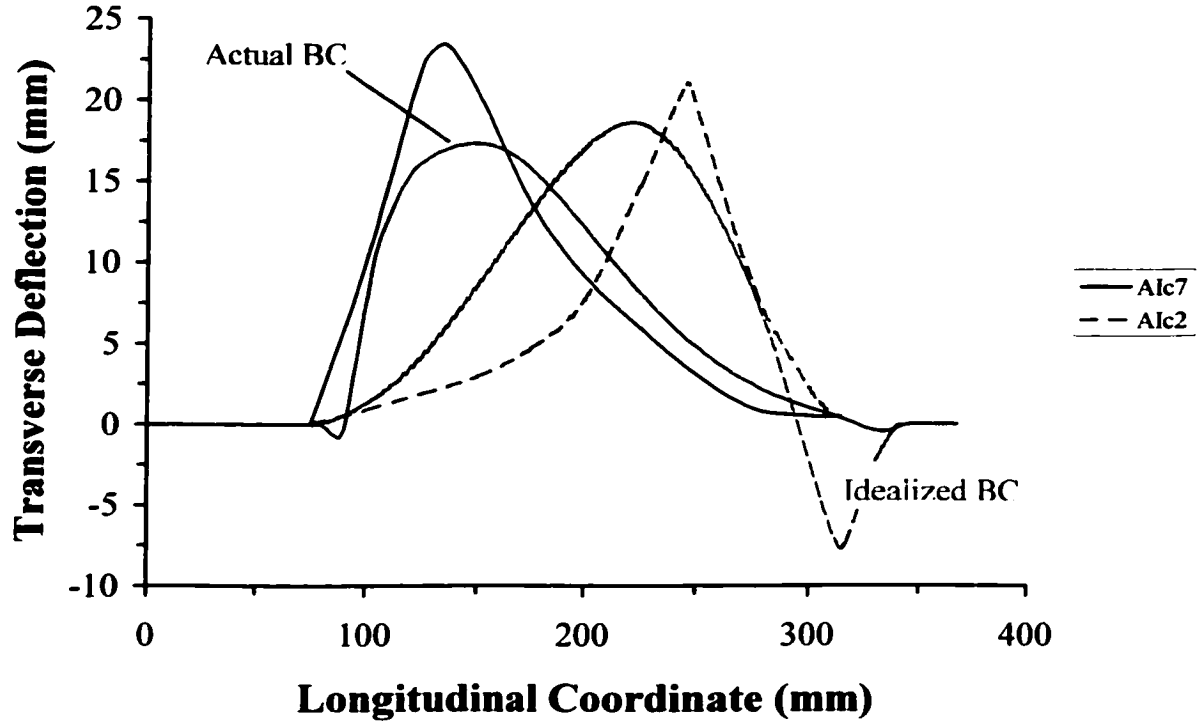

Figure 7-2. Comparison of the Computed Finite Element Response for the Actual and Idealized Boundary Conditions with Respect to the Characteristic (Test *Alc7*) and Spurious (Test *Alc2*) Experimental Buckling Events.

This issue should also be considered with respect to the experimental investigations conducted by Ari-Gur et al. (1982) and discussed in Chapter 5. A similar modal shift, from the lower fixed restraint to the upper slide bearing support, was also observed with increasing slenderness ratio. Unfortunately, an underlying mechanism was not assessed. Finally, the experimental and numerical studies of Sugiura et al. (1985) and Hayashi and Sano (1972a,b) have shown that, for an axially loaded simply supported beam, the peak buckle response was initiated at the impact interface.

7.3.2 Influence of Imperfection Models

The elastic pulse buckling investigations presented in Chapter 3 through Chapter 5 has demonstrated the importance of considering the geometric imperfection model on the computed response. As shown in Figure 5-13(b), Karagiozova and Jones (1995b) have demonstrated the importance of considering the imperfection magnitude on the critical impact velocity for plastic buckling events.

The present sensitivity analysis considered discrete and random geometric imperfection models. The discrete, fundamental mode imperfection was incorporated through Equation (3.17) with the peak amplitude defined by the measured mean imperfection (A_o) presented in Table 6-1, 6-2 or 6-3 for the appropriate experimental impact test being modelled. Local random imperfections were expressed by Equation (3.20). The geometry was discretized by two-dimensional plane strain elements and three-dimensional beam elements.

Based on the analysis presented in Appendix D, influence of the defined imperfection model on the computed pulse buckling response was not significant. This is an important observation, since the maximum amplitude of the local random geometric imperfections is one to two orders of magnitude lower than the maximum global discrete imperfection amplitude. In view of the study conducted by Karagiozova and Jones (1995b), further investigations are warranted to establish the influence of imperfection model type and magnitude on the pulse buckling response over a range of parameters including impulse intensity.

7.3.3 Influence of Element Formulation

Similar to the elastic pulse buckling analysis, conducted in Chapter 4, the computed modal response was dependent on the element formulation. Specifically, the element formulation influenced the peak buckle amplitude and axial position. In general terms, the plane strain element models exhibited improved response over the beam element models with respect to the measured experimental buckled profiles.

There are several factors to consider in assessing the influence of element formulation on the predicted modal behaviour. The beam element was defined by the moment–curvature assumption and nonlinear terms of the axial–strain displacement relationship. For the elastic pulse buckling analysis, in comparison with perturbation theory and plane strain element models, the peak buckle response for the beam elements was associated lower crest amplitudes (Figure 4-5) and smaller weighted mean wavelengths (Figure 4-6). This is consistent with the general response of the Euler-Bernoulli beam formulation, which is associated with a moderately stiff response, as the aspect ratio tends to unity, and thus results in higher natural frequencies of vibration. Matsunaga (1996) stated that for aspect ratios on the order of 1:1, the critical buckling was associated with a higher order modal response, which was more influenced by the axial force than lower order, modal response. These factors could play a role in the frequency response characteristics of the beam element models. In addition, the modal dynamics for both element formulations may be coupled with the axial strain field discontinuity, local stiffness effects (e.g. material and structural), as well as stress wave propagation and boundary interaction effects.

Finally, the sensitivity analysis, detailed in Appendix D, indicated that the effect of element formulation on the numerical computations was weakly coupled with the element aspect ratio and imperfection model. This was associated with the number of nodal points defining the geometric imperfections and higher degrees of freedom. The

quadratic, plane strain element has a greater number of nodes (8) and higher nodal degree of freedom per element (16 DOF) than the beam element formulation (2 nodes and 12 DOF). In terms of the computed pulse buckling response, these factors would be related to numerical modelling performance of the characteristic hyperbolic growth function and the associated amplification or magnification of initial geometric imperfections.

7.3.4 Influence of Constitutive Relationships

For the pulse buckling response of aluminum 6061-T6 beams (Test Series *AI* and *AII*), the finite element analysis considered two material models, which included elastic, perfectly plastic and bilinear, elastoplastic behaviour. Mode analyses of selected numerical models are presented in Appendix D. The analysis demonstrated that for either element formulation (plane strain or beam element), the computed buckling response was not significantly influenced by the constitutive relationships employed. Although a definitive functional relationship in terms of material behaviour and element formulation was not evident, as a general statement, models employing bilinear, elastoplastic behaviour exhibited slightly improved performance in relation to the measured experimental data.

The finite element analysis also investigated the plastic buckling response of cold rolled 1018 steel beams but only considered elastic, perfectly plastic material behaviour. Based on comparison of the predicted and experimentally observed response, the influence of dynamic yield flow and/or rate-sensitive behaviour for the mild steel beams was considered important. Analysis of the transverse modal response provided indirect support that dynamic material properties (e.g. dynamic yield flow stress, strain-rate effects) may be a significant consideration for the development of accurate models. This was consistent with the investigations of Su et al. (1995) and Karagiozova and Jones

(1997), which have demonstrated rate-sensitive behaviour is an important parameter that influences energy response mechanisms during plastic pulse buckling events.

7.3.5 Influence of Contact Mechanics

An overview of the contact mechanics associated with the experimental study will be presented and will be followed by a discussion of the numerical modelling techniques employed during the present investigations.

For the impact tests, the initial potential energy of the mass assembly was primarily transferred into kinetic energy during free-fall. On impact with the beam, at the upper slide-bearing support, a resistive impulsive load was developed and an axial stress wave propagated through the length of the beam toward the lower fixed restraint. Assuming rigid body kinematics and a constant beam cross-sectional area, the impact velocity (V_I) of the free fall hammer mass (M) would decrease according to the expression,

$$V(t) = V_I - \frac{1}{M}\int_0^t P\,dt \tag{7.1}$$

Vertical separation of the impact mass from the beam occurs due to a sign change in acceleration arising from a combination of the return tensile stress wave to the beam–mass interface and elastic rebound. Although during the experimental program, a second impact was observed, the corresponding influence on the buckled response was considered negligible. This was supported by analysis of the proximity switch trigger pulse records, available strain gauge data and experimental observations. Similar studies conducted by Ari-Gur et al. (1982) concluded that the second impact was not significant since the event occurred after the maximum deflection was obtained. The second impact event was associated with elastic vibration. The significant plastic deformation

associated with the development of a peak buckle crest, adjacent to the lower fixed support, consumed the bulk of the initial, finite impact energy.

Due to software limitations in the finite element program NISA, the numerical analysis does not account for the mass separation after impact since the event is defined by an added nodal mass with a prescribed initial velocity condition. Consequently, influence of the adopted modelling procedure on the computed pulse buckling response was assessed through examination of the computed displacement–time, velocity–time and stress–time history data. The analysis considered the parameters listed in Table 7-1 for the finite element models summarized in Table 7-3 with only local random geometric imperfections and an aspect ratio of 1:1.

Representative examples of the axial force–time history for beam and plane strain element models are illustrated in Figure 7-3. The corresponding variation in the velocity–time history for the impact hammer is shown in Figure 7-4. The influence of contact mechanics on the buckled profile development was also examined through an assessment of the displacement–time history data. The buckled response for plane strain element models with discrete and random geometric imperfections for test series *AIc* is illustrated in Figure 7-5. Data for beam and plane strain element models with fundamental mode imperfection for test series *AIe* is illustrated in Figure 7-6. Experimental buckled profiles are also shown for comparison.

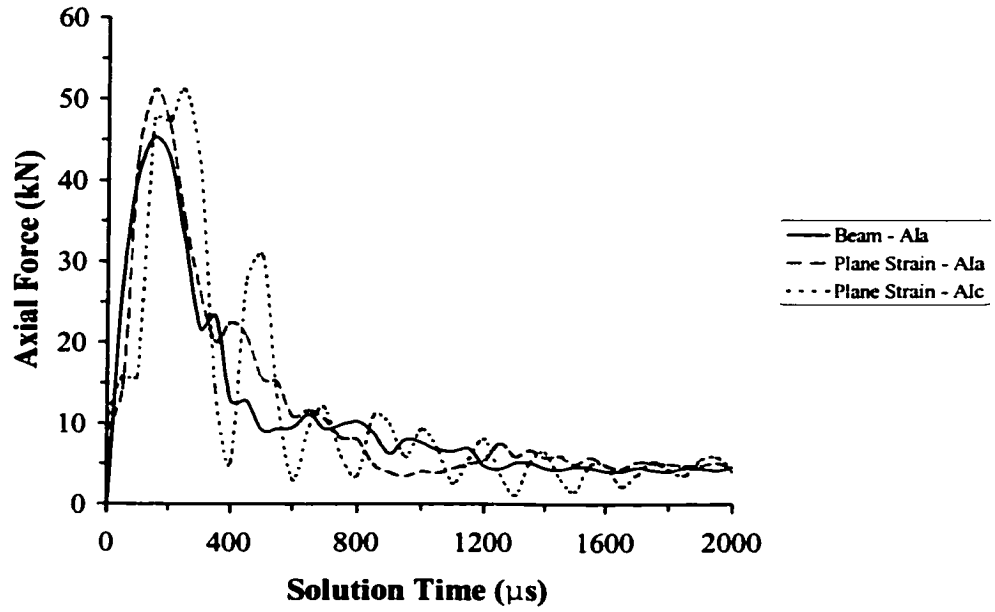

Figure 7-3. Impulse Load–Time History for Beam and Plane Strain Element Models with Random Geometric Imperfections for Test Series *AIa* and *AIc*.

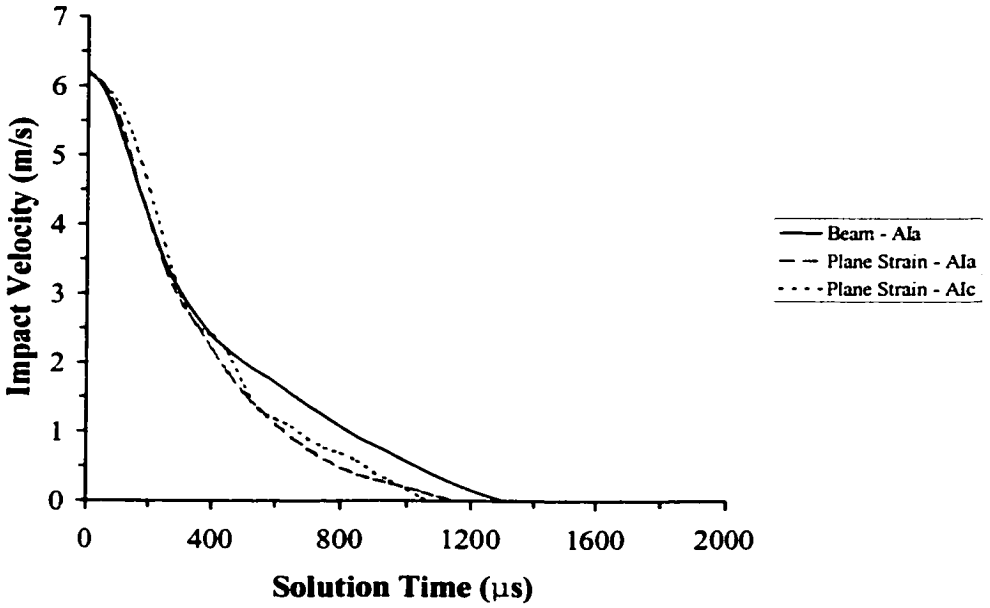

Figure 7-4. Impact Velocity of the Free Fall Hammer for Beam and Plane Strain Element Models with Random Geometric Imperfections for Test Series *AIa* and *AIc*.

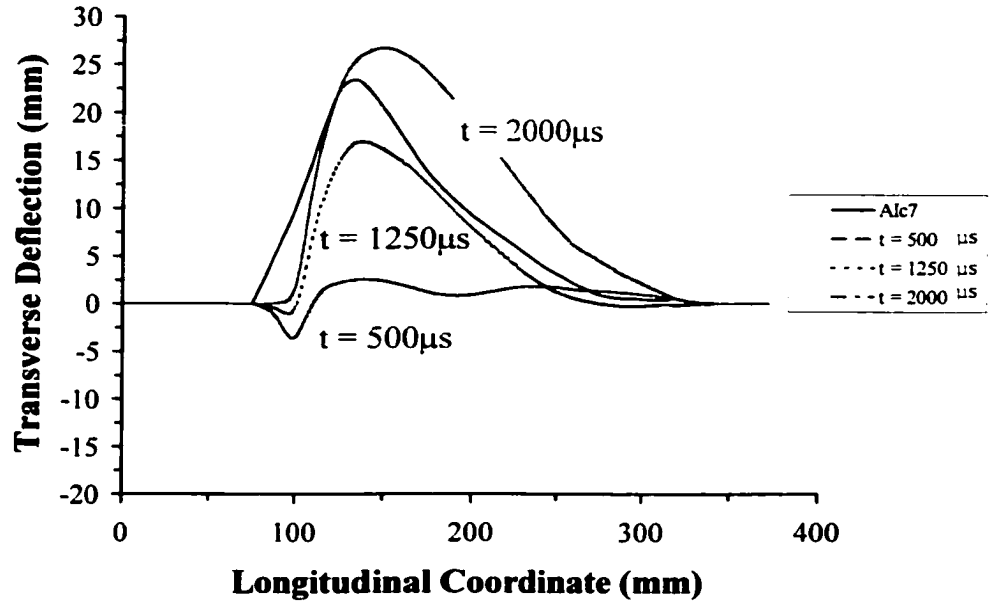

(a)

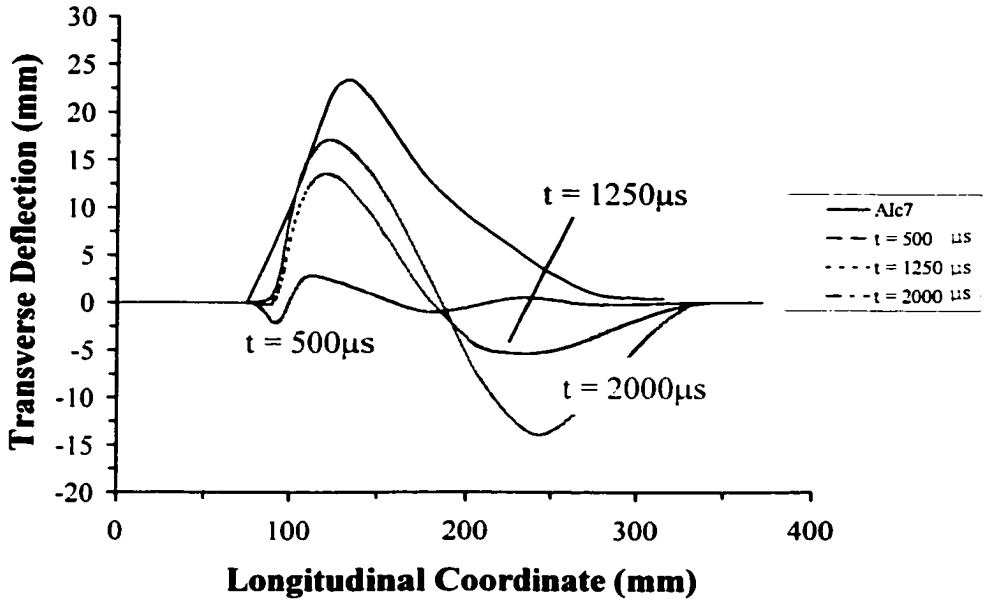

(b)

Figure 7-5. Computed Buckled Profile Displacement–Time History of Series *AIc* for Plane Strain Element Models with (a) Discrete and (b) Random Geometric Imperfections.

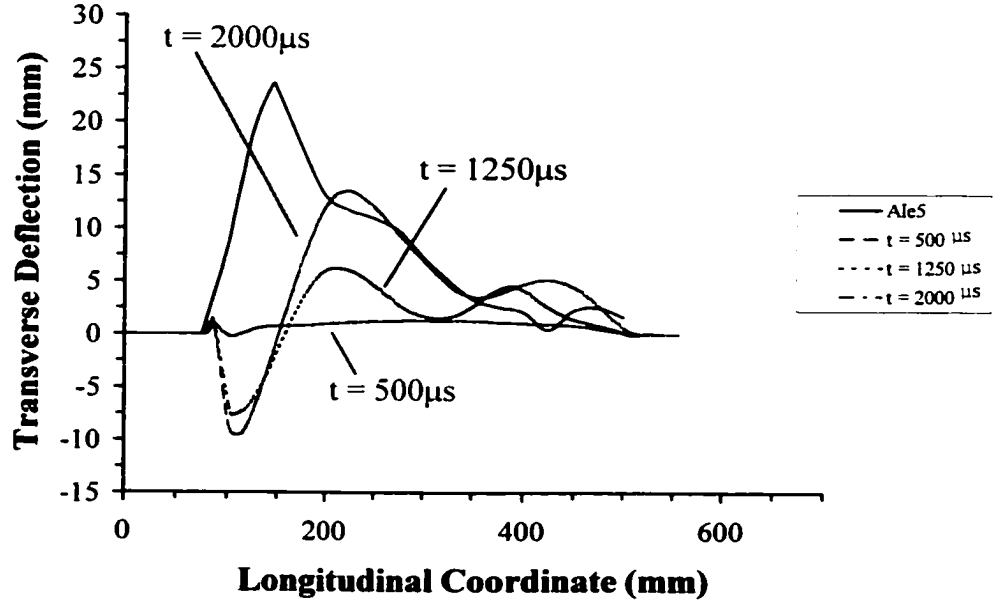

(a)

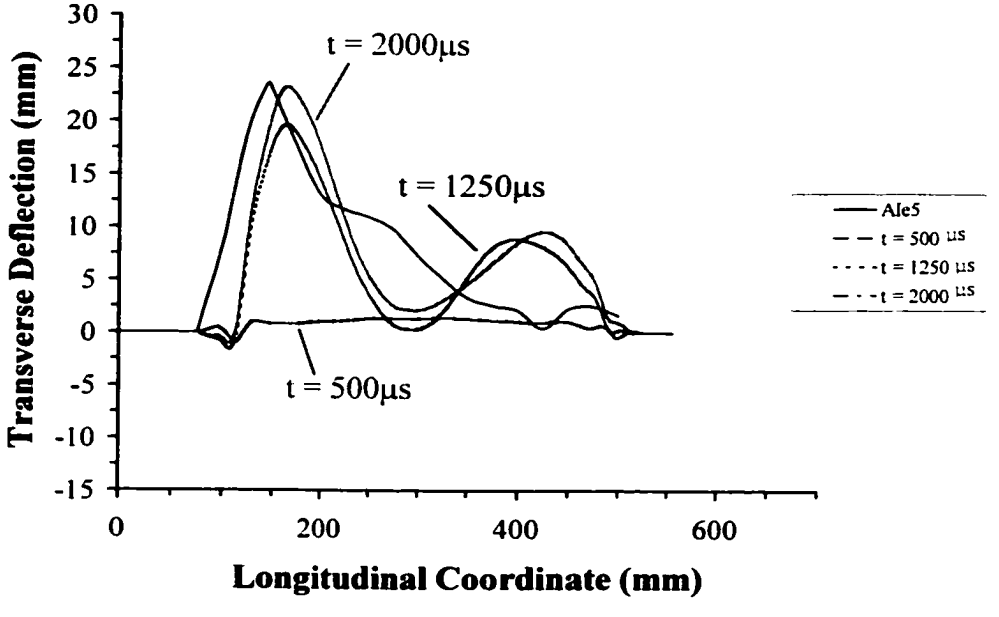

(b)

Figure 7-6. Buckled Profile Displacement–Time History of Series *AIe* for (a) Beam and (b) Plane Strain Element Models with Discrete Geometric Imperfection.

The buckled profiles were examined with respect to parameters such as hammer velocity, slenderness ratio, element formulation and imperfection type. The sensitivity analysis demonstrated that modelling the dynamic plastic pulse buckling response was a complex task. For the parameters investigated, a single dominant parametric relationship with contact mechanics could not be established. In comparison with the applied boundary conditions and element formulation, modelling the contact mechanics by a fixed, added mass element was considered to be of secondary importance on influencing the computed modal response.

Based on the sensitivity analyses conducted, the contact mechanics, in addition to the pulse buckling response, is coupled to a number of parameters. These include slenderness ratio, geometric imperfection type and magnitude, element formulation and frequency characteristics, proportion of axial and flexural strain energy, wave propagation and interaction effects, material response and imposed boundary conditions. Some of these issues were also addressed for relatively simpler mechanical models, which were discussed in Chapter 5. For example Su et al. (1995a, 1995b) and Karagiozova and Jones (1995a, 1995b), demonstrated the importance of considering imperfection amplitude, impact mass and velocity, strain hardening parameter, dynamic material properties on influencing the dynamic plastic buckling response.

For the present analysis, the pulse buckling computations were most consistent with respect to the measured experimental data for the lower slenderness ratio ($L_e/r = 75$). For the higher slenderness ratios, modelling the continuous mass contact at the impact interface tended to bias a local response through the development of a buckle crest adjacent to the upper slide bearing support. This was illustrated in Figure 7-6.

The slenderness ratio has a direct influence on the buckled response through the relative changes in global mechanical rigidity (i.e. axial and flexural terms), relative local

stiffness (i.e. interaction with fixed support) and modal response. Analysis and assessment of the modal response computations is complicated by the interrelated parameters with the slenderness ratio such as wave propagation and interference effects, localized strain gradients and associated material, mechanical and modal behaviour. In terms of the contact mechanics, the dominant factors influencing the pulse buckling computations, with decreasing relative significance, are considered to be the slenderness ratio, element formulation and imperfection model. These characteristics were illustrated in Figure 7-5 and Figure 7-6.

Finally, although probably a relatively minor issue, the finite element analysis also cannot account for any "restoring force" due to elastic curvature recovery of the unsupported beam length after the mass recoiled from the impact interface during the experimental tests.

A number of alternative methods were considered for modelling the impact event, however the efforts were unproductive due to software limitations for application in nonlinear static or linear direct transient analysis. These procedures included defining a time–amplitude curve defining the impulsive force, application of contact elements, defining initial stress–strain field and mode vector (i.e. initial displacement, velocity, acceleration terms).

Although the adopted procedure for modelling the contact mechanics was considered of secondary importance on influencing the plastic pulse buckling response computations, further investigations that can account for the impact mass separation are warranted to more fully explore this issue.

7.3.6 Influence of Element Aspect Ratio

The sensitivity analysis also examined the influence of element aspect ratio on the pulse buckling response computations in parallel with the other parameters considered. For element aspect ratios of 4:1, 2:1 and 1:1, the effect was not significant and was considered weakly coupled to the element formulation and imperfection model.

7.4 Peak Buckle Response Analysis

The computed pulse buckling response was also evaluated in terms of the normalized parameter $(\overline{N})$, which was discussed and developed in Section 6.2.3. Validity of the finite element models was based on direct comparison with the experimental data. Furthermore, the finite element computations were assessed in terms of the issues addressed in the sensitivity analysis, and examination of the displacement–time, velocity–time and stress–time history computations.

The normalized axial response parameter $(\overline{N}\,\bar{x})$ is presented in Figure 7-7. The open data points represent all finite element analyses with an element aspect ratio of 1:1. Results of the numerical computations are differentiated in terms of the element formulation (i.e. beam and plane strain element models). As previously discussed, the sensitivity analysis demonstrated that the modeled boundary conditions and element formulation were the significant parameters to be considered. The lines represent least squares regression curves through measured experimental data for all impact tests, which were presented in Figure 6-11 and Figure 6-12. On this same basis, the normalized transverse response parameter $(\overline{N}\,\bar{y})$ of the peak buckle crest is illustrated in Figure 7-8.

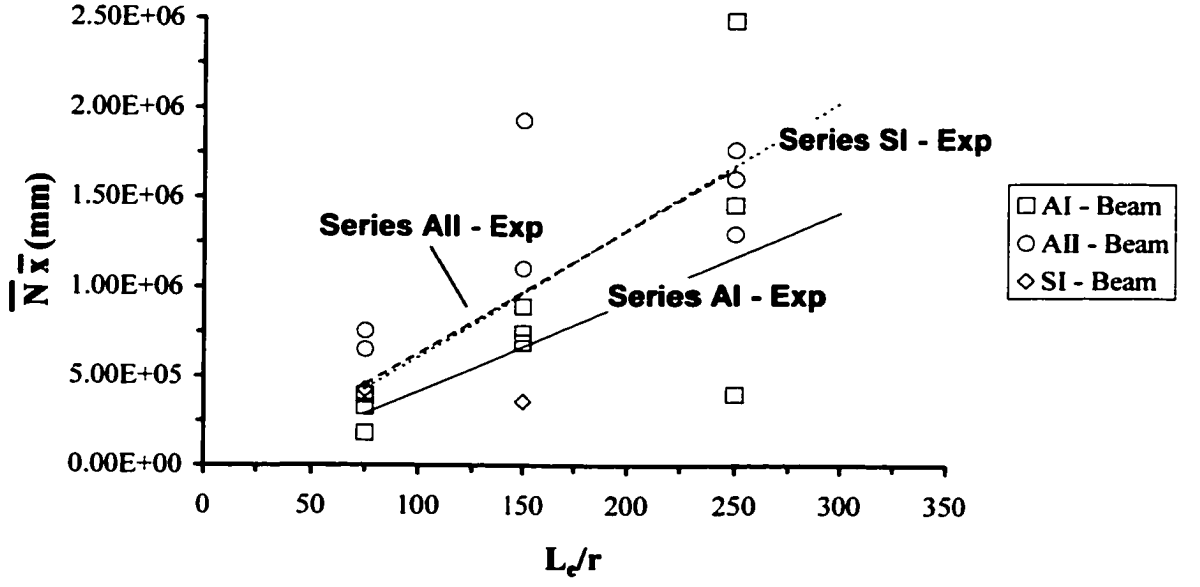

(a)

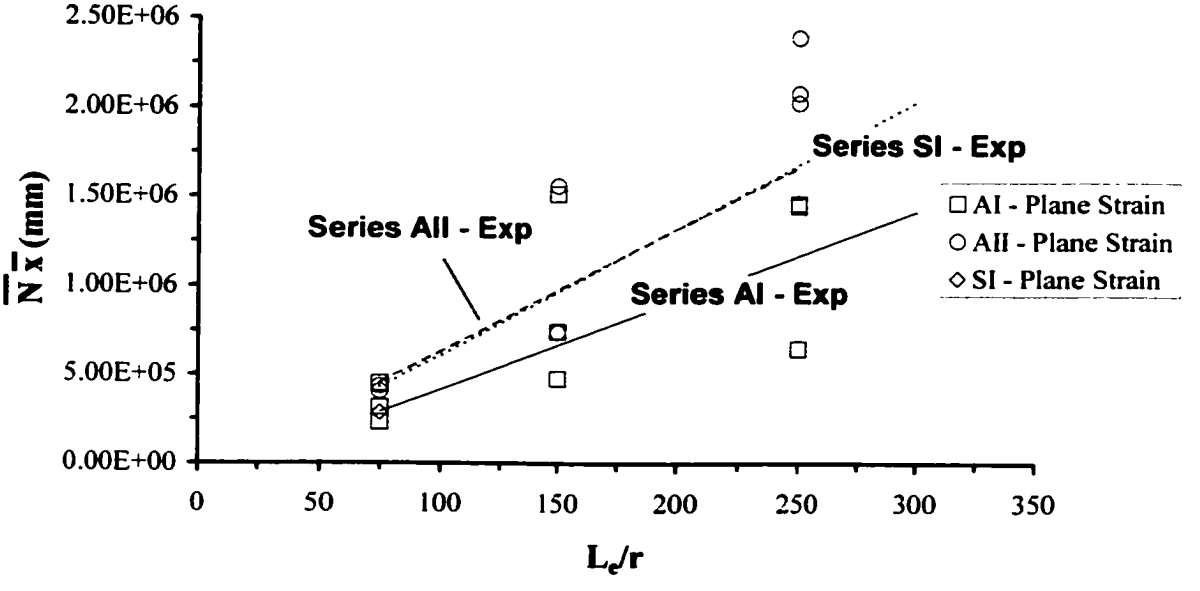

(b)

Figure 7-7. Normalized Axial Modal Response $(\overline{N}x)$ of the Peak Buckle Crest as a Function of the Effective Slenderness Ratio (L_e/r) for Finite Element Models with (a) Beam Elements, (b) Plane Strain Elements.

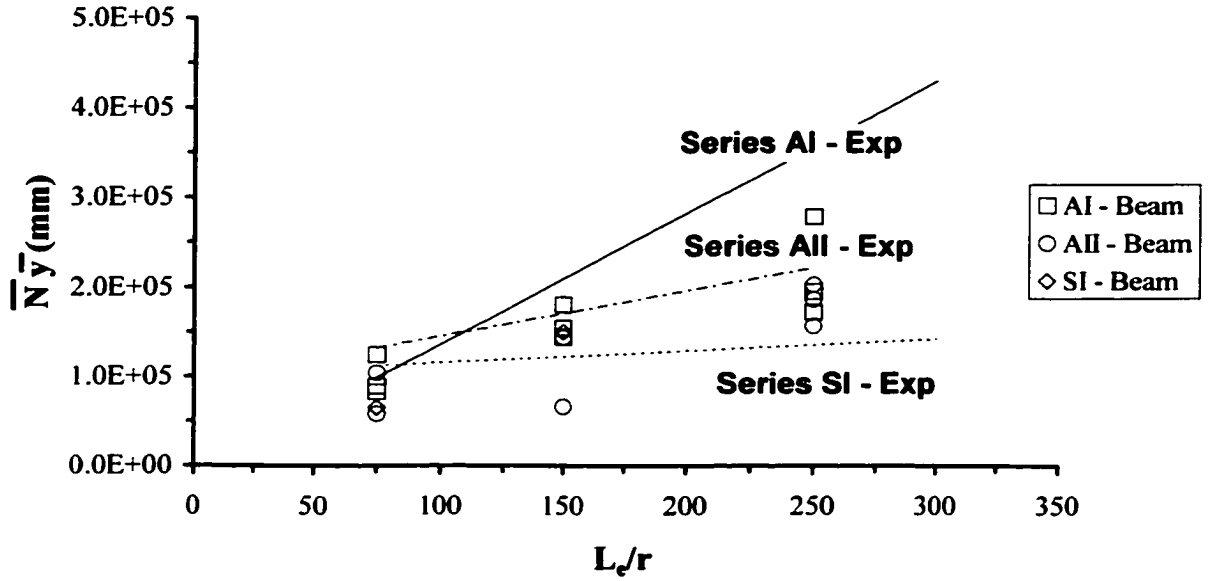

(a)

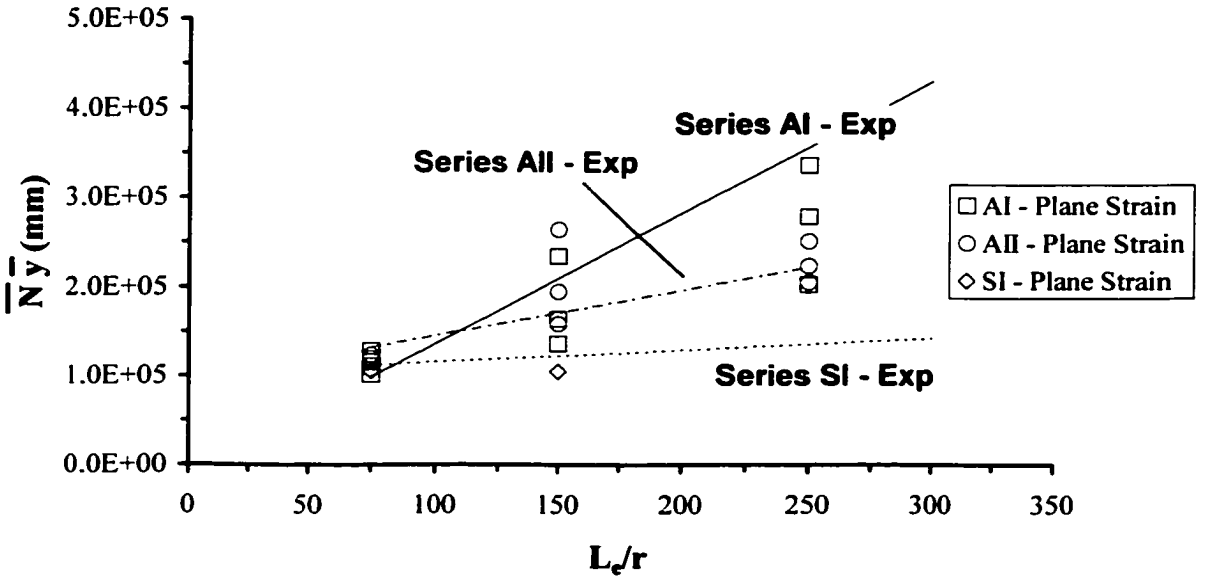

(b)

Figure 7-8. Normalized Mean Transverse Modal Response $(\overline{N}\,y)$ of the Peak Buckle Crest as a Function of the Effective Slenderness Ratio (L_e/r) for Finite Element Models with (a) Beam Elements, (b) Plane Strain Elements.

In general terms, the plane strain element models exhibited somewhat improved performance with respect to the experimental data for the normalized axial $(\overline{N}\,\overline{x})$ and transverse $(\overline{N}\,\overline{y})$ response parameters. As discussed in Section 7.3.3, this may be attributed to the inherent characteristics of the element formulation; for example moment-curvature relationship, and the higher frequency response and greater influence of the axial force on modal behavior for Euler-Bernoulli beams as the aspect ratio tends to unity. The general convergence of the normalized response parameter, for both element formulations, with decreasing slenderness ratio (Figure 7-7 and Figure 7-8) indicates the peak buckle response is coupled with other mechanisms.

Numerical modeling of the dynamic pulse buckling behavior is a complex task that must account for a number of issues including, strain field discontinuity, changes in element behavior (i.e. coupled mechanical and modal characteristics), and stress wave propagation and boundary effects. The modal response is also related to the relative beam stiffness as a function of the slenderness ratio and structural boundary conditions, as well as the interaction between the applied impulsive load and elastic unloading wave characteristics. Furthermore, the stiffness and modal characteristics of the finite element model is a function of the numerical noise, high frequency response components, and energy dissipation mechanisms.

For the lower slenderness ratios, the pulse buckling response approaches the behavior of the relatively simple mechanical model of the "Type II" structure illustrated in Figure 5-11. The analyses presented by Karagiozova and Jones (1995a, 1995b) and Su et al. (1995a, 1995b) stated that impact mass/beam ratio, impact velocity, imperfection amplitude, strain-hardening parameter and rate-sensitivity were important factors that influenced the dynamic buckling response. Thus, the experimental and finite element investigations of the present study indicate that with increasing slenderness ratio, the pulse buckling response becomes increasingly complex and coupled phenomenon.

The potential significance of dynamic material behavior (e.g. flow stress, rate-sensitivity) on the pulse buckling response was recognized by the experimental investigations, in particular for the steel beams was illustrated in Chapter 6 (Figure 6-10). This was further supported through analysis of the numerical computations, which indicated that the finite element models over predicted the transverse deflection with increasing slenderness ratio. The analysis conducted by Su et al. (1995) concluded that the compressive response was primarily equated with axial inertia while the flexural response was strongly influenced by rate-sensitive behavior. Furthermore, a dynamic yield response is associated with an increased flow stress and stored elastic compression energy and a corresponding decrease in the peak buckle amplitude. These factors are consistent with the experimental investigations and assessment of the limited finite element computations.

In consideration of the software limitations for the finite element analysis (e.g. contact mechanics, rate-dependent material behavior, element formulation and integration schemes), the complexity of the numerical computations and the relative simplicity of the normalized response parameter (Section 6.2.3), the general agreement between the numerical analyses (Figure 7-7 and Figure 7-8), analytical expressions, and experimental data (Figure 6-12 and Figure 6-13) show promise. On this basis, it can be stated that the dynamic pulse buckling response can be characterized by the normalized modal parameter as a function of the effective slenderness ratio.

Further confidence in the finite element computations can be realized through an assessment of the peak buckle half-wavelength response. A summary of the half-wavelengths based on Equation (6.5), experimental data and finite element models is presented in Table 7-4. The peak buckle half-wavelength response is also illustrated in Figure 7-9, for the finite element analyses of Series AI and Series AII with models employing beam and plane strain elements with an aspect ratio of 1:1.

Table 7-4. Analytical, Experimental and Finite Element Investigations on the Peak Buckle Half-Wavelength ($\bar{x}$) Response.

Parameter			AI	AII	SI
Equation (6.5) – n = 1		$\bar{x}$	61mm–168mm	79mm–203mm	49mm–134mm
Equation (6.5) – n = 2		$\bar{x}$	31mm–84mm	39mm–01mm	24mm–67mm
Experimental		$\bar{x}$	51mm – 72mm	75mm – 103mm	53mm – 78mm
Finite Element	Plane Strain	$\bar{x}$	34mm–150mm	60mm–142mm	29mm
	Beam	$\bar{x}$	24mm–149mm	77mm–176mm	25mm – 42mm

7.5 Assessment of the Pulse Buckling Analysis

Although the finite element solution was generally consistent with the experimental pulse buckling response, there were several unresolved issues and questions that warrant further investigation.

Future parametric analysis should consider the influence of a variation in impact mass and velocity, initial imperfection formulation and magnitude and materials with significantly different elastic wave speed constants. For example, the discrete fundamental mode should have a greater influence on the buckled response for a combination of increased mass, decreased impact velocity and/or greater imperfection amplitude. Karagiozova and Jones (1995b, 1996) demonstrated this behavior for a simple mechanical model (Figure 5-12) with the nondimensional relationships illustrated in Figure 5-13(b).

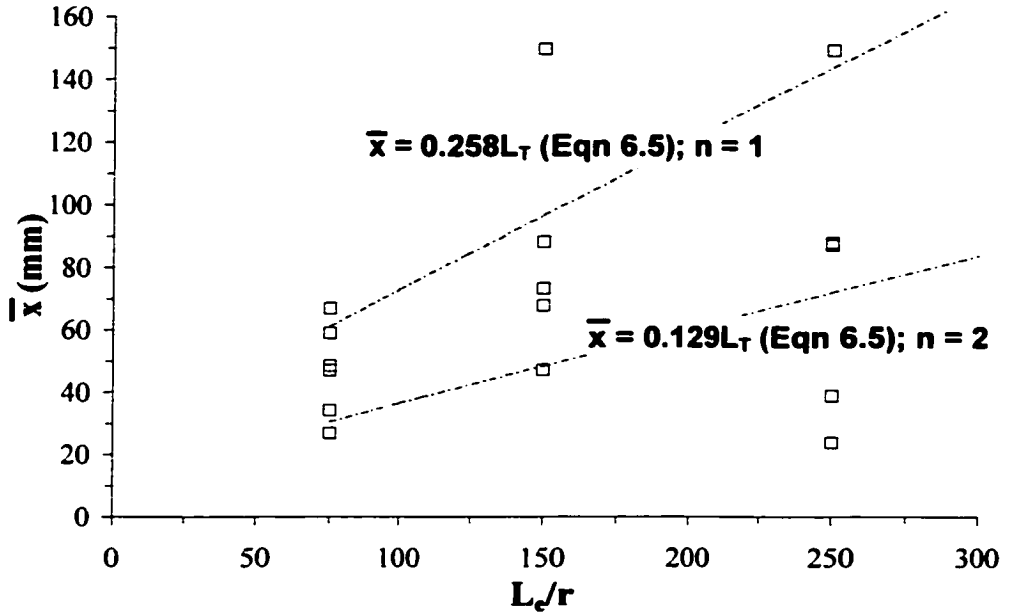

(a)

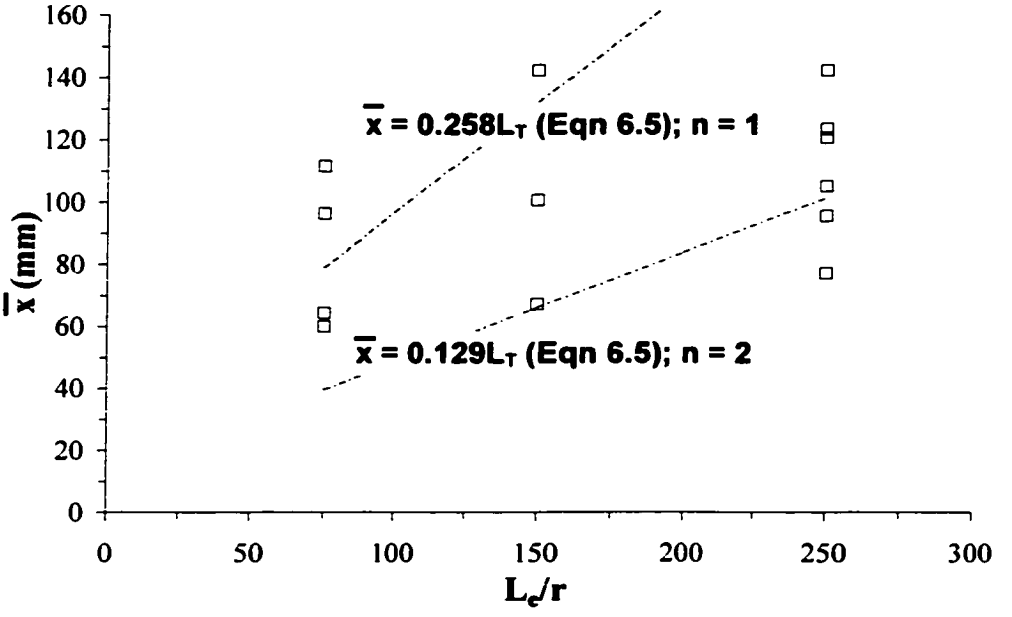

(b)

Figure 7-9. Mean Half-Wavelength Response of the Peak Buckle Crest for the Finite Element Models (a) Series AI, and (b) Series AII.

The studies should be conducted in parallel with investigations that can examine the limitations of the present analysis. The critical issues were related to modelling considerations such as element formulation, constitutive relationships and contact mechanics. Some of these issues are addressed in the following sections on a theoretical basis in terms of finite element procedures within the context of the present experimental and numerical investigations conducted.

7.5.1 Direct Integration Procedures

Typically, dynamic pulse buckling events that have been considered in the present investigations, which are concerned with wave propagation events, are examined using explicit integration schemes (e.g. central difference operator). For NISA, only the implicit procedure was available.

Explicit schemes are favored for a number of reasons. The main advantage of the explicit integration procedure is the computational efficiency for each solution increment since the nodal displacement and velocity is computed at the current time step. Implicit schemes require matrix factorization (i.e. formation and inversion of the effective stiffness matrix), larger core storage and a greater number of operations per time step. The bulk of the computational effort for explicit time integration algorithms is in the formation of the internal force vector. The major disadvantage is the conditional stability of explicit schemes. For analysis of rapid, transient events with high frequency components (e.g. wave propagation, impact, shock loads), however, the critical time step is on the same order as that required by the Courant stability parameter. Furthermore, for discontinuous events or processes, for example stress wave front or significant strain gradients; explicit integration schemes are generally be more efficient than implicit integration due to the modelling of lumped properties.

Consequently, future investigations should examine the influence of explicit integration procedure on the computed pulse buckling response.

7.5.2 Element Formulation

The beam element formulation in NISA is based on the Kirchoff hypothesis with a cubic shape function and the mass distributed on a consistent basis. As previously discussed, the main assumptions include plane section remain plane with deformation, with the behaviour defined by the moment–curvature and axial strain–displacement relationships. For the dynamic buckling events considered in the present investigations, incorporating explicit integration schemes coupled with low order finite elements is generally the most effective modelling procedure. Thus, employing lumped mass, linear beam element formulations (e.g. Timoshenko beam theory) may be beneficial in modelling the longitudinal distribution of the strain gradient associated with the peak buckle crest.

For the plane strain element models, the pulse buckling computations may have been influenced by element characteristics. The higher-order continuum element would introduce greater numerical noise and energy modes to the system response. Low-order plane strain elements would be beneficial in modelling localized plasticity due to the solution gradient or discontinuity along the element edge. Influence of the plane strain element formulation on the pulse buckling response is also coupled with material parameters. For von Mises and Hill plasticity formulations, the material behaviour is fully incompressible and the effects tend to dominate the rate of total deformation with increasing plasticity. The plastic response assumes approximately incompressible behaviour as implied by the normality condition of the flow rule of Equation (5.5). Zienkiewicz and Cheung (1967) state that for plane strain elements, numerical difficulties are encountered due to the nearly incompressible material response where the tangent stiffness matrix becomes indeterminate.

For fully integrated quadratic elements, such as the *NKTP = 2* formulation in NISA, volumetric element locking can potentially occur. This is related to the development of a spurious pressure stress at the Gauss points that results in an over stiff response for deformations that should not result in a volume change. Future investigations should consider employing lower-order plane strain elements with full or reduced integration. From a general modelling perspective, the main drawback of reduced integration is a kinematic, zero energy mode that can result in mesh instability or a spurious singular mode referred to as "hourglassing".

Although not offered in *NISA* for nonlinear dynamic analysis, other formulations include hybrid and incompatible mode elements. The hybrid elements define the singularity as an independent variable related to the displacement solution, governing constitutive model and the compatibility condition. Incompatible modes incorporate shape functions (e.g. bubble functions) to represent internal degrees of freedom to reduce the parasitic shear; an example would be a bilinear quadrilateral with a central mode to negate shear locking when modelling pure flexure. Crisfield (1997) states that numerical difficulties (i.e. eigenmodes and hourglass) can be encountered with the incompatible mode or enhanced strain formulation for problems that involve large compressive strains.

7.5.3 Constitutive Relationship

For the dynamic pulse buckling computations, an important consideration is the numerical procedures employed by the finite element program for defining the material response. Theoretical issues relating to the constitutive relationships in terms of the pulse buckling response are addressed.

As previously discussed, the finite element computations, in comparison with the experimental data, suggest that dynamic flow stress and rate-sensitivity were not

significant factors influencing the pulse buckling response of the aluminum 6061-T6 beams. This is consistent with the studies of Perrone (1965) and Symonds and Frye (1988) for simplified mechanical models. The investigations concluded that a rigid-plastic analysis was adequate for impact energies on the order of three times the elastic strain energy and pulse duration smaller than the natural period of vibration.

In nonlinear analysis, the finite element method must integrate the stress–strain response (i.e. material state), typically evaluated independently at each spatial integration point, over a specified load/time step increment. For a displacement-based solution, the incremental deformation gradient (i.e. strains, rotations) is passed to the specified constitutive relationship algorithm to define the mechanical response through state variables. In terms of the plasticity models considered for the present study, the rate equations that must be integrated include the strain rate decomposition (Equation 5.3), flow rule (Equation 5.5) and the evolutionary hardening parameter. For *NISA*, integration of the stress-strain laws is conducted by an explicit Euler forward technique with sub-increments and/or an implicit generalized trapezoidal scheme.

The generalized form of the material tangent stiffness matrix $[K_t]$ can be defined as,

$$[K_t] = \int_V [B]^T [C_t][B]\, dV \tag{7.2}$$

where $[B]$ is the characteristic strain–displacement matrix defined as $[B]=[\partial][N]$ where $[N]$ is the shape or interpolation function matrix and $[C_t]=\partial\sigma/\partial\varepsilon$ is the tangent modular matrix. For one-dimensional, elastoplastic problem it can be shown that the tangent modulus can be evaluated as,

$$[C_t] = E\left[1 - \frac{E}{E + \left(\frac{d\sigma}{d\varepsilon}\right)_p}\right] \tag{7.3}$$

where $\left(\frac{d\sigma}{d\varepsilon}\right)_p$ is the strain hardening parameter or slope of the plastic response for the bilinear stress-strain relationship.

For elastic, perfectly plastic material behaviour, the significance is related to the tangent stiffness or Jacobian matrix $\left(\partial\sigma/\partial\varepsilon\right)$, where the stress state for a large number of elements exceed yield and a fully, plastic zone has developed. This can lead to an ill-conditioned or singular matrix. The tangent stiffness is required to equate incremental nodal displacement vector with the incremental nodal load vector. Employing the generalized trapezoidal scheme, Gauss point iterations are not required with the von Mises yield criterion where the yield function (Equation 5.1) defines the limit surface and the constitutive model does not evolve during deformation. For the bilinear elastoplastic material mode truncations errors are carried forward through integration of the rate equations (i.e. incremental stress) independent of satisfying equilibrium at the end of each increment. Crisfield (1991) has stated that although this error should be minimal, as it is proportional to the square of the stress increment for the Euler method, the volumetric locking for the plane strain element may compound the errors.

Since the implicit Newmark (dynamic time integration) and the Newton methods (nonlinear equilibrium equations) have been employed, the plasticity algorithm must also account for material stiffness variation through the Jacobian matrix. Furthermore, for rate

dependent models (i.e. incremental plasticity theory), the analysis is coupled with the Jacobian and the plasticity integration procedure employed.

As discussed in Section 5.3.3, for strain rates on the order of 10^3/s, which are of interest for the current impact events, the flow stress for mild steel typically exhibits an increase by a factor of approximately three. In addition, Harding (1987) states that an increase in the quasi-static strength raises the threshold strain rate required for rate dependent behaviour. The constitutive relationships defined in *NISA* could not account for a dynamic material behaviour. Consequently, further investigations on the importance of dynamic yield flow stress and strain rate sensitivity on the pulse buckling computations should be conducted.

From this perspective, the analyses conducted by Karagiozova and Jones (1997, 1996, 1995) and Su et al. (1995a, 1995b), employing relatively simple mechanical models, have provided significant insight. Rate sensitive behaviour increases the peak load (i.e. flow stress) and stored, elastic compression energy, due to the dynamic yield response, and decreases the buckle displacements. The dynamic impact loads for strain rate sensitive, material behaviour was influenced by the impact velocity and large mass ratios. Although, the compression phase was primarily equated with inertia and the flexural response with rate-sensitive behaviour, Su et al. (1995b) states that inertia was a dominant factor throughout the deformation process. As discussed in section 6.2.3 and section 7.4, these issues are consistent with the experimental observations and finite element computations on the dynamic plastic pulse buckling response of beams investigated during the current study.

7.6 Dynamic Plastic Pulse Buckling Criteria

A complete engineering assessment of the dynamic structural response requires the development of a pulse buckling criterion, which defines lower or upper bounds for pulse buckling threshold limits. In contrast with the static counterpart, characterization of limiting criteria for dynamic buckling instability is relatively arbitrary and subject to wide interpretation. The envelope could be defined by excessive growth of a flexural displacement response with respect to the initial geometry configuration. Alternative formulations could be based on critical impulse velocity or load intensity. The parametric relationships defining the pulse buckling criterion could be expressed in terms of the structural geometry (e.g. slenderness ratio, diameter to wall thickness ratio) or mechanical properties (e.g. yield stress, factored plastic strain). In addition to the inherent nature of pulse buckling events, the criterion must also address objective engineering constraints. For example, in terms of crashworthiness the structural support frames of an automobile must be designed for efficient energy absorption and low shock levels imparted to the passengers. The primary considerations for space re-entry vehicles would be structural integrity in terms of geometry, weight and elastic pulse buckling threshold limits.

Few studies have addressed defining dynamic pulse buckling criterion for axially loaded beams. Budiansky and Hutchinson (1966) defined dynamic buckling, with respect to the static counterpart, as an incremental change in load intensity that causes a transition from a bounded to unbounded response. Based on this study, Ari-Gur et al. (1982) defined a critical state, as the dynamic axial strain ($(\varepsilon_{cr})_D$) associated with a rapid change in slope ($dw/d\varepsilon_c$). This was illustrated in Figure 2-9 where the transverse deflection (w) and slope ($dw/d\varepsilon_c$) are presented as a function of the compressive strain (ε_c). The dynamic buckling criterion was presented in terms of a dynamic load amplification factor as a function of the effective slenderness ratio. Ari-Gur et al. (1982) concluded that the main governing parameters were the initial geometric imperfection, impulse duration and slenderness ratio.

The analysis, however, considered only the elastic, midspan deflection and did not investigate the dynamic response of the peak buckle crest.

Ari-Gur and Elishakoff (1993) considered a variant on the dynamic buckling criterion in terms of the peak axial displacement and midspan lateral deflection in terms of the applied load intensity (i.e. load per unit beam width). The pulse duration considered, however, was of the same order as the natural frequency response or approached quasi-static conditions.

Lindberg and Florence (1987) defined an elastic buckling criterion in terms of a nondimensional critical impulse duration to first yield stress as a function of the normalized stress ratio, applied stress to yield stress. The analysis assumed that the buckling motion could be defined based on a "preferred" mode response with a single equivalent single imperfection related to the dominant wavelength. This buckling criterion was illustrated in Figure 2-12 and Figure 2-13.

For the current study, the buckling criterion was based on the transverse deflection–time history of the peak buckle crest and defined by the transition from a bounded to unbounded response. The corresponding solution time was compared with the theoretical buckling time estimate developed by Lindberg and Florence (1987) for plastic buckling events, which was based on the dynamic amplification function and nondimensional time parameter.

The theoretical buckling time was estimated by the expression, $\tau_T = \dfrac{\sigma t}{r\sqrt{E_T P}}$, which was previously defined by Equation (5.12). The nondimensional time parameter, $\tau = 8$ was selected based on the amplification function for geometric imperfections as

illustrated in Figure 5-14(b). The applied load (P) was determined from the finite element computations.

Buckling times for the finite element models based on the midspan and peak buckle transverse displacement response are summarized in Table 7-5 with the corresponding theoretical buckling times (Equation 7.4) presented for comparison. There is general agreement between the numerical and theoretical buckling time estimates. Although not a comprehensive assessment, the analysis demonstrates the importance of considering the peak buckle response. Further parametric investigations are required to more fully address the dynamic pulse buckling criterion in detail. Factors such as slenderness ratio, load intensity, dynamic material behavior, element formulation and contact mechanics should be examined.

Table 7-5. Computed and Theoretical Critical Buckling Times.

Series	FE Analysis (μs)		Theoretical (μs)
	Peak Buckle	Midspan	
AIa	240	250	350
AIc	350	425	
AIe	425	550	
AIIa	300	350	527
AIIc	450	475	

8.0 Summary and Conclusions

A synopsis of the main findings and conclusions developed during the course of the research investigation is presented. Recommended future research areas are also identified and summarized.

8.1 Scope of Analysis

Focus of the current investigations was on the elastic and plastic dynamic pulse buckling response of a slender beam, with geometric imperfections, subject to an intense, axial impulse. Dynamic pulse buckling can be defined as the structural response to a transient forcing function. Dynamic instability is particularly critical for lightweight, thin walled members, which is advantageous in structural design optimization, subject to impulsive loads (e.g. impact, transient). For example, beam elements are an integral component of structural systems for main structural support (e.g. columns, transverse beams) or as stiffening members (e.g. cylindrical shells, box beams). The importance of dynamic pulse buckling is founded in the fields of transportation (e.g. crash worthiness studies), civil structures (e.g. pressure vessels, nuclear reactors), aerospace and military structures.

Numerical analyses, employing the finite difference and finite element methods, as well as experimental investigations were conducted. Quasi-static and shock wave loading events were not considered. The present study was concerned with high order events defined by intense transient loading conditions (i.e. large amplitude, short time period), which exceeded the critical static buckling Euler limit. The pulse buckling event was associated with stress wave propagation, where dynamic instability arises due to the presence of structural geometric imperfections, eccentric loading conditions or nonuniform boundary conditions. Exploitation of these parameters by impulsive loads can lead to

motion perturbations characterised by an unbounded growth of transverse displacements, which can ultimately compromise structural integrity.

8.2 Elastic Pulse Buckling

Historically, research efforts have focused on the fundamental mode response of a simply supported beam defined by a half-sine wave geometric imperfection; for example, Sevin (1960). In general, the load intensity was greater than the static Euler limit by a factor of 3–5 times lower than the yield stress. The relatively low order buckling events could neglect axial inertia and were comparable to uniaxial tests in universial test loading frames. Later efforts considered more intense impact events but were limited to the discrete imperfection mode; for example, Sugiura et al. (1985) and Ari-Gur and Elishakoff (1993).

For the present study, dynamic elastic pulse buckling was defined as the excessive growth of transverse displacements due to an intense transient load, on the order of the proportional limit, which significantly exceeded the critical static Euler load. The buckling response of a slender beam, with initial geometric imperfections, subjected to an elastic axial impulse was considered. The main objective was the advancement of numerical models, via the finite difference and finite element methods, consistent with the "preferred" wavelength theory. Details of the numerical models were presented and the analyses were discussed in terms of the peak buckle displacement amplitude, transverse displacement–time history and modal response.

Historically, only the discrete fundamental mode, imperfection formulation has been considered. Consequently, one of the most important findings of the numerical investigations was that the characteristic unbounded growth of transverse displacements was only initiated when random geometric imperfections were incorporated. The numerical investigations substantiated the validity and utility of the 'simplified' elastic

pulse buckling analysis presented by Lindberg (1965) and Lindberg and Florence (1987). For a slender beam subject to an elastic axial impulse, the peak buckle amplitude and dominant waveform could be effectively defined in terms of a single "preferred" mode.

For early solution times, the assumption of a constant, uniform axial impulse was confirmed. Thus, the longitudinal position of the stress front with respect to the evolved buckled response could be ignored. The analysis was accurate, with respect to the complete pulse buckling response (i.e. peak buckle amplitude growth, modal response and stress state), only for aspect ratios on the order of 1:1. Deviation of the finite element response from the unbounded growth of transverse displacements to a 'limiting' plateau was observed. This was related to a variation in the axial stress state, impulse reduction and axial inertia effects. The superior performance of quadratic, plane strain elements to accurately model the complete pulse buckling response was demonstrated. The limitation for beam element models was related to the inherent element formulation characteristics such as the assumptions of Euler-Bernoulli beam theory, moment–curvature and axial strain–displacement relationships. The plane strain element models, however, required significant computational resources and consideration of nonlinear material behaviour. Finally, a pulse buckling threshold criterion, defined by a nondimensional load duration and normalized stress ratio with respect to the yield stress, was successfully modelled.

In summary, the development of accurate finite element models to represent the elastic pulse buckling of slender beams in reference to the "preferred" wavelength theory requires (i) incorporation of random geometric imperfections, (ii) defining a finely discretised domain with aspect ratios on the order of 1:1, and (iii) consideration of nonlinear geometric analysis coupled with nonlinear material behaviour for plane strain element models

8.3 Experimental Investigations

Extensive investigations have been conducted to define constitutive relationships on the impact behaviour of bars at high strain rates (Meyers 1994). Relatively few studies have addressed the dynamic plastic buckling response of bars subject to an intense axial impact. Historically, majority of the analytical and experimental research efforts has focused on the fundamental mode response and concerned with elastic buckling threshold limits; for example Ari-Gur et al., (1982, 1979, 1978). Numerous studies, however, have shown that for intense impulsive load events the elastic and plastic dynamic buckling instability was characterised by evolution of a higher order modal response; for example, Bell (1988) and Abrahamson and Goodier (1966).

Details of an experimental investigation on the dynamic plastic buckling of slender beams subjected to axial impact were presented. A 10kg free fall impact hammer with a nominal impact velocity of 6.2m/s defined the impact event. Two rectangular cross-sections, for 6061-T6 aluminum and CR1020 steel beams, over a range of slenderness ratios with a clamped–slide bearing boundary condition were investigated.

The initial global geometric imperfections and final buckled profiles were measured along the longitudinal axis of the beam. The peak buckle response was characterized by a normalized modal parameter $(\overline{N})$, which accounted for local stiffness and natural frequency response characteristics, as a function of the effective slenderness ratio. The modal parameter was employed to assess the peak buckle response in terms of the axial position and transverse amplitude. In addition, the influence of dynamic material behaviour on the peak buckle response for the cold rolled steel beams was inferred. Simplified theoretical expressions defining the critical buckle wavelength were in reasonable agreement with the experimental data.

8.4 Plastic Pulse Buckling

Development and analyses of finite element models examining the experimentally observed plastic pulse buckling response, of a slender beam subject to axial impact, was conducted. The parametric study considered the influence of element formulation, element aspect ratio, geometric imperfection model, constitutive relationships, applied boundary condition and contact mechanics. Three main objectives defined the scope of the investigations; (i) to develop accurate numerical models consistent with the experimentally observed pulse buckling response, (ii) to develop relationships that characterize the dynamic peak buckle response and mode behavior, and (iii) to conduct a preliminary assessment on a dynamic pulse buckling criterion

Consequently, the primary objectives of the present thesis investigations are to augment and to extend the current experimental database, to provide an empirical basis to validate numerical models, and to develop relationships that characterize the dynamic pulse buckling response

The finite element analysis substantiated the validity for characterizing the pulse buckling response of a slender beam subject to axial impact by a normalized modal parameter $(\overline{N})$ as a function of the effective slenderness ratio. For the parameters considered, a sensitivity analysis demonstrated that the modelled boundary condition and element formulation had the most significant influence on the computed pulse buckling response. The relative influence of element aspect ratio, imperfection model and contact mechanics was of secondary importance on the computed modal behaviour.

Although a "simple" axial impact event has been considered, numerical modelling of the dynamic, plastic pulse buckling response is a complex and demanding task. The investigations also suggested that additional parameters might be coupled to the nonlinear

dynamic buckling process. These factors include the strain field discontinuity, element frequency characteristics, local stiffness effects (e.g. material and structural), as well as stress wave propagation and boundary interaction effects. The importance of any correlation with the modal response, however, was not resolved in the present study and further investigations are warranted.

Based on comparison of the experimental and computed buckling response, it was inferred that dynamic material properties should be considered. A definitive conclusion could not be developed due to software limitations, where dynamic, rate dependent material properties could not be modelled.

8.5 Recommendations for Future Research

Based on the investigations conducted and conclusions developed during the course of the study, recommendations for areas of future research are forwarded.

8.5.1 Dynamic Elastic Pulse Buckling

The validity and utility of the simplified "preferred" wavelength theory and elastic pulse buckling threshold limit has been demonstrated. The expressed requirements for the development of accurate and realistic phenomenological models defining the complete modal response must be considered. These parameters include the geometric imperfection model, discretised aspect ratio, element formulation and the coupled nonlinear computational routine (i.e. materia, geometric effects). Future research should investigate structures with more complex geometry, loading events, varied boundary conditions or mechanical properties. For these studies, the coupled response and modal competition has to be addressed on a rational basis through computational tools such as the finite element method.

8.5.2 Experimental Investigations

One of the primary objectives for the experimental study was to assess the peak buckle and midspan response in terms of defining a lower bound elastoplastic threshold limit or dynamic pulse buckling criterion. Historically, the response has been based on only the midspan deflection (Ari-Gur et al., 1982; Ari-Gur and Elishakoff, 1993). Unfortunately, the establishment of engineering relationships, based on a comprehensive strain record, was not successful during the experimental investigations due to the loss of strain gauge leads. Acquisition of high-speed imaging techniques and alternative measurement systems for future experimental investigations is recommended. In terms of developing a pulse buckling criterion, parametric investigations should also consider a variation in the applied boundary condition and impulse load intensity. In addition, materials should be selected to examine the wave speed parameter, which is a function of the modulus and density, and dynamic material properties, including strain rate independent and strain rate sensitive behaviour.

8.5.3 Dynamic Plastic Pulse Buckling

Although the finite element analysis was consistent with the measured experimental buckled response data, a number of issues require a further comprehensive study:

- To consider the influence of element formulation on modelling the pulse buckling response and significant strain field discontinuity associated with the stress wavefront and peak buckle crest. Lower order elements with full and reduced integration and/or incompatible mode elements should be examined
- To investigate the influence of modelling procedures for the contact mechanics and boundary conditions on the pulse buckling response
- To incorporate explicit integration schemes

- To examine the influence of dynamic material properties and rate dependent behaviour on the pulse buckling response computations

- To conduct parametric investigations, in parallel with empirical studies, that also examines the imperfection model, load intensity and load character (i.e. mass–velocity, force–time)

- To assess the parametric studies for the development of dynamic pulse buckling threshold limits and a dynamic buckling criterion.

References

Abrahamson, G.R. and Goodier, J.N. (1966). "Dynamic Flexural Buckling of Rods within an Axial Plastic Compression Wave." Journal of Applied Mechanics, Transactions ASME, Volume 33, Series E, pp.241-247.

Abramowicz, W. and Jones, N. (1986). "Dynamic Progressive Buckling of Circular and Square Tubes." International Journal of Impact Engineering, Volume 4, Number 4, pp.243-270.

Abramson, H.N., Plass, H.J. and Ripperger, E.A. (1958). "Stress Wave Propagation in Rods and Beams." Advances in Applied Mechanics, Editors H.L. Dryden and T. von Kármán, Volume V, Academic Press Inc., Publishers, New York, NY, USA, pp.111-194.

ADINA (1996). User's Manual, Finite Element Program for Automatic Dynamic Incremental Nonlinear Analysis, ADINA R&D, Inc., 71 Elton Avenue, Watertown, MA, USA 02172, (http://world.std.com/~adina/).

Al-Bermani, F.G.A. and Zhu, K. (1995). "Nonlinear Elastoplastic Analysis of Spatial Structures under Dynamic Loading using Kinematic Hardening Models." pp.568-576.

Albertini, C., Halleux, J.P. and Montagnani, M. (1978). "Material Behaviour and Modelling in Transient Dynamic Situations." Advanced Structural Dynamics, J. Donéa Editor, Applied Science Publishers Limited, London, UK, pp.427-463.

Ammann, W.J., Liu, W.K., Studer, J.A. and Zimmerman, T. (1988). Impact: Effects of Fast Transient Loadings. Proceedings, First International Conference on Effects of Fast Transient Loadings, Editor W.J. Amman, W.K. Liu, J.A. Studer and T. Zimmerman, A.A. Balkema, Rotterdam, Netherlands, 385p.

Ames, W.F. (1977). Numerical Methods for Partial Differential Equations. Second Edition. Computer Science and Applied Mathematics, A Series of Monographs and Textbooks, Editor W. Rheinboldt, Academic Press Inc., New York, NY, USA, 365p.

ANSYS (1996). Users Manual, ANSYS Version 5.3, Troy Technology Park, 1960 Ring Drive, Troy, MI, USA, 48083, SAS IP Inc., (http://www.ansys.com).

Ari-Gur, J. and Elishakoff, I. (1993). "Dynamic Pulse Buckling of a Transversely Isotropic Column." Proceedings, ASME, Pressure Vessel and Piping, Volume 269, Recent Advances in Structural Mechanics, pp.29-35.

Ari-Gur, J. and Elishakoff, I. (1990). "Effects of Shear Deformation and Rotary Inertia on the Dynamic Pulse Buckling of a Structure." Impact and Buckling of Structures, Transactions ASME, Winter Annual Meeting of the American Society of Mechanical Engineers, AD-Volume 20, Editors, David Hui and Isaac Elishakoff, Dallas, TX, USA, pp.71-75.

Ari-Gur, J., Weller, T and Singer, J. (1982). "Experimental and Theoretical Studies of Columns under Axial Impact." International Journal of Solids and Structures, Volume 18, Number 7, pp.619-641.

Ari-Gur, J., Weller, T and Singer, J. (1979). Theoretical Studies of Columns under Axial Impact and Experimental Verification. Technion Israel Institute of Technology, Department of Aeronautical Engineering, TAE No.377, Haifa, Israel, 59p.

Ari-Gur, J., Weller, T and Singer, J. (1978). Experimental Studies of Columns under Axial Impact. Technion Israel Institute of Technology, Department of Aeronautical Engineering, TAE No.346, Haifa, Israel, 63p.

Bathe, K-J. (1996). Finite Element Procedures. Prentice-Hall, Inc., Englewood Cliffs, NJ, USA, 1037p.

Bažant, Z.P. and Cedolin, L. (1991). Stability of Structures. Oxford University Press, New York, NY, USA.

Belingardi, G. and Vadori, R. (1993). "On the Role of Geometrical Imperfections in the Impact Collapse of Thin-Walled Spot-Welded Beam: Numerical and Expeerimental Results." Crashworthiness and Occupant Protection in Transportation Systems, Transactions ASME, pp.115-125.

Bell, J.F. (1988). "The Dynamic Buckling of Rods at Large Plastic Strain." Acta Mechanica, Volume 74, pp.51-67.

Bell, J.F. (1968). "An Experimental Study of Instability Phenomena in the Initiation of Plastic Waves in Long Rods." Mechanical Behaviour of Materials under Dynamic Loads, Editor Ulric S. Lindholm, Springer-Verlag, New York, NY, USA, pp.10-20.

Bodner, S.R. (1968). "Constitutive Equations for Dynamic Material Behaviour." Mechanical Behaviour of Materials under Dynamic Loads, Editor Ulric S. Lindholm, Springer-Verlag, New York, NY, USA, pp.176-190.

Bolotin, V.V. (1964). The Dynamic Stability of Elastic Systems. Translated by V.I. Weingarten, L.B. Greszczuk, K.N. Trirogroff and K.D. Gallegos, Holden-Day, Inc., San Francisco, CA, USA.

Brebbia, C.A. and Sánchez-Gálvez, V. (1994). Shock and Impact on Structures. Editor C.A. Brebbia and V. Sánchez-Gálvez, Computational Mechanics Publications, Southampton, UK, 278p.

Brooks, W.A. and Wilder, T.W. (1954). "The Effect of Dynamic Loading on the Strength of an Inelastic Column." National Advisory Committee for Aeronautics, NACA Technical Note 3077, Langley Aeronautical Laboratory, Langley, VA, USA, 29p.

Budiansky, B. and Hutchinson, J.W. (1966). "Dynamic Buckling of Imperfection Sensitive Structures." Proceedings, 11th International Congress of Applied Mechanics, Munich, FRG, 1964, Editor H. Görtler, Springer-Verlag, pp.636-651.

Bulson, P.S. (1994). Structures under Shock and Impact. Proceedings, Third International Conference, Editor P.S. Bulson, Computational Mechanics Publications, Southampton, UK, 504p.

Calladine, C.R., and English, R.W. (1984). "Strain-Rate and Inertia Effects in the Collapse of Two Types of Energy-Absorbing Structure." International Journal of Mechanical Science, Volume 26, pp.689-701.

Campbell, J.D (1970). Dynamic Plasticity of Metals. International Centre for Mechanical Sciences, Course and Lectures Number 46, Springer-Verlag, Udine, Italy, 89p.

Chang, K.C., Sugiura, K. and Lee, G.C. (1989). "Rate-Dependent Material Model for Structural Steel." Journal of Engineering Mechanics, Volume 115, Number 3, pp.465-475.

Clifton, .J. (1983). "Dynamic Plasticity." Transactions, ASME, Journal of Applied Mechanics, Volme 50, Number 4b, pp.941-952

Courant, R., Friedrichs, K. and Lewy, H. (128). "Über die partiellen Differenzengleichungen der mathematischen Physik." Mathematische Annalen, Volume 100, pp.32-74.

Cook, R.D., Malkus, D.S. and Plesha, M.E. (1989). Concepts and Applications of Finite Element Analysis, Third Edition. John Wiley & Sons, Inc., New York, NY, USA, 630p.

Crisfield, M.A. (1997). Non-Linear Finite Element Analysis of Solids and Structures. Volume 2 Advanced Topics. John Wiley & Sons, Inc., New York, NY, USA, 494p.

Crisfield, M.A. (1991). Non-Linear Finite Element Analysis of Solids and Structures: Volume 1 Essentials. John Wiley & Sons, Inc., New York, NY, USA, 345p.

Davidson, J.F. (1953). "Buckling of Struts under Dynamic Loading." Journal of the Mechanics and Physics of Solids, Volume 2, Number 1, pp.54-66.

Davies, R.M. (1948). "A Critical Study of the Hopkinson Pressure Bar." Philosophical Transactions, Royal Society of London, Volume 240, Series A, pp.375-457.

Duffy, J. (1982). The Dynamic Plastic Deformation of Metals: A Review. Report Prepared for Material Laboratory (AFWAL/MLLN), Air Force Wright Aeronautical Laboratories (AFSC), Wright-Patterson Air Force base, Ohio, USA, Prepared by Division of Engineering, Brown University, Providence, RI, USA, 227p.

Duffy, J. (1979). "Testing Techniques and Material Behaviour at High Rates of Strain." Mechanical Properties at High Rates of Strain, Editor J. Harding, Institute of Physics Conference Series, Number 47, pp.1-15.

Erickson, B., Nardo, S.V., Patel, S.A. and Hoff, N.J. (1956). "An Experimental Investigation of the Maximum Loads Supported by Elastic Columns in Rapid Compression Tests." Proceedings, Society for Experimental Stress Analysis, Volume 14, Number 1, C.V. Mahlmann and W.M. Murray Editors, Cambridge, MA, USA, pp.13-20.

Gary, G. (1983). "Dynamic Buckling of an Elastoplastic Column." International Journal of Impact Engineering, Volume 1, Number 4, pp.357-375.

Gerard, G. and Becker, H. (1952). "Column Behaviour under Conditions of Impact." Journal of the Aeronautical Sciences, Volume 19, Number 1, pp.58-65.

Gerard, G. and Paprino, R. (1957). "Dynamic Biaxial Stress-Strain Characteristics of Aluminum and Steel." Transactions, American Society for Metals, Volume 49, pp.132-148.

Harding, J. (1987). "The Effect of High Strain Rate on Material Properties." Materials at High Strain Rates. Elsevier Applied Science Publishers, Editor T.Z. Blazynski, London, UK, pp.133-186.

Hartz, B.J. and Clough, R.W. (1957). "Inelastic Response of Columns to Dynamic Loadings." Journal of the Engineering Mechanics Division, Proceedings ASCE, Volume 83, Number EM 2, Paper Number 1213, 14 p.

Hauser, F.E. (1966). "Techniques for Measuring Stress-Strain Relations at High Strain Rates." Experimental Mechanics, Volume 6, pp.395-402.

Hayashi, T. and Sano, Y. (1972a). "Dynamic Buckling of Bars (1st Report, The Case of Low Velocity Impact)." Bulletin of the JSME, Volume 15, Number 88, pp.1167-1175.

Hayashi, T. and Sano, Y. (1972b). "Dynamic Buckling of Bars (2nd Report, The Case of High Velocity Impact)." Bulletin of the JSME, Volume 15, Number 88, pp.1176-1184.

Hill, R. (1971). The Mathematical Theory of Plasticity. Oxford University Press, London, UK.

Hoff, N.J. (1951). "The Dynamics of the Buckling of Elastic Columns." Journal of Applied Mechanics, Transactions ASME, Volume 18, Number 1, pp.68-74.

Hoge, K.G. (1966). "Influence of Strain Rate on Mechanical Properties of 6061-T6 Aluminum under Uniaxial and Biaxial States of Stress." Experimental Mechanics, Volume 6, Number 4, pp.204-211.

Hopkinson, B. (1914). "A Method of Measuring the Pressure Produced in the Detonation of High Explosives or by the Impact of Bullets." Philosophical Transactions, Royal Society of London, Volume 213, Series A, Number 821, pp.375-457.

Housner, G.W. and Tso, W.K. (1962). "Dynamic Behaviour of Supercritically Loaded Struts." Journal of the Engineering Mechanics Division, Proceedings ASCE, Volume 88, Number EM 5, pp.41-65.

Huffington, N.J. (1963). "Response of Elastic Columns to Axial Pulse Loading." Proceedings, AIAA Journal, Volume 1, Number 9, pp.2099-2104.

Hunsaker, B., Vaughan, D.K. and Stricklin, J.A. (1976). "A Comparison of the Capability of Four Hardening Rules to Predict a Material's Plastic Behaviour." Journal of Pressure Vessel Technology, Transactions ASME, Volume 98, Series J, Number 1, pp.66-74.

IIHS (1998). Insurance Institute for Highway Safety. 1005 N. Glebe Road, Suite 800, Arlington, VA, USA 22201, (http://www.hwysafety.org).

Jiang, W. (1994). "New Kinematic Hardening Model." Transactions ASCE, Journal of Engineering Mechanics, Volume 120, Number 10, pp.2201-2222.

Jones, N. (1989). Structural Impact. Cambridge University Press, Cambridge, UK, 575p.

Jones, N. (1974). "Some Remarks on the Strain-Rate Sensitive Behaviour of Shells." Problems of Plasticity, Papers Contributed to the International Symposium on Foundations of Plasticity, Volume 2, Editor A. Sawczuk, Noordhoff International Publishing, A.W. Sijthoff International Publishing Company, B.V., Leyden, The Netherlands, pp.403-407.

Jones, N.A. (1971). "A Theoretical Study of the Dynamic Plastic Behaviour of Beams and Plates with Finite Deflections." International Journal of Solids and Structures, Volume 7, pp.1007-1029.

Kadandale, M., and Ari-Gur, J. (1997). "Dynamic Pulse Buckling of Viscoelastic Columns." Transactions AIAA, 38th AIAA/ASME/ASCE/AHS/ASC Structures, Structural Dynamics and Material Conference and Exhibit, Kissimmee, FL, USA, pp.374-381.

Karagiozova, D. and Jones, N. (1997). "Strain-Rate Effect in the Dynamic Buckling of a Simple Elastic-Plastic Model." Transactions ASME, Journal of Applied Mechanics, Volume 64, Number 1, pp.193-200.

Karagiozova, D. and Jones, N. (1996). "Multi-degrees of Freedom Model for Dynamic Buckling of an Elastic-Plastic Structure." International Journal of Solids and Structures, Volume 33, Number 23, pp.3377-3398.

Karagiozova, D. and Jones, N. (1995a). "A Note on the Inertia and Strain-Rate Effects in the Tam and Calladine Model." International Journal of Impact Engineering, Volume 16, Number 4, 1995, pp.637-649.

Karagiozova, D. and Jones, N. (1995b). "Some Observations on the Dynamic Elastic-Plastic Buckling of a Structural Model." International Journal of Impact Engineering, Volume 16, Number 4, 1995, pp.621-635.

Koning, C. and Taub, J. (1933). "Stossartige Knickbeanspruchung schlanker Stäbe im elastischen Bereich bei beiderseits gelenkiger Lagerung." Luftfahrtforschung, Volume 10, Number 2, July, 1933, p.55-64. Also, "Impact Buckling of Thin Bars in the Elastic range Hinged at both Ends." Translation by J. Vanier, National Advisory Committee for National Advisory Committee for Aeronautics, NACA Technical Memorandum Number 748, 1934, 32p.

Kulak, G.L., Adams, P.F. and Gilmor, M.I. (1990). Limit States Design in Structural Steel. Canadian Institute of Steel Construction (1990), Fourth Edition, Universal Offset Limited, Markham, ON, CA, 358p.

Lavrent'er, M.A. and Ishinskii, A.Yu. (1949). "Dynamic Forms of Loss of Stability of Elastic Systems." Doklady Akademiya Nauk SSSR,Volume 64, pp.779-782, English Translation by R. Cooper in STL-TR-61-5110-41, Space Technology Laboratories, Los Angeles, CA, USA.

Lee, L.H.N. (1981). "Dynamic Buckling of an Inelastic Column." International Journal of Solids and Structures, Editor G. Herrmann, Volume 17, Number 1, pp.271-279.

Langseth, M., Berstad, T., Hopperstad, O.S. and Clausen, A.H. (1994). "Energy Absorption in Axially Loaded Square Thin-Walled Aluminum Extrusions." Structures under Shock and Impact. Proceedings, Third International Conference, Editor P.S. Bulson, Computational Mechanics Publications, Southampton, UK, pp.401-410.

Lindberg, H.E. and Florence, A.L. (1987). Dynamic Pulse Buckling Theory and Experiment. H.H.E. Leipholz and G.Æ. Oravas Editors, Martinus Nijhoff Publishers, Dordrecht, The Netherlands, 384p.

Lindberg, H.E. (1965). "Impact Buckling of a Thin Bar." Transactions ASME, Journal of Applied Mechanics, Volume 32, Series E, pp.315-322.

Lindholm, J.S. and Besseny, R.L. A Survey of Rate Dependent Strength Properties of Metals. Air Force Materials Laboratory, Report AFML-TR-69-119, 1969.

Lindholm, U.S. and Yeakley, L.M. (1968). "High Strain Rate Testing: Tension and Compression." Experimental Mechanics, Volume 8, pp.1-9.

Maiden, C.J. and Green, S.J. (1966). "Compressive Strain-Rate Tests on Six Selected Materials at Strain Rates from 10^{-3} to 10^{-4} in/in/sec." Transactions ASME, Journal of Applied Mechanics, Series E, Number 3, pp.496-504.

Malvern, L.E. (1984). "Experimental and Theoretical Approaches to Characterisation of Material Behaviour at High Rates of Deformation." Mechanical Properties at High Rates of Strain, Editor J. Harding, Institute of Physics Conference Series, Number 70, pp.1-20.

Marsh, K.J. and Campbell, J.D. (1945). "The Effect of Strain Rate on the Post-Yield Flow of Mild Steel." Journal of the Mechanics and Physics and Solids, Volume 11, pp.49-63.

Matsunaga, H. (1996). "Free Vibration and Stability of Thin Elastic Beams Subjected to Axial Forces." Journal of Sound and Vibration, Volume 191, Number 5, pp.917-933.

MIL (1959). Strength of Metal Aircraft Elements. U.S. Department of Defense, Military Handbook, Number 5, MIL-HDBK-5, Armed Forces Supply Support Center, Washington, D.C., U.S.A., 251p.

Meier, J.H. (1945). "On the Dynamics of Elastic Buckling." Journal of the Aeronautical Sciences, Volume 12, Number 1, pp.433-440.

Mendelson,A. (1968). Plasticity: Theory and Application. Macmillan, New York, NY, USA, 353p.

Meyers, M.A. (1994). Dynamic Behaviour of Materials. John Wiley & Sons, Inc., Wiley-Interscience Publication, Toronto, ON, Canada, 668p.

Ng, D.H.Y., Delich, M. and Lee, L.H.N. (1979). "Yielding of 6061-T6 Aluminum Tubings under Dynamic Biaxial Loadings." Experimental Mechanics, Volume 19, Number 6, pp.200-206.

Newland, D.E. (1993). An Introduction to Random Vibrations, Spectral and Wavelet Analysis, 3rd Edition. Longman Scientific & Technical, Longman Group UK Limited, co-published in the USA with John Wiley & Sons, Inc., New York, NY, USA, 477p.

Nicholas, T. (1982). "Material Behaviour at High Stain Rates." Impact Dynamics, Editor Jonas A. Zukas, Theodore Nicholas, Hallock F. Swift, Longin B. Greszczuk and Donald R. Curran, Wiley-Interscience Publication, John Wiley & Sons, New York, NY, USA, Chapter 8, pp.227-332.

NISA (1997). NISA Users Manual, Version 7.0. Numerically Integrated Elements for System Analysis (NISA), Engineering Mechanics Research Corporation, P.O. Box 696, Troy, Michigan, USA 48099, (http://www.emrc.com).

Nurick, G.N., Jones, N., and von Alten-Reuss, G.V. (1994). "Large Inelastic Deformations of T-Beams Subjected to Impulsive Loads." Structures under Shock and Impact. Proceedings, Third International Conference, Editor P.S. Bulson, Computational Mechanics Publications, Southampton, UK, pp.191-206.

Owen, D.R.J. and Hinton, E. (1980). Finite Elements in Plasticity : Theory and Practice. Pineridge Press Limited, Swansea, U.K., 594p.

Pegg, N.G. (1992). Dynamic Pulse Buckling of Unstiffened and Ring-Stiffened Cylindrical Shells. Thesis, Doctor of Philosophy, Department of Civil Engineering, Technical University of Nova Scotia (presently DalTech, Dalhousie University), Halifax, NS, Canada, 185p.

Perrone, N. (1965). "On a Simplified Method for Solving mpulsively Loaded Structures of Rate-Sensitive Materials." Journal of Applied Mechanics, Volume 32, pp.489-492.

Perzyna, P. (1966). "Fundamental Problems in Viscoplasticity." Advances in Applied Mechanics, Volume 9, Editors G.G. Chernyi et al., Academic Press Inc., New York, NY, USA, pp.243-377.

Perzyna, P. (1963). "The Constitutive Equations for Rate Sensitive Plastic Materials." Quarterly of Applied Mathematics, Volume 20, pp.321-332.

Pian, T.H.H. and Siddall, J.N. (1950). Dynamic Buckling of Slender Struts. Technical Report for Contract N5 ori-07833 to Office of Naval Research, Department of Aeronautical Engineering, Massachusetts Institute of Technology, 1950, 68p.

Prager, W. (1959). An Introduction to Plasticity. Addison-Wesley, London, UK.

Reid, S.R., Edmunds, A.J. and Johnson, W. (1981). Bending of Long Steel and Aluminum Rods During End Impact with a Rigid Target. Journal of Mechanical Engineering Science, Volume 23, Number 2, pp.85-92

Rice, J.R. (1975). "Continuum Mechanics and Thermodynamics of Plasticity in Relation to Microscale Deformation Mechanisms." Constitutive Equations in Plasticity, Editor A.S. Argon, MIT Press, Cambridge, MA, USA.

Schmitt, A.F. (1956). "A Method of Stepwise Integration Problems of Impact Buckling." Journal of Applied Mechanics, Transactions ASME, pp.291-294.

Sevin, E. (1960). "On the Elastic Bending of Columns due to Dynamic Axial Forces Including Effects of Axial Inertia." Journal of Applied Mechanics, Transactions ASME, Volume 27, Series E, pp.125-131.

Shin, Y.S., and Hooker, D.T. (1994). "Damage Response of Submerged Imperfect Cylindrical Structures to Underwater Explosion." Structures under Shock and Impact, Proceedings, Third International Conference, Editor P.S. Bulson, Computational Mechanics Publications, Southampton, UK, pp.435-448.

Southwell, R.V. (1932). "On the Analysis of Experimental Observations and Problems of Elastic Stability." Proceedings Royal Society, London, Series A, Volume 135, pp.601-616.

SRI (1998). SRI International. 333 Ravenswood Avenue Menlo Park, CA 94025-3493, USA, [http://www.sri.com].

Stronge, W.J. and Yu, T.X. (1993). Dynamic Models for Structural Plasticity. Springer-Verlag, London, UK, 275p.

Su, X.Y., Yu, T.X. and Reid, S.R. (1995a). "Inertia-Sensitive Impact Energy-Absorbing Structures Part I: Effects of Inertia and Elasticity." Journal of Impact Engineering, Volume 16, Number 4, pp.651-672.

Su, X.Y., Yu, T.X. and Reid, S.R. (1995b). "Inertia-Sensitive Impact Energy-Absorbing Structures Part II: Effect of Strain Rate." Journal of Impact Engineering, Volume 16, Number 4, pp.673-689.

Sugiura, K., Mizuno, E. and Fukumoto, Y. (1985). "Dynamic Instability Analyses of Axially Impacted Columns." Journal of Engineering Mechanics, Volume 111, Number 7, pp.893-908.

Symonds, P.S. and Frye, C.W.G. (1988). "On the Relation Between Rigid-Plastic and Elastic-Plastic Dynamic Structural Analysis." Journal of Impact Engineering, Volume 7, Number 2, pp.139-149.

Symonds, P.S. Kolsky, H. and Mosquera, J.M. (1984). "Simple Elastic-Plastic Method for Pulse Loading Comparisons with Experiments and Finite Element Solutions." Mechanical Properties at High Rates of Strain, Editor J. Harding, Institute of Physics Conference Series, Number 70, pp.479-486.

Symonds, P.S. (1980). "Finite Elastic and Plastic Deformations of Pulse Loaded Structures by an Extended Mode Technique." International Journal of Mechanical Sciences, Volume 22, pp.597-605.

Symonds, P.S. (1967). Survey of Methods of Analysis for Plastic Deformation of Structures under Dynamic Loading. Brown University, Division of Engineering Report.

Tam, L.L. and Calladine, C.R. (1991). "Inertia and Strain-Rate Effects in a Simple Plate-Structure under Impact Loading." International Journal of Impact Engineering, Volume 11, Number 4, pp.349-377.

Taub, J. (1933). "Stossartige Knickbeanspruchung schlanker Stäbe im elastischen Bereich." Luftfahrtforschung, Volume 10, Number 2, July 1933, p.65-85. Also, "Impact Buckling of Thin Bars in the Elastic Range for any End Condition." Translation by J. Vanier, National Advisory Committee for National Advisory Committee for Aeronautics, NACA Technical Memorandum Number 749, 1934, 60p.

Thomas, T.J., Nair, S. and Garg, V.K. (1983). "A Numerical Study of Plasticity Models and Finite Element Types." Computers and Structures, Editor H. Liebowitz, Volume 16, Number 5, Permagon Press, Oxford, UK, pp.669-675.

Timoshenko, S.P. and Gere, J.M. (1962). Elements of Strength of Materials. 4th Edition, D. van Nostrand Company Incorporated, New York, NY, USA, 377p.

Timoshenko, S.P. and Gere, J.M. (1961). Theory of Elastic Stability. 2nd Edition, McGraw-Hill Book Company, New York, NY, USA, 541p.

Ugural, A.C. and Fenster, S.K. (1987). Advanced Strength and Applied Elasticity. Second SI Edition, P T R Prentice-Hall, Inc., A Simon & Schuster Company, Englewood Cliffs, NJ, USA, 471p.

von Kármán, T. and Duwez, P. (1950). "On the Propagation of Plastic Deformation in Solids." Journal of Applied Physics, Volume 21, pp.987-994.

Weller, T., Abramovich, H and Yaffe, R. (1989). "Dynamic Buckling of Beams and Plates Subjected to Axial Impact." Computers and Structures, Special Issue: Nonlinear Finite Element Analysis and ADINA, Editor H. Liebowitz, Volume 32, Number 3/4, Permagon Press, Oxford, UK, 1989, pp.835-851.

Wilkins, M.L. (1984). "Modelling the Behaviour of Materials." Proceedings, International Conference, Structural Impact and Crashworthiness, Volume 2, Editor J. Morton, Elsevier Applied Science Publishers, London, UK, pp.243-277.

Wirsching, P.H., Paez, T.L. and Oritz, K. (1995). Random Vibrations, Theory and Practice. Wiley-Interscience Publication, John Wiley & Sons, Inc., New York, NY, USA, 448p.

Yu, J-L. and Jones, N. (1997). "Numerical Simulation of Impact Loaded Steel Beams and the Failure Criteria." International Journal of Solids and Structures, Volume 34, Number 30, pp.3977-4004.

Yu, T.X., Yang, J.L. and Reid, S.R. (1997). "Interaction Between Reflected Elastic Flexural Waves and a Plastic 'Hinge' in the Dynamic Response of Pulse Loaded Beams." Journal of Impact Engineering, Volume 19, Number 5-6, pp.457-475.

Zhang, T.G., and Yu, T.X. (1989). "A Note on Velocity Sensitive Absorbing Structures." Journal of Impact Engineering, Volume 8, Number 1, pp.43-51.

Zhang, T.G., Stronge, W.J. and Yu, T.X. (1995). "Dynamic Deformation of Rigid Plastic Beams for General Impulsive Loading: A Phenomenological Model." Journal of Impact Engineering, Volume 16, Number 4, pp.535-562.

Ziegler, H. (1959). "A Modification of Prager's Hardening Rule." Quarterly Applied Mathematics, Volume 17, pp.55-65.

Zienkiewicz, O.C. and Cheung, Y.K. (1967). The Finite Element Method in Structural and Continuum Mechanics. McGraw-Hill Publishing Company Ltd., London, UK, 274p.

Appendix A Preliminary Elastic Pulse Buckling Analysis

A.1 Introduction

Analysis of finite element models investigating the elastic pulse buckling response of a slender beam subject to an axial impulse is presented. The issues addressed include mesh topology, applied impulse magnitude, imperfection type, element formulation and requirements for nonlinear analysis.

A.2 Beam Element Models

A.2.1 Fundamental Mode Imperfection

A.2.1.1 Introduction

Historically, analytical and numerical investigations on the dynamic pulse buckling response of beams have generally only considered the fundamental mode response. Finite element analysis on the elastic pulse buckling response of a slender beam with a discrete half-sine wave imperfection is presented. The analysis will demonstrate that the dynamic response of models defined by a discrete mode imperfection was not consistent with the "preferred" wavelength theory for the intense pulse buckling events considered.

The finite element packages *ANSYS* (1996) version 5.3 and *NISA* (1997) version 7.0 were used for the analysis employing beam elements. Model parameters such as element formulation, mesh topology, integration time step and imperfection model form are discussed later. The two-dimensional *BEAM3* element of *ANSYS* (1996) and *3D General Beam (NKTP=39)* element of *NISA* (1997) were employed for the finite element pulse buckling analysis. The usual assumptions associated with Euler-Bernoulli beam behaviour were considered and the effects of transverse shear deformation and rotary inertia were ignored.

Table A-1 summarizes the minimum time step required, as a function of the mesh aspect ratio (*AR*), for numerical stability during integration of the dynamic equation of motion. For stability considerations, the lower bound listed in Table A-1 was selected as the critical time step.

Table A-2 summarizes the finite element model parameters considered for the pulse buckling investigations of beam element models that incorporated a fundamental mode imperfection. The half-sine waveform geometric imperfection was defined by Equation

(3.17). The Courant number (C_n) was determined using Equation (3.16) based on the critical time step listed in Table A-1.

For all models, except *ANB1*, the beam geometry was *762mm×12.7mm×0.3175mm*. Model *ANB1* was developed to compare with analysis conducted by Sevin (1960) and had the dimensions *525mm×10mm×3.5mm*. The elastic properties for Aluminium 6061-T6 were defined as $E = 69MPa$, $\rho = 2700kg/m^3$ and $\nu = 0.33$. The essential boundary conditions were pinned $(\overline{X} = 0)$ and roller support $(\overline{X} = 1)$. The parameters were selected for comparison with experimental studies presented in Lindberg (1965) and Lindberg and Florence (1987).

A.2.1.2 Linear Transient Baseline Analysis

The finite difference study conducted by Sevin (1960), which included the effects of axial inertia, was used as a comparative benchmark for the initial finite element analysis. Sevin (1960) concluded that axial inertial effects could be neglected for bars with slenderness ratios ($L_e/r \leq 150$) subjected to constant nondimensional axial velocities within the range *0.00023-0.001*. These forcing velocities were equivalent to axial impulses of *16-69MPa*. Model *ANB1* had an effective slenderness ratio of ($L_e/r = 150$) and was subjected to an axial impulse of *69MPa*. The modelling considerations and adopted procedure for the current investigations are discussed in Chapter 4.

The computed displacement field for the 1st, 5th, 10th and 20th axial stress wave traverse, for Model *ANB1*, as a function of the normalized axial coordinate $(\overline{X})$ is illustrated in Figure A-1. The dominance of the midspan response and computed displacement–time history record was consistent with Sevin (1960) and the finite difference analysis (Figure 3-1) conducted in the present investigations. The longitudinal distribution of the normalized axial stress, defined as the ratio of computed normal stress (σ_{xx}) to initial applied impulse (σ_o), is shown in Figure A-2. The axial stress response was directly related to the axial position of the propagating stress wave. Thus, the finite element analysis substantiates the study conducted by Sevin (1960) with respect to the assumption of a constant, uniform axial thrust and neglect of axial inertia.

For the pulse buckling events considered in the current investigations, a linear transient analysis was initially conducted. This was based on the comparative analysis with the investigation of Sevin (1960) and the assumption, that for early buckling times the deflections and rotations could be considered small, whereby second order terms due to bending could be neglected.

Analysis of the computed response, for the models presented in Table A-2, demonstrated that the linear transient finite element solution was not representative of either the

theoretical analysis or experimental observations of Lindberg (1965). Comparison of the *ANSYS* and *NISA* solutions, which examined the evolution of peak buckle displacement and buckle wavelength, revealed an effectively identical response. The finite element models exhibited a low ordered, bounded response that was dominated by axial displacement. Furthermore, the time histories for axial displacement and stress response were consistent with the classical linear, elastic wave propagation solution. Although a range of mesh aspect ratio and imperfection magnitudes were considered (Table A-2), the finite element models did not exhibit an exponential growth of transverse displacements consistent with the "preferred" wavelength theory.

Based on these investigations, it was concluded that for intense impulsive loading conditions, of primary consideration for the present study, the importance of coupled nonlinear displacement terms was significant. Consequently, all subsequent analysis, for the finite element models listed in Table A-2, considered a nonlinear geometric formulation.

A.2.1.3 Nonlinear Geometric Analysis

Examination of the nonlinear transient solution for Model *ANB1* was consistent with the linear solution (Figure A-1) and further validates the conclusions stated by Sevin (1960). This was not the case, however, for the other models listed in Table A-1 that were subjected to a greater impulse magnitude ($\sigma_{xx} = 276MPa$).

Figure A-3 illustrates the axial displacement response for several longitudinal stations of Model *ANB6*, which was computed by nonlinear transient analysis. During the time frame ($0 \le \tau \le 66$; $0 \le t \le 300\mu s$), the axial response was consistent with the linear theoretical solution and exhibited a characteristic sawtooth waveform. For the time frame, $0 \le \tau \le 33$ ($0 \le t \le 300\mu s$), the propagating compressive stress wave acts only to relieve the initial static tensile stress and thus only linear behaviour was observed.

Deviation from the linear response occurs with the development of significant perturbations to the transverse motion. For the quarter-point node $\left(\overline{X} = 0.25\right)$, of Model *ANB6* shown in Figure A-3, this occurs after $\tau \approx 70$ ($t \approx 320\mu s$) as supported by the nondimensional transverse displacement–time history illustrated in Figure A-4.

A similar computed response was also exhibited for the nonlinear transient solutions of the Models *ANB3* through *ANB7* and Models *NB1* through *NB5* summarized in Table A-2. In contrast, linear behaviour was observed for Model *ANB2* throughout the entire solution (up to the 12^{th} wave traverse). This was attributed to the coarsely meshed domain and the limited degrees of freedom available to develop the higher order modal response.

Buckling can only be initiated after the compressive stress wave has propagated a critical wavelength from the lower support $(\overline{X} = 0)$. For clarity, the time scale was shifted to accommodate the required time period for the longitudinal stress wave to travel the length of the beam. Thus, the nondimensional time ($\tau = 0$) would now represent the instant when the stress front is reflected from the lower pinned support. To demonstrate by example, this is illustrated in Figure A-5, which presents an adjusted time scale plot for Model *ANB6* from Figure A-4.

For the beam element models defined only by discrete fundamental mode imperfections, the growth of transverse displacements was not consistent with either the theoretical analysis or experimental observations discussed by Lindberg (1965) or Lindberg and Florence (1987). This is illustrated in Figure A-6 where the peak buckle amplitude (w_{max}) is plotted as a function of time (τ). Data for the finite difference models (*FD2* and *FD3*) from Figure 3-6, was plotted for comparison. A peak nondimensional imperfection amplitude, $w_o = 16.628$ ($A_o = 1.524mm$) for Models *ANB6* and *ANB7*, was used to plot the theoretical Equations (3.18) and (3.19). Detailed analysis revealed that growth of transverse deflections was initiated around $\tau \approx 20$ ($t \approx 90\mu s$). Comparison with the experimental studies (Figure 3-11), where growth was observed at t $\approx 18\mu s$, the buckling response was significantly delayed by a factor of approximately 5.

Although the initial imperfection was defined by a half-sine waveform, a dominant higher order modal response was prevalent. The computed wavelengths (λ_w), for Models *ANB6* and *NB5*, increased with time and the mean response was on the order of $\lambda_w = 20$. This corresponds to almost three times the "preferred" mode ($\lambda_p = 2\pi\sqrt{2}$). An increase in the mesh density (Model *ANB7*) did not significantly influence the computed peak amplitudes or observed waveforms.

The investigations demonstrated that the finite element models, which incorporated only a fundamental mode imperfection, were not consistent with the "preferred" wavelength theory. The peak buckle response was not representative of the characteristic unbounded growth of transverse displacements. Furthermore, the modal response significantly over predicted the mean buckle wavelengths. The importance of the coupled nonlinear terms associated with the axial strain–displacement relationship, however, was recognized.

A.2.2 Combined Geometric Imperfections

A.2.2.1 Introduction

The significant influence of random imperfections on the pulse buckling response was demonstrated by the finite difference investigations. Consequently, finite element models that incorporated combined imperfections (i.e. discrete and random), through linear

superposition of Equations (3.17) and (3.20), were developed. Table A-3 summarizes the parameters for the beam element models with combined imperfections.

A.2.2.2 Buckled Displacement Response

The presence of local random imperfections initiated higher order flexural oscillations that dominated the buckling response throughout the solution. This is demonstrated through comparison of the buckled profile for Model *ANB9* (Table A-3) as shown in Figure A-7, with the response of Model *ANB6* illustrated in Figure A-5. Although the half-sine waveform imperfection amplitude, for Model *ANB9*, was approximately *50* times greater than local random imperfections, the pulse buckling response was dominated by higher order modes. The buckled waveform was "biased" towards the lower support due to the finite time required for the axial impulse to propagate a critical length and initiate flexural oscillations. Furthermore, impulse duration, relative stiffness and eccentricity effects also influence the modal competition near the support boundary. The transverse buckle amplitudes were on the order of 3-5 times the maximum discrete, fundamental mode imperfection amplitude. Similar pulse buckling response was observed for the other models listed in Table A-3.

Exploitation of random geometric imperfections by the axial impulse was critical for initiating the enhanced growth rate of transverse displacements. This is illustrated by comparison of the combined imperfection models (Figure A-8) with models defined only by the discrete fundamental mode imperfection (Figure A-6). The maximum and minimum Fourier coefficients (A_o), for the models listed in Table A-3, were selected to plot Equation (3.18). The nondimensional buckle amplitudes for both the peak buckle (open symbols), located near the lower fixed support (Figure A-7), and midspan response (solid symbols) are presented.

For early solution times ($\tau < 6$), the numerical models underpredict the threoretical growth as defined by Equation (3.18). Although the midspan deflections increased with time, the peak buckle amplitude dominated the solution. The limiting plateau observed in Figure A-8, for solution times greater than $\tau \approx 15$, was related to a reduction in the axial impulse and coupled nonlinear terms defined by the axial strain–displacement relationship. Further discussion is presented in Chapter 4. The behaviour was also consistent with experimental evidence (Lindberg and Florence, 1987) from time-frame photographs as shown in Figure 3-11. The finite difference solution, which assumes a assumed a constant, uniform axial thrust, exhibited an unbounded growth rate in accordance with the "preferred" wavelength theory.

The comparative buckling response for 3-D beam elements (*NISA*) and 2-D beam elements (*ANSYS*) is illustrated in Figure A-9. The finite element models with an aspect ratio of 2:1 and 1:1 (Table A-3) were analysed. The maximum initial imperfection coefficient

($A_o = 0.56$) was selected to plot Equations (3.18) and (3.19). The results are in excellent agreement.

A.2.2.3 Modal Response Analysis

Modal response analysis of the buckled profile was also conducted. The nondimensional buckle wavelength ($\lambda = {}^{2sL}/_{r}$) response as a function of the dimensionless time parameter (τ) is presented in Figure A-10. The finite difference Model FD10 is also shown in Figure A-10(b) for comparison. The solid data points represent the average wavelength (λ_{avg}) and the open data points represent the weighted mean response (λ_{wm}). Details of the numerical algorithm employed to determine the wavelength parameters are presented in Chapter 4.

The buckle wavelength response was not significantly influenced by an increase in the imperfection amplitude. This was illustrated through comparison of the modal response of Model *ANB8* with Model *ANB9* and Model *ANB10*, where the fundamental mode imperfection amplitudes was 7 and 34 times that of Model *ANB8*, respectively.

The importance of considering mesh discretization, however, was observed. For early solution times ($\tau \leq 12$), behaviour of the coarsely meshed models (*ANB8* and *ANB9*), with an aspect ratio of 10:1, was erratic. In addition the average (λ_{avg}) and weighted mean (λ_{wm}) wavelength response was similar in character, which implied that the modal response was uniformly distributed along the beam length. Finite element models with a more finely discretised domain (*ANB10* and *ANB11*), however, demonstrated that the smaller amplitude pulse buckling response away from the fixed support (Figure A-7) was characterised by higher frequency components than the dominant, large buckle amplitudes defined by the average wavelength (λ_{avg}). Furthermore, the average wavelength response (λ_{avg}) exhibited general agreement with the theoretical expressions and converged toward the "preferred" mode at $\tau \approx 12$. The modal response characteristics for the beam element models were consistent with recent analysis on elastic beam dynamics by Matsunaga (1996), which investigated the free-vibration and stability of a simply supported, thin elastic beam, using a power series expansion method.

A.2.3 Random Geometric Imperfections

The parameters for beam element models incorporating only local random imperfection is presented in Table A-4. A fixed boundary condition for Model *ANB13* (Table A-3), which was more representative of the experiments conducted by Lindberg (1965), was developed to compare with the pinned support of Model *ANB12*. The finite element models considered a pinned support to compare directly with the "preferred" wavelength theory. Analysis of the pulse buckling response demonstrated that influence of the

modelled boundary conditions was insignificant. A detailed discussion on the peak buckle displacement and mode response analysis is presented in Chapter 4.

A.3 Pulse Buckling Analysis – Plane Strain Elements

Investigations, employing quadratic, plane strain elements, were also conducted to study the influence of the element formulation on the computed pulse buckling response. Table A-5 summarizes the critical time step required as a function of aspect ratio for plane strain element models.

A.3.1 Buckled Displacement Response

The influence of element formulation on the computed pulse buckling response can be appreciated through visual comparison of the buckled profiles for the plane strain element model (*AP2*, Figure A-11), beam element model (*ANB9*, Figure A-7) and experimental investigations (Figure 3-11). Although the plane strain element model was discretized by a relatively coarse mesh (aspect ratio 8:1), there was good agreement with experimentally observations. The influence of aspect ratio is illustrated in Figure A-12 for Model *AP8*, which is more representative of the observed experimental observations. A sharp buckle ampltude decay was exhibited and the response was dominated by a "single sine wave" near the lower fixed support $\left(\overline{X} = 0\right)$.

The beam element model response was limited due to inherent characteristics of the element formulation such as plane sections, moment–curvature assumptions and the explicit nonlinear terms of the axial strain–displacement relationship. The quadratic plane strain element can more accurately model the high degree of curvature developed near the fixed support, which was probably influenced by the relative stiffness disparity (between the beam and support), axial impulse duration and local eccentric effects arising from random geometric imperfections.

For the plane strain element models, during the initial propagation of the compressive relief wave, the computed displacement field was consistent with linear, wave propagation theory. This is illustrated in Figure A-13 for several nodal points of Model *AP8*. Deviation from linear behaviour was concurrent with the significant growth of transverse displacements and the behaviour was consistent with analysis of the beam element models. For the nodal point located at $\overline{X} = 0.05$ this event occurs around $\tau \approx 10$ $(t \approx 45\mu s)$ and the buckle amplitude was on the order of *1.5d*. According to elastic theory (Lindberg and Florence, 1987), buckling should occur after the stress front has traversed a distance equal to the characteristic "preferred" wavelength. For Model *AP8*, the "preferred" half-wavelength was ($L_p = 12.88mm$) and stress wave speed ($c = 5055m/s$). The time required for the wave front to reach the nodal point $\left(\overline{X} = 0.05\right)$ is $\tau = 1.7$ $(t = 7.5\mu s)$ and propagate the "preferred"

wavelength is $\tau \approx 0.6$ ($t \approx 2.5\mu s$). Thus, a lead time ($\tau \approx 7.7$; $t \approx 35\mu s$) would be required for the growth of transverse deflections before nonlinear effects dominate the pulse buckling response. The stress front would have travelled a distance of approximately 14 times the "preferred" half-wavelength. Consequently, the plane strain element models further substatiates, one of the key assumptions for the "preferred" wavelength theory, that the position of the stress front can be ignored with respect to the growth of lateral buckle displacements.

A.3.2 Requirement for Nonlinear Plastic Analysis

The requirements for a fully nonlinear dynamic analysis with elastoplastic constitutive relationships, when employing plane strain elements can be demonstrated through an investigation of the computed axial stress state. In addition, Lindberg and Florence (1987) reported the development of local plastic wrinkles or hinges that occasionally formed at the peak crests near the fixed support during experimental elastic pulse buckling investigations. Figure A-14 illustrates the axial stress time history for the elastic analysis for Model *AP7*. The data was extracted at Gauss points and normalized with respect to the yield stress for selected longitudinal stations $\bar{X} \leq 0.20$. The axial stress state exceeded the material yield stress for solution times greater than $\tau \approx 5$. For later solution times ($\tau > 10$) unrealistic stress magnitudes, on the order of 4 times the yield stress, were observed for a wholly elastic analysis. The diamond-shaped data points (◊) in Figure A-14, represent the computed elastic stress for the first crest waveform adjacent to the support. The normal stress was determined using classical linear, elastic Euler-Bernoulli beam theory. An algorithm was developed to calculate the modal response including the magnitude and location of peak buckles. The program determined the radius of curvature from nodal displacement data and calculated the corresponding elastic flexural stress. For a rectangular cross-section, the flexural stress is defined as,

$$\sigma = \frac{Mc}{I} = \frac{Ed}{2}\frac{\partial^2 y}{\partial x^2}, \tag{A.1}$$

where the curvature relation ($\partial^2 y / \partial x^2$) was calculated by a second order quadratic finite difference expression. As an example, for Model *AP7*, at $\tau = 22$ ($t = 100\mu s$), the characteristics of the first buckle were, $w = 4.66$ ($y = 0.519mm$), $\lambda = 14.27$ ($L = 22.1mm$) and $\partial^2 y / \partial x^2 = 0.0486 / mm$. Assuming an elastic modulus ($E = 69MPa$) and beam depth ($d = 0.3175mm$), the flexural stress due to bending was $533MPa$. Combined with the axial stress, $276MPa$, yields a total normal stress of $\sigma_{xx} = 809MPa$.

The computed theoretical elastic stress data points (◊) were consistent with the linear transient finite element analysis illustrated in Figure A-14. The slight discrepancy was due to the assumptions of the simplified analysis. The significant inelastic stress state was attributed to the high degree of curvature developed and local element distortion. In contrast with the beam element formulation, the quadratic plane strain elements are not limited by the assumptions of plane sections and uniform curvature. Although the maximum axial stress significantly exceeded the yield stress, analysis of buckled amplitude growth was in reasonable agreement with the "preferred" wavelength theory.

The analysis demonstrated that the nonlinear geometric and material behaviour must be considered for finite element models employing plane strain elements. Consequently, the plane strain element models were defined by an elastoplastic constitutive relationship with a von Mises yield criterion and linear, strain hardening rule. This model is widely adopted in engineering practice to describe the stress-strain behaviour of common engineering materials such as metals. The kinematic formulation selected was large displacement and small strain. Supplementary investigations demonstrated negligible differences between small and large strain formulations. As shown in Figure A-15, the fully nonlinear analysis resolved the numerical difficulties encountered with the computed stress state. The diamond-shaped data points (◊) represented the computed elastic stress state based on beam curvature. Stability of the stress state for solution times $\tau \leq 5$, further demonstrates validity for the assumption of an uniform axial impulse. During the time frame, the wave front has traversed almost one-fifth of the bar length, which is on the order of 10 times the "preferred" wavelength (λ_p). Although an elastoplastic material relationship was adopted for the analysis, the buckling event is still considered elastic because the applied impulse was less than the material yield stress.

A.3.3 Discrete Fourier Transform Analysis

Discrete Fourier transforms (DFT) were initially employed to analyse the deformed geometry profiles of the plane strain element models. The "real" magnitude of the Fourier coefficients, however, could not be determined accurately. This was due to an averaging effect where the Fourier coefficient was masked or scaled down. The sparse number of large amplitude crests near the support (Figure A-12) was dominated by the more abundant but smaller amplitude wavelengths prevailing throughout the beam length. Analysis demonstrated that the Fourier magnitudes were 10-20 times less than the peak buckle amplitudes. A typical DFT analysis is illustrated in Figure A-16, where the dimensionless Fourier coefficient (a_n) is presented as a function of wavenumber (γ) and wavelength (λ).

For the beam geometry investigated, the "preferred" wavelength is ($L_p = 12.88mm$) and the corresponding wave number ($\gamma = {}^{2\pi}/_{L_p} = 0.488$). The nondimensional wavelength

(λ) is defined as $\lambda = {}^{2sL}/_{r}$. For the DFT analysis, the bar length considered was a function of the wave front position (i.e. solution time). For example, at time $\tau = 22$ ($t = 100\mu s$), the wave front would have propagated approximately $L \approx 505mm$ $\left(\overline{X} = 0.66\right)$. As shown in Figure A-16, the coefficient amplitudes were one order less than the peak buckle amplitudes, near the fixed support $\left(\overline{X} = 0\right)$, which is also illustrated by the deformed buckled profiles shown in Figure A-12. Consequently, modal analysis was conducted using the same algorithms developed for the beam element models as discussed in Chapter 4.

Table A-1. Critical Integration Time Step as a Function of Aspect Ratio for Beam Elements.

Elements	Aspect Ratio	Δt_{cr} (μs) Eqn (3.13)	Δt_{cr} (μs) Eqn (3.15)	Δt_{cr} (μs) Eqn (4.3)
16	150:1	9.42	2448	706
240	10:1	0.628	10.9	3.14
480	5:1	0.314	2.72	0.785
1200	2:1	0.126	0.435	0.126
2400	1:1	0.0628	0.109	0.0314

Table A-2. Parameters for Beam Element Models with Discrete Fundamental Mode Imperfection.

ANSYS Finite Element Models						
Model	Mesh	AR	Δt (μs)	C_n	$\%d_{max}$	A_{max}/L
ANB1	16×1	150:1	5.0	0.53	25	0.0058
ANB2	16×1	150:1	5.0	0.53	25	0.0001
ANB3	240×1	10:1	0.5	0.80	25	0.0001
ANB4	240×1	10:1	0.5	0.80	100	0.0004
ANB5	240×1	10:1	0.5	0.80	200	0.0008
ANB6	240×1	10:1	0.5	0.80	500	0.002
ANB7	1200×1	2:1	0.1	0.80	500	0.002
NISA Finite Element Models						
Model	Mesh	AR	Δt (μs)	C_n	$\%d_{max}$	A_{max}/L
NB1	16×1	150:1	5.0	0.53	10	0.0001
NB2	240×1	10:1	0.5	0.80	50	0.0002
NB3	240×1	10:1	0.5	0.80	100	0.0004
NB4	240×1	10:1	0.5	0.80	200	0.0008
NB5	240×1	10:1	0.5	0.80	500	0.002

Notes: *Mesh* specifies the number of longitudinal × transverse elements, *AR* is the aspect ratio of the longitudinal to transverse element length, Δt is the integration time step, C_n is the Courant number, $\%d_{max}$ is the peak imperfection amplitude as a percentage of the beam depth and A_{max}/L is the nondimensional imperfection parameter.

Table A-3. Parameters for Beam Element Models with Combined Geometric Imperfections.

ANSYS Finite Element Models						
Model	Mesh	AR	Δt (μs)	C_n	$\%d_{max}$	A_{max}/L
ANB8	240×1	10:1	0.500	0.80	15	0.00006
ANB9	240×1	10:1	0.500	0.80	104	0.0004
ANB10	1200×1	2:1	0.100	0.80	504	0.002
ANB11	2400×1	1:1	0.025	0.80	205	0.00085
NISA Finite Element Models						
Model	Mesh	AR	Δt (μs)	C_n	$\%d_{max}$	A_{max}/L
NB6	1200×1	2:1	0.100	0.80	207	0.00086
NB7	2400×1	1:1	0.025	0.80	208	0.00087

Notes: *Mesh* specifies the number of longitudinal × transverse elements, *AR* is the aspect ratio of the longitudinal to transverse element length, Δt is the integration time step, C_n is the Courant number, $\%d_{max}$ is the peak imperfection amplitude as a percentage of the beam depth and A_{max}/L is the nondimensional imperfection parameter.

Table A-4. Parameters for Beam Element Models with Random Geometric Imperfections.

ANSYS Finite Element Models							
Model	Mesh	AR	Δt (μs)	C_n	$\%d_{max}$	A_{max}/L	Comments
ANB12	1200×1	2:1	0.10	0.80	9	0.000037	Pinned BC
ANB13	1200×1	2:1	0.10	0.80	9	0.000037	Fixed BC
ANB14	2400×1	1:1	0.01	0.55	9	0.000037	Pinned BC
NISA Finite Element Models							
Model	Mesh	AR	Δt (μs)	C_n	$\%d_{max}$	A_{max}/L	Comments
NB8	1200×1	2:1	0.10	0.80	9	0.000038	Pinned BC
NB9	2400×1	1:1	0.01	0.55	8	0.000038	Pinned BC

Notes: *Mesh* specifies the number of longitudinal × transverse elements, *AR* is the aspect ratio of the longitudinal to transverse element length, Δt is the integration time step, C_n is the Courant number, $\%d_{max}$ is the peak imperfection amplitude as a percentage of the beam depth and A_{max}/L is the nondimensional imperfection parameter.

Table A-5. Critical Integration Time Step as a Function of Aspect Ratio for Plane Strain Element Models.

Mesh	AR	Eqn (3.13) (μs)	Eqn (3.15) (μs)	Eqn (4.9) (μs)	Eqn (4.10) (μs)	Eqn (4.23) (μs)
150×1	16:1	0.502	6.96	0.411	8.04	0.290
300×1	8:1	0.251	1.74	0.206	2.01	0.145
600×1	4:1	0.126	0.435	0.103	0.502	0.073
1200×1	2:1	0.063	0.109	0.051	0.126	0.036
2400×1	1:1	0.031	0.027	0.026	0.031	0.018

Table A-6. Parameters for Plane Strain Element Models with Random Geometric Imperfections.

NISA Finite Element Models							
Model	Mesh	AR	Δt (μs)	Cn	%davg	%dmax	Comments
NP1	600×1	4:1	0.01	0.14	3	6	E
NP2	600×1	4:1	0.01	0.14	2	7	E
NP3	600×1	4:1	0.01	0.14	3	6	E, Lε
ADINA Finite Element Models							
Model	Mesh	AR	Δt (μs)	Cn	%davg	%dmax	Comments
AP1	300×1	8:1	0.05	0.34	2	8	EP
AP2	300×1	8:1	0.10	0.69	2	8	EP
AP3	300×2	16:1	0.10	0.34	2	8	EP
AP4	600×1	4:1	0.05	0.69	2	9	EP
AP5	600×2	4:1	0.05	0.69	2	11	EP
AP6	1200×1	2:1	0.01	0.28	2	9	EP
AP7	1200×1	2:1	0.01	0.28	2	9	E
AP8	2400×1	1:1	0.01	0.55	2	8	EP
AP9	1200×1	2:1	0.01	0.28	2	9	EP, Lε

Notes: *Mesh* specifies the number of longitudinal × transverse elements, *AR* is the aspect ratio the longitudinal to transverse element length, Δt is the integration time step, C_n is the Courant number, $\%d_{avg,max}$ is the average and maximum peak imperfection amplitude as a percentage of the beam depth, *E,EP* denotes elastic, elastoplastic constitutive relationship respectively, and $L\varepsilon$ indicates large strain analysis.

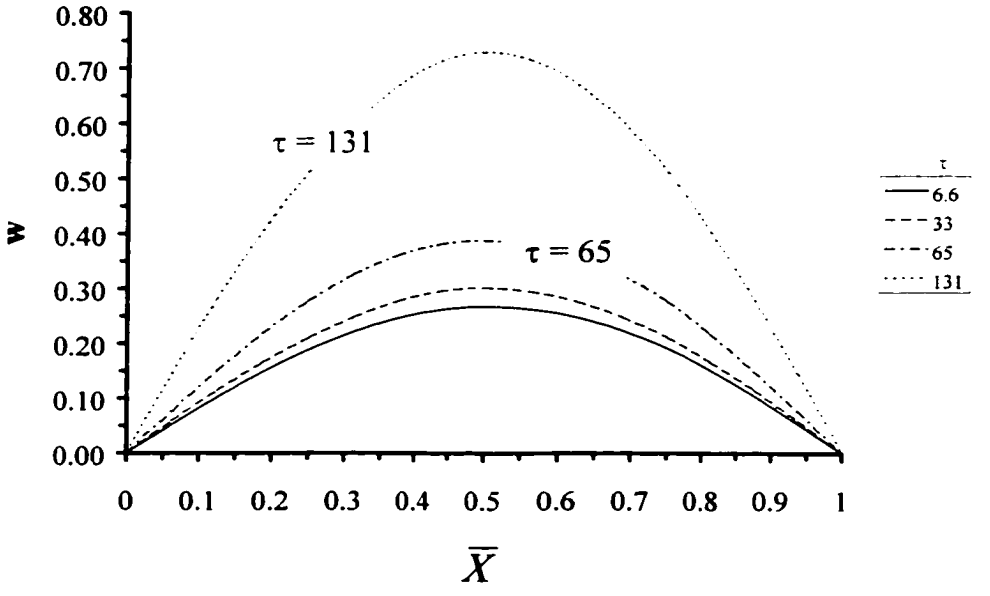

Figure A-1. Deformed Buckled Profiles for Beam Element Model *ANB1* as a Function of Normalized Axial Coordinate $(\overline{X})$ for Solution Times (τ).

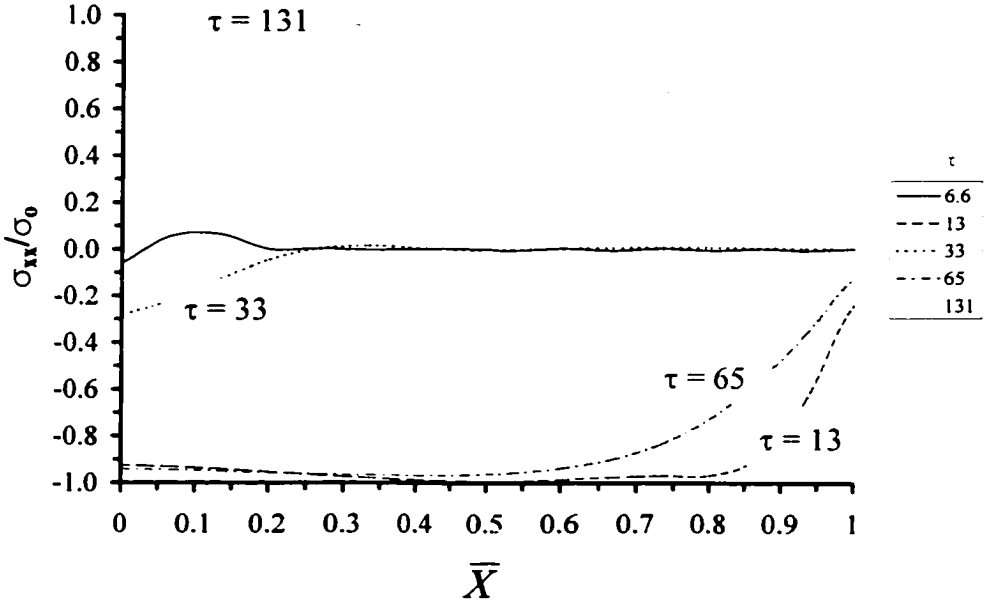

Figure A-2. Normalized Axial Stress Distribution for Beam Element Model *ANB1* as a Function of Normalized Axial Coordinate $(\overline{X})$ and Time (τ).

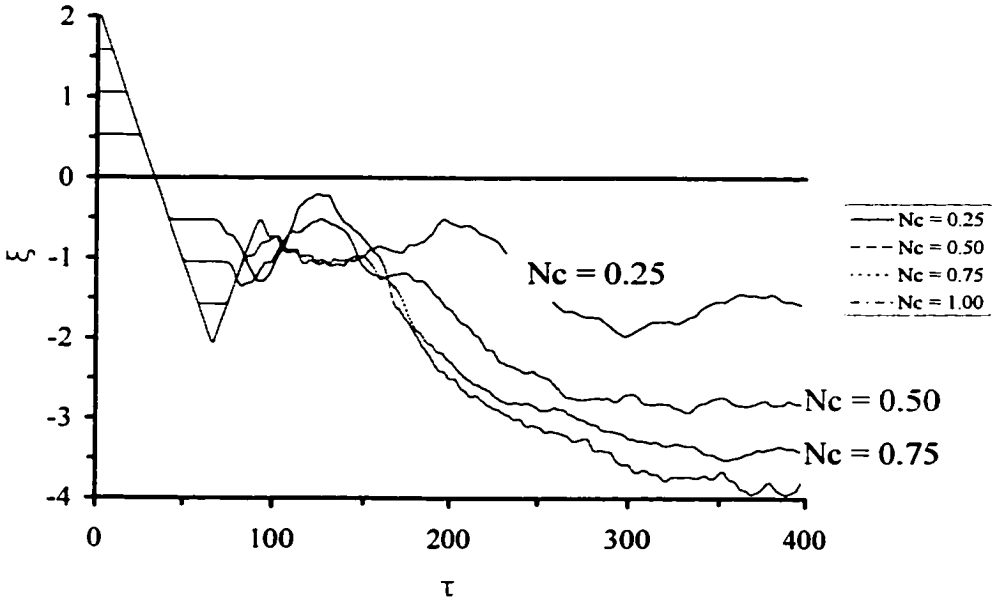

Figure A-3. Nondimensional Axial Displacement for Beam Element Model *ANB6*.

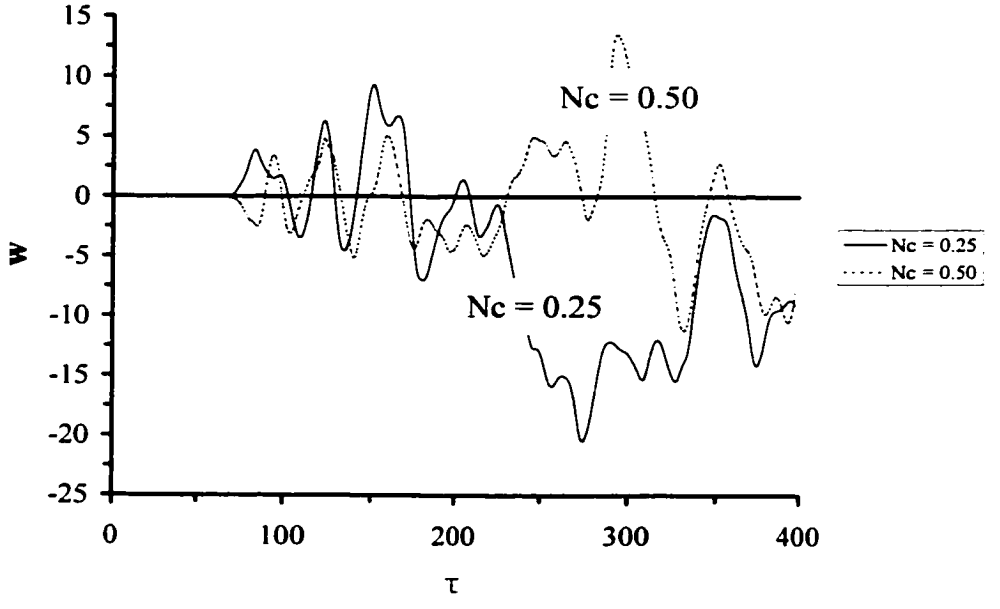

Figure A-4. Nondimensional Transverse Displacement for Beam Element Model *ANB6*.

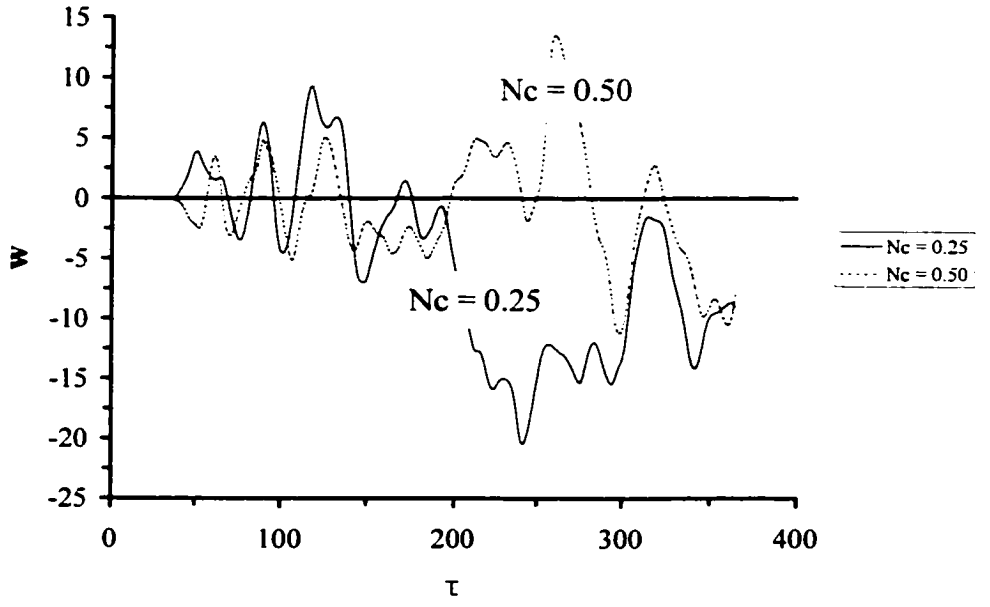

Figure A-5. Adjusted Time Scale Plot of Nondimensional Transverse Displacement for Beam Element Model *ANB6* Illustrated in Figure A-4.

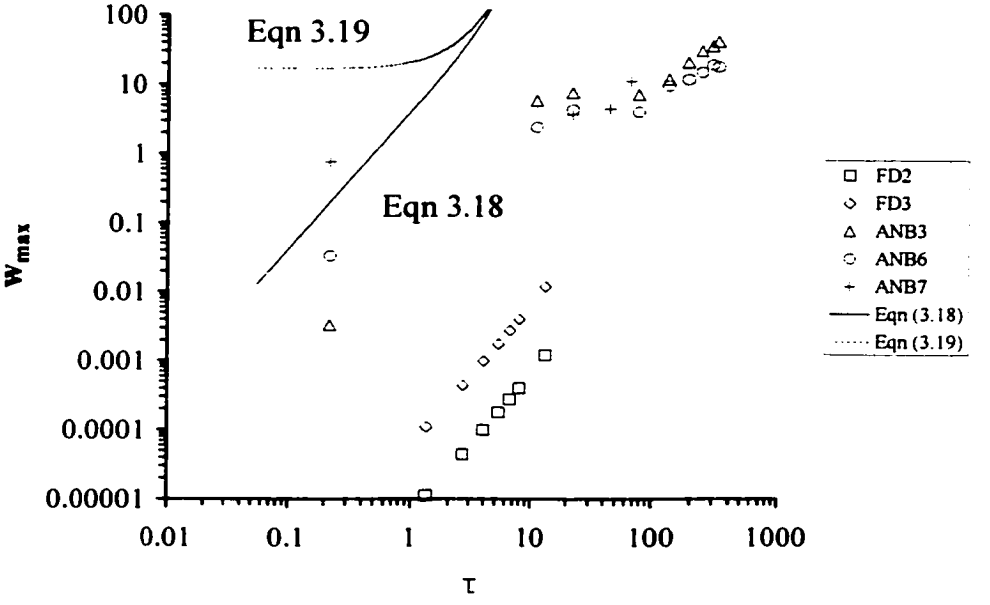

Figure A-6. Nondimensional Peak Buckle Amplitude (w_{max}) as a Function of Time (τ) for Beam Element Models with Discrete Fundamental Mode Imperfection.

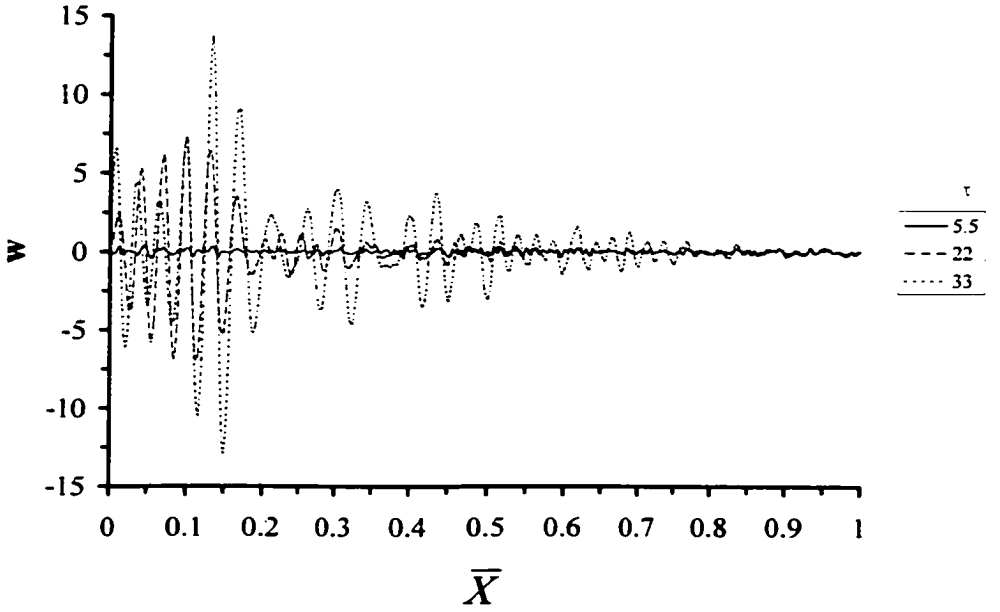

Figure A-7. Nondimensional Buckled Profiles as a Function of Normalized Axial Coordinate $(\overline{X})$ for Beam Element Model *ANB9*.

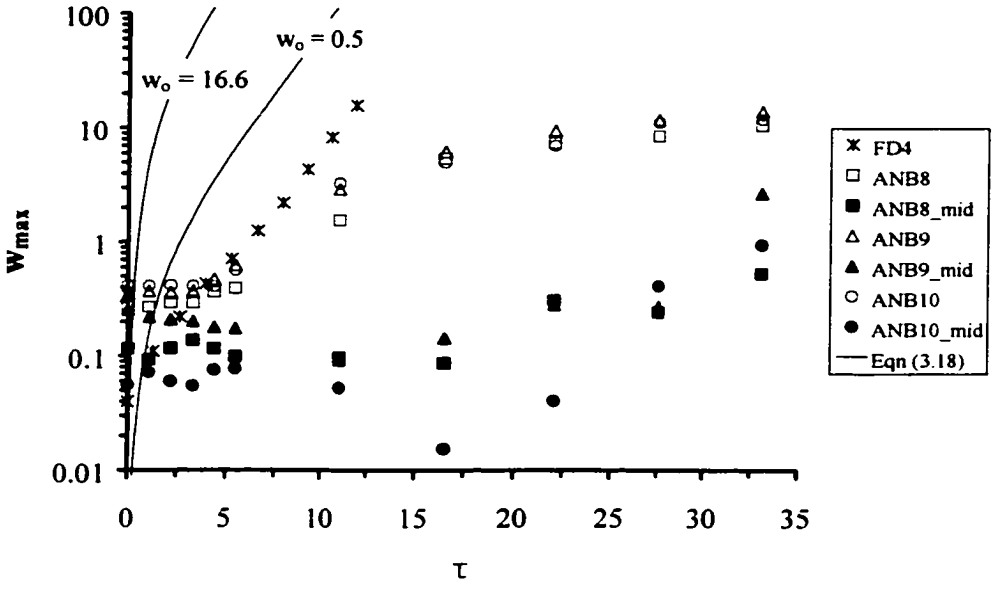

Figure A-8. Nondimensional Peak Buckle (w_{max}) and Midspan Amplitude as a Function of Time (τ) for Beam Element Models with Combined Geometric Imperfections.

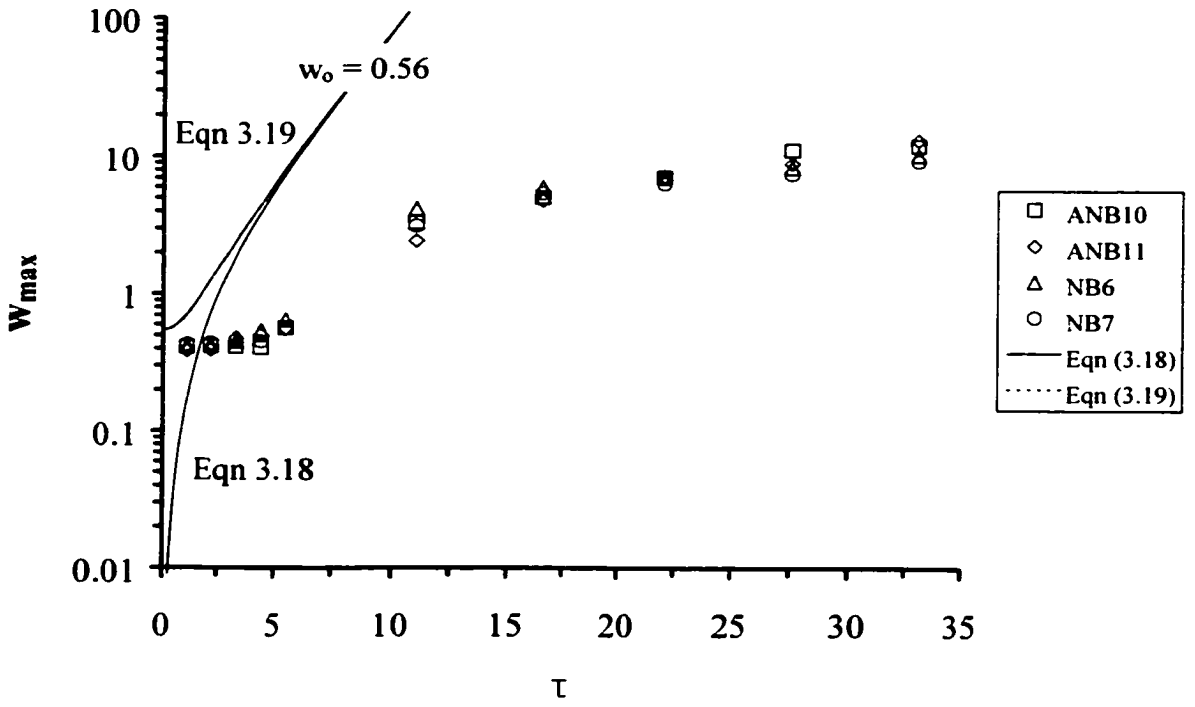

Figure A-9. Nondimensional Peak Buckle Amplitude (w_{max}) as a Function of Time (τ) for Beam Element Models with Combined Geometric Imperfections.

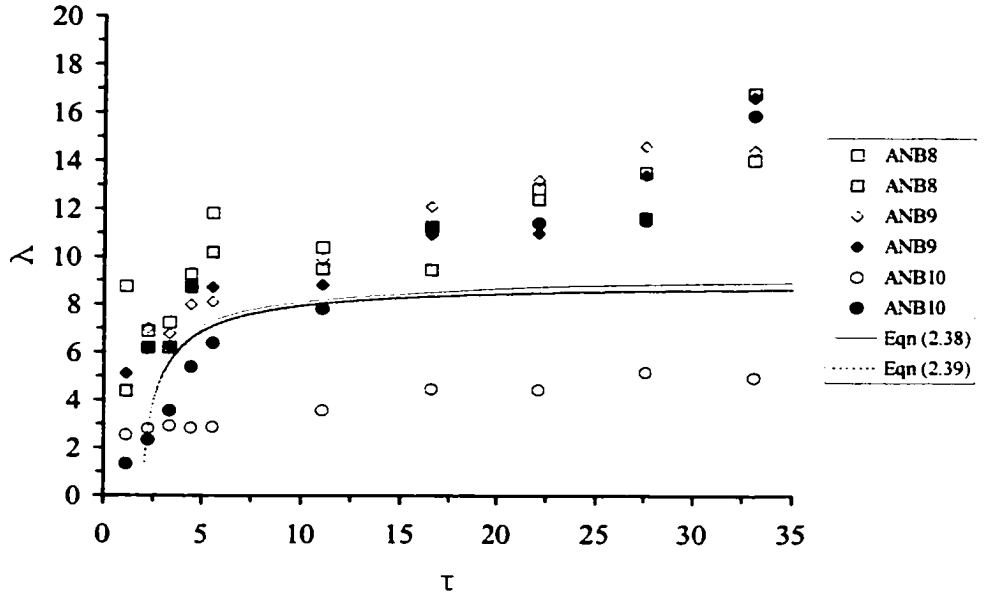

(a)

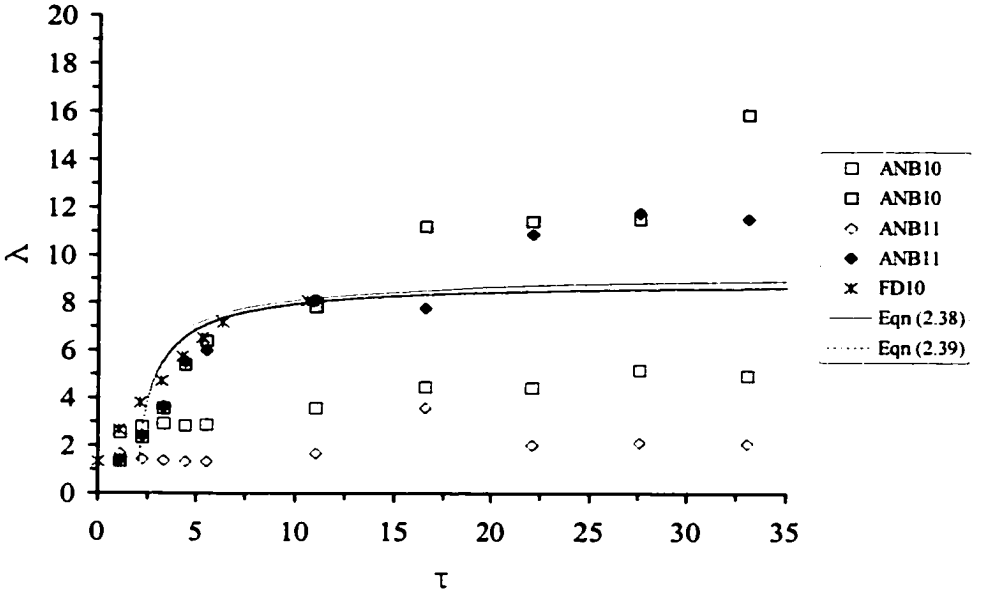

(b)

Figure A-10. Nondimensional Buckled Wavelength (λ) as a Function of Time (τ) for Beam Element Models with Combined Geometric Imperfections (■ λ_{avg} , □ λ_{wm}).

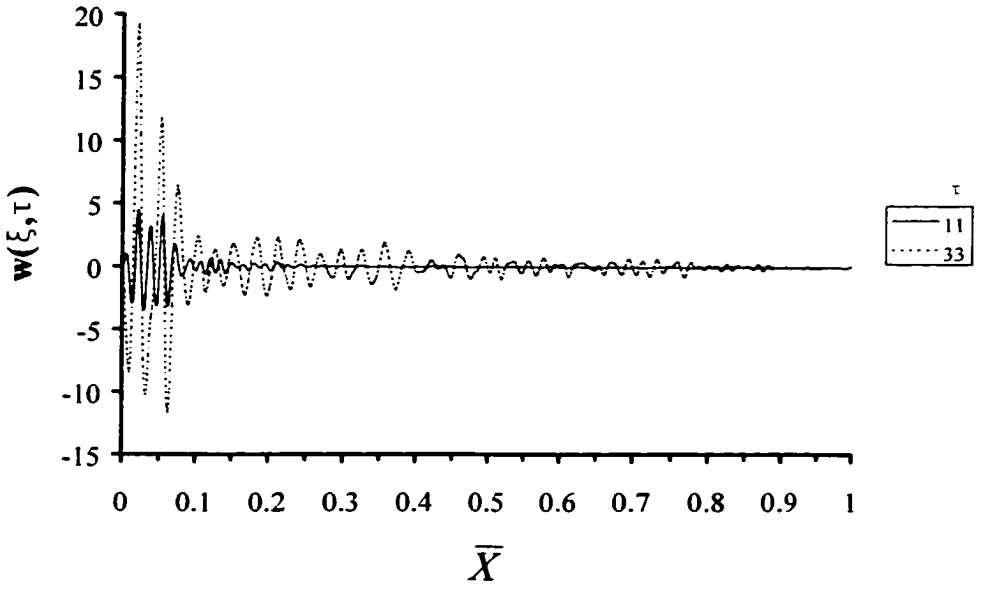

Figure A-11. Nondimensional Buckled Profiles as a Function of Normalized Axial Coordinate $(\overline{X})$ for Plane Strain Element Model *AP2*.

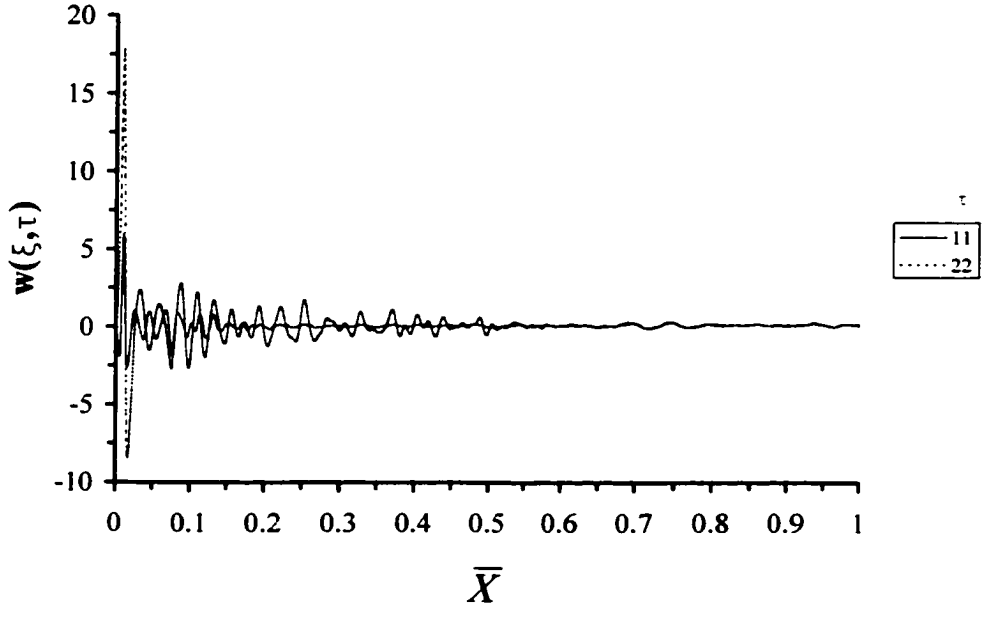

Figure A-12. Nondimensional Buckled Profiles as a Function of Normalized Axial Coordinate $(\overline{X})$ for Plane Strain Element Model *AP8*.

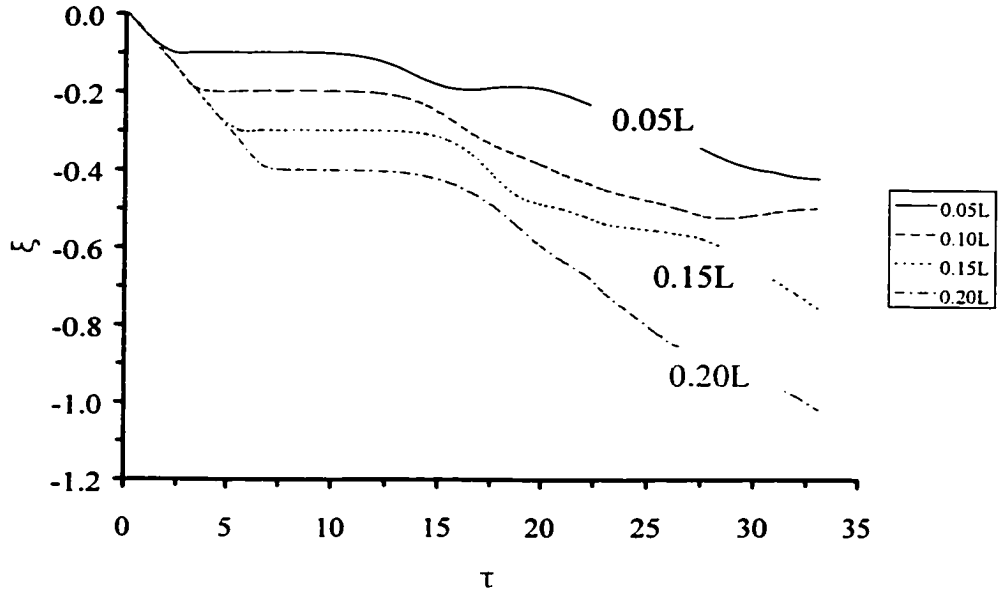

Figure A-13. Axial Displacement Time History for Nodal Points Near the Fixed Support for Plane Strain Element Model *AP8*.

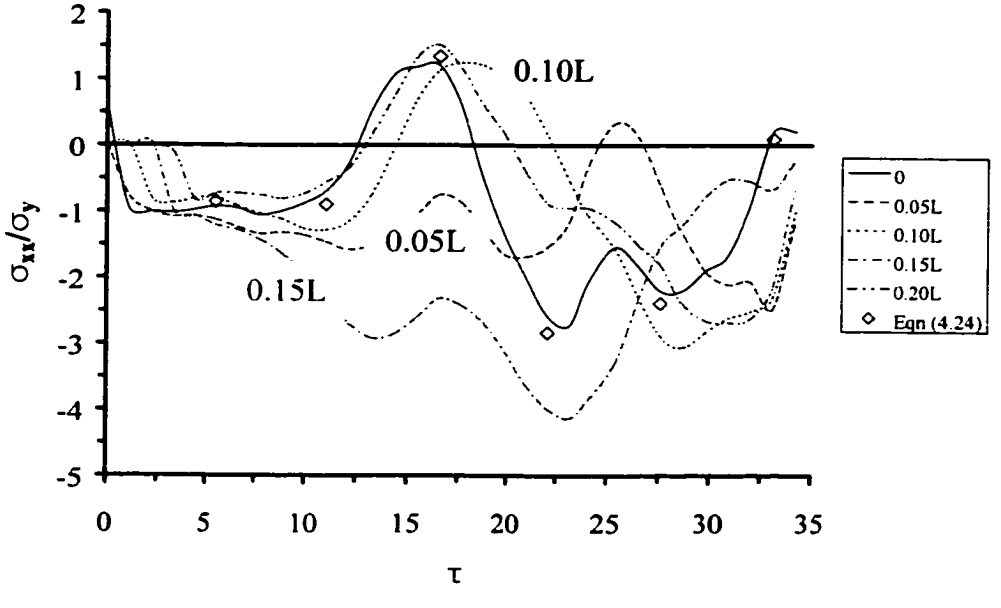

Figure A-14. Normalized Axial Stress State as a Function of Time (τ) for Plane Strain Element Model *AP7*.

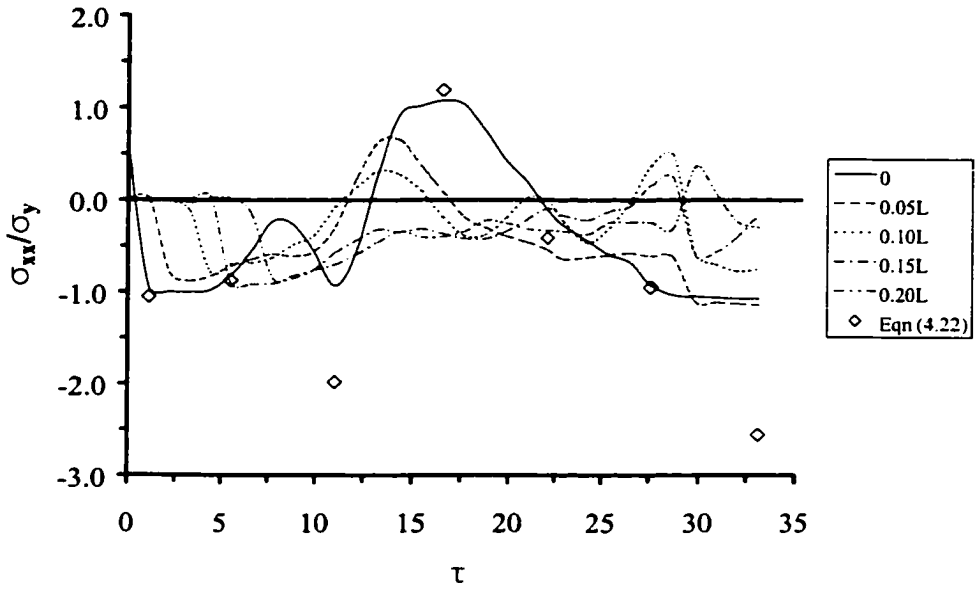

Figure A-15. Normalized Axial Stress State as a Function of Time (τ) for Plane Strain Element Model *AP8*.

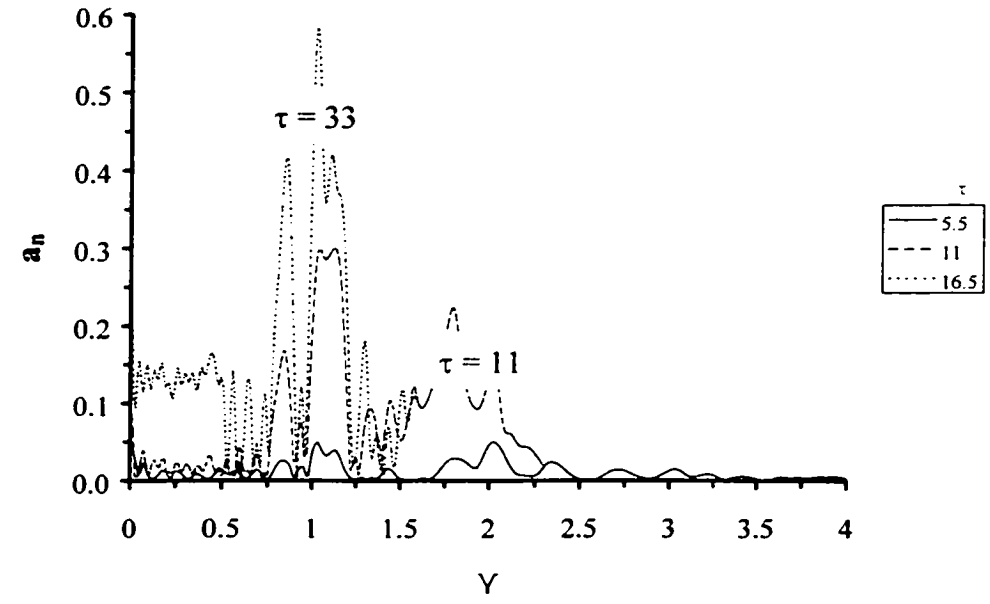

(a)

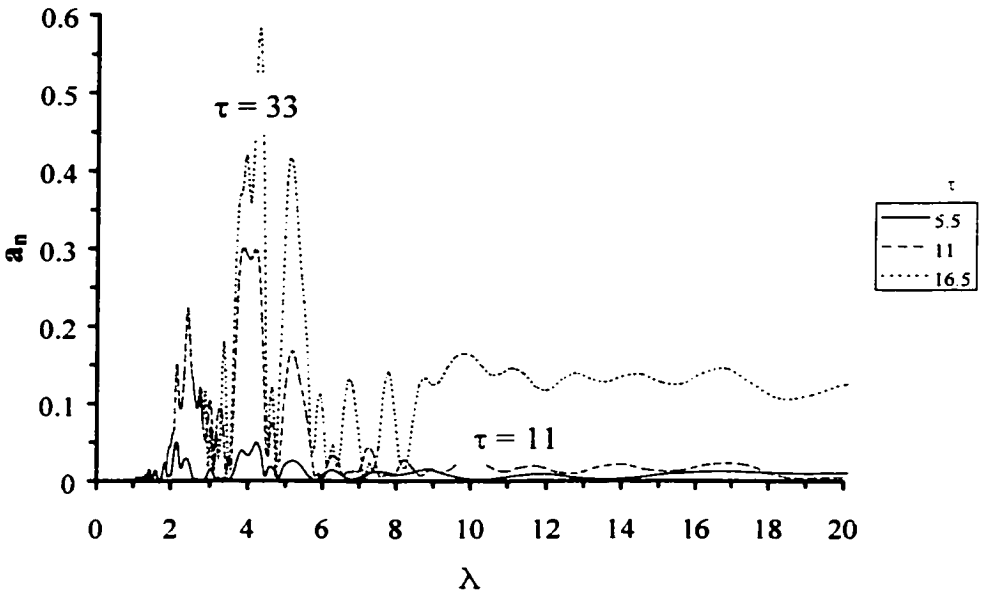

(b)

Figure A-16. Discrete Fourier Transform Analysis for Plane Strain Element Model *AP8* as a Function of (a) Wave Number, (b) Nondimensional Wavelength.

Appendix B Notes on Experimental Investigations

Details on the experience gained and observations developed from preliminary investigations are presented. Additional information that complements the discussion in Chapter 6, on the test apparatus, data acquisition system, measurement devices, and experimental procedure is also addressed. Furthermore, difficulties encountered during the test program are highlighted.

B.1 Preliminary Impact Investigations

During the preliminary stages of the experimental program, significant effort was expended modifying the initial design of the test apparatus through iterative trials. The primary issue was related to the structural configuration of the upper boundary condition, where the axial impulse was applied to the beam. The primary objective for the preliminary investigations was to achieve consistent and repeatable observed buckled mode response for a given slenderness ratio. The preliminary investigations considered a free upper support and a pinned upper support. The lower boundary condition was always set as fixed.

For the fixed-free boundary condition, during the impact event there was considerable lateral displacement of the beam at the point of contact and significant rotation about the lower fixed support. Consistent buckled response with repeated impact tests was extremely difficult to achieve due to the changes in contact dynamic (i.e. angle of impact, eccentricity, beam-mass rotation) with the relatively simple fixed-free boundary condition. Consequently, the applied impulse was not axial and these preliminary investigations were rejected.

Subsequently, a series of rollers were machined and a support fixture was bolted to the underside of the test frame to impose a pinned restraint. This boundary condition allowed axial translation, at the point of impact, and rotation about the roller supports while restraining lateral displacement. Unfortunately, a consistent pulse buckling response with successive impact events was not achieved. This is illustrated in Figure B-1, which shows the deformed profiles for *6061-T6* Aluminum beams (*500mm* $\times$ *25.4mm* $\times$ *4.76mm*) impacted by a *10kg* mass at a nominal velocity of *6.0m/s*. The lower support ($x = 0$) was fixed and the boundary condition at the beam-mass interface ($x = L$) was pinned. Although the boundary condition and test procedure was nominally equivalent for the four impact events, the resultant buckled mode response exhibited significant discrepancy. The response was attributed to the imposition of an inconsistent pinned boundary condition for successive impact tests. A variation in the degree of lateral restraint (i.e. stiffness) and frictional resistance of the roller pins, as well as the influence

of eccentric impact was considered the main factors. This was supported by examination of the impact interface, which generally exhibited a bias through the development of significant local plastic deformation and rotation about the roller support. Approximately 50 impact tests, with several modifications of the pinned support were investigated; however, the observed buckled mode shape was not consistent over the range of slenderness ratios investigated during the preliminary trials.

As discussed in Chapter 6, a mode transition toward the impact interface was predominantly related to the structural integrity of the imposed upper boundary condition. A similar mode transition was also observed by Ari-Gur et al. (1982,1978), although the contributing mechanism was not discussed. Finite element analysis, presented in Chapter 7, also demonstrated the importance of considering the imposed boundary condition on the computed pulse buckling response.

Consequently, the development of an alternative system was developed and was defined as a fixed lower support and upper slide-bearing restraint. The final apparatus design and experimental procedure was discussed in section 6.1.1.

B.2 Experimental Data Measurement

During the experimental investigations real-time (e.g. impact velocity, acceleration, and strain) and static (i.e. initial configuration, post-test buckled profile) data acquisition procedures were employed. A description of the data measurement systems, recorded data sets and difficulties encountered during the experimental investigations will be discussed.

B.2.1 Data Acquisition System

The data acquisition system was a *BE490™ Series Advanced Transient Recorder Plug-in (ATP)* card by ***Bakker Electronics Dongen bv***. The main features include a *12-bit* resolution, internal storage capacity of *128kSamples*, peak sampling rate of *1MHz* for one channel and *100kHz* for eight analog input channels per card with simultaneous sampling. For the current experimental test program, the sampling rate was held constant at *100kHz*. The board was installed on a *486-33MHz* personal computer. The companion application software *TEAM490™ Version 5.20A* defined the parameters for data acquisition and controlled the *ATP* card. The personal computer and data acquisition system is illustrated in Figure B-2. The system provided signal conditioning, span adjustment and conversion of analog signals to digital record for data storage for the measurement devices sampling displacement, strain, velocity and acceleration.

B.2.2 Impact Velocity

Three capacitive proximity switches (Omron Model E2K-F10MC1) determined the impact velocity of the striking mass. The sensors were positioned at a nominal *70mm* center-to-center spacing where the general location is shown in Figure 6-1 by the three wires leading from the drop tower assembly. The devices provided a trigger for the data acquisition card and determined the impact velocity, which was on the order of 6.2m/s. A typical record, measured in voltage as a function of time, is presented in Figure B-3 for Test *SIc4*. As the lower alignment disc passed the lead proximity switch, the output signal from the lead proximity switch also served as a trigger pulse for the acquisition card. This is shown in Figure B-3 by the initial, square wave signal. The transient response was a result of the capacitor discharging after the alignment disc had passed the proximity switch. The velocity of the hammer prior to impact can be calculated based on the center-to-center spacing of proximity switch pairs and recorded time intervals to pass the proximity switches.

B.2.3 Accelerometer and Displacement Transducer Sensors

Initially, accelerometers were attached to the beam to directly measure the buckling response. In comparison with conventional strain gauge methods, this would have the potential for considerable savings in both preparation time and cost. Due to the intense lateral stress wave and buckling motion, however, the accelerometers would only remain attached to the beam through a stud-mounted, threaded connection. Various configurations using the standard wax 'bond adhesive' were unable to withstand the effects of the applied impulse. Although, the stud mounted accelerometers proved successful in capturing the impact event, one accelerometer sensor was destroyed when the buckled crest of the beam bent the signal output stem. A dynamic displacement transducer was also employed but the trials were unsuccessful due to the low transducer core inertia and significant momentum transfer during the impact event. Lindberg and Florence (1987) state that the lateral velocity, of the peak buckle crest, during the elastic buckling studies was on the order of 23m/s. Furthermore, based on finite element analysis presented in Chapter 7, the maximum velocity of the peak buckle crest was on the order of 37m/s. The primary objective for direct measurement was to obtain real-time data, of the peak buckle crest and midspan locations, in order to conduct a comparative assessment of the pulse buckling response. The data would be required for validation of finite element models and also the development of dynamic buckling criteria. Consequently, strain gauges were opted as the preferred direct instrumentation method but as discussed in the next section this method also encountered significant difficulties.

B.2.4 Foil Strain Gauges

Epoxy bonded, foil strain gauges were also employed, to measure axial and flexural deformations at several longitudinal positions along the length of the beam. Stations were marked on the beam and the surface was prepared, according to the manufacturer's guidelines, to attach the foil strain gauges. For all tests, at least two gauges were surface mounted on the beam at the midspan, which were attached in pairs and symmetrically distributed on opposite faces of the beam. Additional strain gauge locations, for a given slenderness ratio, were defined by the nominal position of the observed peak buckle from previous impact tests. Specific details on the longitudinal strain gauge distribution are presented in Figure B-4, Figure B-5 and Figure B-6. The objective was to measure the strain response on or near the peak buckle crest to compare with the midspan response and to assess the dynamic buckling criterion proposed by Ari-Gur et al. (1982), which was based only on the midspan deflection.

The foil gauges were ***Measurements Group*** *EP-series* with a 120Ω resistance and a capability of measuring $\pm 20\%$ strain and *EA-06-250BG-120* with a $\pm 5\%$ strain range. The specific gauge locations will be discussed later. As shown in Figure B-2, a bridge completion module (***Omega*** *BCM-1*) and strain gauge, bridge signal conditioner (***Omega*** *OM2-165*) completed the circuit. The amplifier output for each channel was separately patched into an 'in-house' designed and manufactured span adjustment unit so that the residual strain, due to curing of the epoxy, could be offset. The modified signal was then input to the data acquisition card for analog to digital conversion and storage on the hard disk for post-processing.

Figure B-7 and Figure B-8 illustrates the initial configuration and post-test buckled profile for impact test *AIId9*, which was instrumented with foil strain gauges. A more complete strain data record (Test *AIf4*) is presented in Figure B-9. For clarity, the strain magnitude was arbitrarily offset by 10,000μs. As detailed in Figure B-4, the gauges were 75mm (Gauges #1 and #2), 110mm (Gauges #3 and #4) and 275mm (Gauges #5 and #6) from the fixed lower support ($x = 0$). The latter pair was located at midspan, whereas the former two sets were positioned to capture characteristics of the peak transverse displacement. The data records illustrate the significant plastic deformation associated with the peak buckle response, Figure B-9(a), in comparison with the off-peak, Figure B-9(b), and midspan, Figure B-9(c).

Although some tests were successful, significant difficulties were encountered during the experimental investigations to maintain working foil gauges. This was attributed to the intense stress wave and transverse velocity associated with the pulse buckling events. There problems encountered with the instrumented foil gauges could be categorized as:

- the solder weld connecting the coupled negative and ground leads to the foil gauge occasionally failed.
- the bonded strain gauge located on the tension side of the peak buckle lifted off the beam surface
- the foil on the compressive side of the peak buckle was damaged through local buckling of the gauge.

The main cause for these events was attributed to the intense lateral stress wave, in particular for the peak buckle location. In addition to the strain gauge epoxy, fast curing resins, adhesives (Automotive GOOP™, tape) and silicone gel (SILPRUF™ SC6-2000) were also applied during the course of the experimental investigations, in an attempt to prevent failure of the foil gauge sensors. Table B-1 summarizes various test difficulties encountered where 32 of 73 strain gauges failed. Consequently, the establishment of engineering relationships, based on a comprehensive experimental strain record, across the range parameters investigated was not successful due to the loss of strain gauge instrumentation.

B.2.5 Applied Boundary Condition

Although a majority of the impact experiments conducted were successful, 94 out of 115 tests, invariably some results were discarded. This was demonstrated by the measured initial and final deformed profiles for tests *AId1* and *AId4* (Figure 6-3) and also illustrated by the buckled profiles of series *AIc* presented in Figure B-10. The response was attributed to problems encountered with the upper support boundary condition and related to either a loss of structural integrity or a "dead" impact. Table B-2 summarizes the problems encountered during the current experimental investigations for specific impact tests.

Evolution of the peak buckle crest was typically developed near the lower fixed support ($x = 0$), as illustrated in Figure B-10 for impact tests *AIc1*, *AIc3* and *AIc4*. Establishing the basis for defining a representative buckled response, for a given slenderness ratio, was founded on experience gained from the preliminary investigations, observations of the predominant buckled mode response and parallel finite element analysis. For the impact tests *AIc2* and *AIc5* a shift in the peak buckle location away from the lower fixed boundary toward the upper support ($x = L$) was observed. A shift in location of the peak buckle crest was characteristic of impact events where the slide bearing disc was partially or fully driven out of the support collar. The structural integrity of the upper support ($x = L$) was compromised and unrestrained. This is illustrated by the beam rotation about the upper boundary condition ($x = L$) as shown in Figure B-10 for impact tests *AIc2* and *AIc5*. Consequently, for these impact events, the recorded data was not analyzed.

The importance of these observations should be placed in context with the experimental investigations of Ari-Gur et al. (1982, 1978). A similar response was observed where the peak buckle location shifted toward the upper support (i.e. impact interface) for effective slenderness ratios (L_e/r) on the order of 200, which was illustrated in Figure 5-6. For the experimental investigations of Ari-Gur et al. (1982,1978), a single column was successively impacted by the same mass with increasing drop heights until buckling occurred, where the final deformed profile exhibited plastic mode response. Although recognized, the contributing mechanism was not discussed by Ari-Gur et al. (1982, 1979). Finite element analysis, presented in Chapter 7, supported the experimental observations of a shift in the peak buckle location toward the upper restraint associated with the imposed structural boundary condition.

For the higher slenderness ratios ($L_e/r > 250$), acceptable impact test results were difficult to achieve and data for the longer column lengths of *Series AIIe* and *AIIf* were discarded completely.

A "dead" impact was also encountered where the hammer would exhibit little or no recoil. These events are listed in Table B-2 as N^3. This event was probably due to a slight rotation of the impact hammer assembly about the longitudinal axis of the drop tower during free fall, which subsequently caused the mass assembly and/or the slide-bearing disc to become slightly "jammed".

B.3 Detailed Experimental Procedure

For a given slenderness ratio, the crosshead for the static test frame was lowered into position, such that the lower edge of the bearing disc within the drop tower was aligned with a marking on the beam sample. A nominal distance of 35mm (≈1.25") from the top of the beam was scribed on the surface with an indelible marker. The bearing disc thickness was approximately 25mm. This would ensure that the pre-test configuration was consistent for all impact events. Experimental observations suggested that axial deformations were on the order of 5mm.

For all tests, the bearing surface on the *PVC* disc was sprayed with *Teflon* coating to reduce axial friction. The test specimen was pushed through the slotted *PVC* disc and the beam was placed in the lower vice grip support. The upper slide bearing was then raised in position within the collar support of the drop tube assembly. Markings etched on the vice grip platens, ensured that the beam was centered on the longitudinal axis of the drop tower. The only constraint was that beam mill stamp was facing the same direction in the test frame for all impact events. A torque wrench, set to *50N-m*, was used to secure the beam within the lower fixed support. The threaded, transverse support rod and a dial gauge mounted to a support frame, illustrated in Figure 6-1, were used to align the upper boundary support with the fixed lower restraint within *±0.0508mm* (*±2/1000"*). The

threaded rods would then be locked in place using hex nuts and lock washers to act as a bracing system to stabilize the drop tower during the free-fall decent of the impact hammer and to resist the reaction loads developed at the upper support boundary.

The initial global geometric imperfections of the beam sample, in the test frame, were measured and prior to each impact test the dial gauge was removed. The initial beam profiles were measured with respect to the same reference point. The zero datum, for both axial and transverse measurements, was defined by the position of the beam end within the fixed lower support of the vice grip (Figure B-11). The initial geometric profile was measured at *25mm* stations along the beam length by a mechanical, spring-loaded dial gauge with an accuracy of $\pm 0.0254mm$ ($\pm 0.001"$).

The main support frame of the measurement assembly was fabricated from aluminum C-channel section. This was welded to an aluminum beam and bolted to the steel base plate attached to the static test frame. A machinist level table ensured that the imperfection measurement apparatus was at right angles to the base support. A slot was cut into the C-channel to accommodate a sliding block to support the dial gauge and was secured by a centrally located wing nut.

For test samples instrumented with strain gauges, a conductivity check was also conducted, which ensured that proper electrical connections were developed prior to the impact event. The span adjustment unit zeroed the voltage signal output of the strain gauges in order to accommodate the $\pm 5V$ range of the data acquisition card.
A wire-pulley system was used to raise the hammer, through the tube to the desired drop height, in order to initiate the free-fall and subsequent impact event. Once the striking mass was raised to the desired drop height, via the pulley system, the data acquisition trigger was armed and the mass was released. As the hammer passed the first proximity switch, the data acquisition system was tripped and the buckling event was recorded (Figure B-3). Occasionally a second impact was observed but was considered negligible in terms of the effect on the buckled response, which was based on analysis of the data records for the recorded trigger pulse and strain response. The conclusion was also consistent with the findings of Ari-Gur et al. (1982, 1978).

After the impact event was completed, the mass was secured in a neutral position. The buckled mode shape (i.e. transverse deflection) was profiled at *25mm* stations along the length of the impacted beam. In addition to the specified measurements, the location of a local minima or maxima was also recorded.

Table B-1. Notes for the Impact Tests Instrumented with Foil Strain Gauges.

Series *AI*		Series *AII*		Series *SI*	
Test	Notes	Test	Notes	Test	Notes
AIa4	N^2 (2/2)	*AIIa3*	N^2 (1/2)	*SIa5*	N^2 (1/2)
AIa6	N^2 (2/2)	*AIIb5*	N^2 (4/4)	*SIc4*	N^2 (1/4)
AIc5	N^2 (4/4)	*AIIb10*	N^3	*SIc9*	N^2 (2/5)
AIc10	N^2 (2/5)	*AIId3*	N^2 (3/6)	*SIf5*	N^2 (1/6)
AIf4	N^1, N^2 (1/6)	*AIId9*	N^2 (4/6)	*SIf6*	N^2 (0/6)
AIf10	N^1, N^2 (1/6), N^3			*SIf12*	N^2 (3/7), N^3

Notes: N^1 - slide bearing not fully restrained by support collar, N^2 – solder connection or epoxy bond of foil gauges failed and (n/N) represents the number of Strain Gauges that failed with reference to the total number of strain gauges, N^3 – data acquisition trigger failed.

Table B-2. Notes for Individual Impact Tests of the Experimental Investigations with Questionable Buckling Response.

Series AI		Series AII		Series SI	
Test	Notes	Test	Notes	Test	Notes
AIc1	N^1, N^2	*AIIb8*	N^1/N^3	*SIc5*	N^3
AIc2	N^1, N^2	*AIIc2*	N^3	*SId3*	N^1
AIc8	N^3	*AIIc5*	N^3	*SIf1*	N^1
AId1	N^1	*AIId9*	N^3	*SIf12*	N^1
AIe1	N^1	*AIIe2*	N^1/N^3		
AIf2	N^1	*AIIe3*	N^3		
AIf4	N^1				
AIf10	N^1,N^2				

Notes: N^1 - slide bearing not fully restrained by support collar, N^2 – rotation about lower support, N^3 – inconsistent buckled response associated with the bearing support and a "dead" impact with little or no recoil of the free fall hammer.

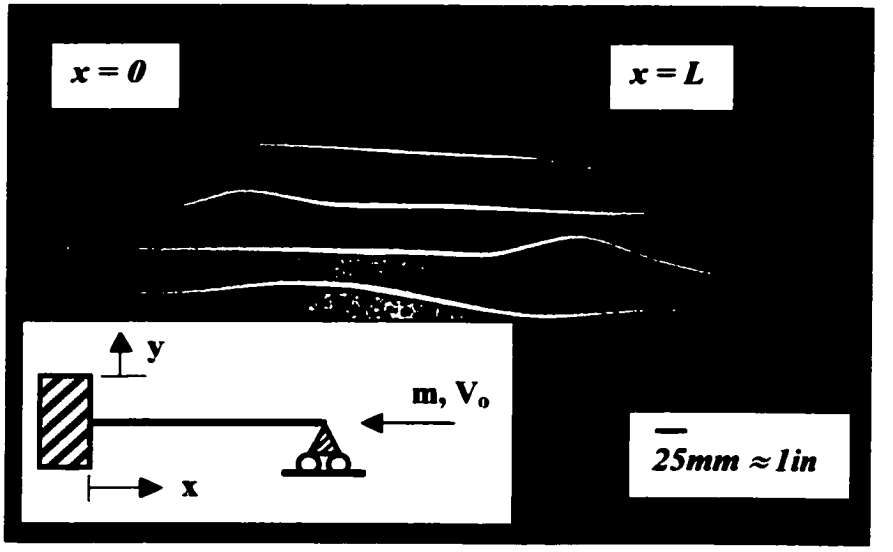

Figure B-1. Typical Deformed Buckled Profile During Preliminary Investigations.

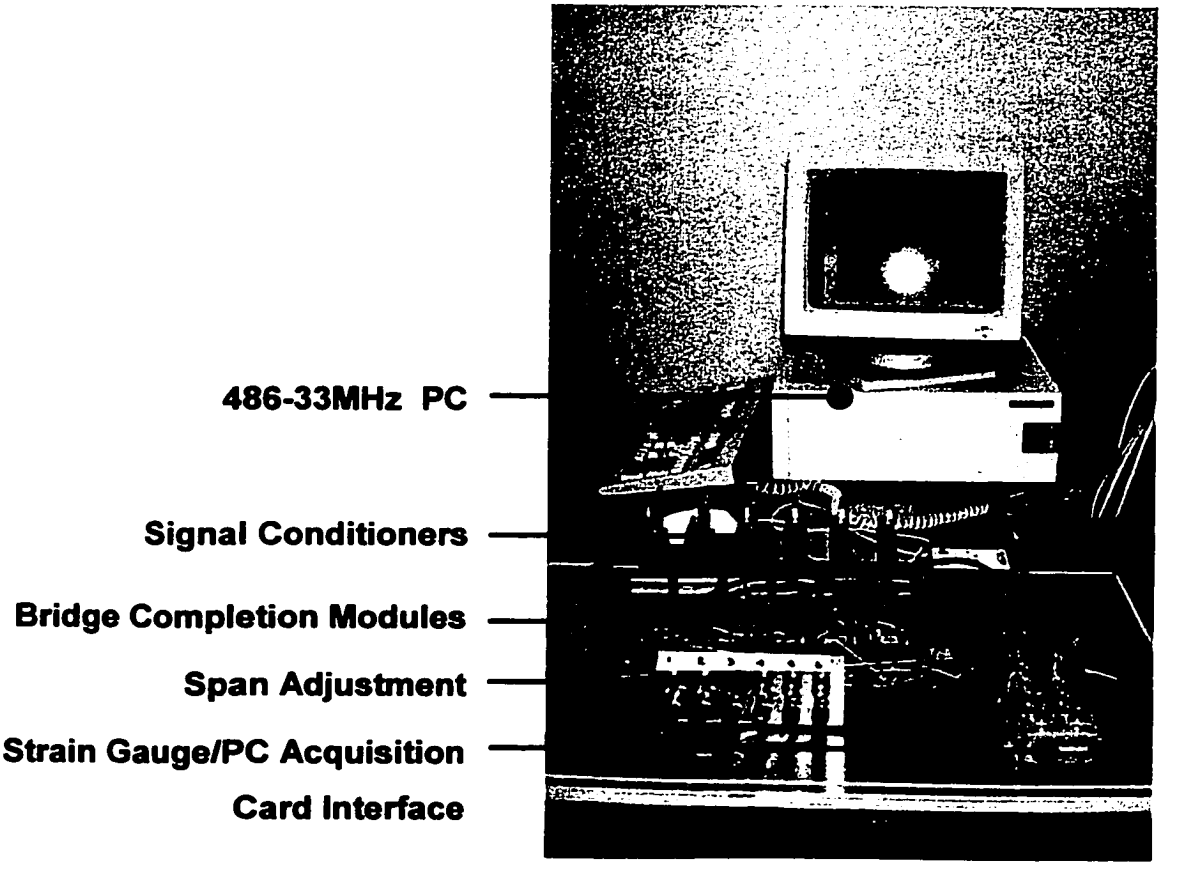

Figure B-2. Data Acquisition System.

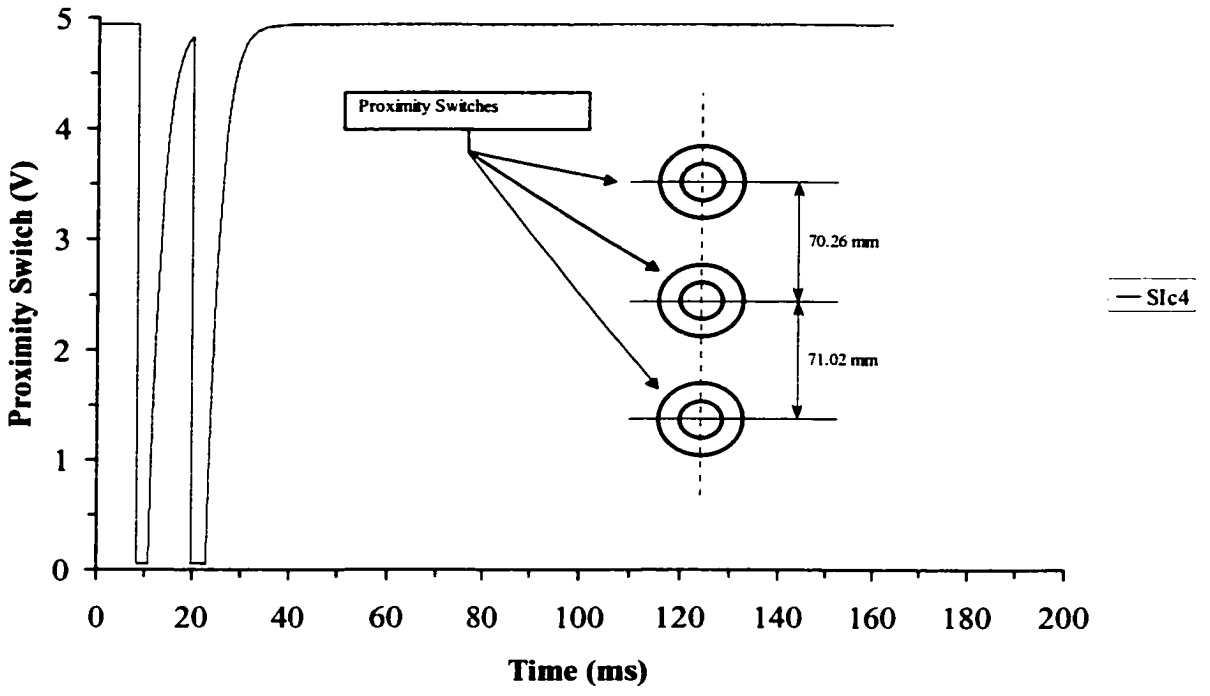

Figure B-3. Typical Record for the Proximity Switches from Test *SIc4*.

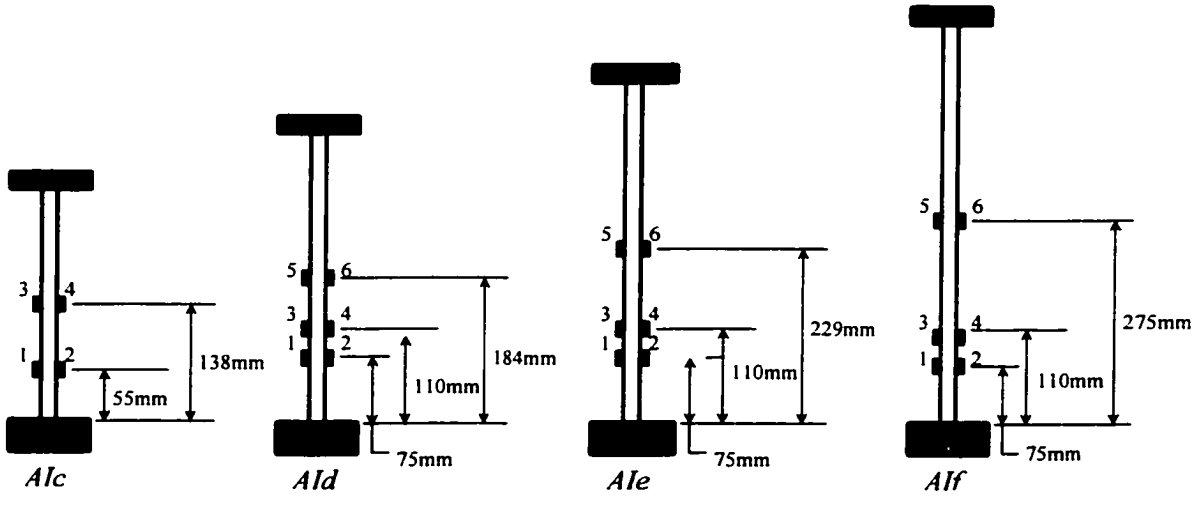

Figure B-4. Instrumented Strain Gauge Locations for Series *AI* (Tests *AIc* , *AId*, *AIe*, *AIf*).

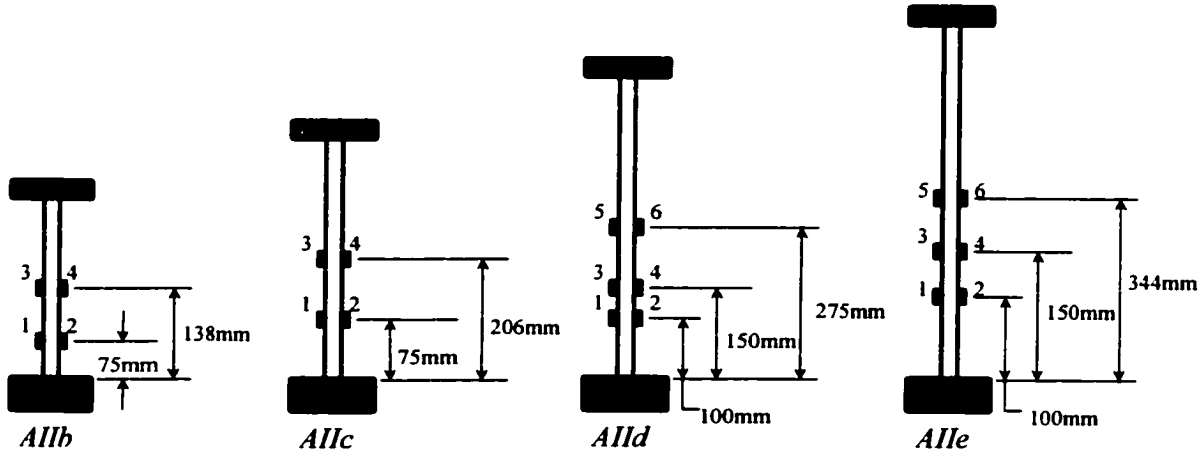

Figure B-5. Instrumented Strain Gauge Locations for Series *AII* (Tests *AIIb* , *AIc*, *AIId*, *AIIe*).

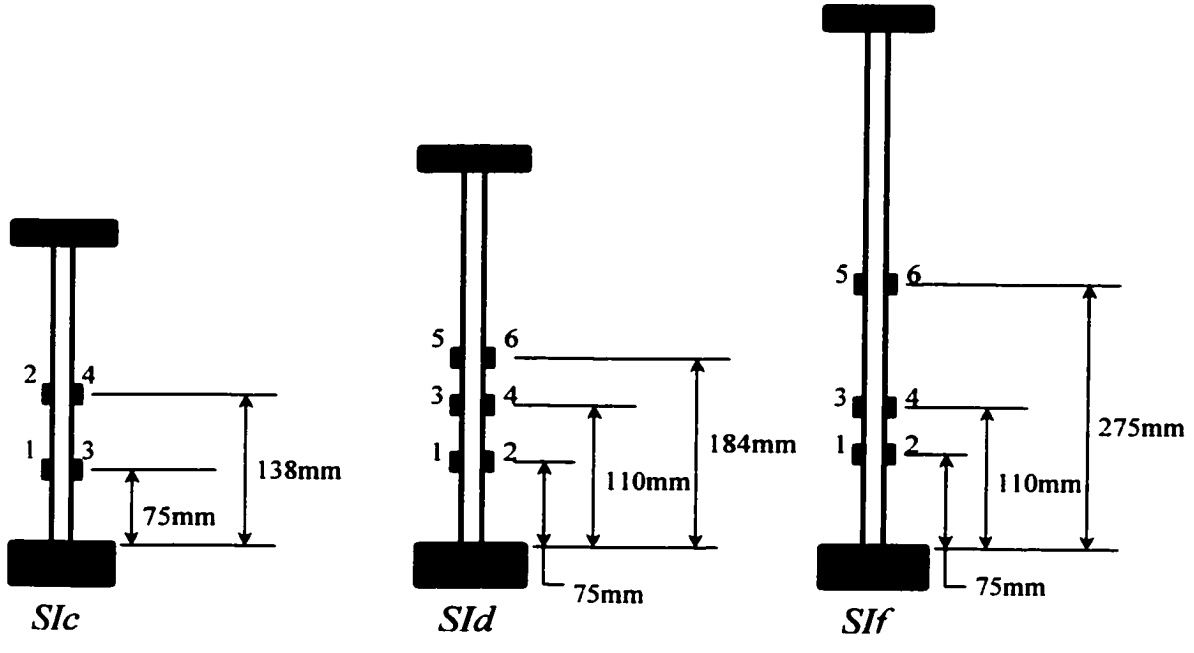

Figure B-6. Instrumented Strain Gauge Locations for Series *SI* (Tests *SIc* , *SId*, *SIf*).

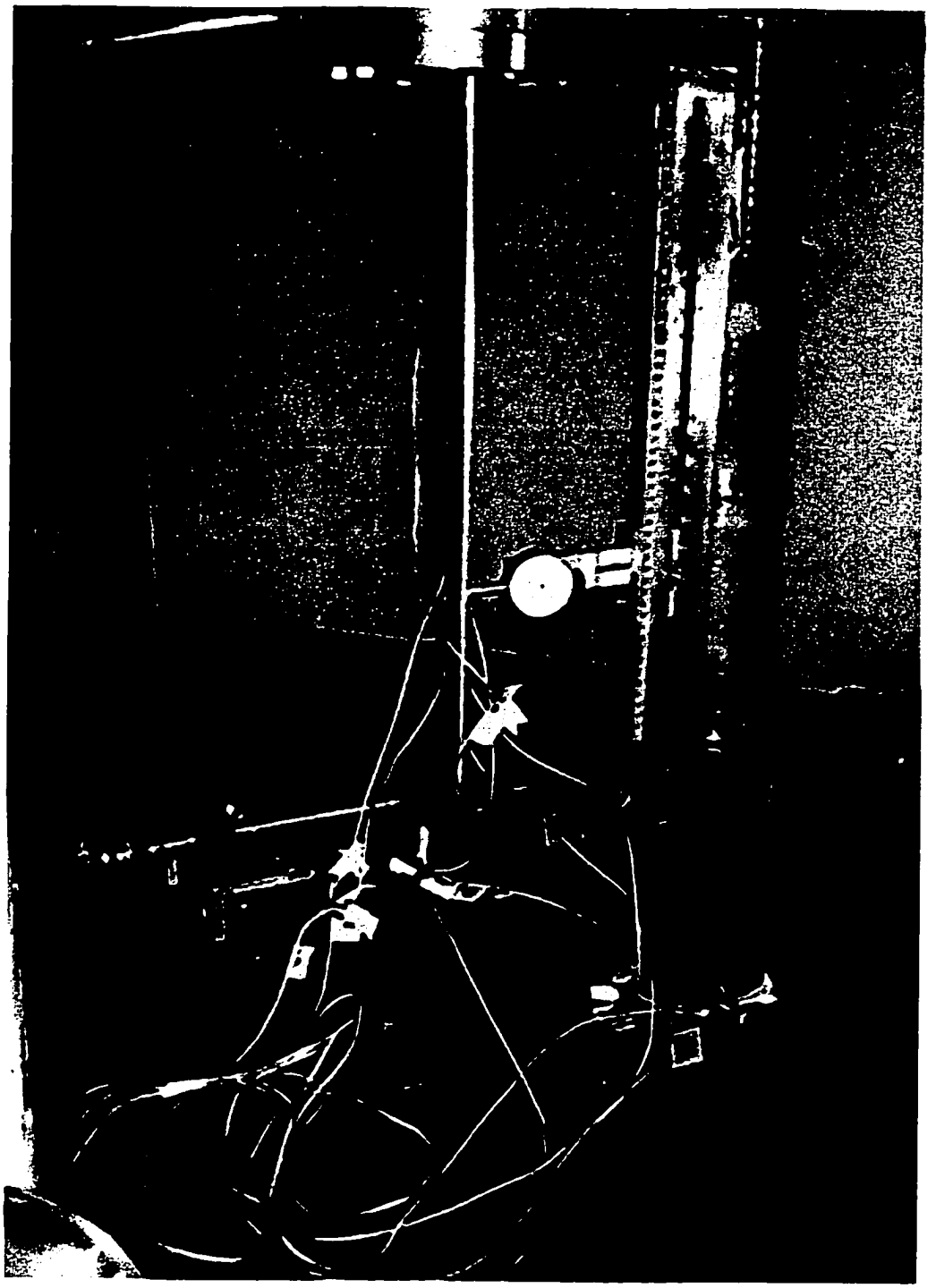

Figure B-7. Initial Configuration for Test *AIId9*, ($d = 4.7625mm$) with Slenderness Ratio ($L_e/r = 200$), Instrumented with Strain Gauges.

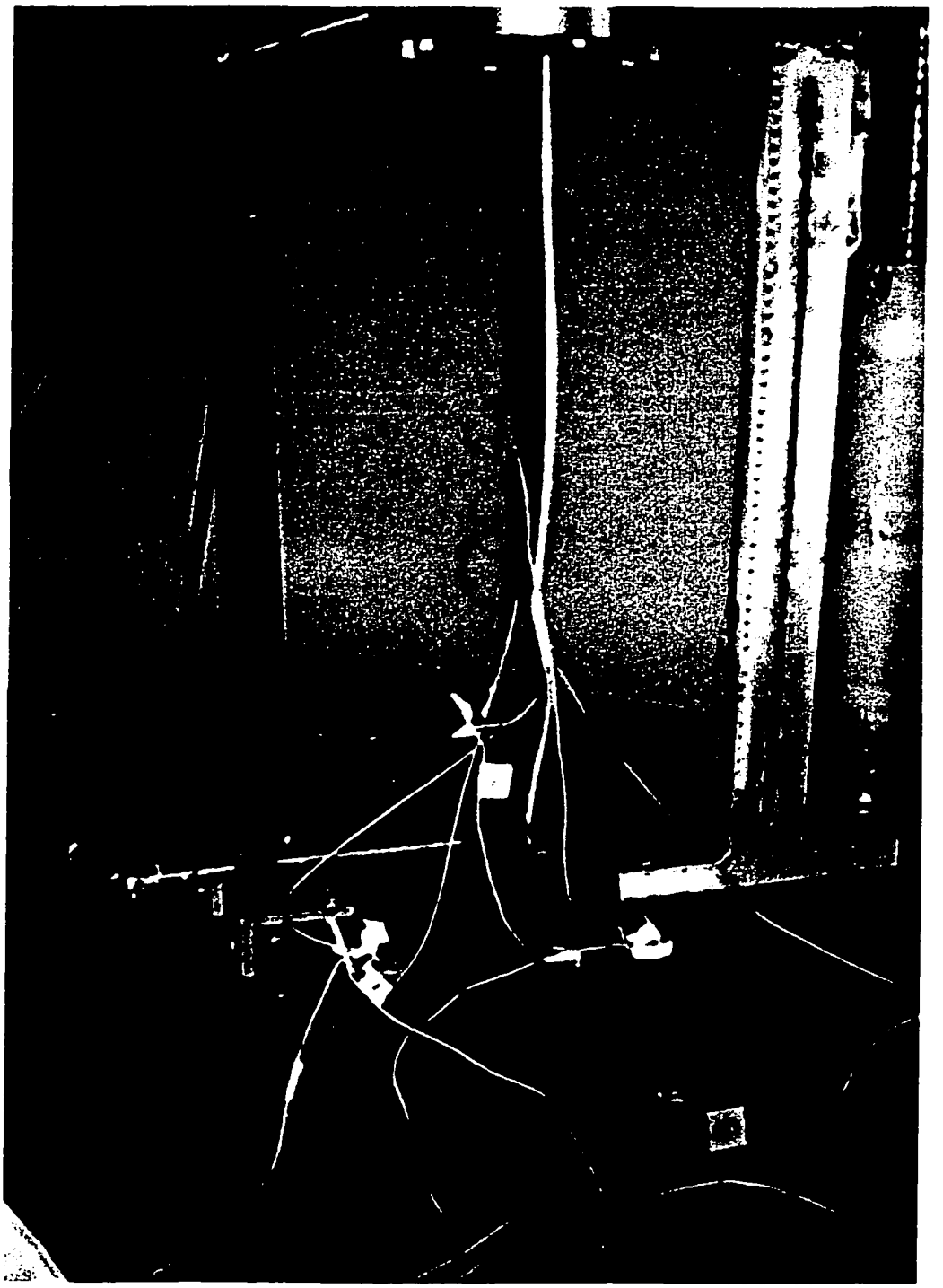

Figure B-8. Deformed Buckled Profile for Test *AIId9* Instrumented with Strain Gauges.

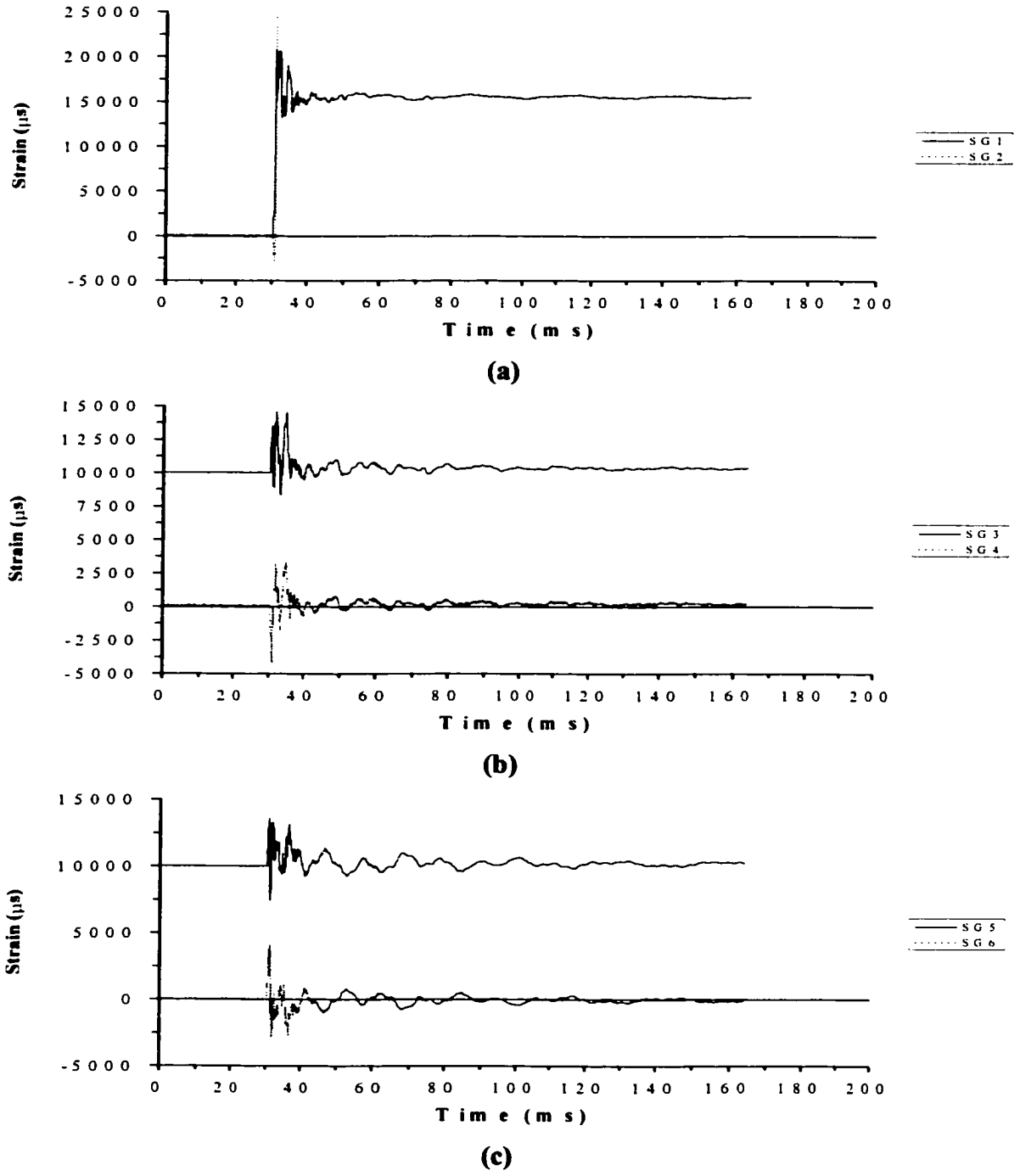

Figure B-9. Strain Record for Test *Alf4*, (a) Gauges #1 and #2 (Peak), (b) Gauges #3 and #4 (Off-Peak), and (c) Gauges #5 and #6 (Midspan).

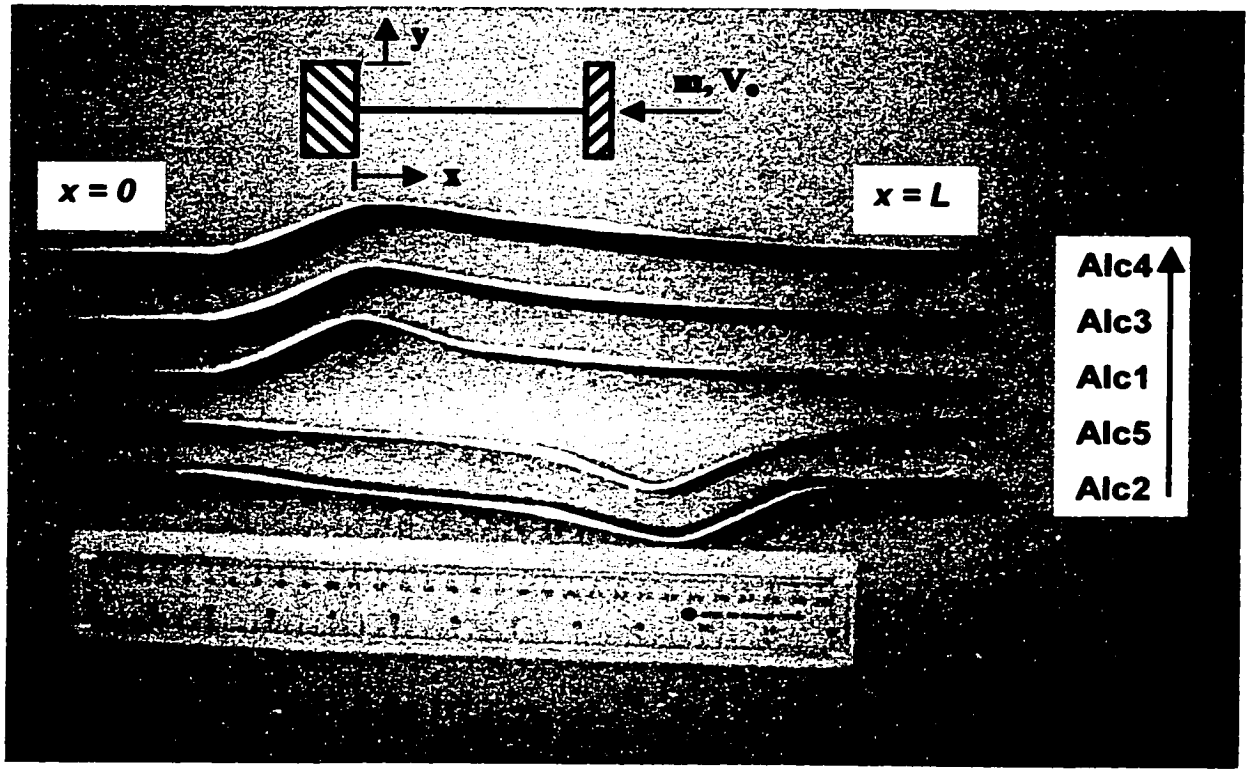

Figure B-10. Buckled Profiles for Tests Series *Alc1* to *Alc5*.

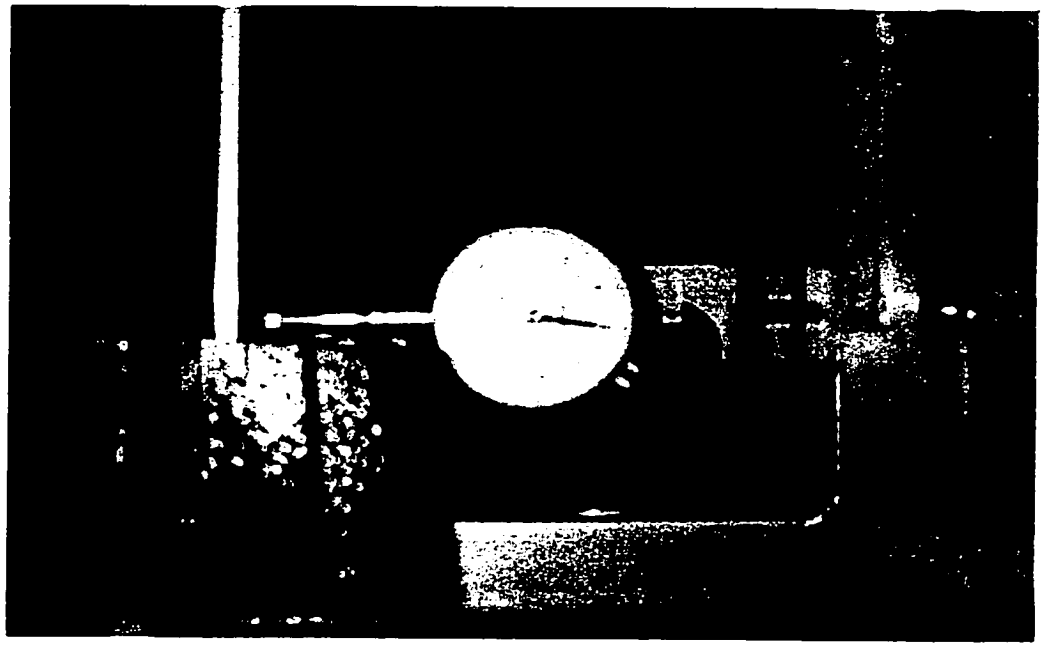

Figure B-11. Datum Level for Measurement of Initial Geometric Imperfections and Final Buckled Profile.

Appendix C Experimental Data

This appendix documents the measured physical test data compiled during the experimental impact investigations. Profiles of the initial bar geometry and final buckled mode shape are presented. The geometric data was consistently measured with respect to the same reference point. The zero datum, for both axial and transverse measurements, was defined by the position of the bar end within the fixed lower support of the vice grip. This is illustrated in Figure C-1. Lateral deflections (y) were measured by a spring-loaded dial gauge (± 0.001") and referenced to the initial baseline reading. The bar geometry data was sampled at 25mm intervals along the longitudinal axis (x). Furthermore, location and amplitude of the peak buckle crests were also recorded. For impact tests, which included foil gauge instrumentation, the complete strain data record is illustrated.

The total number of tests for each series and respective slenderness ratios are listed in Table C-1. A total of 115 impact tests were conducted. Notes detailing problems encountered during the test program, which question the observed buckling response, are listed in Table C-2. Typically this would be a result of the PVC slide bearing not being fully restrained by the support. Consequently, the integrity of the upper boundary condition was compromised. In general the resultant buckling motion could be characterized by a higher order response with a shift in the peak buckle location toward the upper restraint. This errant boundary condition, however, occurred for only 12 of the 115 impact tests conducted with a greater proportion occurring at the higher slenderness ratios. Finally, specific notes on impact tests instrumented with strain gauges are presented in Table C-3.

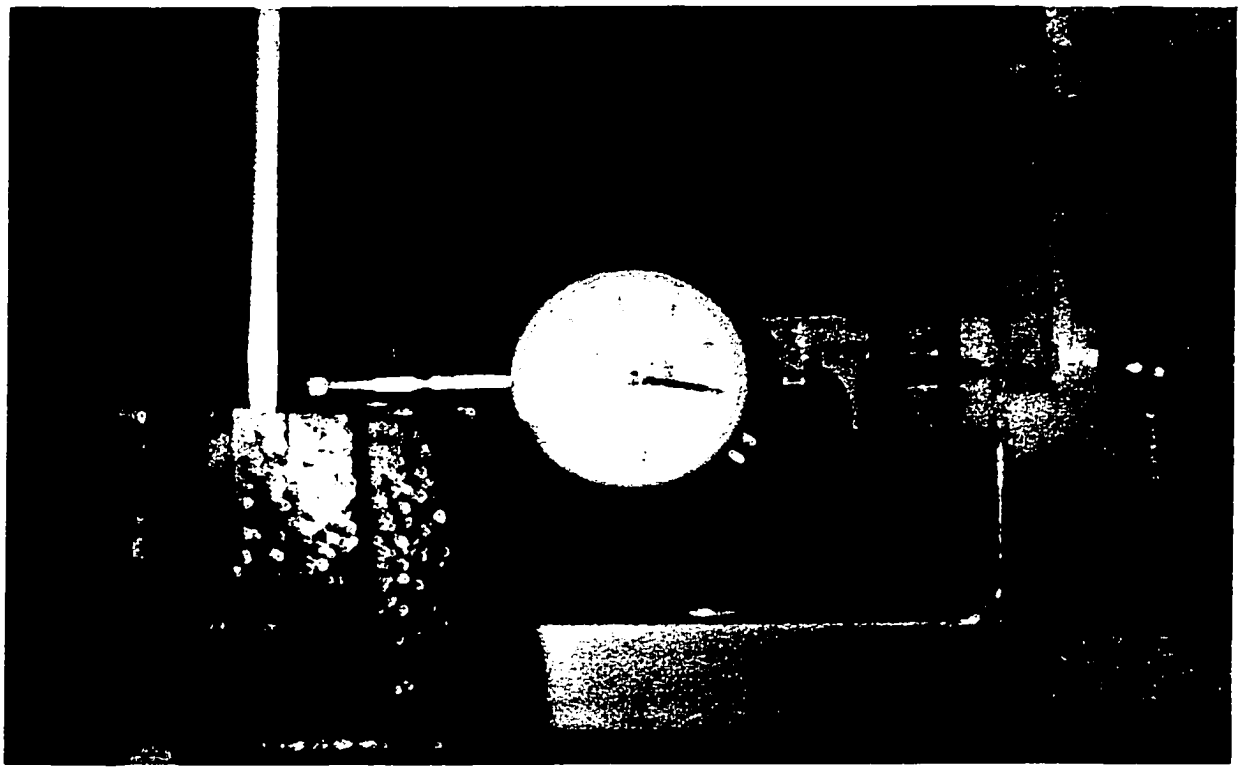

Figure C-1. Datum Level for Measurement of Initial Geometric Imperfections and Final Buckled Profile.

Table C-1. Total Number of Impact Tests for the Experimental Investigations.

Test	L_e/r	Series AI	Series AII	Series SI
a	75	6	3	5
b	100	5	10	6
c	150	10	5	9
d	200	5	9	6
e	250	5	4	5
f	300	10	-*	12

* - difficulty in obtaining consistent buckled response with the increased bar length (925mm) and was associated with a 'magnified' error over this length and interplay with the fixed end boundary conditions.

Table C-2. Notes for Individual Impact Tests of the Experimental Investigations with Questionable Buckling Response.

Series AI		Series AII		Series SI	
Test	Notes	Test	Notes	Test	Notes
AIc1	N^1, N^2	*AIIb8*	N^1/N^3	*SIc5*	N^3
AIc2	N^1, N^2	*AIIc2*	N^3	*SId3*	N^1
AIc8	N^3	*AIIc5*	N^3	*SIf1*	N^1
AId1	N^1	*AIId9*	N^3	*SIf12*	N^1
AIe1	N^1	*AIIe2*	N^1/N^3		
AIf2	N^1	*AIIe3*	N^3		
AIf4	N^1				
AIf10	N^1,N^2				

Notes: N^1 - slide bearing not fully restrained by support collar, N^2 – rotation about lower support, N^3 – inconsistent buckled response associated with the bearing support and a "dead" impact with little or no recoil of the free fall hammer.

Table C-3. Notes for the Impact Tests Instrumented with Strain Gauges.

Series AI		Series AII		Series SI	
Test	Notes	Test	Notes	Test	Notes
AIa4	N^2 (2/2)	*AIIa3*	N^2 (1/2)	*SIa5*	N^2 (1/2)
AIa6	N^2 (2/2)	*AIIb5*	N^2 (4/4)	*SIc4*	N^2 (1/4)
AIc5	N^2 (4/4)	*AIIb10*	N^3	*SIc9*	N^2 (2/5)
AIc10	N^2 (2/5)	*AIId3*	N^2 (3/6)	*SIf5*	N^2 (1/6)
AIf4	N^1, N^2 (1/6)	*AIId9*	N^2 (4/6)	*SIf6*	N^2 (0/6)
AIf10	N^1, N^2 (1/6), N^3			*SIf12*	N^2 (3/7), N^3

Notes: N^1 - slide bearing not fully restrained by support collar, N^2 – solder connection or epoxy bond of foil gauges failed and (n/N) represents the number of Strain Gauges that failed with reference to the total number of strain gauges, N^3 – data acquisition trigger failed.

C.1 Series AI – 6061-T6 Aluminum Bars

Figure C-2. General Deformed Buckled Profiles for Series *AI* (Tests *AIa* to *AIf*) Impacted by a 10kg Free Fall Impact Hammer at a Nominal Velocity of 6m/s.

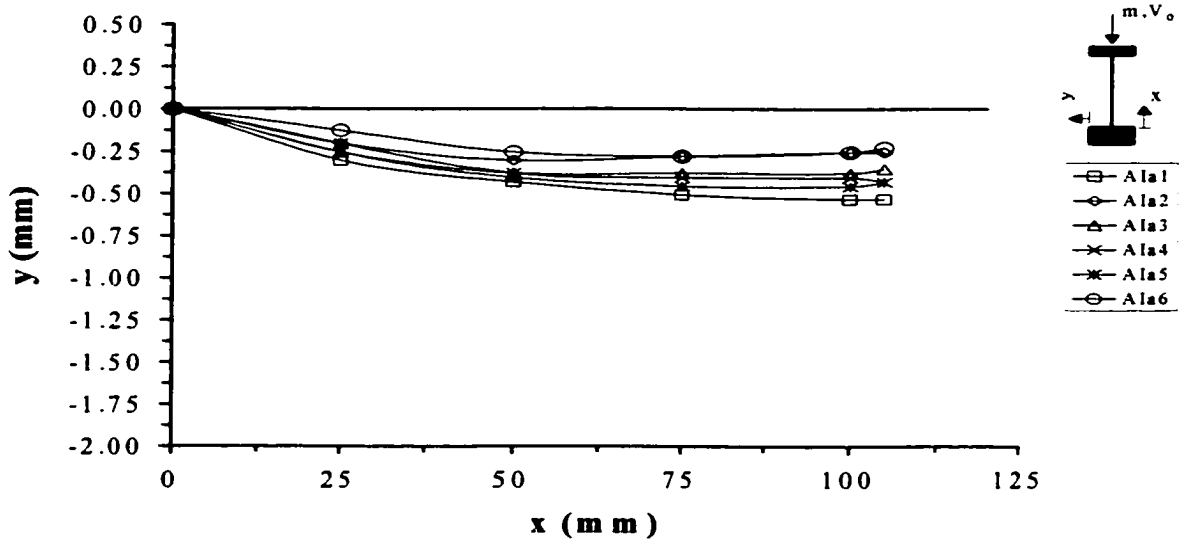

(a)

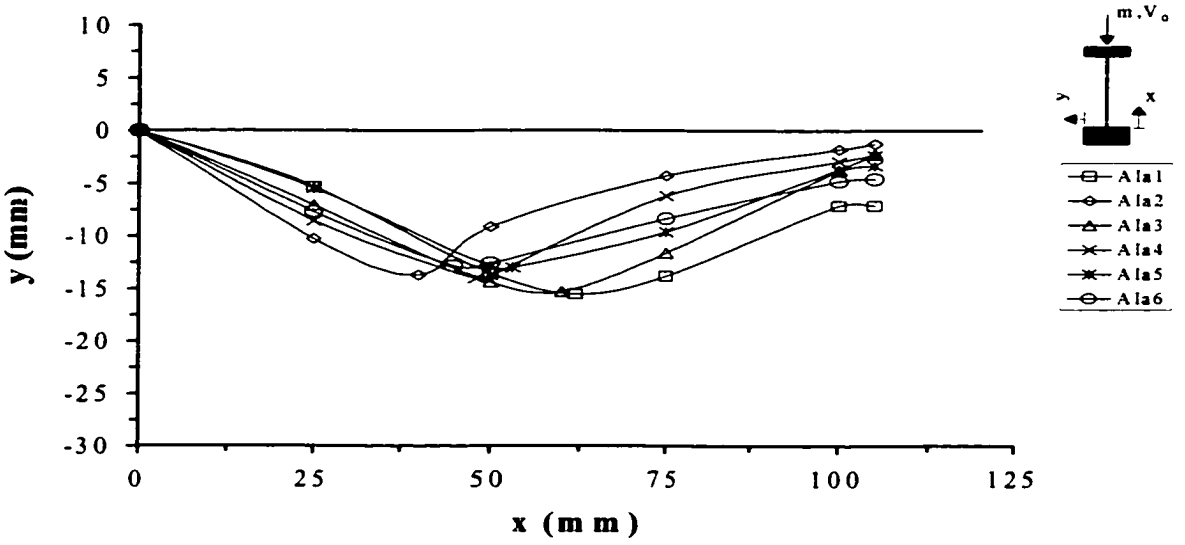

(b)

Figure C-3. Series *AIa*, Tests: 1 to 6, (a) Initial Global Imperfections and (b) Deformed Buckled Profiles.

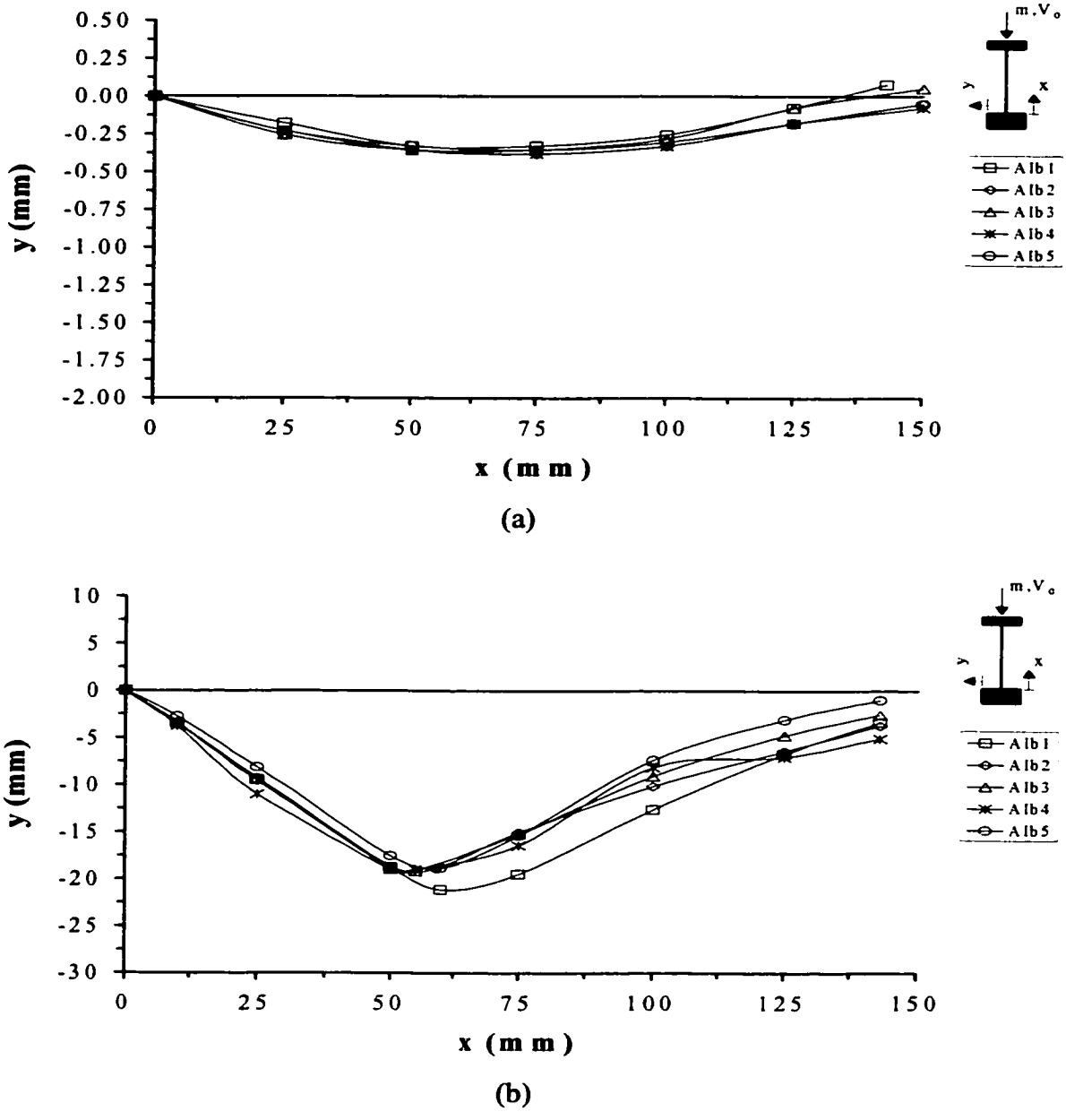

Figure C-4. Series *Alb*, Tests: 1 to 5, (a) Initial Global Imperfections and (b) Deformed Buckled Profiles.

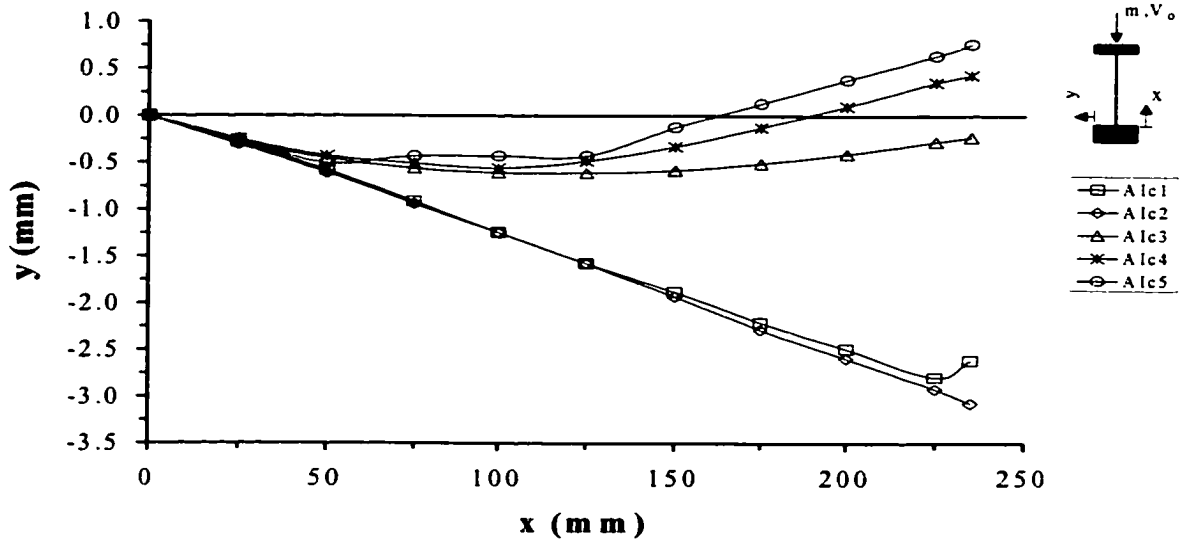

(a)

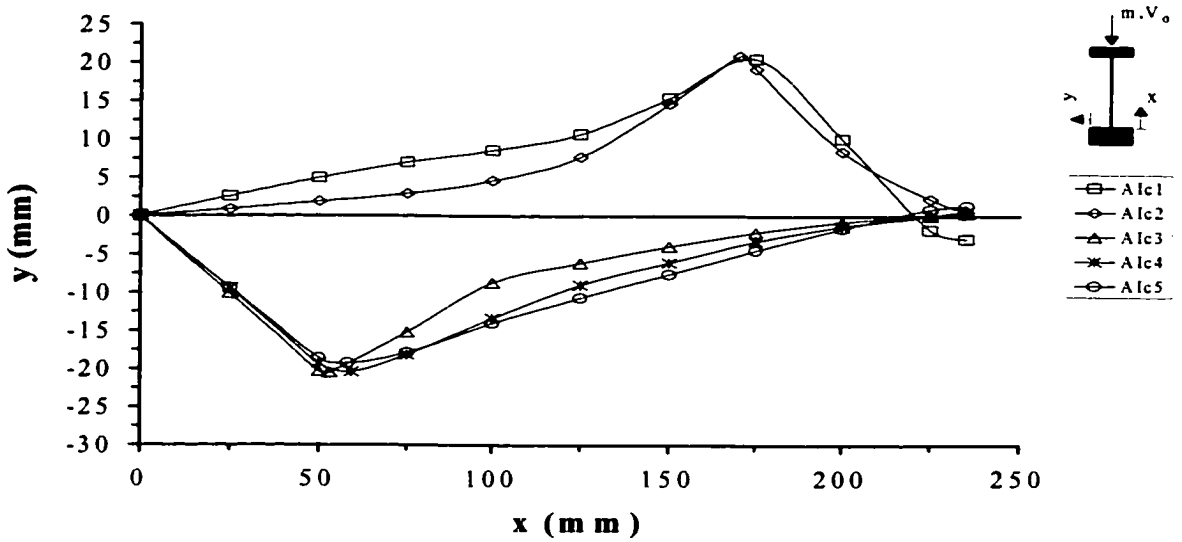

(b)

Figure C-5. Series *AIc*, Tests: 1 to 5, (a) Initial Global Imperfections and (b) Deformed Buckled Profiles.

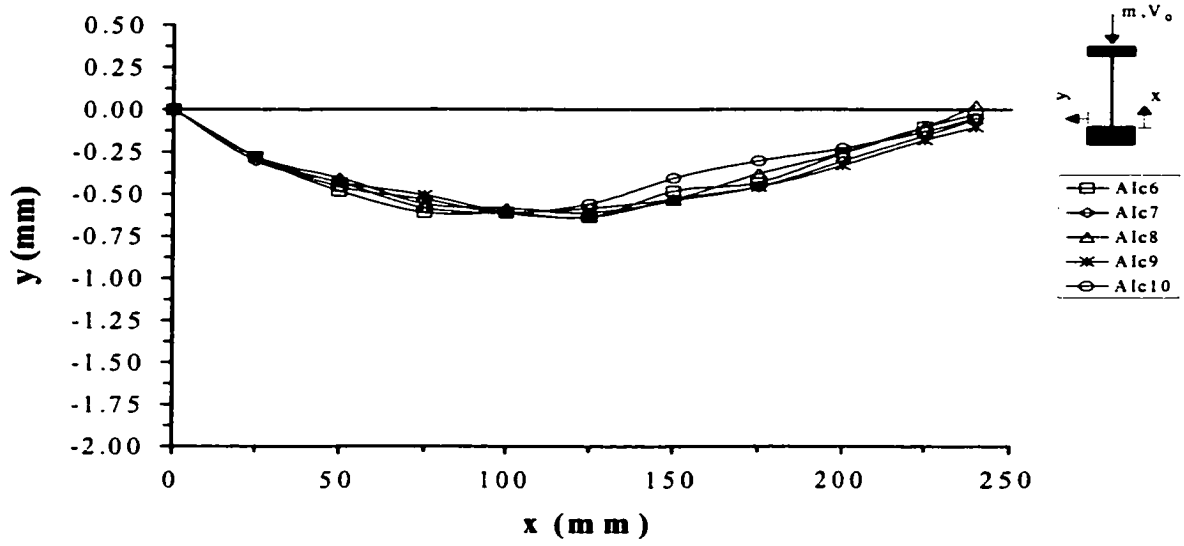

(a)

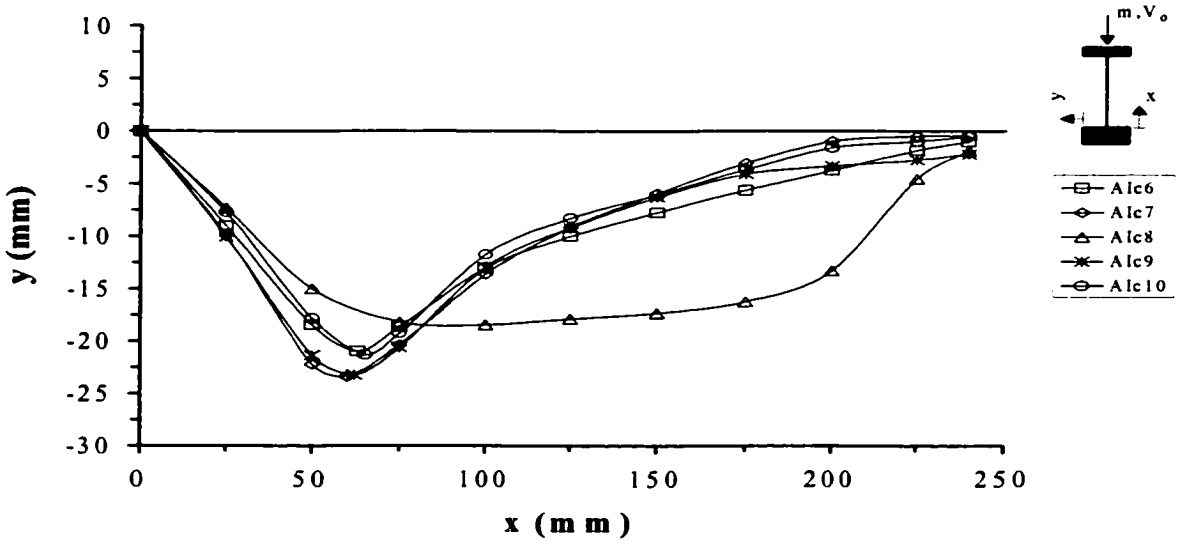

(b)

Figure C-6. Series *AIc*, Tests: 6 to 10, (a) Initial Global Imperfection and (b) Deformed Buckled Profiles.

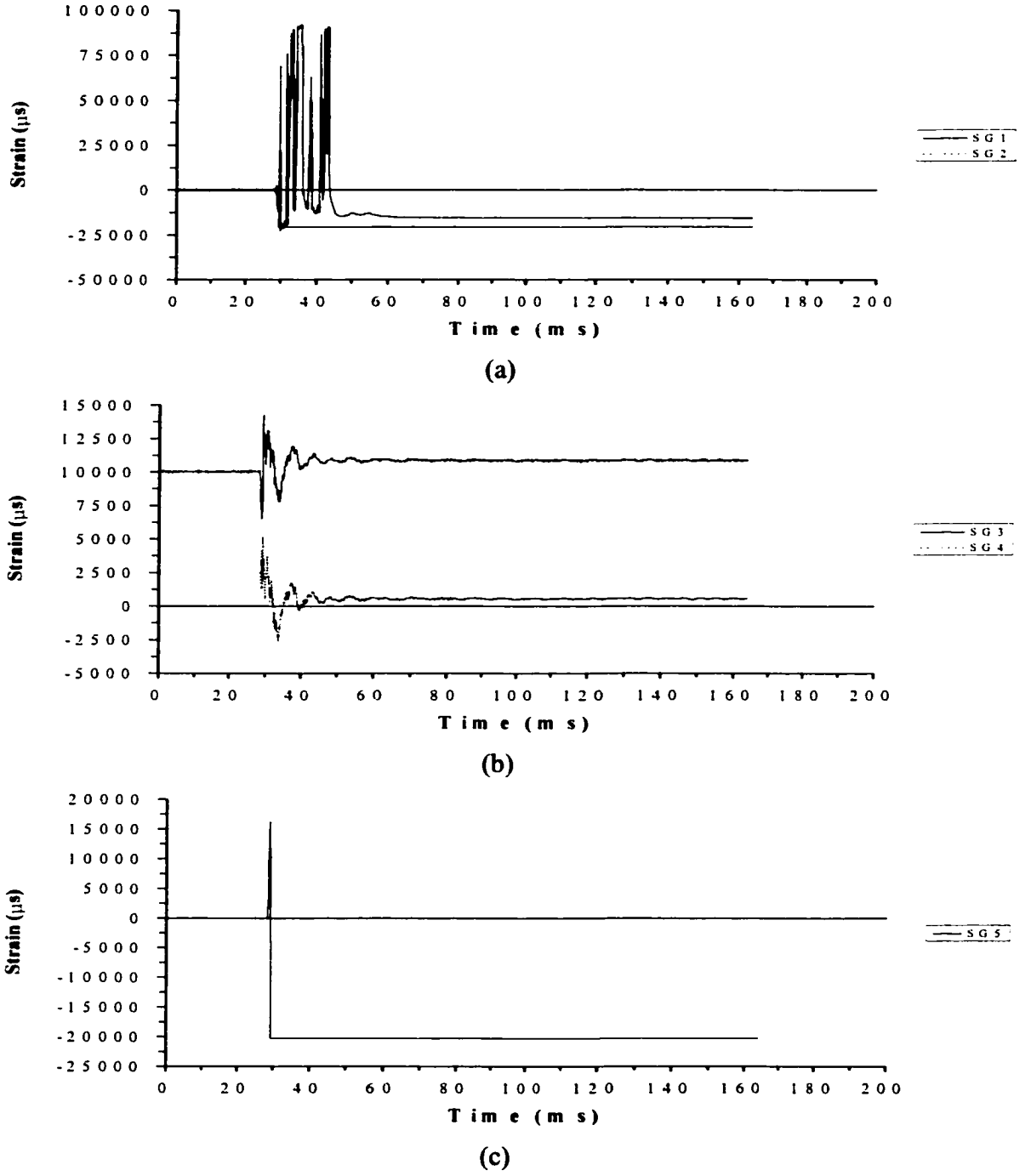

Figure C-7. Strain Record for Test *Alc10*. (a) Strain Gauges #1 and #2, (b) Strain Gauges #3 and #4, and (c) Strain Gauges #5.

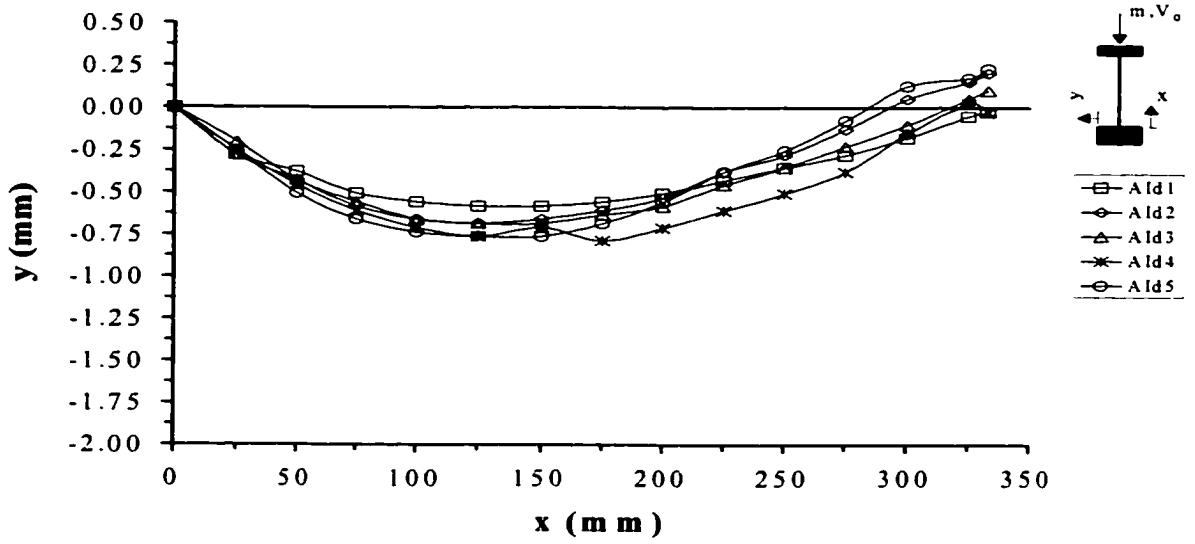

(a)

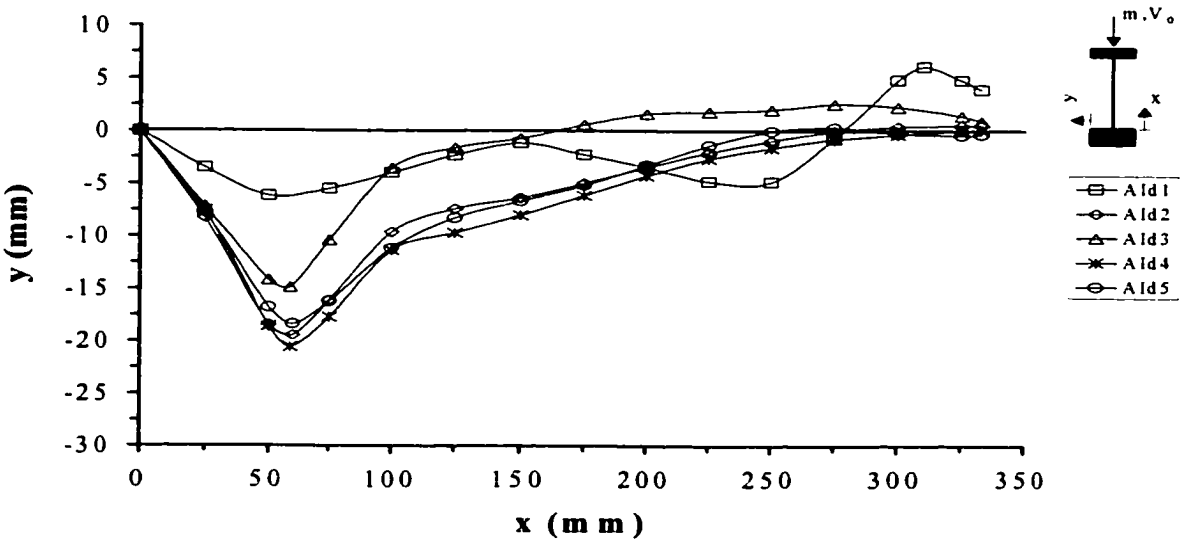

(b)

Figure C-8. Series *AId*, Tests: 1 to 5, (a) Initial Global Imperfection and (b) Deformed Buckled Profiles.

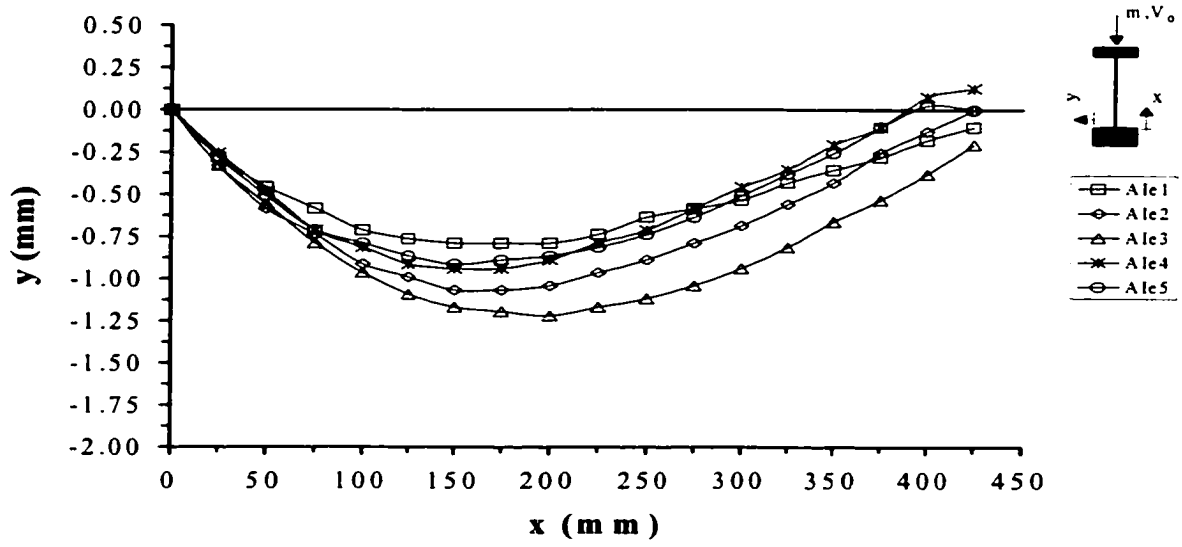

(a)

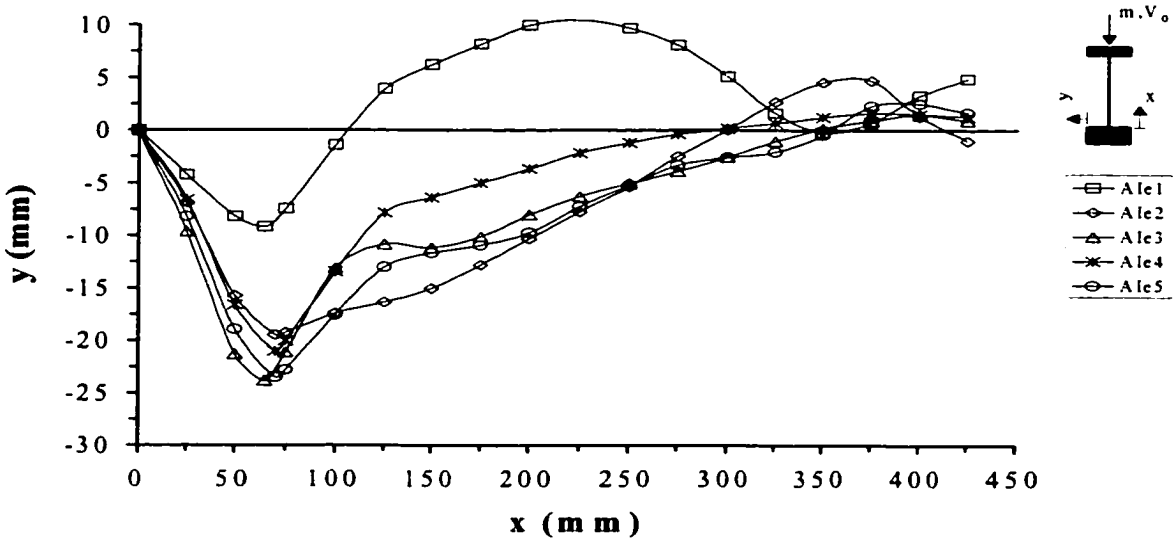

(b)

Figure C-9. Series *AIe*, Tests: 1 to 5, (a) Initial Global Imperfection and (b) Deformed Buckled Profiles.

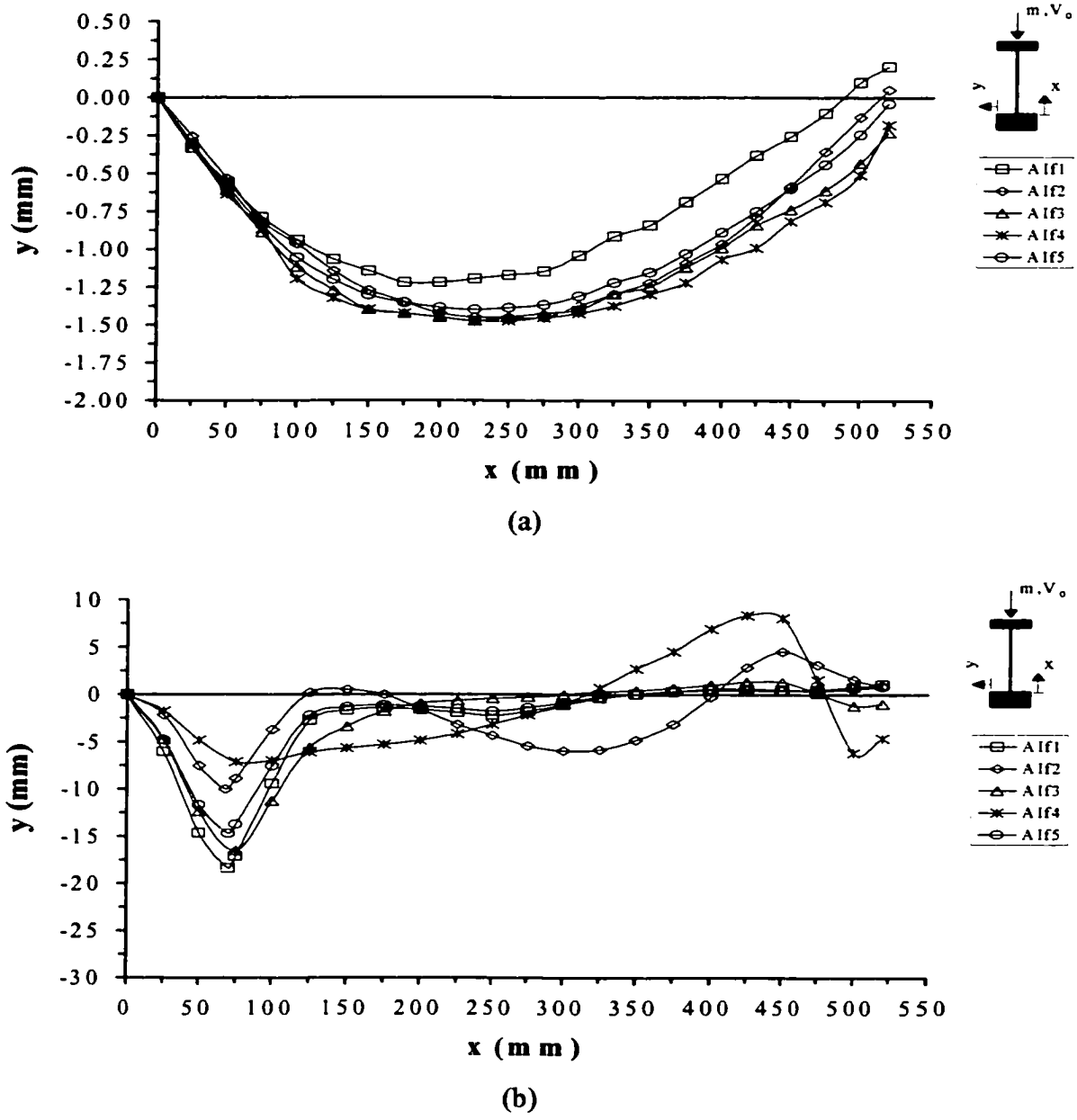

Figure C-10. Series *AIf*, Tests: 1 to 5, (a) Initial Global Imperfection and (b) Deformed Buckled Profiles.

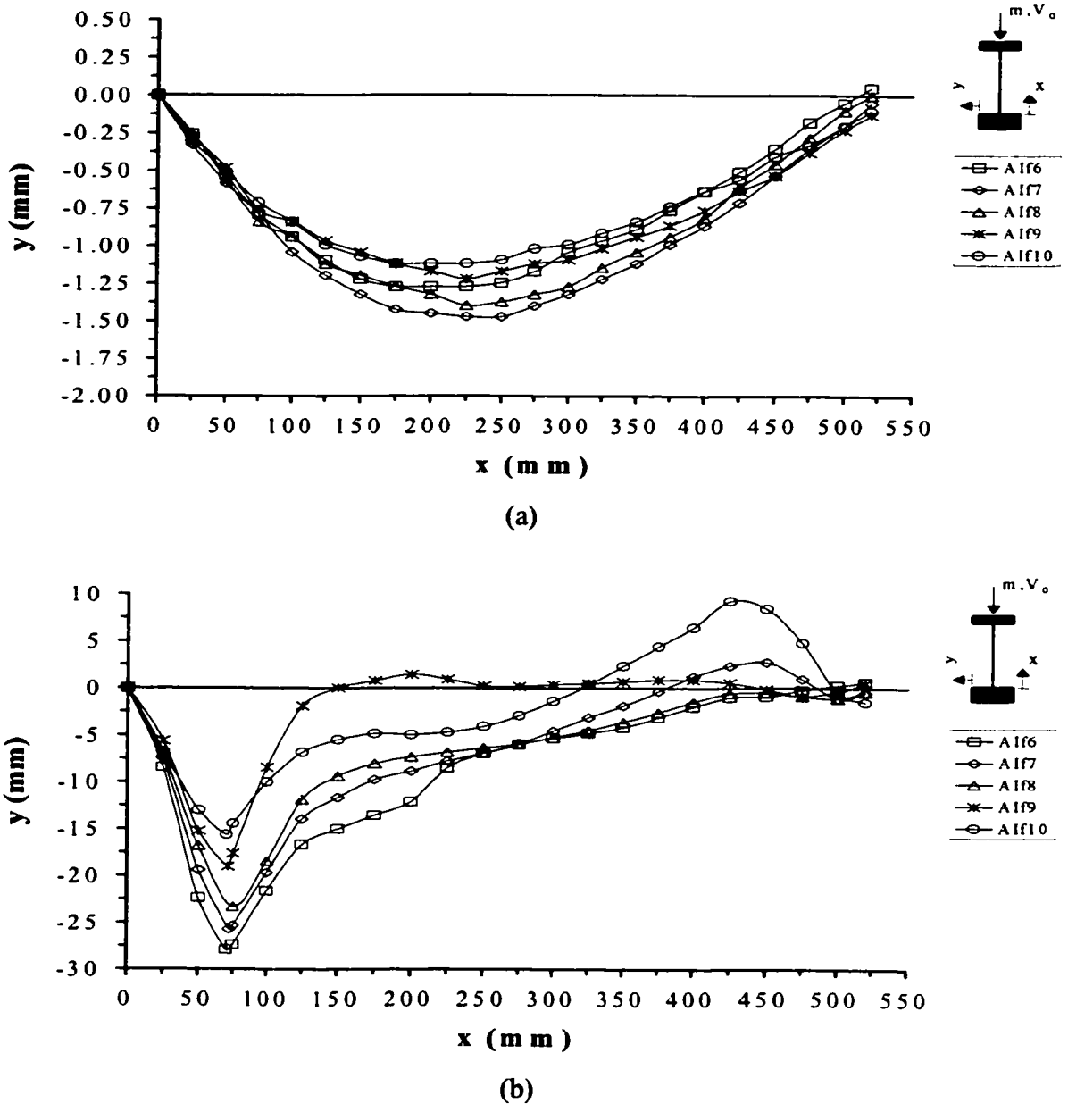

Figure C-11. Series *AIf*, Tests: 6 to 10, (a) Initial Global Imperfection and (b) Deformed Buckled Profiles.

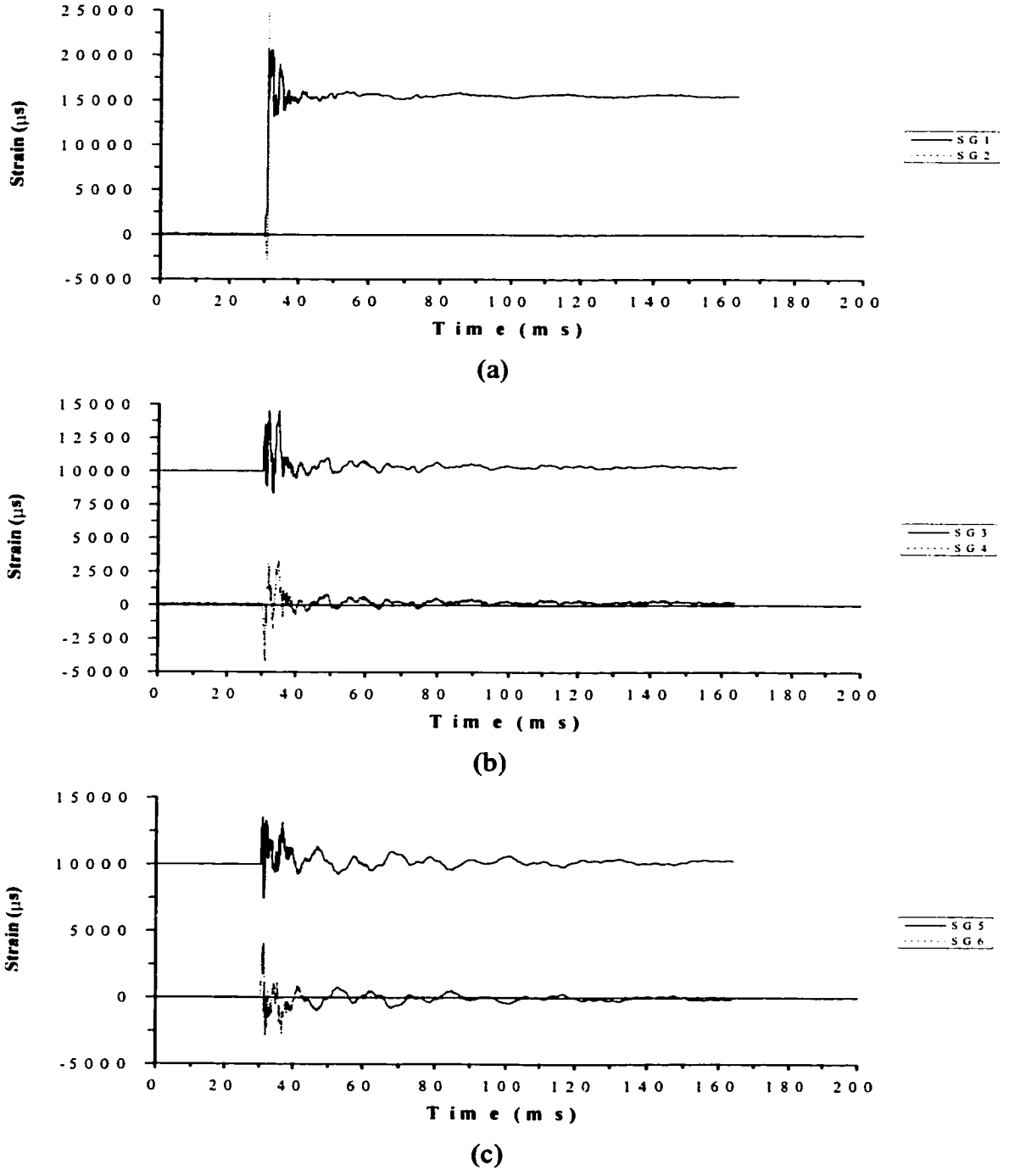

Figure C-12. Strain Record for Test *AIf4*, (a) Strain Gauges #1 and #2, (b) Strain Gauges #3 and #4, and (c) Strain Gauges #5 and #6.

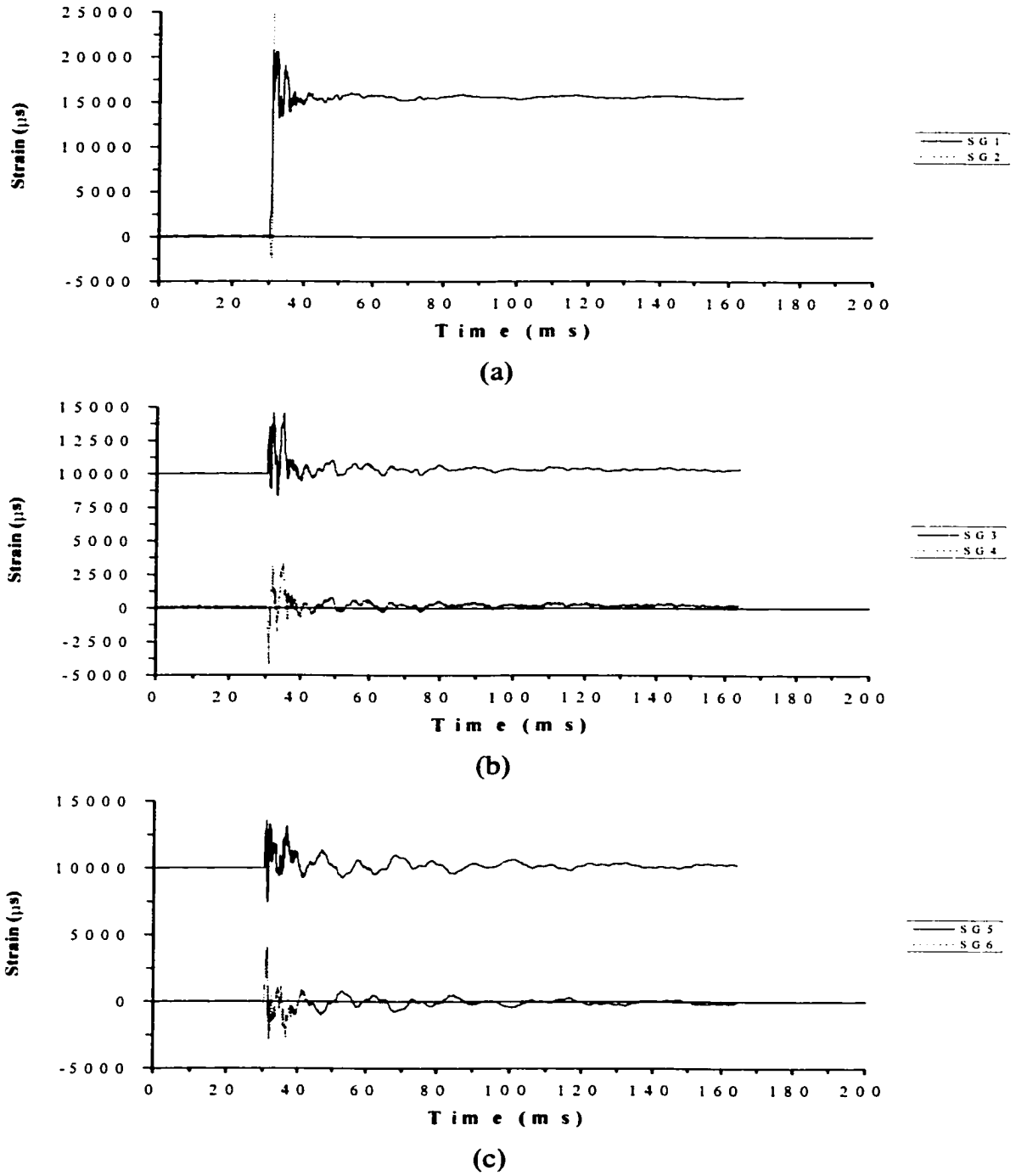

Figure C-13. Strain Record for Test *Alf10*, (a) Strain Gauges #1 and #2, (b) Strain Gauges #3 and #4, and (c) Strain Gauges #5 and #6.

C.2 Series AII – 6061-T6 Aluminum Bars

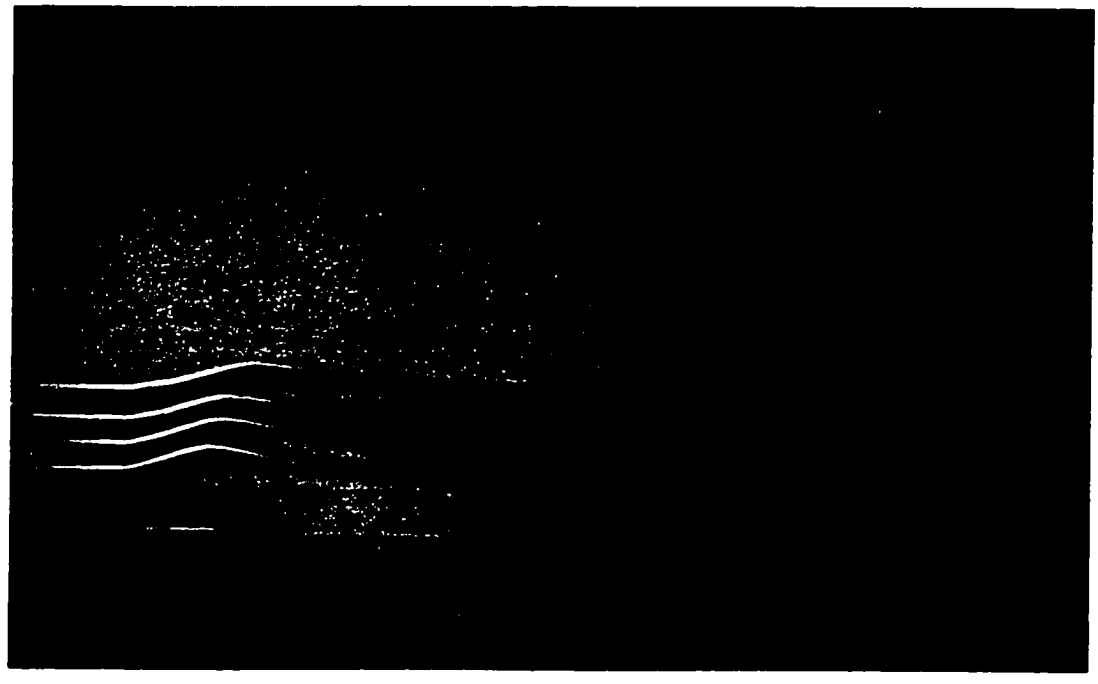

Figure C-14. General Deformed Buckled Profiles for Series *AII* (Tests *AIIa* to *AIId*) Impacted by a 10kg Free Fall Impact Hammer at a Nominal Velocity of 6m/s.

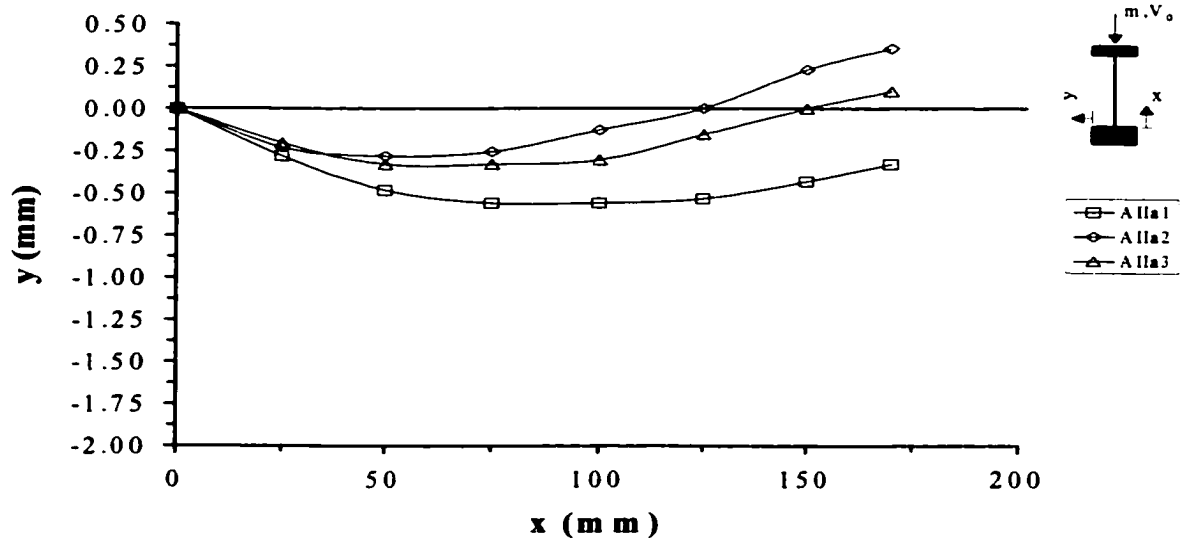

(a)

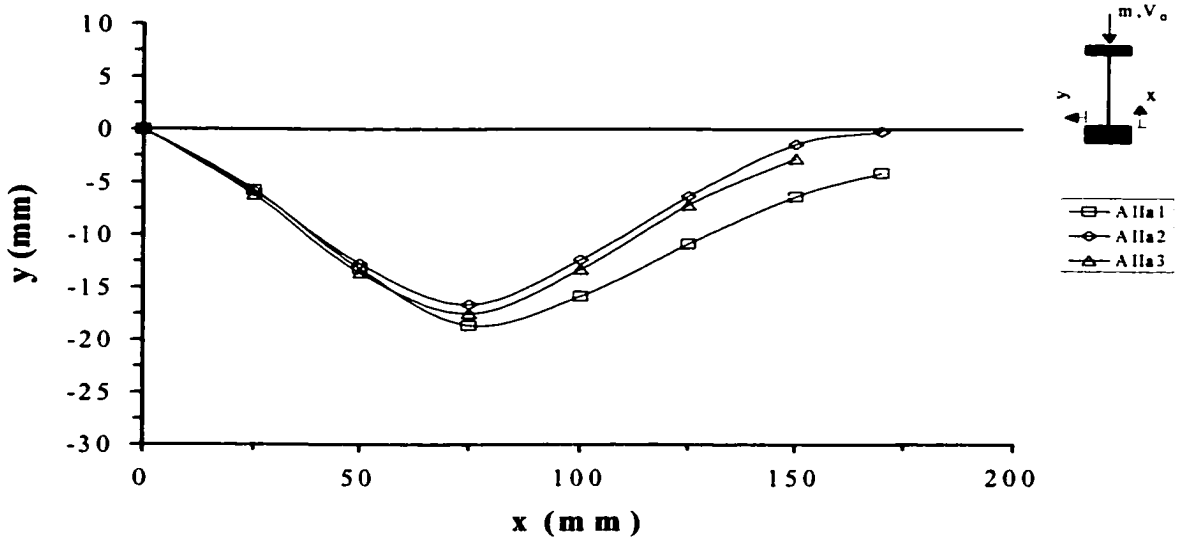

(b)

Figure C-15. Series *AIIa*, Tests: 1 to 3, (a) Initial Global Imperfections and (b) Deformed Buckled Profiles.

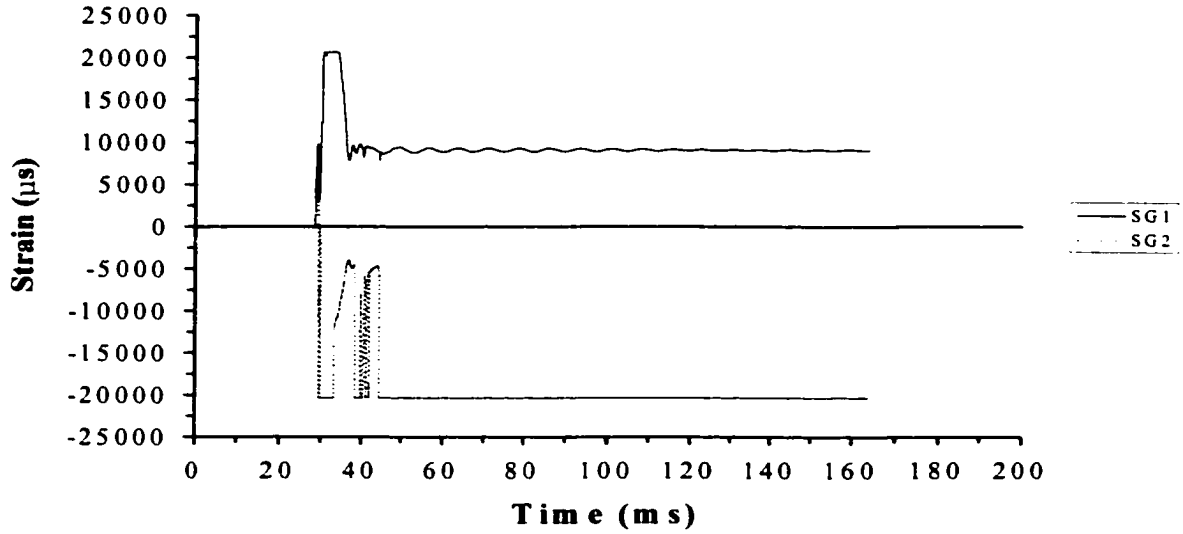

Figure C-16. Strain Record for Test *AIIa3*, Strain Gauges #1 and #2.

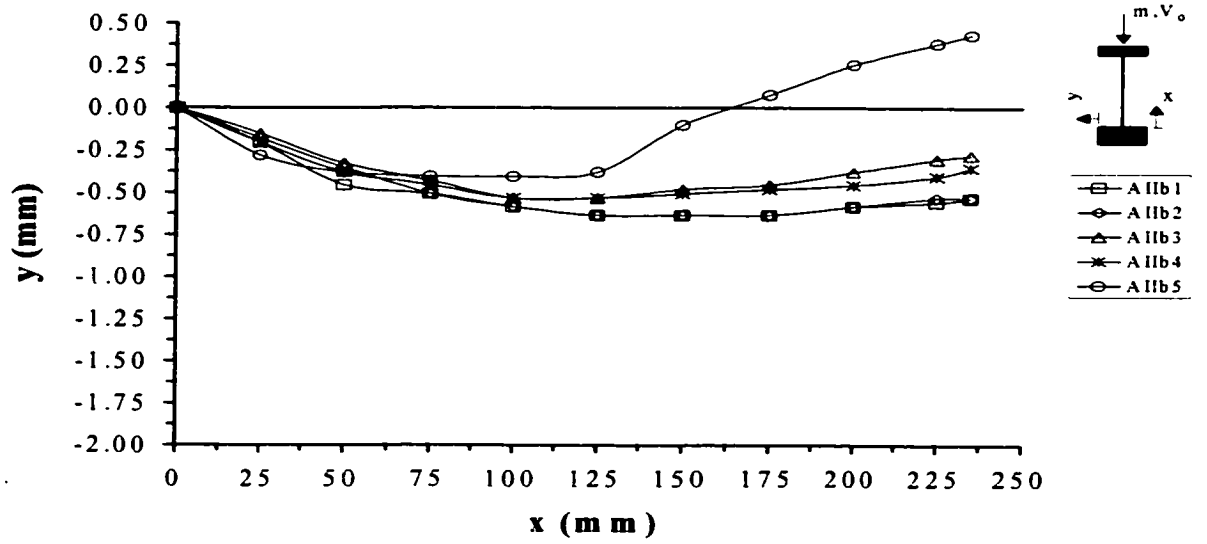

(a)

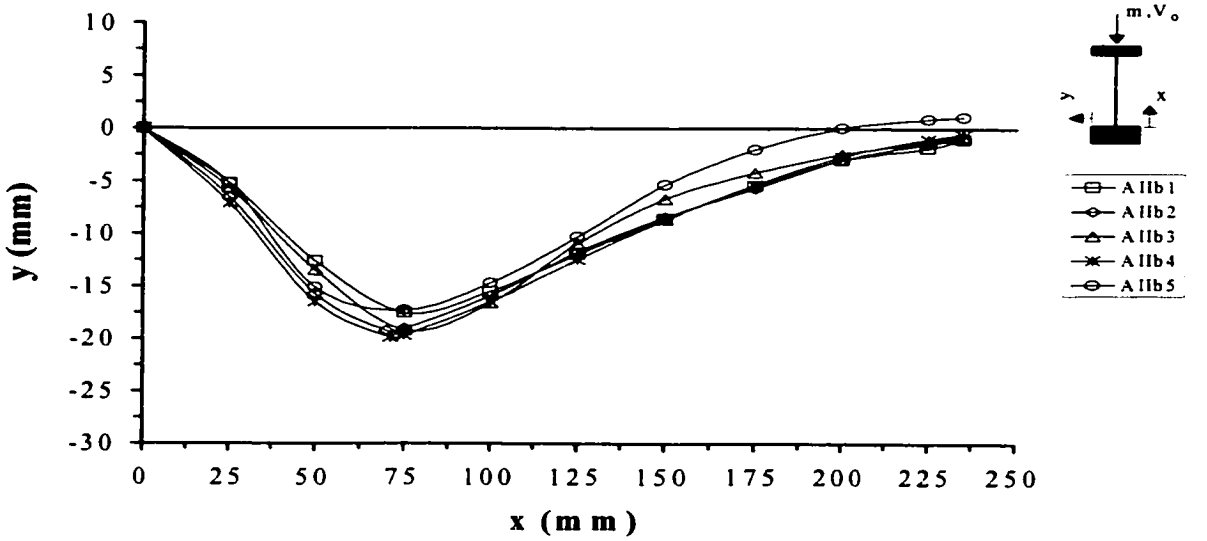

(b)

Figure C-17. Series *AIIb*, Tests: 1 to 5, (a) Initial Global Imperfections and (b) Deformed Buckled Profiles.

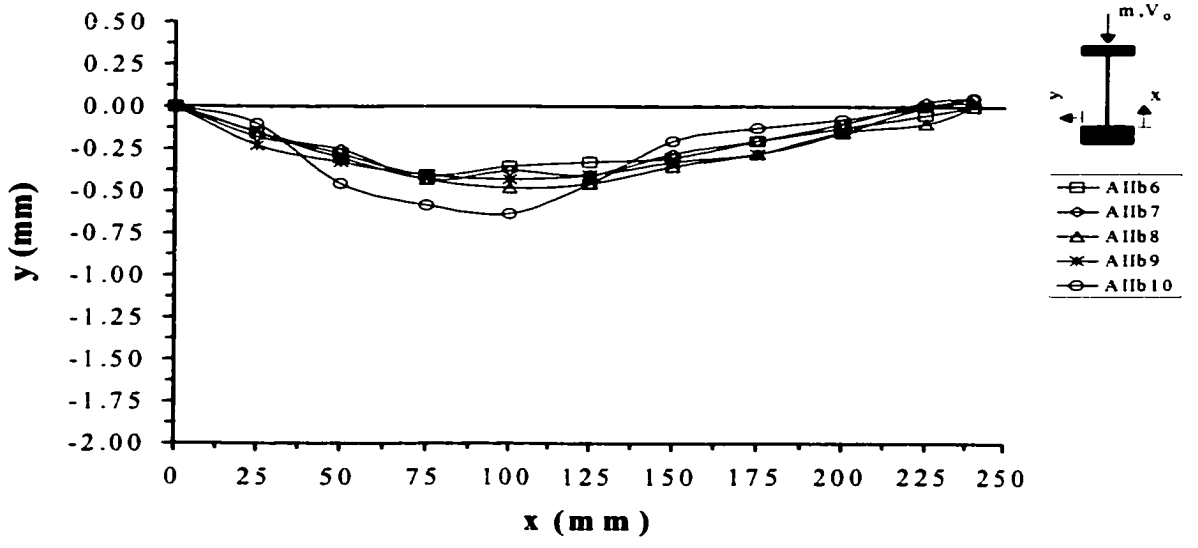

(a)

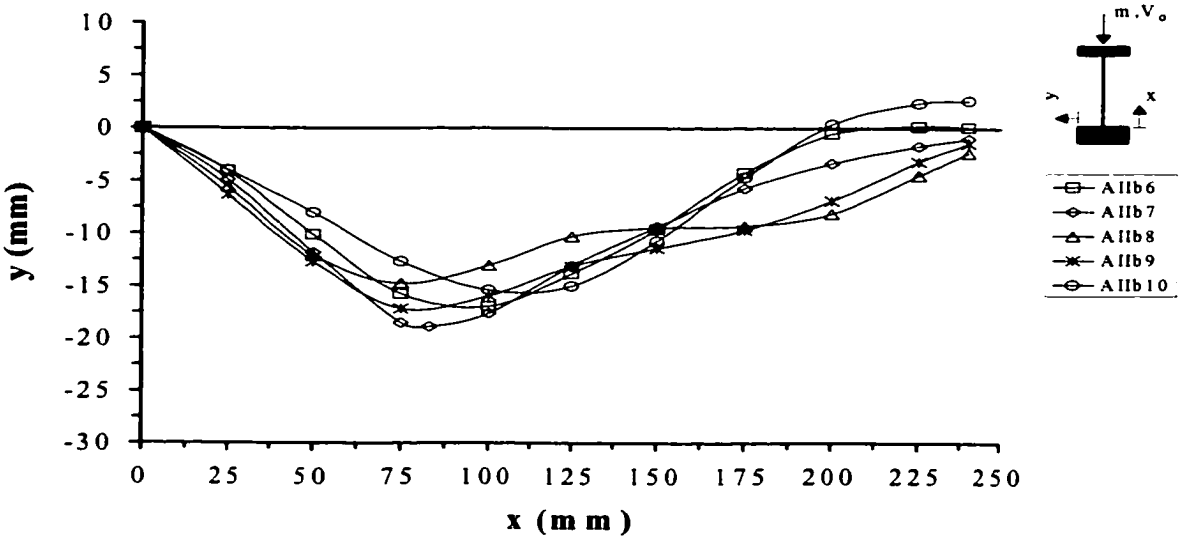

(b)

Figure C-18. Series *AIIb*, Tests: 6 to 10, (a) Initial Global Imperfections and (b) Deformed Buckled Profiles.

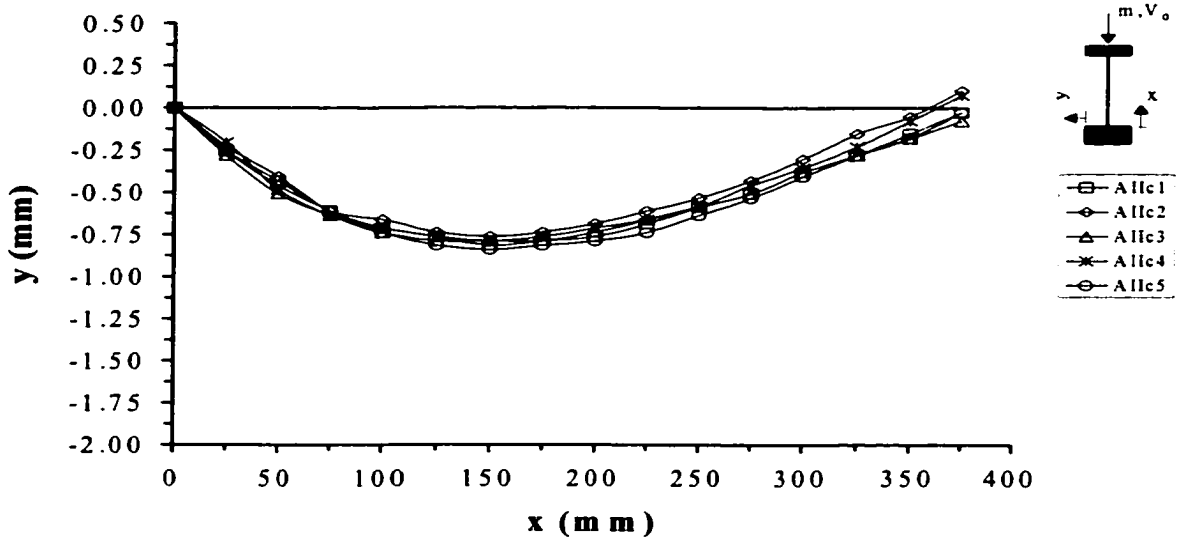

(a)

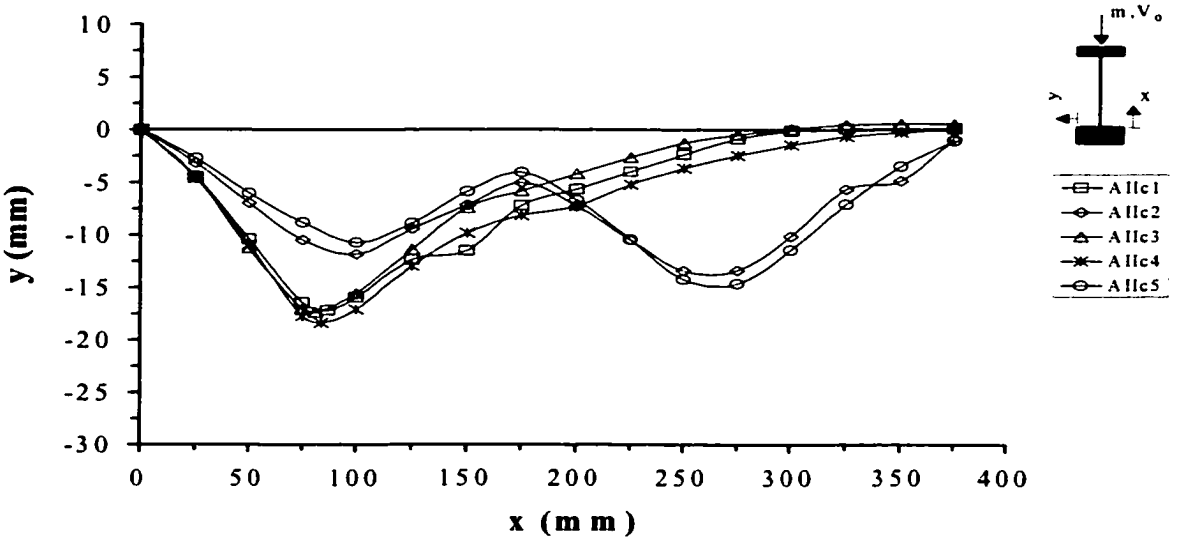

(b)

Figure C-19. Series *AIIc*, Tests: 1 to 5, (a) Initial Global Imperfections and (b) Deformed Buckled Profiles.

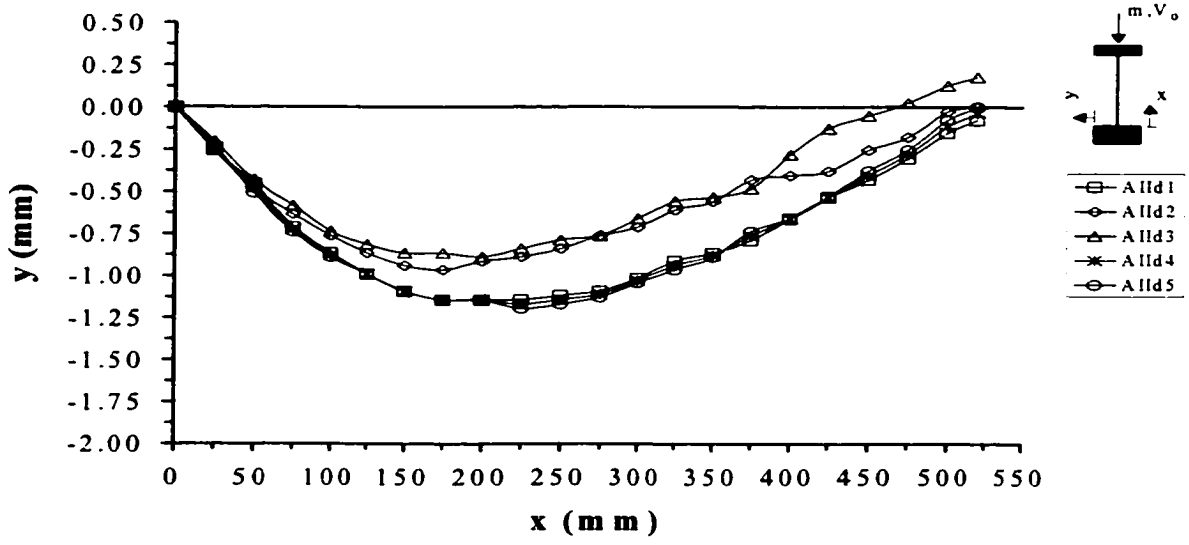

(a)

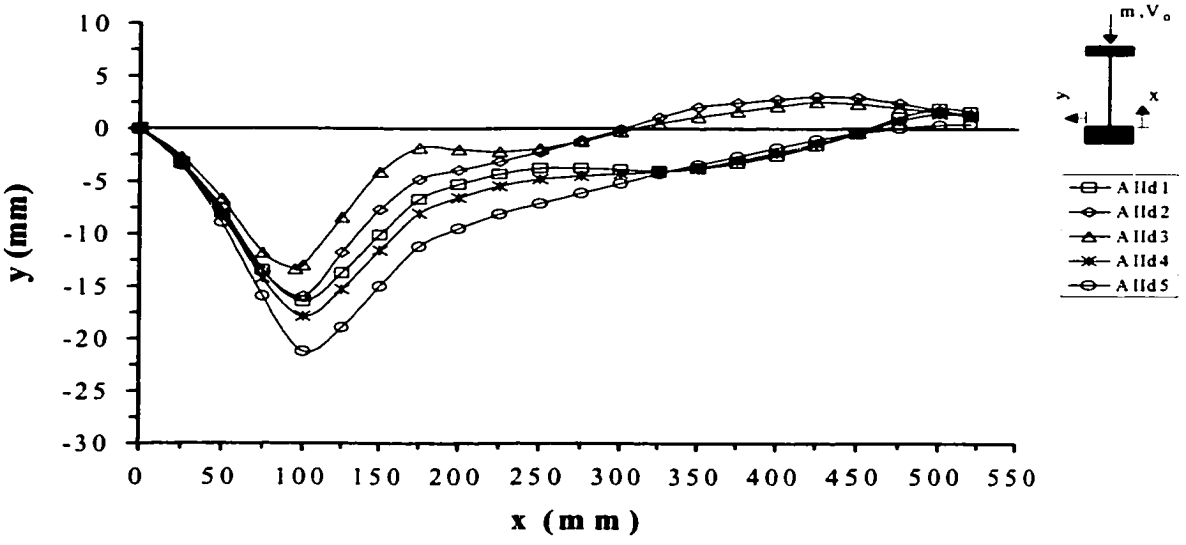

(b)

Figure C-20. Series *AIId*, Tests: 1 to 5,
(a) Initial Global Imperfections and (b) Deformed Buckled Profiles.

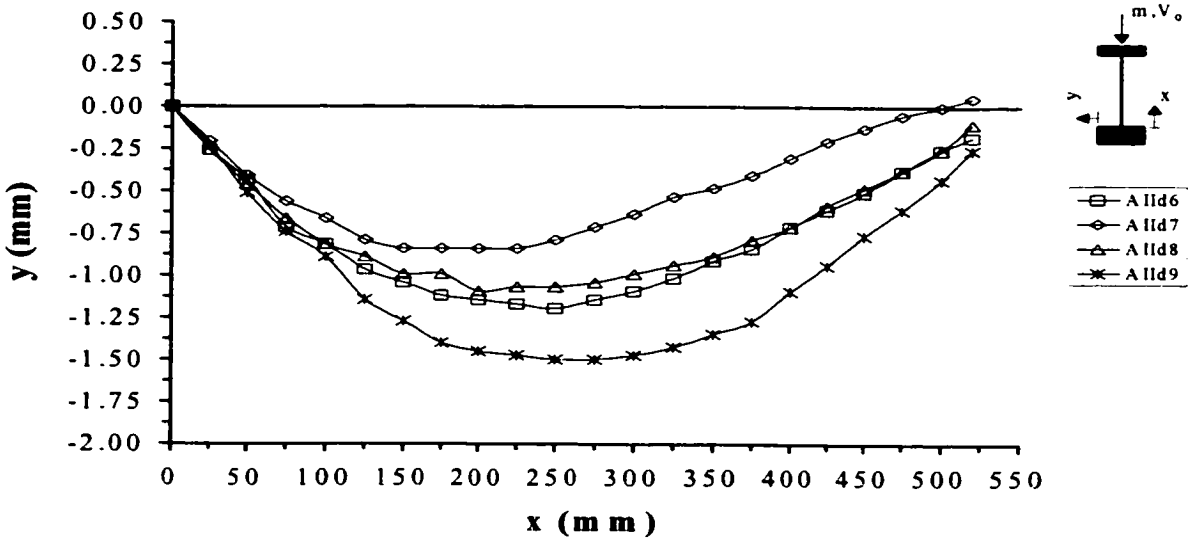

(a)

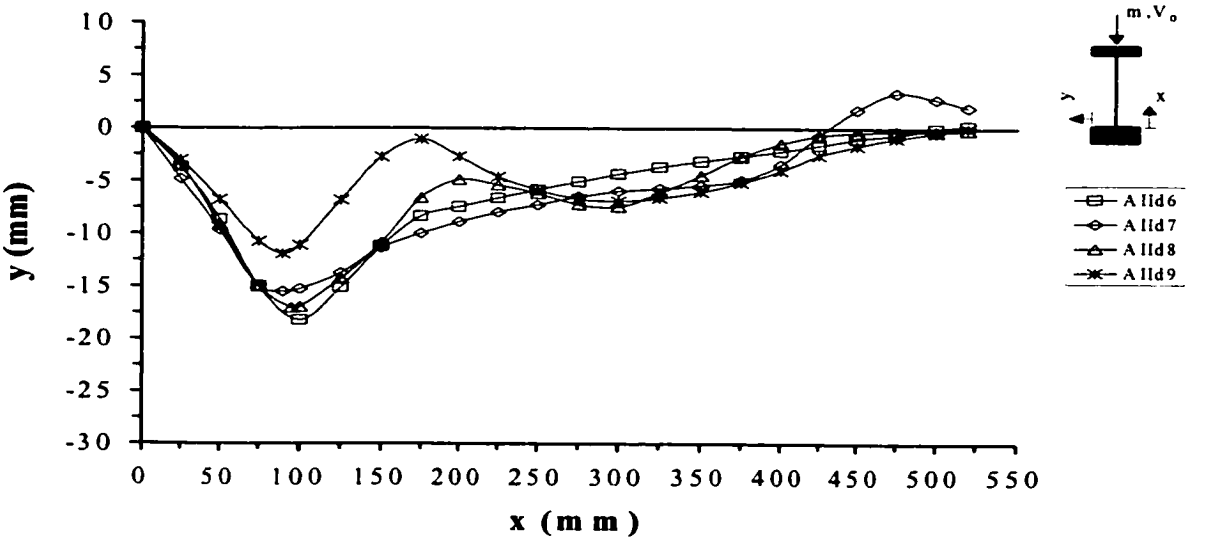

(b)

Figure C-20. Series *AIId*, Tests: 6 to 9, (a) Initial Global Imperfections and (b) Deformed Buckled Profiles.

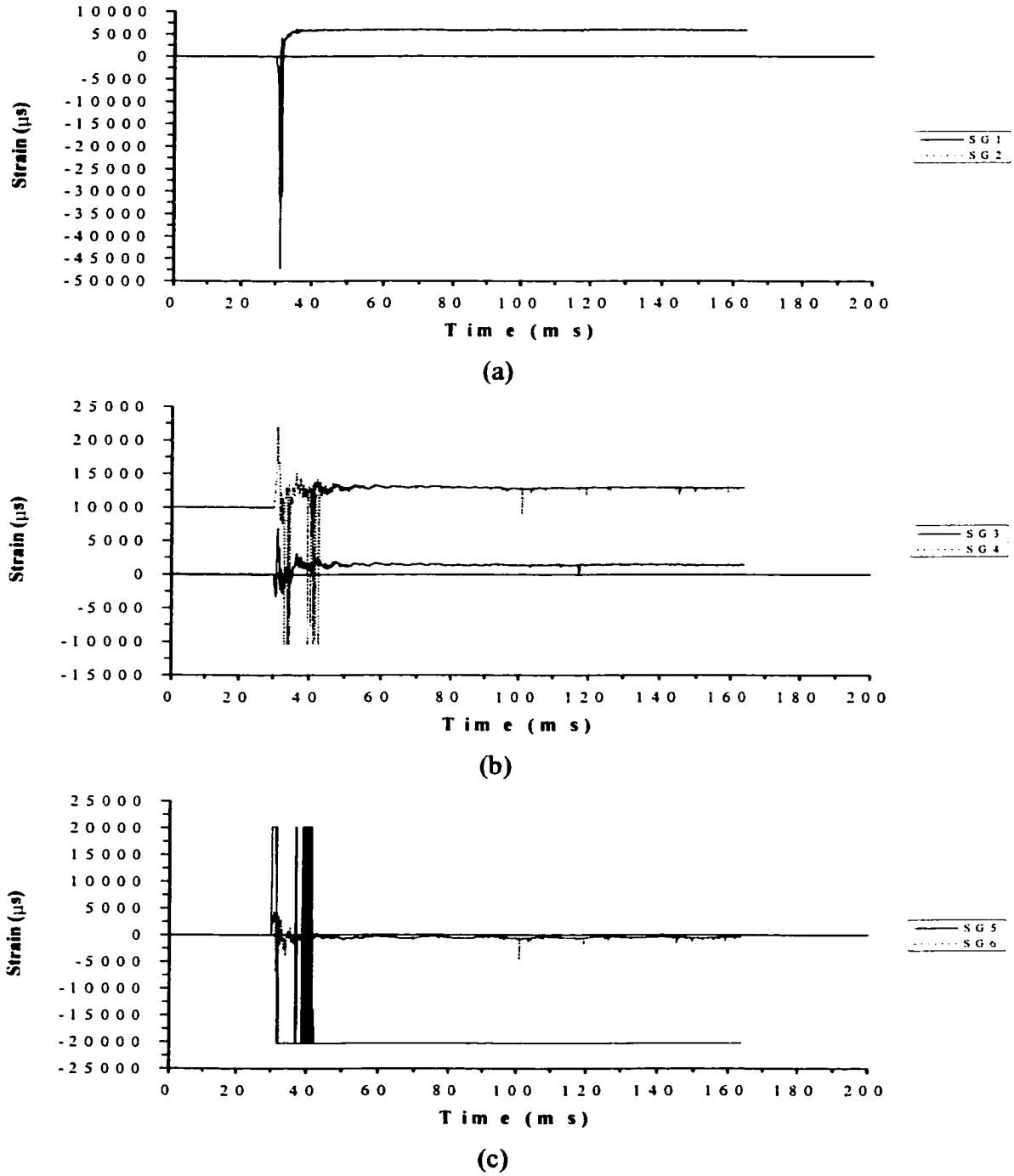

Figure C-21. Strain Record for Test *AIId3*, (a) Gauges #1 and #2, (b) Gauges #3 and #4 and (c) Gauges #5 and #6.

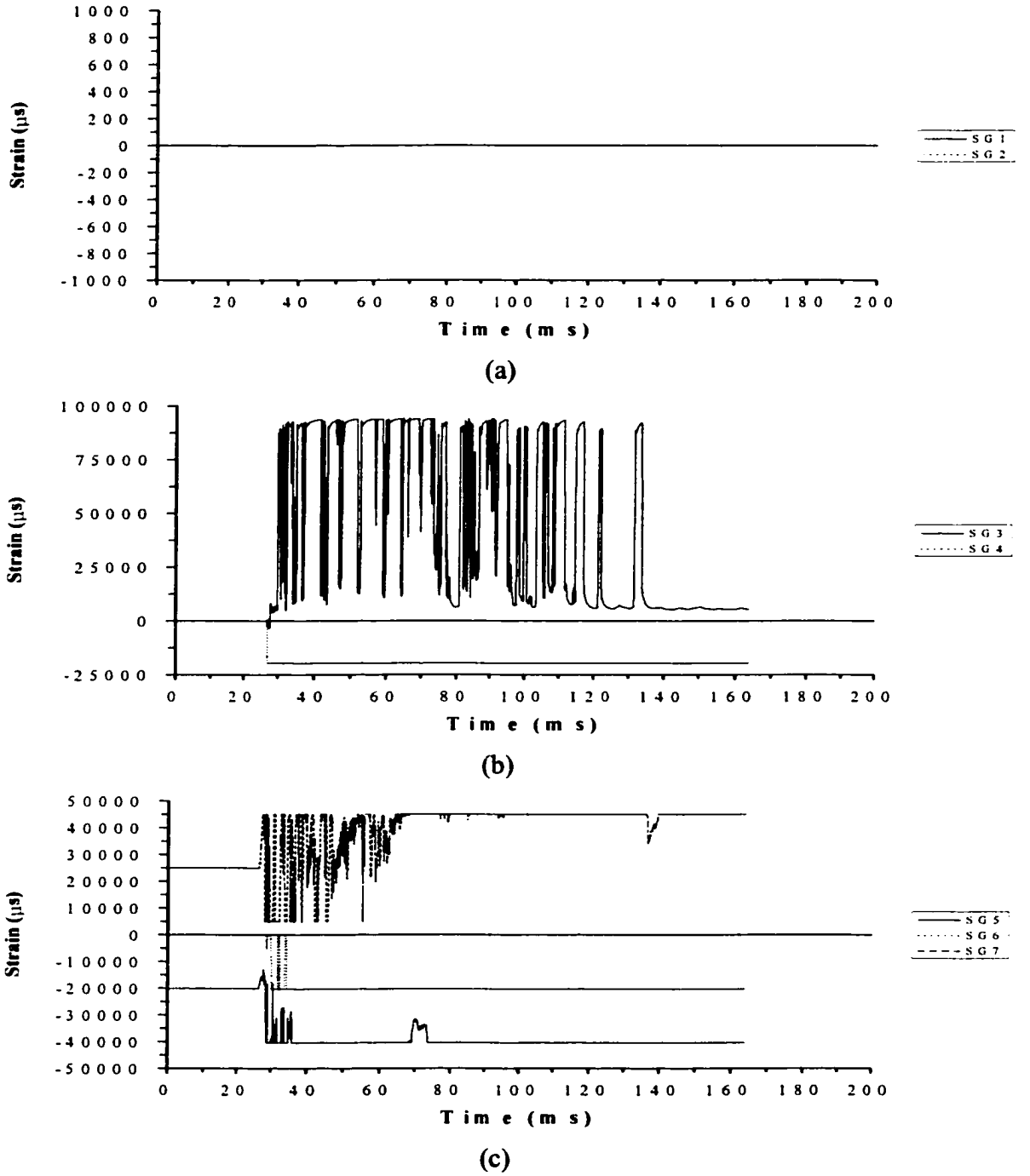

Figure C-22. Strain Record for Test *AIId9*, (a) Gauges #1 and #2, (b) Gauges #3 and #4 and (c) Gauges #5, #6 and #7.

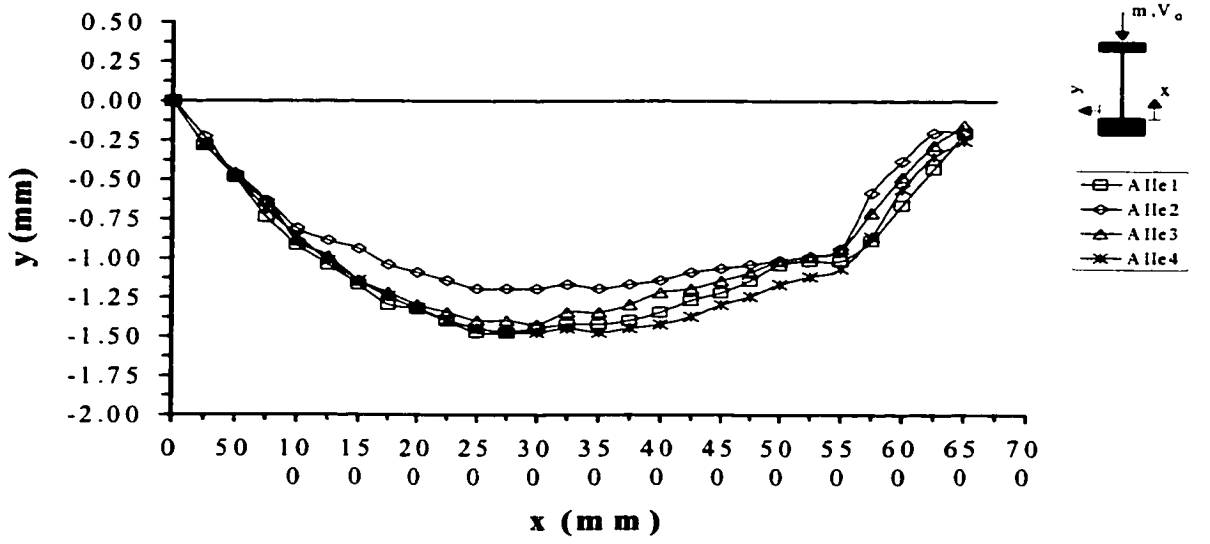

(a)

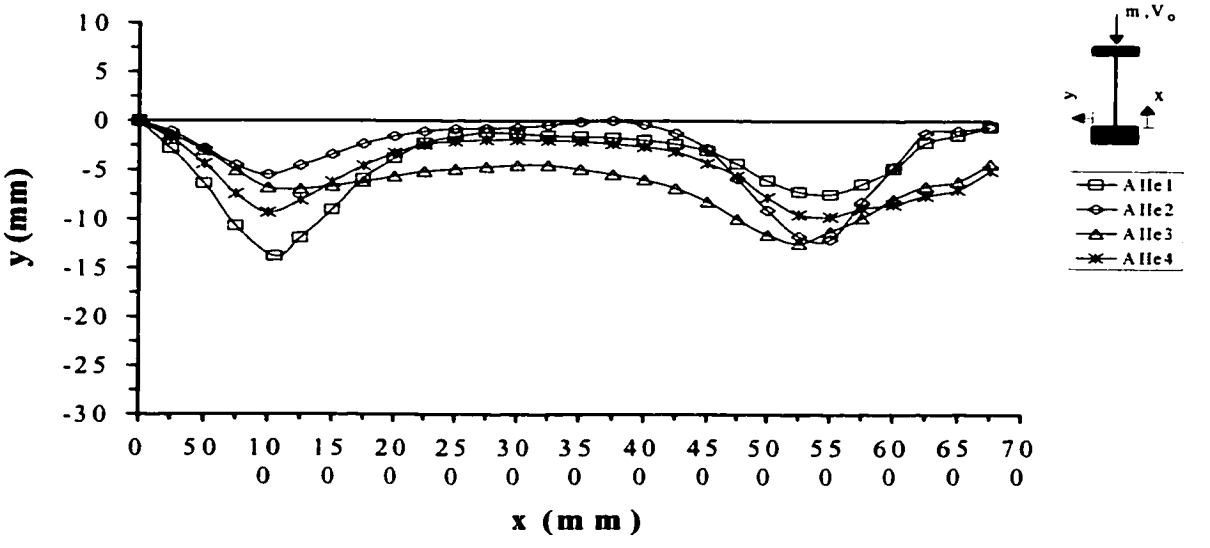

(b)

Figure C-23. Series *Alle*, Tests: 1 to 4, (a) Initial Global Imperfections and (b) Deformed Buckled Profiles.

C.3 Series SI – Cold Rolled 1018 Steel

Figure C-24. General Deformed Buckled Profiles for Series *AII* (Tests *SIa* to *SIf*) Impacted by a 10kg Free Fall Impact Hammer at a Nominal Velocity of 6m/s.

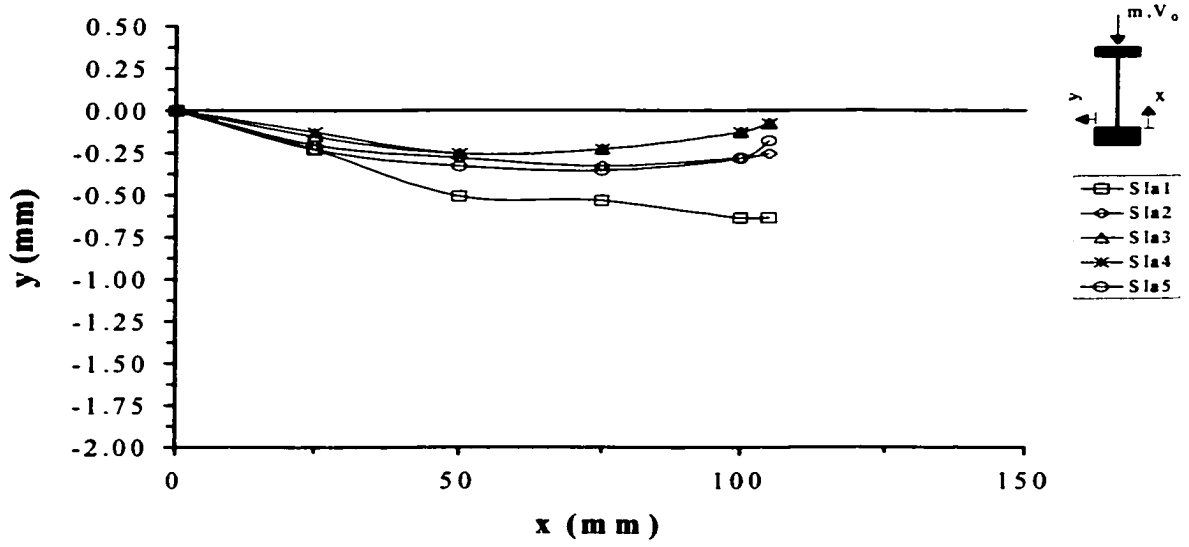

(a)

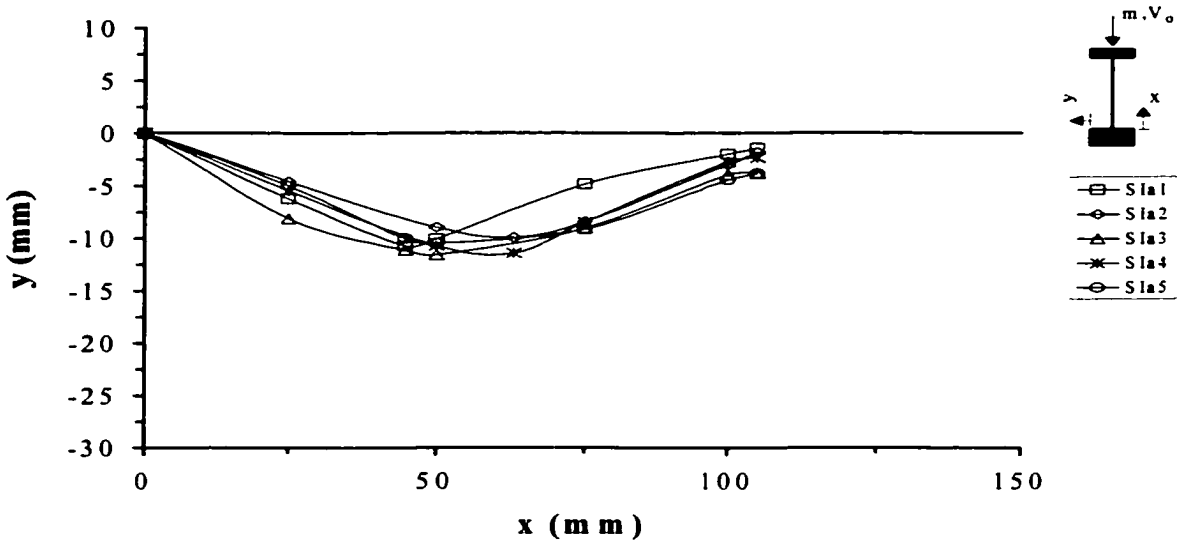

(b)

Figure C-25. Series *SIa*, Tests: 1 to 5, (a) Initial Global Imperfections and (b) Deformed Buckled Profiles.

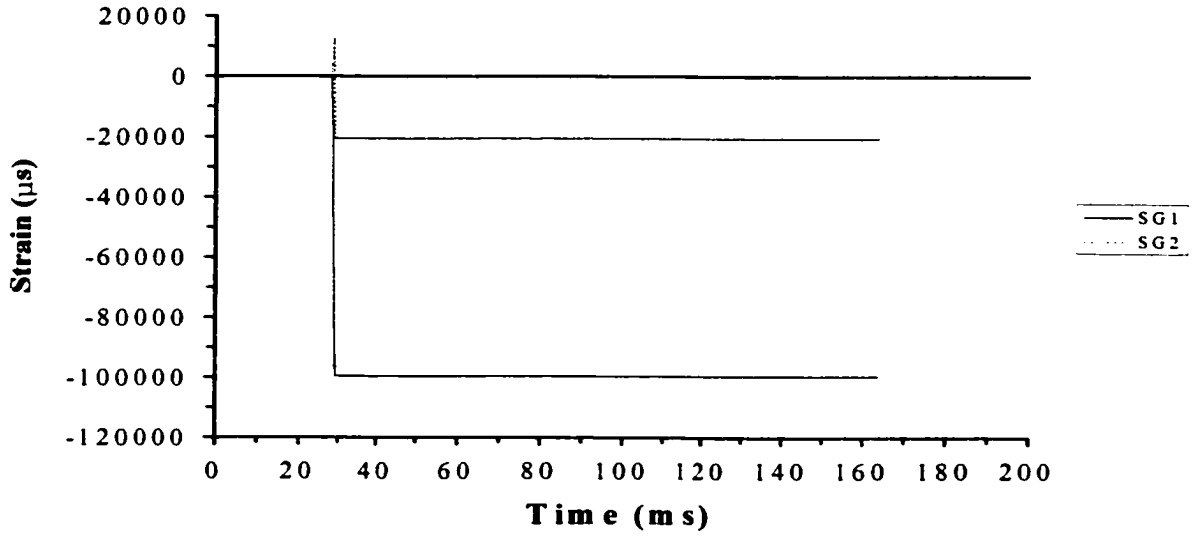

Figure C-26. Strain Record for Test *SIa5*, Strain Strain Gauges #1 and #2.

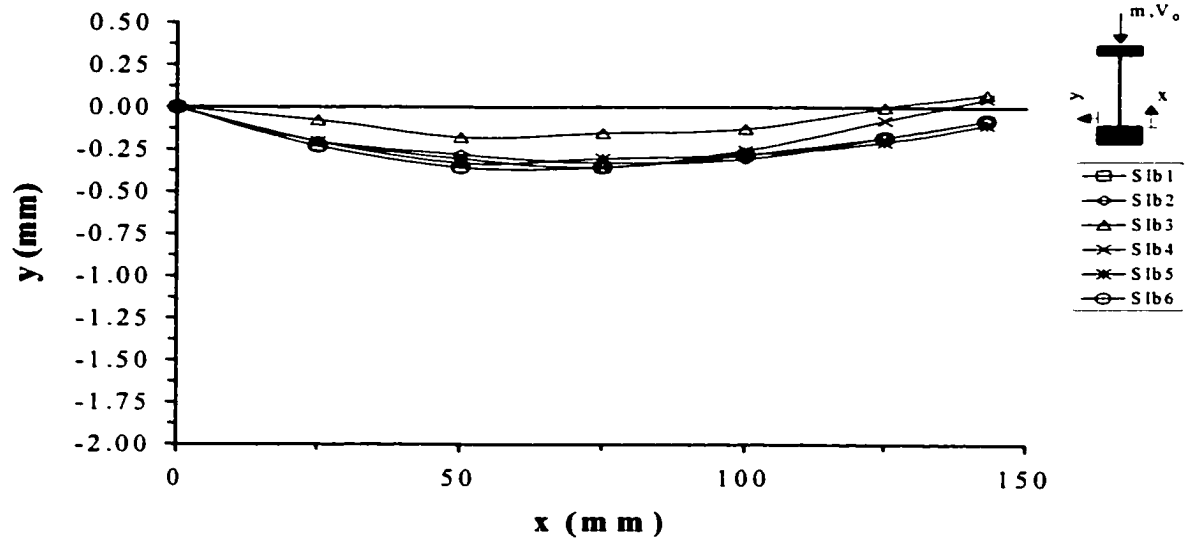

(a)

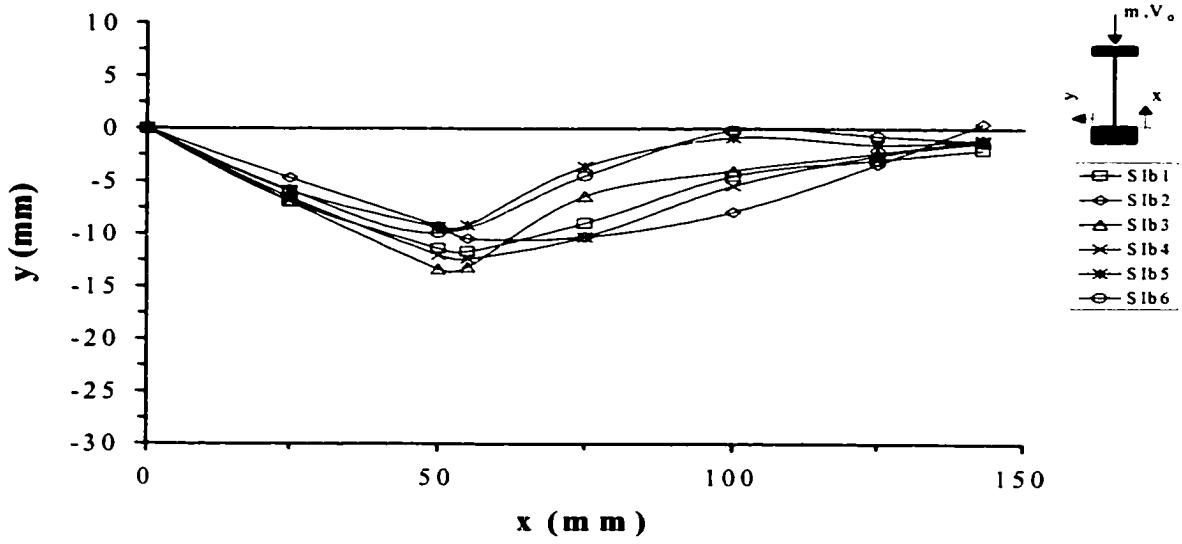

(b)

Figure C-27. Series *Slb*, Tests: 1 to 6, (a) Initial Global Imperfections and (b) Deformed Buckled Profiles.

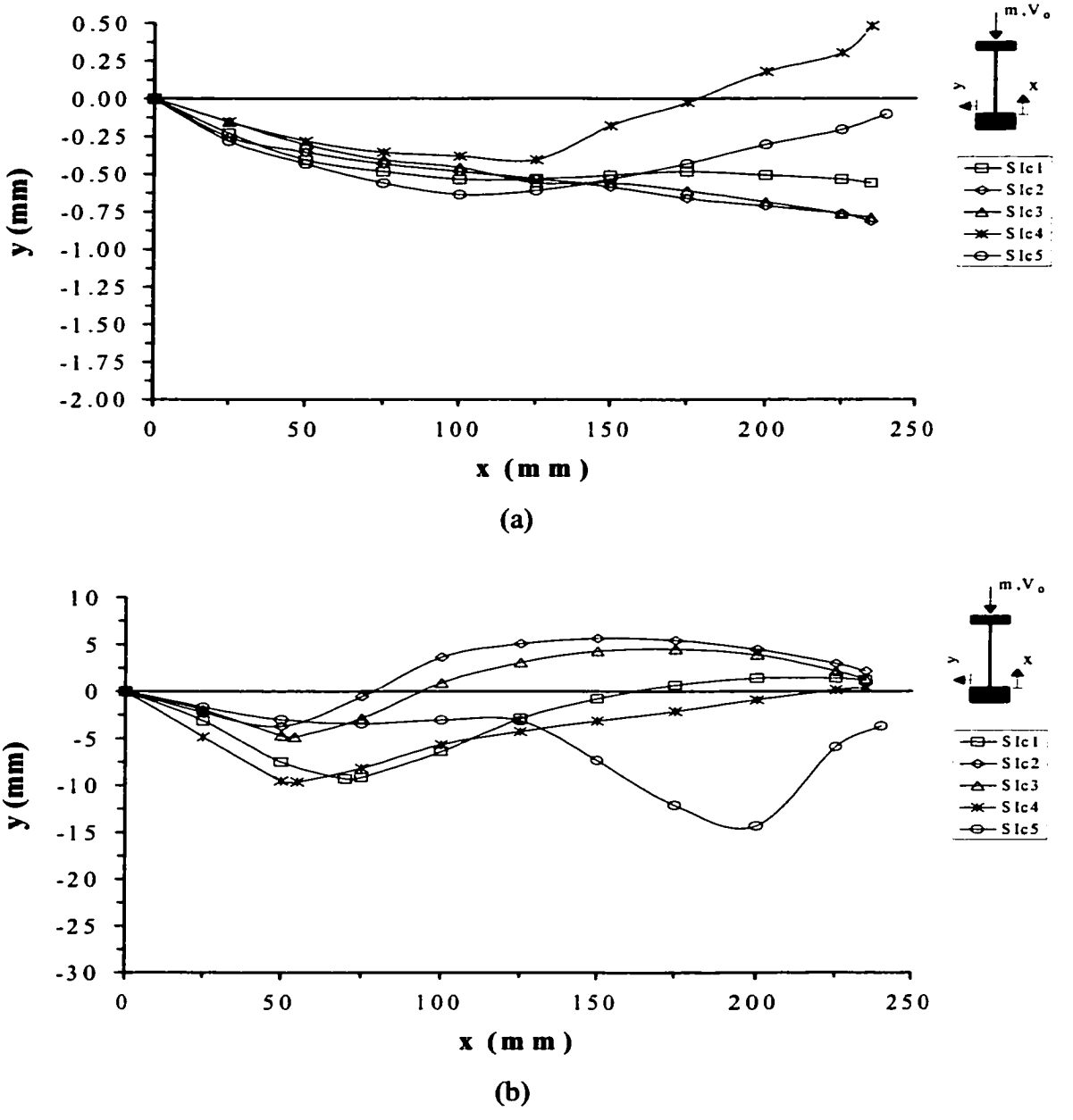

Figure C-28. Series *Slc*, Tests: 1 to 5, (a) Initial Global Imperfections and (b) Deformed Buckled Profiles.

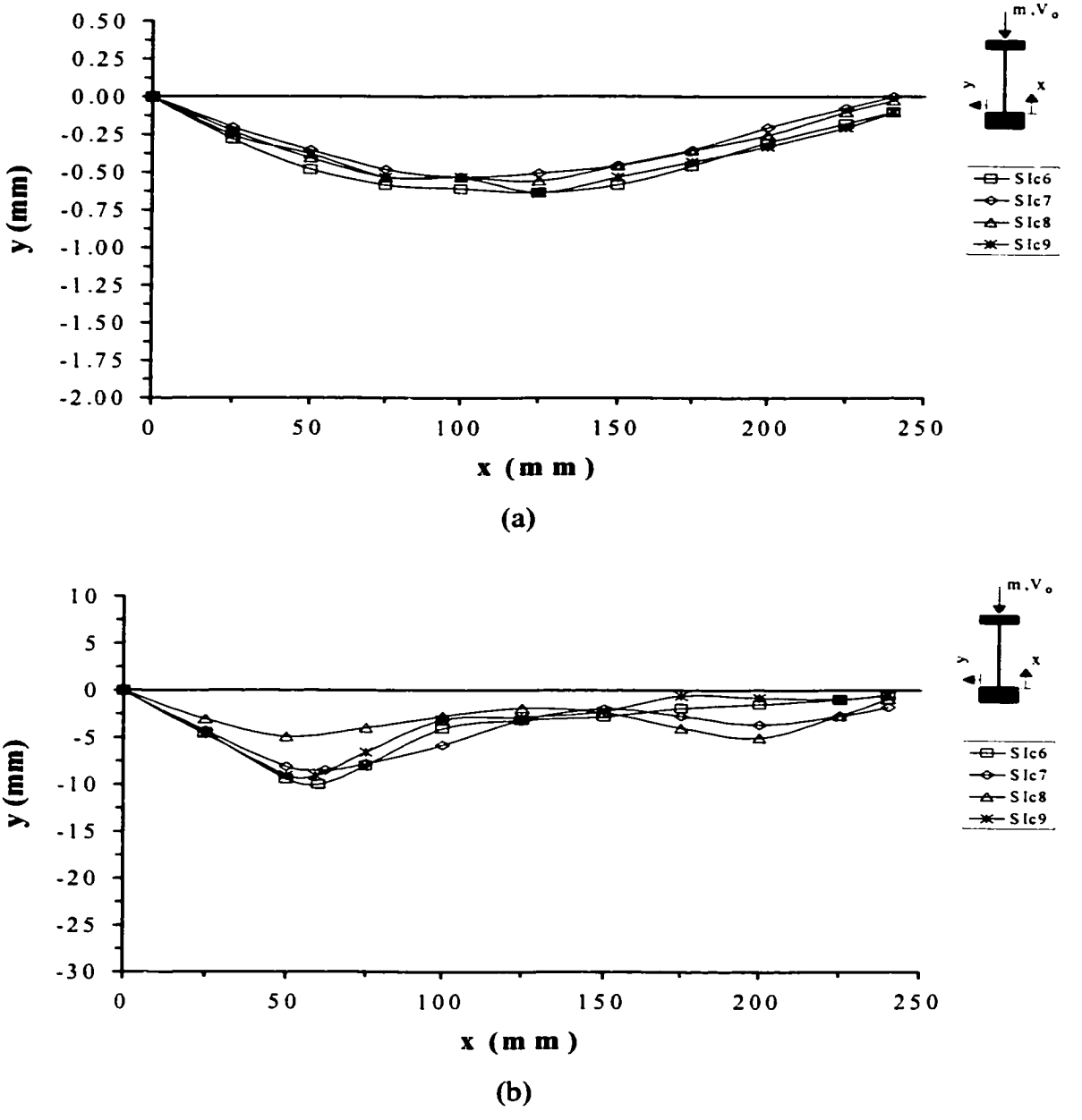

Figure C-29. Series *Slc*, Tests: 6 to 9, (a) Initial Global Imperfections and (b) Deformed Buckled Profiles.

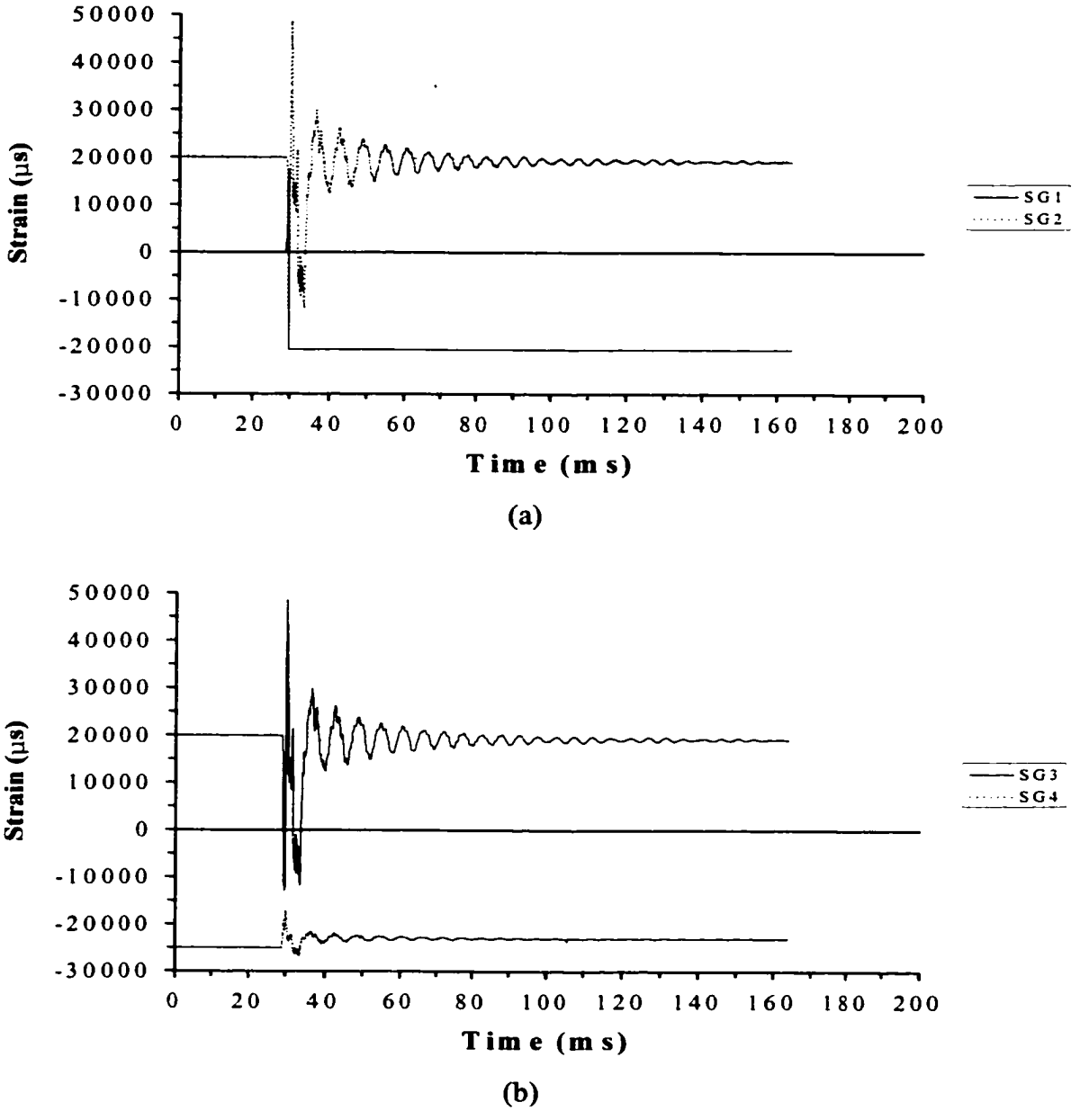

Figure C-30. Strain Record for Test *SIc4*, (a) Strain Gauges #1 and #2 and (b) Strain Gauges #3 and #4.

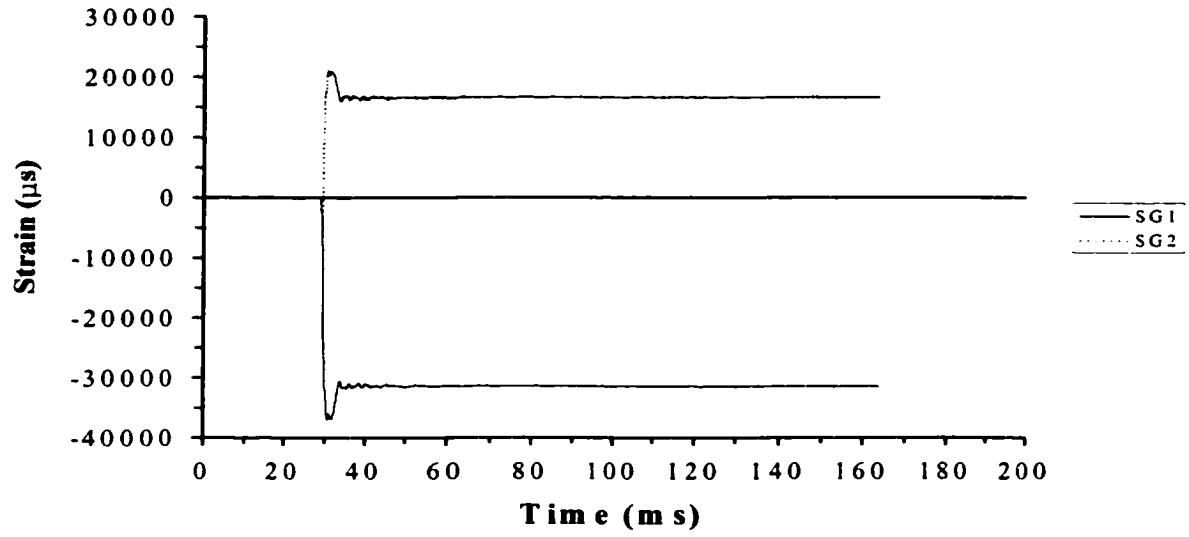

(a)

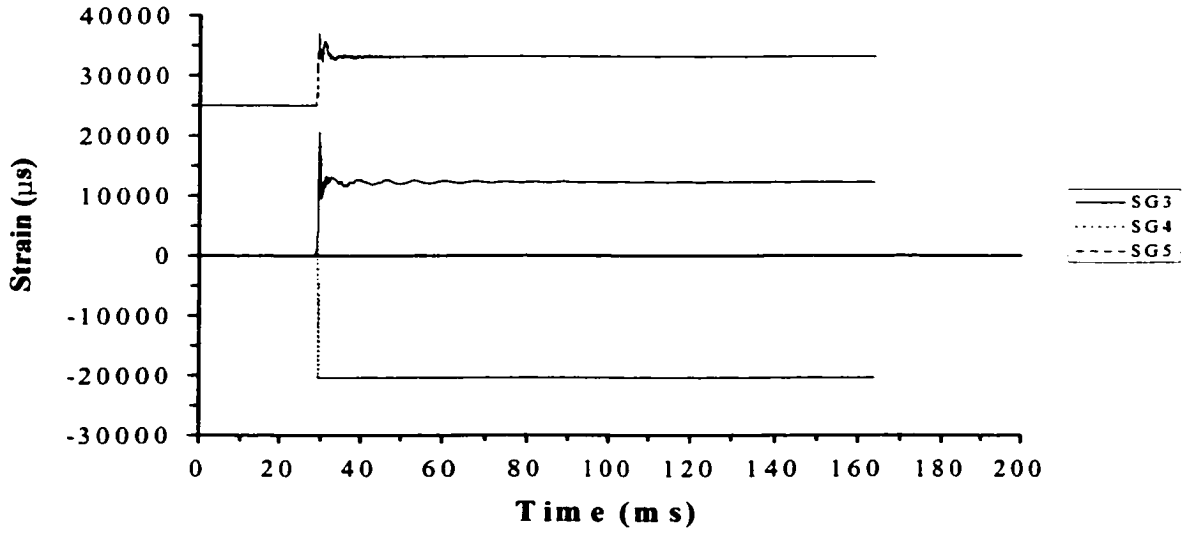

(b)

Figure C-32. Strain Record for Test *SIc9*, (a) Strain Gauges #1 and #2 and (b) Strain Gauges #3, #4 and #5.

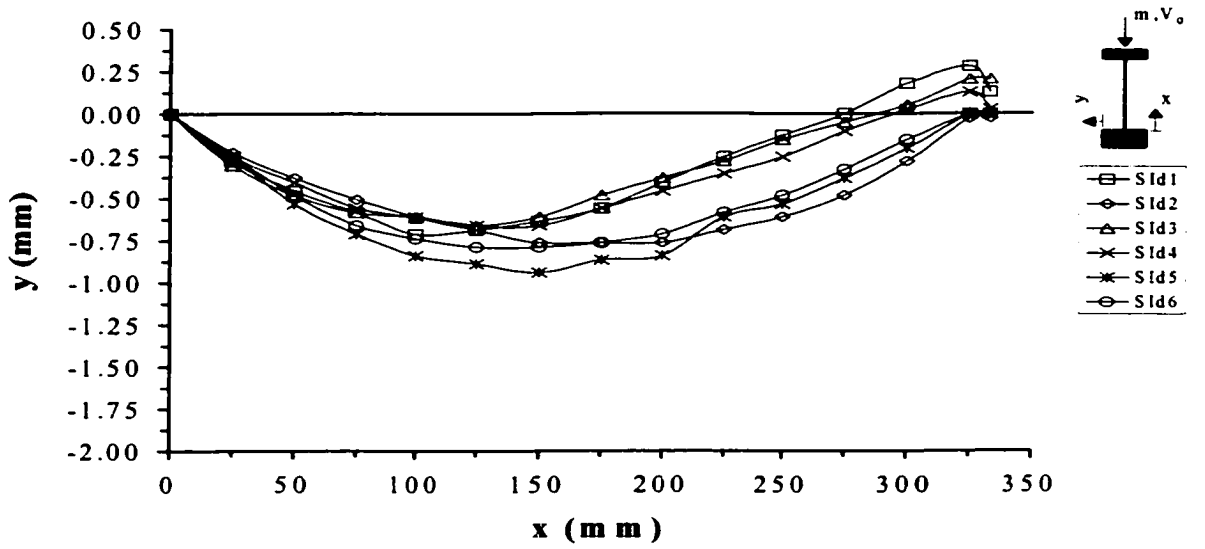

(a)

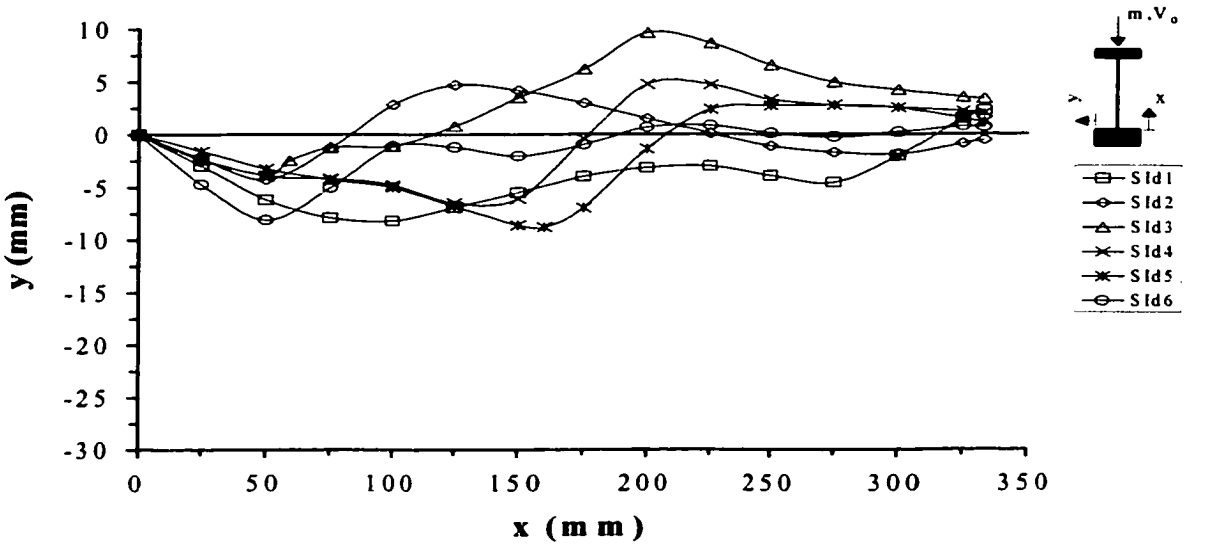

(b)

Figure C-31. Series *SId*, Tests: 1 to 6, (a) Initial Global Imperfections and (b) Deformed Buckled Profiles.

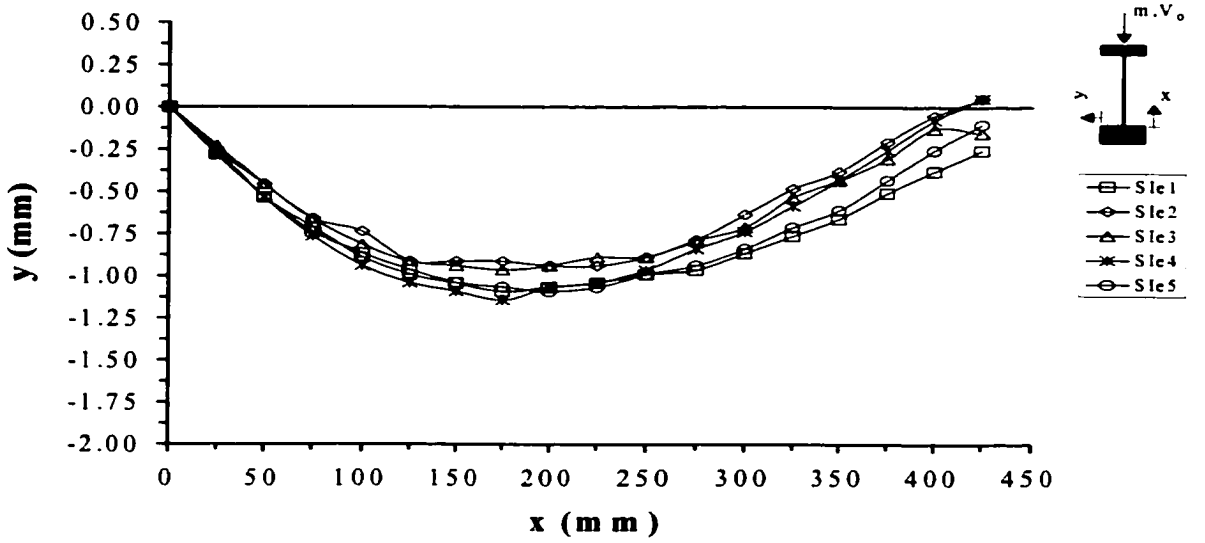

(a)

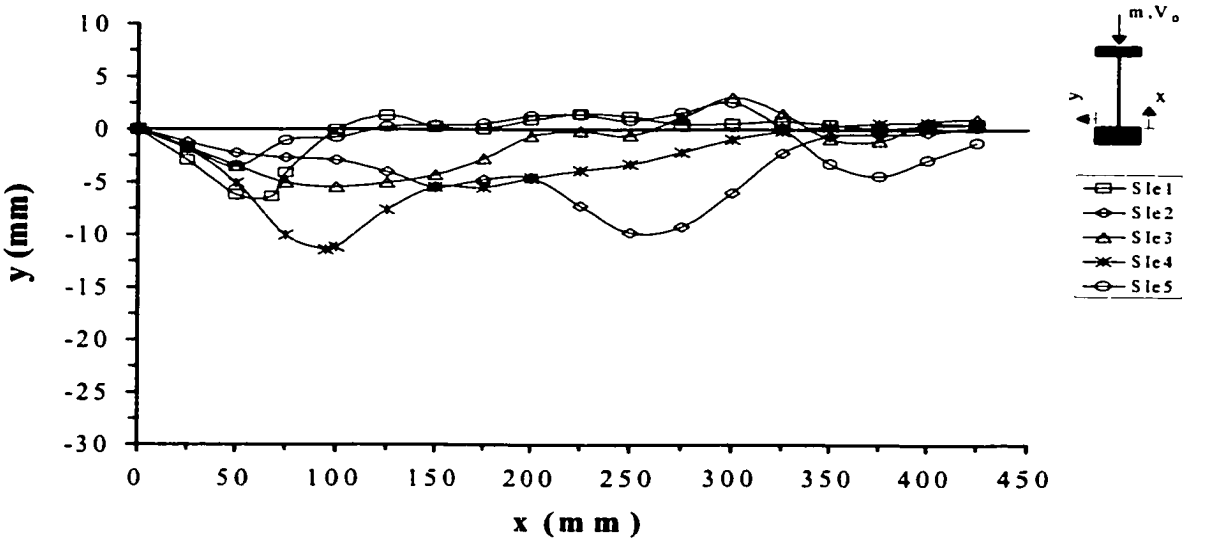

(b)

Figure C-32. Series *SIe*, Tests: 1 to 5, (a) Initial Global Imperfections and (b) Deformed Buckled Profiles.

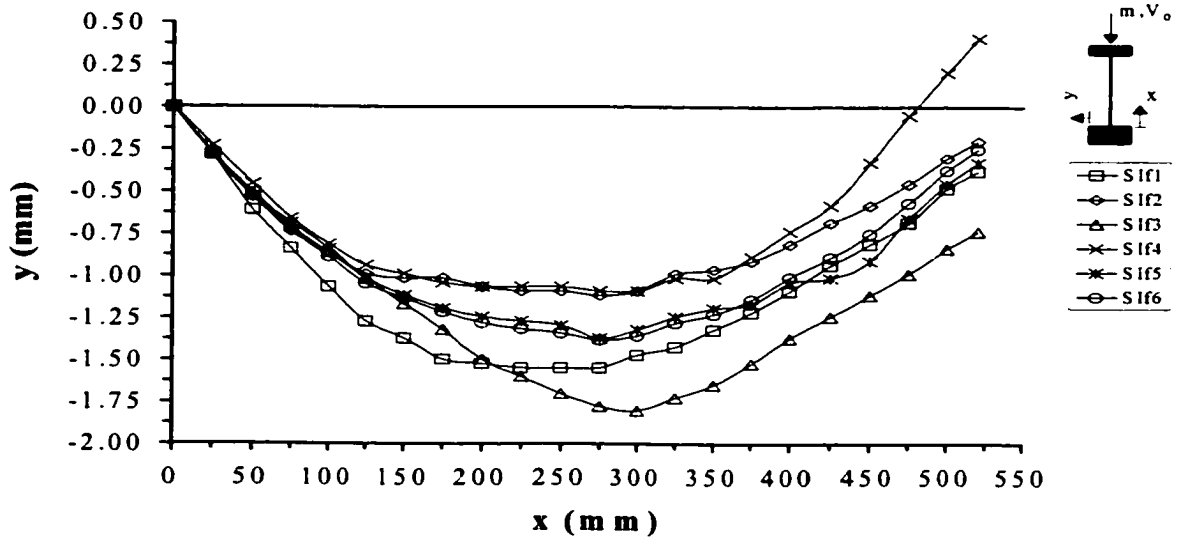

(a)

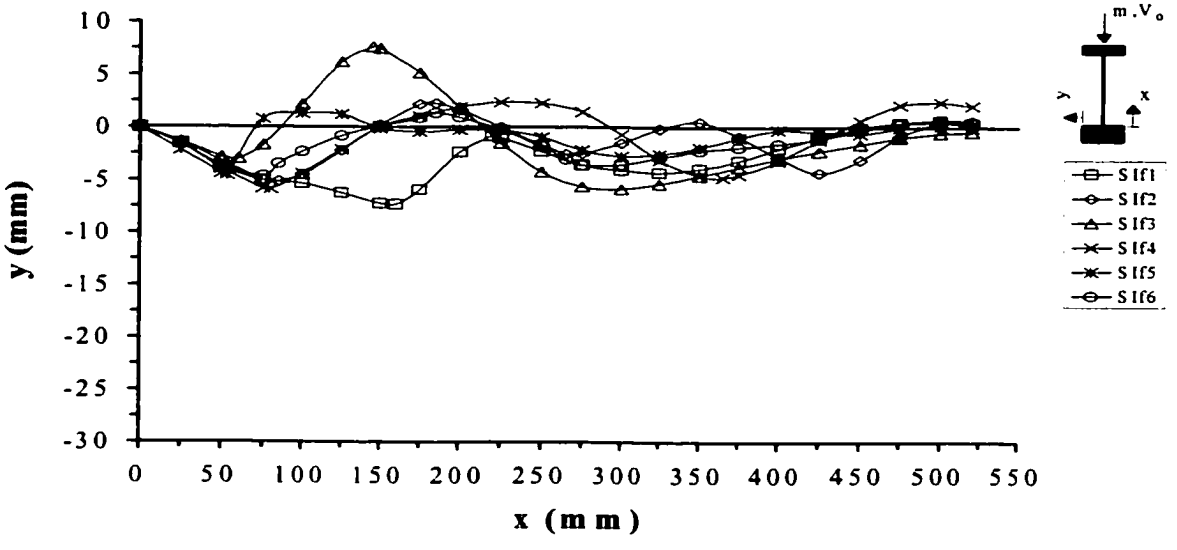

(b)

Figure C-33. Series *Sif*, Tests: 1 to 6, (a) Initial Global Imperfections and (b) Deformed Buckled Profiles.

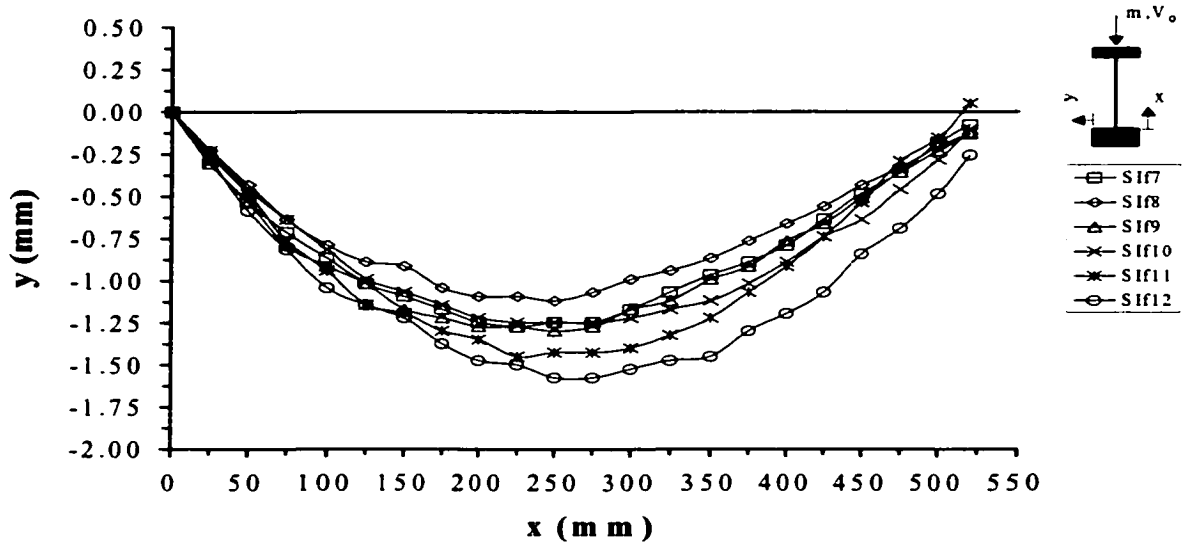

(a)

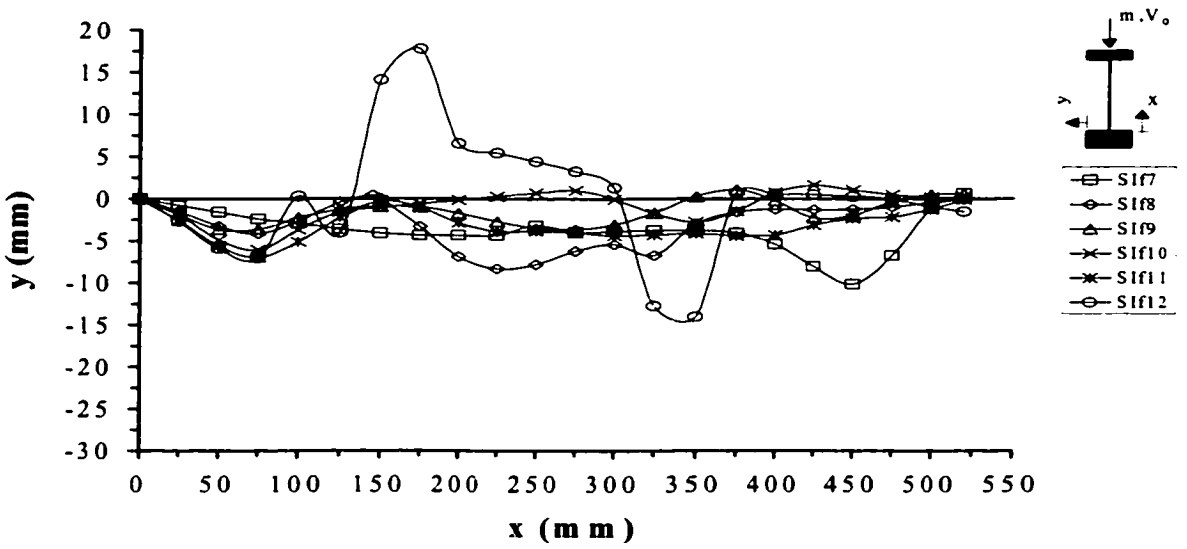

(b)

Figure 34. Series *SIf*, Tests: 7 to 12, (a) Initial Global Imperfections and (b) Deformed Buckled Profiles.

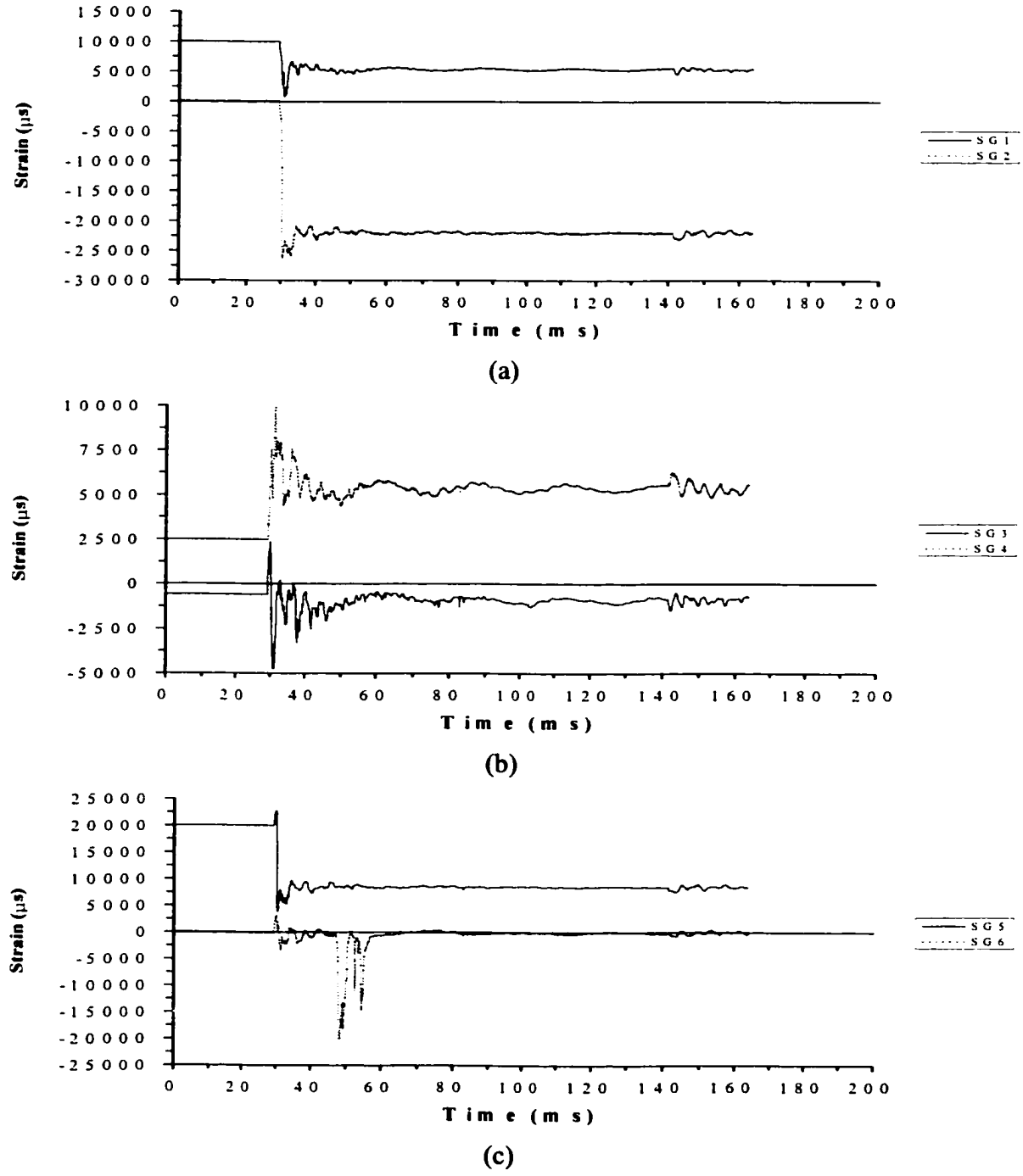

Figure C-35. Strain Record for Test *SIf5*, (a) Strain Gauges #1 and #2, (b) Strain Gauges #3 and #4 and (c) Strain Gauges #5 and #6.

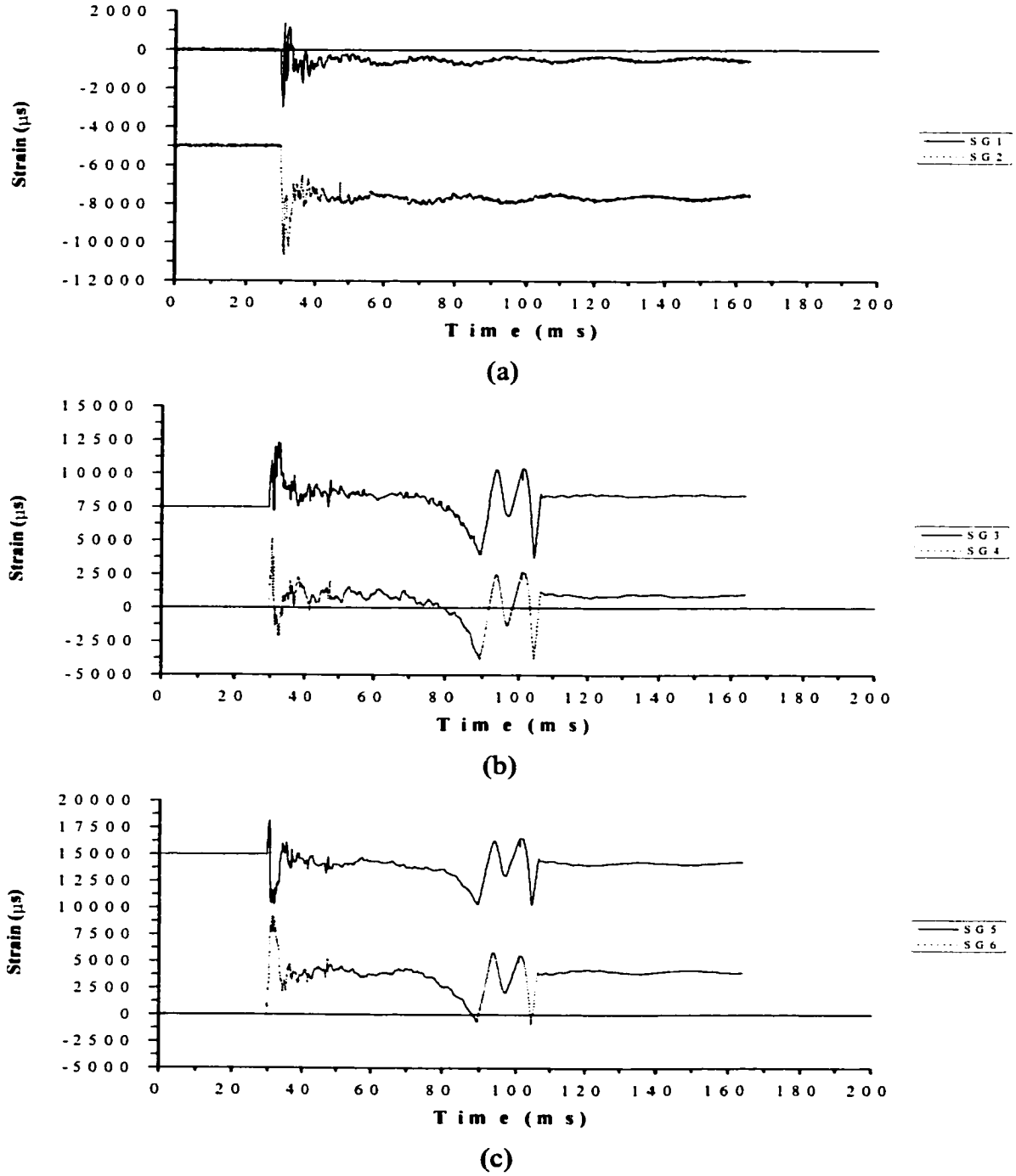

Figure C-36. Strain Record for Test *Slf6*, (a) Strain Gauges #1 and #2, (b) Strain Gauges #3 and #4 and (c) Strain Gauges #5 and #6.

Appendix D Sensitivity Analysis of Plastic Pulse Buckling

A series of preliminary investigations was conducted to assess the influence of several parameters on the computed dynamic plastic pulse buckling response with respect to the observed experimental modal behaviour. These factors include structural boundary conditions, imperfection magnitude and type, discretised element aspect ratio, material properties and element formulation. The sensitivity of these issues are further detailed in Appendix E.

D.1 Analysis of Boundary Conditions

A series of finite element models were developed to investigate the influence of the applied structural boundary condition on the computed pulse buckling response for the slenderness ratios (L_e/r = *75, 150, 250*) of series *AI*. Details of the model parameters and applied structural boundary conditions are discussed in Section 7.1 and Section 7.2. Influence of the imposed boundary condition on the computed displaced mode shapes for the intermediate series *AIc* (L_e/r = *150*, L_u = *275mm*), is illustrated in Figure D-1 for models with a discrete imperfection (Equation 3.17). Models that incorporated random imperfections (Equation 3.20) are shown in Figure D-2. The buckled profile data for Test *AIc7* is also illustrated as a representative experimental modal response for comparison with the numerical analyses. The 75m fixed restraint and 25mm slide bearing support can be seen in Figure D-1(a) and Figure D-2(a). The models with random geometric imperfections did not exhibit the same sensitivity to the idealized boundary condition in comparison with models defined by a global fundamental mode imperfection. Examination of the numerical computations for series *AIa*, however, demonstrated that the beam element models were more influenced by changes in the displacement boundary conditions than the plane strain element models when random geometric imperfections were considered. The essential point to be recognized is that, for the parameters investigated, the actual imposed structural boundary condition must be considered for the numerical computations in order to develop an accurate pulse buckling response.

D.2 Analysis of Imperfection Models

For the sensitivity analysis, beam and plane strain element models with an aspect ratio of *AR* = *1:1* were developed. Only elastic, perfectly plastic material behaviour was considered. Discrete, combined and random geometric imperfections were incorporated through Equation 3.17 (discrete) and Equation 3.20 (random).

Pulse buckling computations investigating the lower slenderness ratio ($L_e/r = 75$) for test series *AIa* ($L_u = 137m$, $d = 3.175mm$) are presented in Figure D-3, for beam element and plane strain element models with discrete and random imperfections. The experimental test series data (*AIa3*) is also shown for comparison as a representative measured buckled displacement profile. Similarly, the computed buckled response for the intermediate slenderness ratio ($L_e/r = 150$) of test series *AIIc* ($L_u = 412m$, $d = 4.7625mm$) is illustrated in Figure D-4. Experimental data from impact test *AIIc4* is also plotted for reference.

As shown in Figure D-1(a), D-2(a), D-3 and D-4, the computed displaced profiles were consistent in character for both the beam and plane strain element models with either discrete or random geometric imperfections. Analysis of the finite element computations for other models, represented by the parameter matrix of Table 7-2 and Table 7-3, exhibited similar response characteristics. Thus, based on the parameters investigated, the influence of imperfection model (i.e. discrete, random) on the computed pulse buckling response was of secondary importance.

D.3 Analysis of Element Formulation

The peak crest amplitudes, however, between the beam and plane strain element models were different. In terms of the peak buckle amplitude, the plane strain element models, defined by either discrete or random geometric imperfections, generally exhibited improved response with respect to the representative, experimentally measured displaced profile. This is shown in Figure D-3 and Figure D-4(b). Comparison with Figure D-1(a) and Figure D-2(a) further illustrates the influence of element formulation and imperfection type on the computed buckled response. The computed displaced mode for the plane strain element model of series *AIIc* in Figure D-4(a) illustrates the complex interaction of beam geometry, element type, imperfection formulation and stress wave response.

D.4 Analysis of Constitutive Relationships

The coupled influence of material parameters, aspect ratio and imperfection model on the computed pulse buckling response was also investigated. This is illustrated in Figure D-5 and Figure D-6 for beam and plane strain element models. For the parameters investigated, the analysis demonstrated that for either element formulation (plane strain or beam element), the computed buckling response was not significantly influenced by the constitutive relationships employed. The importance of dynamic material behaviour, however, should be investigated in future studies.

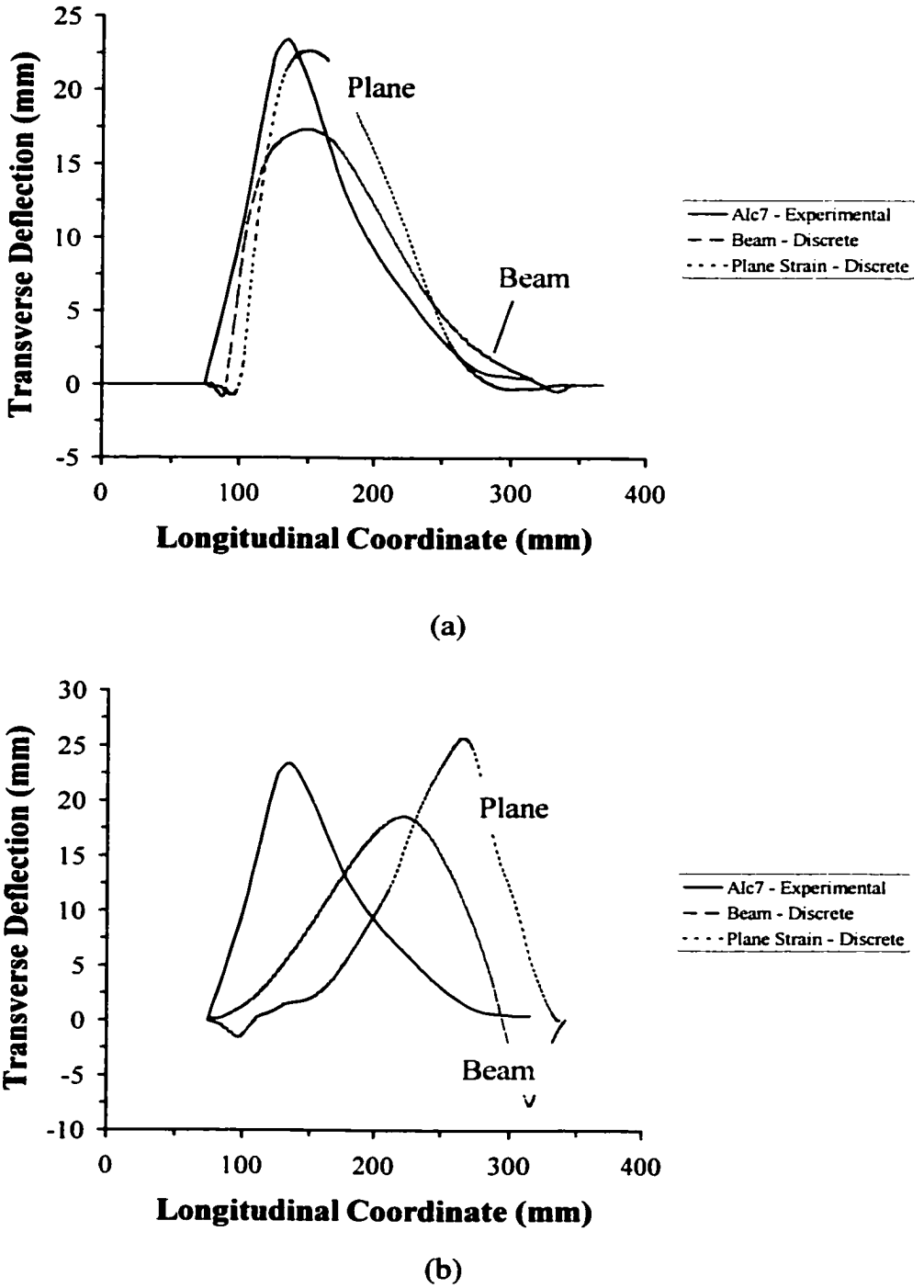

Figure D-1. Buckled Response for Beam and Plane Strain Element Models with Discrete Imperfections (a) Experimental and (b) Idealized Boundary Conditions.

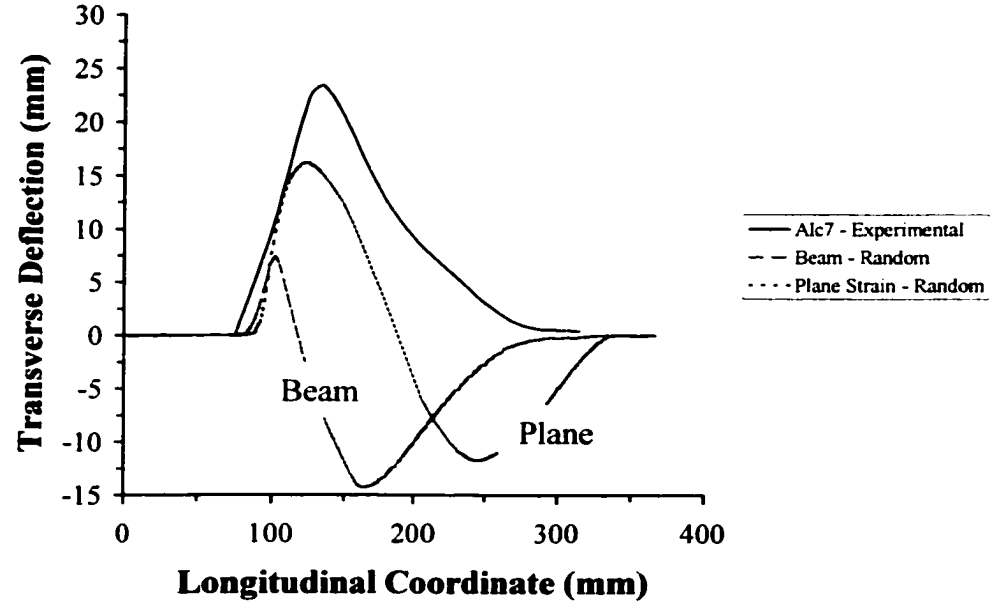

(a)

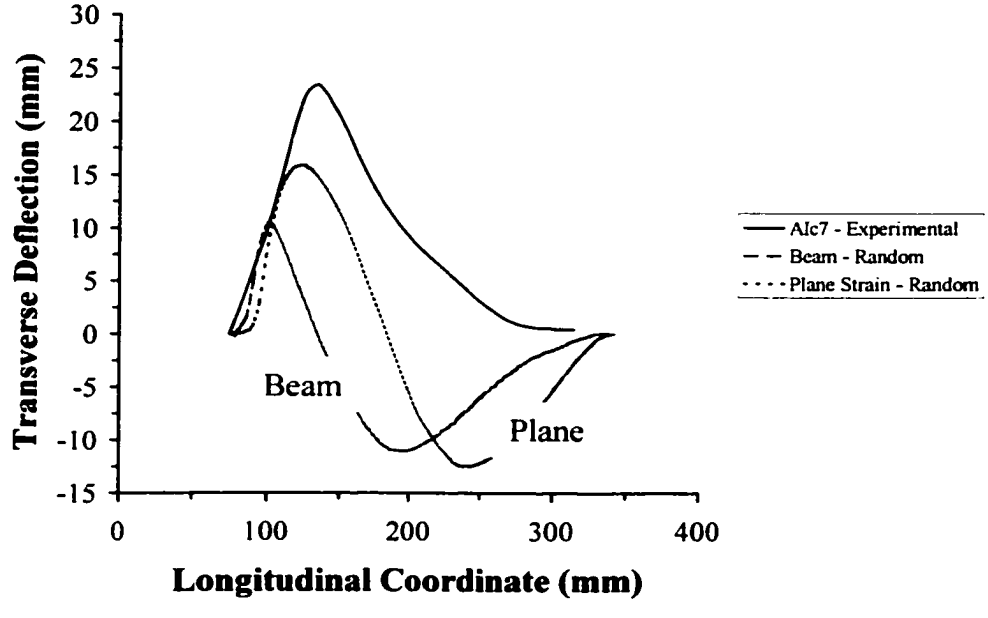

(b)

Figure D-2. Buckled Response for Beam and Plane Strain Element Models with Random Imperfections (a) Experimental and (b) Idealized Boundary Conditions.

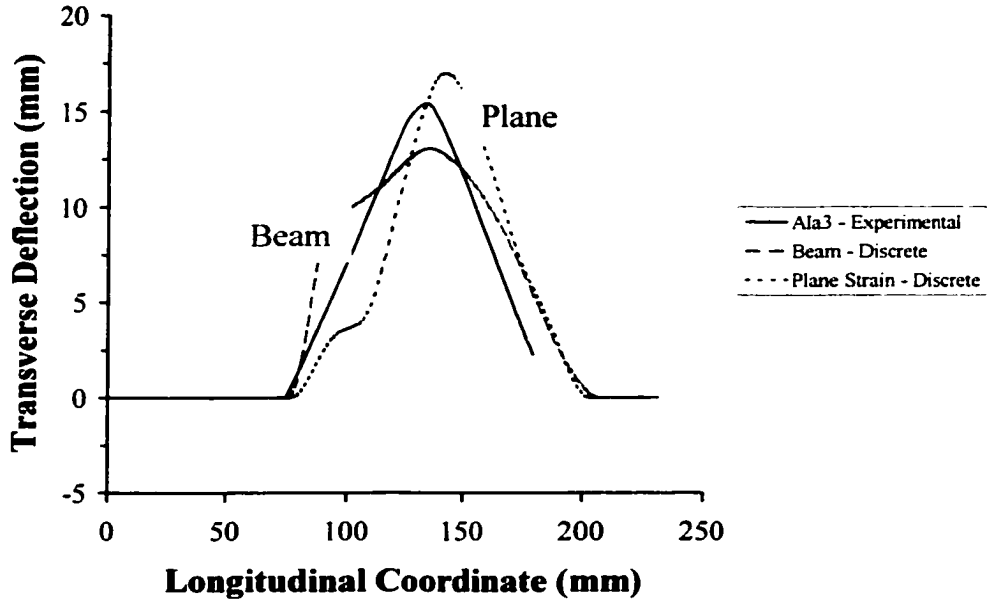

(a)

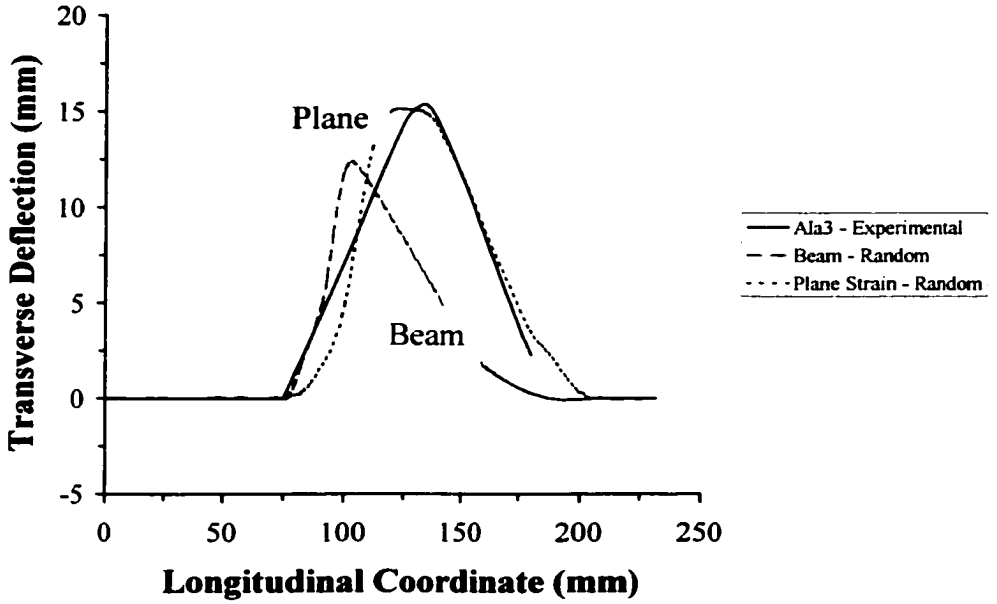

(b)

Figure D-3. Influence of Geometric Imperfection Formulation on the Computed Buckled Response for Series *Ala* (a) Discrete (b) Random.

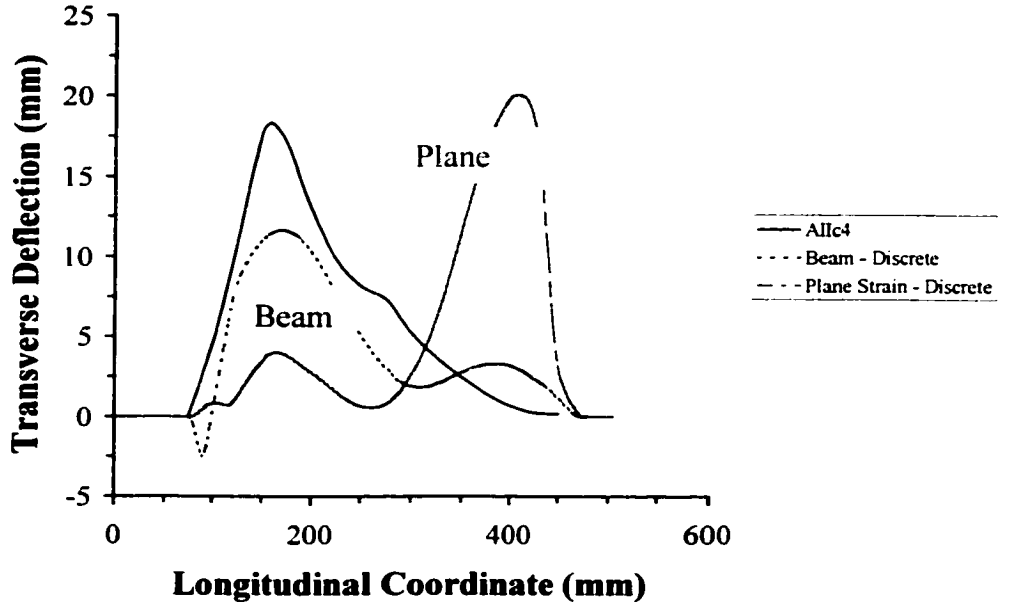

(a)

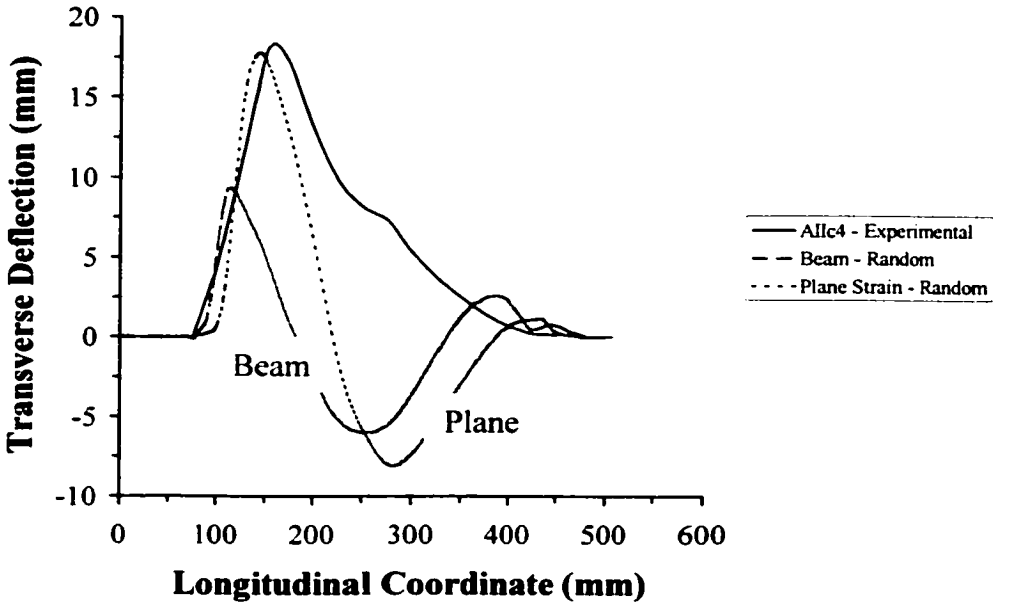

(b)

Figure D-4. Influence of Geometric Imperfection Formulation on the Computed Buckled Response for Series *AIIc* (a) Discrete (b) Random.

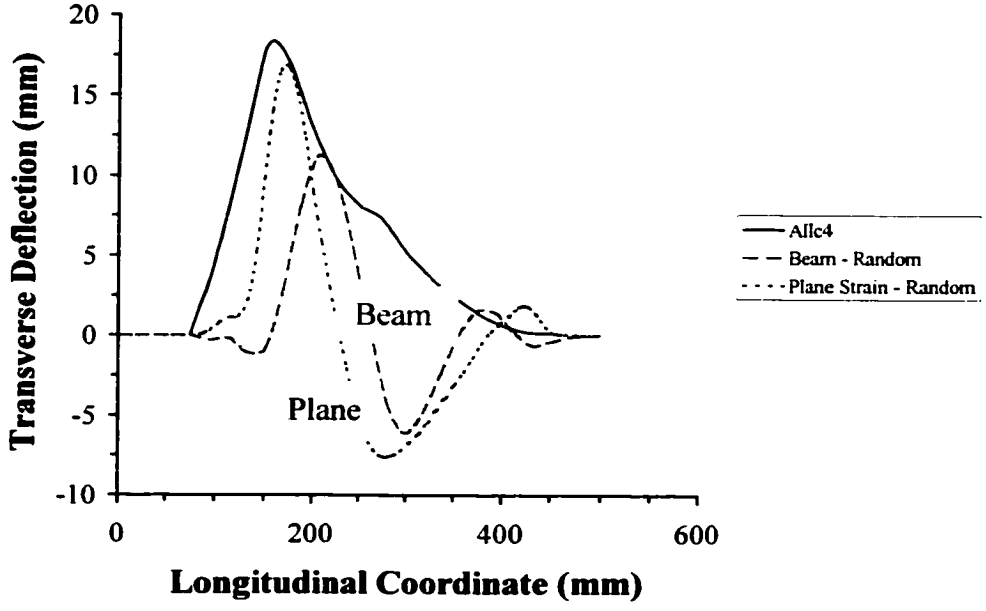

(a)

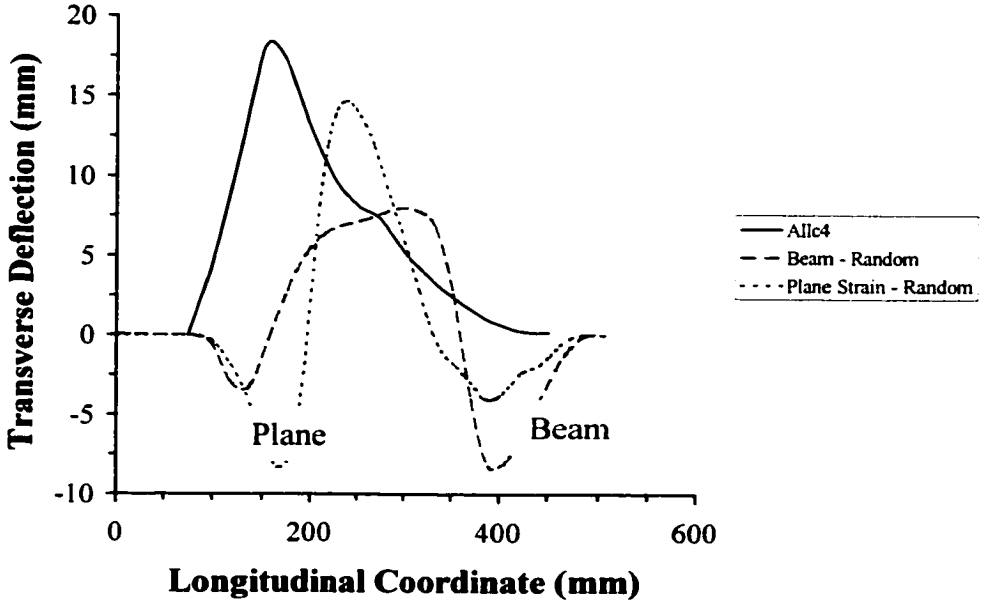

(b)

Figure D-5. Influence of Material Behaviour on the Computed Buckled Response for Series *AIIc* (a) Bilinear Elastoplastic (b) Elastic, Perfectly Plastic Material Response with Aspect Ratio (*AR = 4:1*).

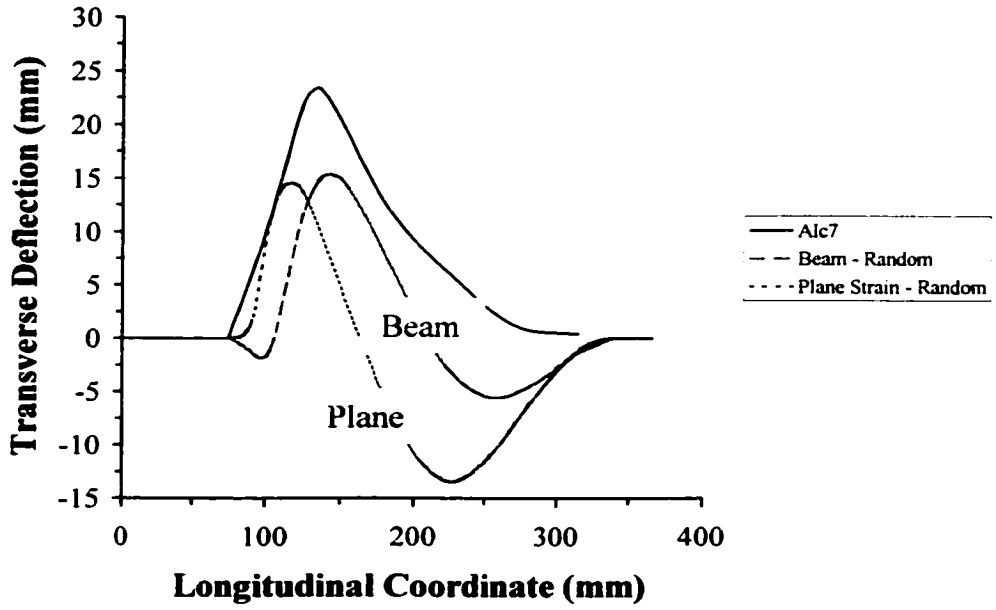

(a)

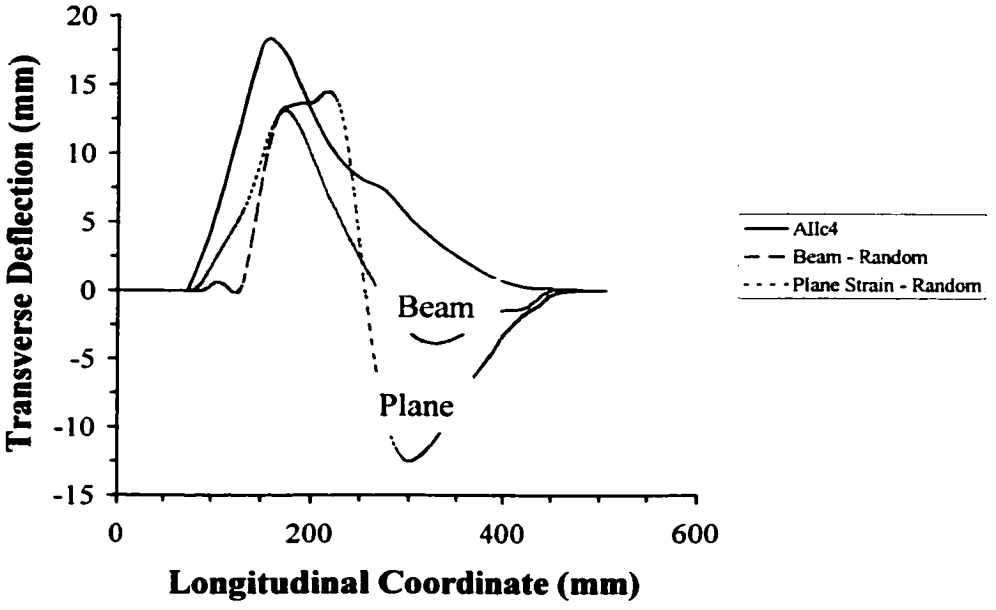

(b)

Figure D-6. Influence of Bilinear Elastoplastic Material Behaviour on the Computed Buckled Response for (a) Series *AIc* (b) Series *AIIc* with Aspect Ratio (*AR = 1:1*).